Durham E-Theses

Multi-jet Phenomenology for Hadron Colliders in the High Energy Limit

BROOKS, HELEN,MARGUERITE

How to cite:

BROOKS, HELEN,MARGUERITE (2017) *Multi-jet Phenomenology for Hadron Colliders in the High Energy Limit*, Durham theses, Durham University. Available at Durham E-Theses Online: http://etheses.dur.ac.uk/12313/

Use policy

Multi-jet Phenomenology for Hadron Colliders in the High Energy Limit

Helen Marguerite Brooks

A thesis submitted for the degree of

Doctor of Philosophy

Institute for Particle Physics Phenomenology

Department of Physics

Durham University

England

July 2017

Multi-jet Phenomenology for Hadron Colliders in the High Energy Limit

Helen Marguerite Brooks

Submitted for the degree of Doctor of Philosophy

July 2017

Abstract

We have incorporated next-to-leading logarithmic corrections into the High Energy Jets (HEJ) formalism and parton-level Monte Carlo generator for W plus inclusive dijet production. This has involved an analytic demonstration of factorisation for the relevant configurations, an extraction of the effective current and proof of its gauge invariance. We have thoroughly validated our numerical implementation and matching of the cross section to leading order accuracy. We have studied the impact of these corrections upon transverse momentum distributions and found a significant improvement in the description of data.

We also present a new merging algorithm, inspired by the CKKW-L method, for combining high energy and soft-collinear logarithms. This has been implemented for HEJ+Pythia. Multiple parton interactions and hadronisation effects are also accounted for, allowing for an accurate description of jets shapes. We find good agreement with data for observables such as the average number of jets and gap fractions which are relevant for understanding the impact of jet vetoes.

Contents

Contents

Declaration

The work in this thesis is based on research carried out at the Institute for Particle Physics Phenomenology, the Department of Physics, Durham University, England. This thesis is based on research which has been carried out in collaboration with Jeppe R. Andersen, Jennifer M. Smillie and Leif Lönnblad. No part of this thesis has been submitted elsewhere for any other degree or qualification and it is all my own work unless referenced to the contrary in the text.

Acknowledgements

First and foremost I would like to thank Jeppe Andersen for his patient supervision and guidance. I would also like to thank my collaborators Jenni Smillie and Leif Lönnblad, for their frequent help and insightful comments.

I am very grateful towards Lund University and everyone in the Theoretical High Energy Physics group for being incredibly welcoming during my short-term MCnet studentship.

I gratefully acknowledge financial support from the UK Science and Technology Facilities Council for the duration of my studies and additionally from the European Union Marie Curie Research Training Network MCnetITN (contract PITN-GA-2012-315877) for funding my short-term studentship in Lund University and my attendance at numerous network meetings.

I would like to thank the incredible community of postdocs and PhD students at the IPPP, without whom my experience would not have been the same. It has been a pleasure to work alongside you. In particular, I would also like to thank the following individuals:

Tuomas Hapola, for helping me right at the beginning when I was getting started, and teaching me how to use the grid.

Andreas Maier, for your advice on all manner of topics, from coding to academia.

Richard Ruiz, for your stimulating conversations and excellent company.

Simon Armstrong, for helping me resolve many programming dilemmas, happily discussing anything from science to politics with me, and for being a wonderful office-mate and friend.

Jessica Turner, for your encouragement, positivity and friendship.

James Black, for challenging me with questions about HEJ and other subjects on a frequent basis.

In addition, thank you to Richard, Andreas, James B, James Whitehead, Giuseppe De Laurentis and Stephen Webster for kindly agreeing to proofread parts of this thesis.

I would like to thank Linda Wilkinson and Trudy Forster, for always ensuring the smooth running of the IPPP, and for always being there to provide a smile. I am extremely grateful to all the IT staff: Oliver Smith, Adam Boutcher and George Fleming. Thank you for maintaining the grid, without which I would likely never have completed any of my work.

Thank you to all of my teammates in ultimate frisbee, for giving me a reason to leave the office from time to time and helping to preserve my sanity.

Finally, to my family, thank you for your constant love and support. To Nick, thank you for always being there through the ups and the downs, for giving me strength every day, and for doing far more than your share of the household chores while this thesis was being written.

Preface

The goal of particle physics is to classify the most fundamental constituents of the universe, and determine how their interactions give rise to physical laws. One of the primary methods for gleaning information in this subject is still to accelerate beams of particles to very high energies and by colliding them convert their energy into new particles. Since different particles leave different signatures in the detectors, in this manner we can determine the particle content of the universe. By measuring how frequently we produce certain particles, we can infer the strength of their interactions.

Our current best description of elementary particle physics is known as the *Standard Model of Particle Physics*, which was completed with the momentous discovery of the Higgs boson by the ATLAS and CMS collaborations [1,2] in 2012. The Standard Model is an interacting quantum field theory, locally invariant under the gauge group $\mathbf{SU}(3) \times \mathbf{SU}(2) \times \mathbf{U}(1)$. This symmetry results in the wonderfully rich phenomenology which we observe in nature. From the $\mathbf{SU}(3)$ gauge group emerges the physics of the strong force which is responsible for the confinement of quarks and gluons into hadrons (such as protons and neutrons which form chemical nuclei). The gauge group $\mathbf{SU}(2) \times \mathbf{U}(1)$ describes the electroweak sector which, through the mechanism of electroweak symmetry breaking mediated by the Higgs (H) boson, determines the interactions of the $W^{\pm}$ and Z bosons and photons (γ). From this arises the more familiar forces of electromagnetism and radioactive decay.

The Standard Model is one of the most predictive and well-tested theories in the history of physics. At the LHC alone, hundreds of measurements have been made, spanning more than ten orders of magnitude and so far there have been no deviations from the Standard Model observed which surpass the to 5σ golden standard required

to constitute a discovery (see for example the summary plots shown in fig. 1 produced by the ATLAS and CMS collaborations [3,4]). The Standard Model however cannot be the final story. The observation of neutrino oscillations [5,6] and implication of non-zero neutrino masses cannot be accommodated into the picture without some extension [7]. Furthermore, astrophysical observations of galaxies and structure formation continue to indicate the presence of matter which couples weakly to regular matter but which is visible through its gravitational effects [8]. Identifying the particle content of this so-called *dark matter* is one of the major goals of the Large Hadron Collider (LHC).

The enormous discovery potential of the LHC is due to the fact that the protons which are collided are not fundamental particles, but composite objects. The protons' energy is shared amongst their constituents, entailing that the centre of mass energy of a given collision is not fixed. This enables a huge spectrum of energies to be explored (and ultimately led to the discovery of the aforementioned Higgs boson). This enticing feature, however, comes at a cost. The fragments of the protons, being charged under the strong force, emit vast amounts of radiation giving rise to streams of particles known as jets. These jets often contribute to large backgrounds which are difficult to reduce.

Given that the Standard Model continues to withstand an onslaught of tests, it is likely that any evidence of new physics will be manifest only as small discrepancies in measurements of couplings or production rates of Standard Model particles. If such signals are to be extracted it is necessary to have precise theoretical modelling of the expected Standard Model backgrounds, in particular those arising from jets which are usually dominant. It is with this objective in mind that this thesis is presented.

This thesis has been written from a phenomenological standpoint. By this we mean that although the topics encountered are inherently theoretical, it is intended the connection with and relevance for experiments is emphasised throughout. There will be a focus on improving the accuracy of predictions for quantities that are experimentally interesting and informative. In chapter 1 we provide an introduction to the quantum field theory of the strong interaction and how

perturbative calculations are performed. We discuss some key concepts such as infrared safety, factorisation and what observables can be measured in collider experiments. Chapter 2 is another introductory chapter, in which we discuss the need for more advanced computational techniques than those of chapter 1. In particular, we introduce the formalisms on which the majority of work in later chapters is based. After a brief detour on numerical methods in chapter 3, we discuss two separate areas in chapters 4 and 5 where tools for improving the precision of calculations involving jets have been developed. In these two chapters we present the main results of the thesis. Finally in chapter 6 we summarise the thesis, and provide some overall conclusions and an outlook on future work.

It is hoped that the most relevant background material has been reviewed sufficiently in chapters 1 and 2. Of course, in a field as diverse as particle physics it is impossible to cover everything, and we comment now on some of the more notable omissions. We do not provide a general introduction to quantum field theories. We also do not discuss electroweak symmetry breaking. Finally, although we sometimes mention the relevance of measurements to searches for new physics, we remain agnostic as to what this might be. For these and many other interesting topics, we refer the reader to any of the many existing texts on the subject, such as [9–13].

(a)

(b)

Figure 1: Summary plots of Standard Model cross section measurements produced by the (a) ATLAS [3] and (b) CMS [4] collaborations, as of July 2017.

Chapter 1

Foundations

In this chapter we explore some of the core concepts that underpin the rest of the thesis. We review what are the minimal steps required for making predictions for observables that can be measured in hadron collider experiments. We begin in sections 1.1 and 1.2 with an introduction to the theory of the strong force. In principle, this is a theory that permits a perturbative expansion in the coupling strength, allowing the use of Feynman rules for calculating scattering amplitudes (see section 1.3). However, in attempting to define this theory down to arbitrarily small distance scales, we are faced by the appearance of unphysical divergences. The procedure for removing such divergences, discussed in section 1.4, results in a coupling strength that not only varies with scale, but also is only defined with respect to an arbitrary reference value, leading to potentially large systematic uncertainties.

One characteristic behaviour that results from the varying coupling is confinement at small scales. This has the consequence that the asymptotic states which formally should be used in calculations are different from those at scales where perturbation theory becomes applicable and at which the calculation is feasible. Fortunately, the factorisation theorem discussed in section 1.5 allows us to circumvent this problem. Nevertheless, there remain restrictions on which observables it is meaningful to calculate. Furthermore we find in section 1.6 that there are some observables whose computation requires methods that go beyond those presented in this chapter.

1.1 Colourful Beginnings

During the 1960s it was observed that the spectrum of baryons and mesons being produced in cloud chamber experiments possessed an approximate $SU(3)$ symmetry [14]. This feature could be explained if these objects were not fundamental, but were instead composed of other particles. Quarks (and antiquarks, their antimatter counterparts) - particles with spin-$\frac{1}{2}$ and fractional electric charge - were proposed to explain the apparent substructure [15–17]: mesons were expected to be bound states of a quark and an antiquark, and baryons (antibaryons) bound states of three quarks (antiquarks). The light quarks, known as up (u), down (d) and strange (s), and those responsible for the approximate symmetry observed were the first to be discovered. Later followed the discoveries of the heavier charm (c) [18, 19], bottom (b) [20] and top (t) [21, 22] quarks. The u, c and t ('up-type') quarks possess charge $+\frac{2}{3}e$, while the d, s and b ('down-type') quarks have charge $-\frac{1}{3}e$. These six species of quarks (plus the six antiquarks with opposite charge) are known as *flavours.*

This was not enough, however. Two spin-$\frac{3}{2}$ baryons composed of identical flavour quarks with their spins aligned, the Δ^{++} (uuu) and Ω^- (sss), were known. As each of these baryons also have zero orbital angular momentum, to obtain the totally anti-symmetric wave-function required by Fermi-Dirac statistics, another degree of freedom was needed. The solution was provided by the proposal that quarks carry an additional quantum number [23], named *colour.*

This implied the existence of a new fundamental symmetry of nature, the simplest being the non-Abelian group $SU(N_c)$. Each quark would be associated with a multiplet of Dirac fields ψ_i in the fundamental representation of $SU(N_c)$, where the index i runs from 1 to $N_c = 3$, representing the possible number 'colours' a quark could be, often labelled as red, green and blue. Similarly, antiquarks would be associated with Dirac fields $\bar{\psi}_i$ in the anti-fundamental representation of $SU(N_c)$. The quark fields then transform according to:

$$\psi_i(x) \to U_{ij}\psi_j(x) \ , \tag{1.1.1}$$

where $U = e^{i\alpha^a T^a}$ is an element of $SU(N_c)$; T^a are generators of $SU(N_c)$ in the

13

1.1. Colourful Beginnings

fundamental representation and obey the Lie algebra:

$$[T^a, T^b] = i f_{abc} T^c \, , \tag{1.1.2}$$

where f_{abc} are known as *structure constants*. By convention, $\text{Tr}(T^a T^b) = \frac{1}{2}\delta^{ab}$ in the fundamental representation, fixing the quadratic Casimir operators[1] for all irreducible representations of $SU(N_c)$. In the fundamental representation we obtain $C_F = \frac{N_c^2 - 1}{2N_c} = \frac{4}{3}$ and in the adjoint representation $C_A = N_c = 3$ [9].

Since we do not see colour on macroscopic scales in nature, hadrons must be singlet representations of this transformation. Such singlet states can be constructed as $\psi_i \bar{\psi}^i$, $\varepsilon^{ijk} \psi_i \psi_j \psi_k$, and $\varepsilon^{ijk} \bar{\psi}_i \bar{\psi}_j \bar{\psi}_k$, giving a natural representation for meson, baryons and antibaryons respectively. The totally anti-symmetric tensor ε^{ijk} automatically ensures the anti-symmetry of baryons under colour exchange that is needed to explain the observations of Δ^{++} and Ω^-.

Yet the addition of this new symmetry seemed somewhat arbitrary, and neglected to provide an explanation of why quarks should only exist in bound colour-singlet states. This picture also seemed inconsistent with deep inelastic scattering experiments, where it had been observed that the point-like components of hadrons were loosely bound [24]. The resolution came by requiring invariance under eq. (1.1.1) for the general class of continuous functions $\alpha(x)$ depending on the spacetime point x, thereby promoting our $SU(3)$ invariance to a local *gauge* symmetry:

$$\psi_i(x) \to U_{ij}(x) \psi_j(x) \, , \tag{1.1.3}$$

with elements $U(x) = e^{i\alpha^a(x)T^a}$. It was realised that non-Abelian gauge theories naturally give rise to the phenomenon of *asymptotic freedom* in which fields behave freely at high energies, and interact strongly at low energies leading to confinement (which we discuss further in section 1.4) [25, 26]. Thus both the observations of hadron spectroscopy and deep inelastic scattering could explained simultaneously.

Invariance of nature under a local $U(1)$ phase transformation of the electron field had already been seen to imply the existence of the vector potential A^μ

---

[1] For a general representation r of $SU(N)$ the quadratic Casimir operator is defined as $T_r^a T_r^a = C_2(r)\mathbf{1_r}$, with $\mathbf{1_r}$ a unit matrix in the dimension of the representation r.

corresponding to the photon, and gave rise to the theory of quantum electrodynamics (QED). The generalisation of this idea to invariance under any continuous symmetry transformation, which is manifest as a fundamental property of nature, is known as the *gauge principle*.

In the next section we construct a model invariant under the gauge transformation in eq. (1.1.3). The resulting theory of colour and the strong force, Quantum Chromodynamics (or QCD) has a rich phenomenology which we proceed to expose in the rest of this chapter.

1.2 The QCD Lagrangian

The starting point in any quantum field theory is the Lagrangian density $\mathcal{L}$ (which hereafter is simply referred to as the Lagrangian). It provides a way of specifying the degrees of freedom in a system, which are determined by the symmetries which exist in nature. In a quantum field theory, the degrees of freedom are manifest as operator-valued functions of space and time, or *fields* $\phi(x)$; the Lagrangian is a function of these fields and their derivatives $\partial_\mu \phi(x)$, and relates to the action functional through

$$S = \int \mathrm{d}^4 x \, \mathcal{L}(\phi(x), \partial_\mu \phi(x)) \,. \tag{1.2.1}$$

All particle content, interactions and coupling strengths of a given model are specified in the Lagrangian, the usefulness of which ultimately arises through its connection to observable quantities. For example, in the context of perturbative field theories, the Lagrangian can be used to derive Feynman rules, from which it is possible to compute the cross section, which in turn can be measured in collider experiments. This is discussed in greater detail in section 1.3.

The Lagrangian of QCD must be a function of the spin-$\frac{1}{2}$ quark fields $\psi(x), \bar{\psi}(x)$ described in the preceding section, and must be invariant under the transformation 1.1.3 (known as *gauge invariance*). It must be Lorentz invariant and also satisfy *renormalisability* which is a property we discuss further in section 1.4. The result is the Yang-Mills Lagrangian, given by [9]:

$$\mathcal{L}_{\text{Yang-Mills}} = -\frac{1}{4} F_{\mu\nu}^a F^{a\mu\nu} + \bar{\psi}(x)(i\slashed{D} - m)\psi(x) \,. \tag{1.2.2}$$

1.2. The QCD Lagrangian

Here we have suppressed flavour indices for convenience, and summation over repeated indices is implied. The parameter m is the quark mass. The field strength tensor $F_{\mu\nu}^a$ is given by:

$$F_{\mu\nu}^a = \partial_\mu A_\nu^a - \partial_\nu A_\mu^a + g_s f^{abc} A_\mu^b A_\nu^c \,, \tag{1.2.3}$$

where g_s is the strong coupling, and A_μ^a is the gauge field whose quanta correspond to the gauge bosons of QCD, *gluons*. The gluon field transforms in the adjoint representation, according to [9]:

$$A_\mu^a(x)T^a \to U(x)\left(A_\mu^a(x)T^a + \frac{i}{g_s}\partial_\mu\right)U^\dagger(x) \tag{1.2.4}$$

In eq. (1.2.2) we have used the 'slashed' notation to denote:

$$\slashed{D} = \gamma^\mu D_\mu \,, \tag{1.2.5}$$

where the four γ-matrices satisfy the Clifford algebra:

$$\{\gamma^\mu, \gamma^\nu\} = 2\eta^{\mu\nu} \,. \tag{1.2.6}$$

The covariant derivative is given by:

$$D_\mu\psi(x) = \gamma^\mu\left(\partial_\mu - ig_s A_\mu^a T^a\right)\psi(x) \,. \tag{1.2.7}$$

Equation (1.2.2) is sometimes referred to as the *classical* QCD Lagrangian. If we want to quantise the theory and derive the Feynman rules, some additional terms need to be included. Using the Faddeev-Popov method of gauge fixing we obtain the following contribution to the Lagrangian [9]:

$$\mathcal{L}_{\text{gauge-fixing}} = -\frac{1}{2\xi}\left(\partial^\mu A_\mu^a\right)^2 \,, \tag{1.2.8}$$

where ξ may be any finite constant. Two frequently used choices are:

$$\xi \to 0 \qquad\qquad \text{Landau gauge,}$$

$$\xi \to 1 \qquad\qquad \text{Feynman gauge,}$$

where it is understood that the limit is taken after quantisation. A term of this kind is needed to quantise any locally invariant theory. It is needed to prevent

the integration over a continuously infinite set of physically equivalent degrees of freedom in the functional integral that is used to compute correlation functions (needed to derive the Feynman rules). In addition, in non-Abelian gauge theories, negative degrees of freedom must be added to cancel the non-physical timelike and longitudinal polarisation states of the gauge bosons: these are manifest as anticommuting complex scalar fields, c and $\bar{c}$, known as *Faddeev-Popov ghosts*[2]. These ghosts give rise to their own set of Feynman rules, and the corresponding diagrams must be included in loop diagram calculations. The corresponding Lagrangian is given by [9]:

$$\mathcal{L}_{\text{ghost}} = \bar{c}^a \left(-\partial^2 \delta^{ac} - g_s \partial^\mu f^{abc} A_\mu^b \right) c^c , \tag{1.2.9}$$

where δ^{ac} is the Kronecker delta. The full Lagrangian of QCD is then given by the sum all terms:

$$\mathcal{L}_{\text{QCD}} = \mathcal{L}_{\text{Yang-Mills}} + \mathcal{L}_{\text{gauge-fixing}} + \mathcal{L}_{\text{ghost}} . \tag{1.2.10}$$

Although we have explicitly broken gauge invariance at the level of the Lagrangian by fixing the gauge, it may be shown that the Faddeev-Popov method nevertheless gives rise to gauge invariant S-matrix elements (a quantity we discuss in the next section), and hence physically measurable quantities such as the cross section do not depend on the choice of gauge. It should be noted however that intermediate steps of a given calculation do depend on the gauge choice; a particular example of this is the precise form of the gluon propagator.

We conclude this section by noting that although eq. (1.2.2) is consistent with the conditions of gauge invariance and renormalisability, it is not the most general Lagrangian which we could have written down. In particular, we could have included the so-called 'theta term' [9]:

$$\mathcal{L}_\theta = \frac{\theta g_s^2}{64\pi^2} \epsilon^{\mu\nu\lambda\sigma} F_{\mu\nu}^a F_{\lambda\sigma}^a . \tag{1.2.11}$$

This CP-violating term can be written as a total divergence, contributing only a surface term to the action, and is thus not relevant for perturbation theory and

---

[2]In fact, this is only true if we have used a covariant gauge as the gauge choice. There exist certain non-covariant gauge choices for which ghosts are not required.

the derivation of Feynman rules. However, a non-perturbative analysis of this term suggests it would give rise to an electric dipole moment in the neutron, a phenomenon that has been searched for with very high precision and not seen; the coefficient θ is therefore constrained to be very close to zero [27]. Yet a priori there is no reason or symmetry which would suggest that this term should be suppressed; its unexplained smallness is known as the *strong CP problem.* One possible solution is to convert θ to a parameter which may be dynamically driven to be small. This may be achieved in the Peccei-Quinn mechanism [28], which also predicts the existence of pseudo-scalar fermions known as *axions*, though such particles have not yet been observed.

1.3   Feynman Rules and the Cross Section

In order to test whether our theory of fundamental particles and interactions encoded by the Lagrangian is correct, we must connect it to a quantity which is measurable in experiments. The modern approach to probing such interactions is through scattering experiments in which two beams of particles may collide. The number of scattering events per unit time N is related to the to number of incoming beam particles per unit area per unit time, or *flux F*, by the *cross section σ*:

$$\sigma = \frac{N}{F} \ .$$

(1.3.1)

The cross section, which is an effective area, may be connected to the probability for a given scattering to occur. This in turn can be related to the transition amplitude between a set of asymptotically defined 'in' and 'out' states of definite momentum, given by:

$$
\begin{aligned}
{}_{\text{out}}\langle \mathbf{p}_1 \mathbf{p}_2 \ldots | \mathbf{k}_A \mathbf{k}_B \rangle_{\text{in}} &= \lim_{T \to \infty} \langle \underbrace{\mathbf{p}_1 \mathbf{p}_2 \ldots}_{T} | \underbrace{\mathbf{k}_A \mathbf{k}_B}_{-T} \rangle \\
&= \lim_{T \to \infty} \langle \mathbf{p}_1 \mathbf{p}_2 \ldots | e^{-iH(2T)} | \mathbf{k}_A \mathbf{k}_B \rangle \\
&= \lim_{T \to \infty} \langle \mathbf{p}_1 \mathbf{p}_2 \ldots | S | \mathbf{k}_A \mathbf{k}_B \rangle \ .
\end{aligned}
$$

(1.3.2)

In the last two lines the states are defined at some common reference time. The unitary operator in the last line is known as the *S-matrix*. Typically we isolate the

part of the S-matrix that corresponds to interactions as follows:

$$S = \mathbf{1} + iT \ . \tag{1.3.3}$$

The matrix elements for the T operator should encode four momentum conservation, and we therefore anticipate it will contain the factor $\delta^4(k_A + k_B - \sum p_f)$; by extracting this factor we can define the *Lorentz invariant matrix element* $\mathcal{M}$:

$$\langle \mathbf{p}_1 \mathbf{p}_2 \dots | iT | \mathbf{k}_A \mathbf{k}_B \rangle = (2\pi)^4 \delta^4(k_A + k_B - \sum p_f) i\mathcal{M}(k_A k_B \to \{p_f\}) \ . \tag{1.3.4}$$

The cross section then relates to the matrix element through:

$$\sigma = \int \left(\prod_f \frac{d^3 p_f}{(2\pi)^3} \frac{1}{2E_f} \right) \frac{|\mathcal{M}(k_A k_B \to \{p_f\})|^2}{2E_A E_B |v_A - v_B|} (2\pi)^4 \delta^4(k_A + k_B - \sum p_f) \ . \tag{1.3.5}$$
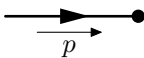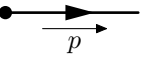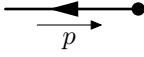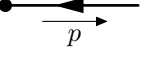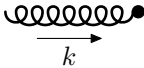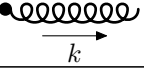
The matrix elements $\mathcal{M}$ may be computed directly using the Feynman rules. These state that the quantity $i\mathcal{M}$ is equal to the sum of all *connected, amputated* Feynman diagrams. By connected we mean that there are no vacuum bubbles, and that all external lines are all connected with each other; diagrams which violate this condition only give rise to an overall phase shift of the vacuum energy and are not relevant to the S-matrix. By amputated we mean that there should exist no loops whose internal propagators have both ends connecting to the same external leg. The importance of this condition will become apparent in section 1.4.

Each diagram is evaluated by making the replacements summarised in table 1.1 (for the case of QCD), noting that Dirac indices should be contracted along fermion lines, and additionally one must:

- Impose momentum conservation at each vertex.

- Integrate over each undetermined loop momentum p_l with the measure $\frac{d^4 p_l}{(2\pi)^4}$.

- Multiply by a factor of -1 for each odd permutation of fermions relative to a reference order.

- Multiply by a factor of -1 for each fermion or ghost loop.

- Divide by the symmetry factor.

External lines	
	$= u^s(p)$
	$= \bar{u}^s(p)$
	$= \bar{\nu}^s(p)$
	$= \nu^s(p)$
	$= \varepsilon_\mu(k)$
	$= \varepsilon_\mu^*(k)$
Internal lines	
	$= \dfrac{i\delta_{ij}(\not{p}+m)}{p^2 - m^2 + i\epsilon}$
	$= \dfrac{-i\delta^{ab}}{k^2 + i\epsilon}\left(g_{\mu\nu} - (1-\xi)\dfrac{k_\mu k_\nu}{k^2}\right)$
	$= \dfrac{i\delta^{ab}}{k^2}$

Vertices

a, μ

$i \qquad\qquad j$

$$= ig_s \gamma^\mu T_{ij}^a$$

a, μ

$c \qquad\qquad b$
$\quad k$

$$= -g_s f^{abc} k^\mu$$

b, ν
$\downarrow p$

$a, \mu \qquad\qquad c, \rho$
$\quad k \qquad q$

$$= \begin{aligned} g_s f^{abc} [\quad & g^{\mu\nu}(k-p)^\rho \\ & +g^{\nu\rho}(p-q)^\mu \\ & +g^{\rho\mu}(q-k)^\nu] \end{aligned}$$

$a, \mu \qquad\qquad b, \nu$

$c, \rho \qquad\qquad d, \sigma$
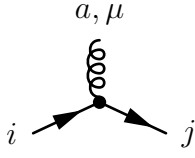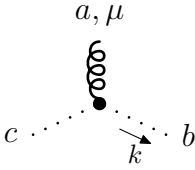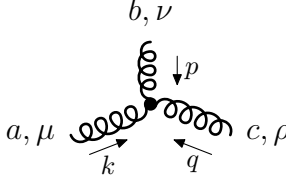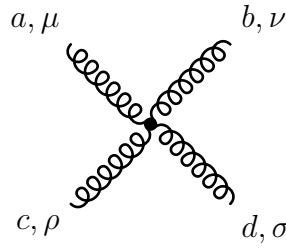
$$= \begin{aligned} -ig_s^2 [& f^{abc}f^{cde}(g^{\mu\rho}g^{\nu\sigma} - g^{\mu\sigma}g^{\nu\rho}) \\ & +f^{ace}f^{bde}(g^{\mu\nu}g^{\rho\sigma} - g^{\mu\sigma}g^{\nu\rho}) \\ & +f^{ade}f^{bce}(g^{\mu\nu}g^{\rho\sigma} - g^{\mu\rho}g^{\nu\sigma})] \end{aligned}$$

Table 1.1: The momentum space Feynman rules of QCD for the general class of Lorentz (covariant) gauges [9].

1.3. Feynman Rules and the Cross Section

In principle there are an infinite number of Feynman diagrams to write down for a given process; however, it is understood that the coupling strength g_s is small and thus we can expand the cross section to a given order in g_s to which only a finite number of diagrams contribute.

External quark and antiquark lines in Feynman diagrams correspond to the four component spinors $u^s(p)$ and $\nu^s(p)$ which respectively are the positive frequency ($\psi(x) = u^s(p)e^{-ip.x}$) and negative frequency ($\psi(x) = \nu^s(p)e^{+ip.x}$) solutions to the Dirac equation:

$$(i\slashed{\partial} - m)\psi(x) = 0 \ . \tag{1.3.6}$$

The general solution to the Dirac equation can be written as a linear combination of these plane wave solutions. The spinors satisfy the spin sums:

$$\sum_s u^s(p)\bar{u}^s(p) = \slashed{p} + m \ , \tag{1.3.7}$$

$$\sum_s \nu^s(p)\bar{\nu}^s(p) = \slashed{p} - m \ . \tag{1.3.8}$$

Here we use the notation $\bar{\psi} = \psi^\dagger \gamma^0$. In the *chiral* basis, in which the gamma matrices have the representation[3]:

$$\gamma^\mu = \begin{pmatrix} 0 & \sigma^\mu \\ \bar{\sigma}^\mu & 0 \end{pmatrix} \tag{1.3.9}$$

and the spinors can be explicitly represented by:

$$u^s(p) = \begin{pmatrix} \sqrt{p \cdot \sigma}\xi^s \\ \sqrt{p \cdot \bar{\sigma}}\xi^s \end{pmatrix} \qquad \nu^s(p) = \begin{pmatrix} \sqrt{p \cdot \sigma}\eta^s \\ -\sqrt{p \cdot \bar{\sigma}}\eta^s \end{pmatrix} \qquad s = 1, 2 \tag{1.3.10}$$

where ξ^s and η^s each correspond to a basis of two component spinors. The choice $\xi^1 = \begin{pmatrix} 1 \\ 0 \end{pmatrix}$ and $\xi^2 = \begin{pmatrix} 0 \\ 1 \end{pmatrix}$ corresponds to spin-up and spin-down aligned along the z-axis. The same choice for η^s leads to spins aligned in the opposite direction.

At this point it is convenient to introduce the concept of *helicity*, which is defined as the projection of spin angular momentum along the direction of momentum.

---

[3]Here $\sigma^\mu = (1, \boldsymbol{\sigma})$, $\bar{\sigma}^\mu = (1, -\boldsymbol{\sigma})$ and $\boldsymbol{\sigma} = (\sigma_1, \sigma_2, \sigma_3)$ are the conventional Pauli-Dirac matrices.

Spin-$\frac{1}{2}$ particles whose spin is aligned with their momentum have helicity $+\frac{1}{2}$ and are said to be right-handed, whilst those with anti-aligned spin have helicity $-\frac{1}{2}$ and are said to be left-handed. Thus the choice of basis $\xi^1 = \left(\begin{smallmatrix}1\\0\end{smallmatrix}\right)$ and $\xi^2 = \left(\begin{smallmatrix}0\\1\end{smallmatrix}\right)$ corresponds to right- and left-handed spinors respectively. Similarly, the same choice for η^s leads to left- and right-handed spinors respectively.

We can project out the left- and right-handed components from a general spinor:

$$u_\pm(p) = P_{\substack{R\\L}} u(p) = \left(\frac{1 \pm \gamma^5}{2}\right) u(p) \tag{1.3.11}$$

$$\nu_\mp(p) = P_{\substack{R\\L}} \nu(p) = \left(\frac{1 \pm \gamma^5}{2}\right) \nu(p) \,, \tag{1.3.12}$$

where $\gamma^5 = -i\gamma^0\gamma^1\gamma^2\gamma^3$. This is useful because the only term which couples the left and right handed spinors is the mass term. As quark masses are typically small[4] they can usually be neglected, and the Dirac equation decouples into two separate *Weyl* equations. Furthermore, in the massless limit we find that:

$$u_\pm(p) = \nu_\mp(p) \,. \tag{1.3.13}$$

Thus we can use the more compact *spinor-helicity* notation:

$$u_\pm(p) = \nu_\mp(p) = |p^\pm\rangle \tag{1.3.14}$$

$$\bar{u}_\pm(p) = \bar{\nu}_\mp(p) = \langle p^\pm| \,. \tag{1.3.15}$$

External gluons are denoted by the *polarisation vector* $\varepsilon_\mu(k)$. Massless gluons of definite helicity $\lambda = \pm 1$ may be represented in spinor-helicity formalism by [29]:

$$\varepsilon_\mu^\pm(k) = \pm\frac{\langle q^\mp|\gamma_\mu|k^\mp\rangle}{\sqrt{2}\langle q^\mp|k^\pm\rangle} \,, \tag{1.3.16}$$

where k is the gluon momentum, and q is any massless reference vector not proportional to k. The polarisation vectors then satisfy the sum rule:

$$\sum_{\lambda=\pm1} \varepsilon_\mu^\lambda(\varepsilon_\nu^\lambda)^* = -g_{\mu\nu} + \frac{k_\mu q_\nu + k_\nu q_\mu}{k \cdot q} \,. \tag{1.3.17}$$

---

[4]The exception to this is the top mass; however we do not consider the top quark to be 'free'.

1.4 Renormalisation and the Running Coupling

In principle we now have the tools to calculate any partonic scattering process. In practice, this is not the case, and as soon as we attempt to calculate beyond leading order we encounter infinities. Let us suppose we want to compute the next-to-leading order correction to the quark propagator, known as the *quark self-energy* $\Sigma(\not p, m)$, or a correction to the quark-gluon vertex, $\Gamma^\mu(p, q, m)$, as shown in figs. 1.1a and 1.1b respectively.

Each of these diagrams contains a loop, and according to the Feynman rules discussed in the previous section we must integrate over any unconstrained momenta. Omitting factors for external legs, the Feynman rules give us:

$$\Sigma(\not p, m) = -g_s^2 \left(T^a T^a\right)_{ij} \int \frac{d^4 k}{(2\pi)^4 i} \frac{\gamma^\mu(\not p + \not k + m)\gamma_\mu}{[(p+k)^2 - m^2]} \tag{1.4.1}$$

$$\Gamma^\mu(p, q, m) = g_s^3 \left(T^b T^a T^b\right)_{ij} \int \frac{d^4 k}{(2\pi)^4} \frac{\gamma_\nu(\not p + \not q + \not k + m)\gamma_\mu(\not q + \not k + m)\gamma^\nu}{[(p+q+k)^2 - m^2][(q+k)^2 - m^2]k^2} . \tag{1.4.2}$$

Performing naive dimensional analysis tells us that the integrand in eq. (1.4.1) for $\Sigma(\not p, m)$ has mass dimension -3, whilst the integration measure has mass dimension +4, so the integral itself has mass dimension 1 and scales as the loop momentum k. Since we integrate over $k \in [0, \infty]$ we therefore expect this term to diverge as $k \to \infty$; a more careful analysis (for example, using the method of Feynman parameters [9]) tells us this is indeed the case. In eq. (1.4.2) the mass dimension of the integral is zero; a careful analysis tell us that this diagram has a logarithmic divergence as $k \to \infty$. In both cases, since they occur at large momentum scales, these are known as *ultraviolet* (UV) divergences.

These diagrams are examples of higher order corrections that we might insert into a given tree-level diagram. Since these corrections diverge, this could signify the break-down of perturbation theory and the Feynman diagram formalism. However, as we discuss in this section, UV divergences do not affect physical observables and can be safely removed in a procedure known as *renormalisation*. We start with an example of renormalisation, after which we will justify the steps taken, before finally stating the formal rules. The notation used follows that of [9], to which the
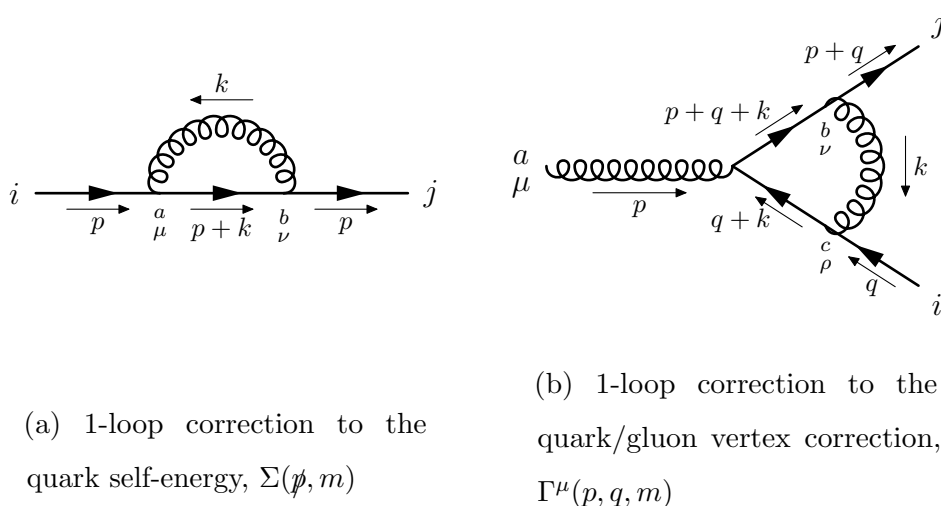
(a) 1-loop correction to the quark self-energy, $\Sigma(\not{p}, m)$

(b) 1-loop correction to the quark/gluon vertex correction, $\Gamma^\mu(p, q, m)$

Figure 1.1: Examples of divergent 1-loop corrections in QCD.

reader is referred for further details, or alternatively see [10].

The expression in eq. (1.4.1) is the next-to-leading order correction to the Dirac propagator, which can be derived from the two-point function of Dirac fields. A non-perturbative examination of this object utilising complex analysis tells us that it has the structure:

$$\int \mathrm{d}^4x\, e^{ip\cdot x} \langle \Omega | T\psi(x)\bar{\psi}(y) | \Omega \rangle = \frac{iZ_2(\not{p}+m)}{p^2 - m^2 + i\epsilon} + \ldots \qquad (1.4.3)$$

where we have omitted terms corresponding to multi-particle bound states. This expression differs from that given for the propagator in the Feynman rules in multiple ways. Firstly, the denominator has a pole at $p^2 = m^2$ corresponding to the *physical* mass m, as opposed to the *bare mass* parameter which appears in the Lagrangian, which we hereafter denote as m_0 (and similarly for other bare parameters in the Lagrangian). Secondly there is the appearance of the constant Z_2, which gives the probability to create or annihilate an exact one-particle eigenstate of the Hamiltonian:

$$Z_2 = |\langle \Omega | \psi(0) | p, s \rangle|^2 . \qquad (1.4.4)$$

The goal now is to compare eq. (1.4.3) to the expression we would obtain from using the Feynman rules to all orders. Let us define $-i\Sigma(p)$ as the sum of all one-particle irreducible diagrams with two external quark lines, for which eq. (1.4.1) is the leading order term. With this notation we can express the two-point function

as

$$\int \mathrm{d}^4 x\, e^{ip\cdot x}\langle\Omega|T\psi(x)\bar{\psi}(y)|\Omega\rangle = \frac{i(\not{p}+m_0)}{p^2-m_0^2} + \frac{i(\not{p}+m_0)}{p^2-m_0^2}(-i\Sigma)\frac{i(\not{p}+m_0)}{p^2-m_0^2} + \dots$$

$$= \frac{i}{\not{p}-m_0}\left(1 + \frac{\Sigma}{\not{p}-m_0} + \left(\frac{\Sigma}{\not{p}-m_0}\right)^2 + \dots\right)$$

$$= \frac{i}{\not{p}-m_0-\Sigma}\,, \tag{1.4.5}$$

where the final expression is obtained by noting the previous line is a geometric series. The location of the physical pole mass m is given by the solution to the equation:

$$[\not{p}-m_0-\Sigma(\not{p})]|_{\not{p}=m} = 0\,. \tag{1.4.6}$$

The pole mass and the bare mass are related by:

$$m-m_0 = \Sigma(\not{p})|_{\not{p}=m}\,. \tag{1.4.7}$$

This appears to suggest that our original bare mass was formally divergent. Expanding eq. (1.4.6) around the pole mass and comparing to eq. (1.4.3) we find that:

$$Z_2^{-1} = 1 - \left.\frac{d\Sigma}{d\not{p}}\right|_{\not{p}=m}\,. \tag{1.4.8}$$

This exercise demonstrates that were we to perform a *renormalisation* of the bare fields in the Lagrangian, such as

$$\psi_0 = \sqrt{Z_2}\psi\,, \tag{1.4.9}$$

we could have used the physical pole mass in our Feynman rules. The LSZ reduction formula tells us that such factors always cancel out in the calculation of S-matrix elements, provided that we only sum over fully amputated diagrams [30]. We should view Z_2 as a book-keeping device. The operation of multiplying by Z_2 or Z_2^{-1} should be interpreted as the adding or subtracting of a divergent term derived to a given order in perturbation theory. There will be further consequences from making the replacement (1.4.9), which we discuss later in the section.

Performing an infinite shift in the field strength and quark mass at first sight seems like an unsettling and unjustified manoeuvre. However, we shall shortly see

how such shifts can arise naturally. To begin, we examine why the divergences appeared in the first place. Both divergences in eqs. (1.4.1) and (1.4.2) arise because we allow the exchange of a virtual particle whose momentum can fluctuate up to arbitrarily high values, which is equivalent to saying fluctuations can occur over arbitrarily small distances. This is where the flaw arises: it is unreasonable to expect that our theory is valid down to arbitrarily small length scales. We could have regulated the divergence by introducing a cutoff Λ, at which scale we expect some new physics to become important. Adding a cutoff however simply reformulates the problem: since we do not know the scale of new physics, it is not at all obvious where such a cutoff should be placed. Somewhat miraculously, we can avoid this problem, as there exist a class of *renormalisable* Lagrangians which may be transformed such that they exhibit no dependence on the cutoff Λ.

In a quantum field theory the degrees of freedom are encapsulated by the generating functional $Z[J]$, which may be used in the derivation of correlation functions (and hence Feynman rules). It is given by:

$$Z[J] = \int \mathcal{D}\phi \, e^{i \int [\mathcal{L} + J\phi]} = \left(\prod_k \int \mathrm{d}\phi(k) \right) e^{i \int [\mathcal{L} + J\phi]} \, , \qquad (1.4.10)$$

where we have used ϕ to schematically denote some collection of fields. Imposing a cutoff Λ is then equivalent to integrating only over $\phi(k)$ for $|k| \leq \Lambda$. If now we want to determine the impact of the high momentum modes, we could perform the integral over a shell of momentum by introducing the field:

$$\hat{\phi}(k) = \begin{cases} \phi(k) & \text{for } b\Lambda \leq |k| < \Lambda \\ 0 & \text{otherwise.} \end{cases} \qquad (1.4.11)$$

Redefining $\phi(k)$ as identical for the low momentum modes, $|k| < b\Lambda$, and zero otherwise, we can replace ϕ by $\phi + \hat{\phi}$ in eq. (1.4.10):

$$Z[0] = \int \mathcal{D}\phi \int \mathcal{D}\hat{\phi} \exp\left(i \int \mathcal{L}(\phi + \hat{\phi}) \right) \, , \qquad (1.4.12)$$

where we have set $J = 0$ for simplicity. Performing the integral over $\hat{\phi}$ we obtain an expression of the form:

$$Z[0] = \int [\mathcal{D}\phi]_{b\Lambda} \exp\left(- \int \mathrm{d}^d x \mathcal{L}_{\text{eff}}(\phi) \right) \, , \qquad (1.4.13)$$

where now we have replaced our original Lagrangian with an effective Lagrangian, $\mathcal{L}_{\text{eff}}$. If $\mathcal{L}$ is renormalisable, then we can recover our original Lagrangian by performing a change of variables $k' = k/b$, $x' = xb$, and performing a suitable transformation of the fields and redefinitions of the parameters. Let us suppose that we now perform multiple iterations of integrating out a momentum shell. If we make the shell of momentum over which we integrate infinitesimal, the transformation becomes continuous, and the Lagrangian will flow along a trajectory in the space of all possible Lagrangians. The set of continuously generated transformations is known as the *renormalisation group.*

In general, the coefficient of an operator in the Lagrangian with N powers of a field ϕ (having dimension d_ϕ) and M derivatives to leading order will transform as:

$$C'_{N,M} = b^{d_{M,N}-d} C_{N,M} \, , \tag{1.4.14}$$

where $d_{M,N} = N d_\phi + M$ is the mass dimension of the operator. Since $b < 1$, operators for which $d_{M,N} - d$ is negative will have coefficients which grow, and the operator is known as *relevant.* If $d_{M,N} - d$ is positive, the coefficient will vanish, and the operator is known as *irrelevant.* Finally, if $d_{M,N} - d = 0$, the operator is known as *marginal* and one must retain higher order terms to determine its behaviour. Thus, if our original Lagrangian was only composed of relevant and marginal operators, its form will be preserved after integrating out high momentum modes; this is the condition for renormalisability. The caveat is that the masses and couplings will experience potentially very large shifts with respect to the original bare parameters; however, it is understood that this occurs only after a large number of iterations of the renormalisation group transformation. For this condition to be met it is sufficient that the trajectory pass arbitrarily close to a point that is unchanged by the transformation, known as a *fixed point.* Typically the free-field Lagrangian $\mathcal{L}_0$ is a fixed point of the transformation. To determine the precisely which trajectory we are on, we must specify some *renormalisation conditions* which are satisfied at a specific scale μ_R known as the *renormalisation scale.*

With the above understanding, we now proceed to outline the procedure for

renormalisation in QCD. We start by rescaling the quark, gluon and ghost fields:

$$\psi_0 = \sqrt{Z_2}\psi \ ,$$
$$A_{0\mu}^a = \sqrt{Z_3}A_\mu^a \ ,$$
$$c_0 = \sqrt{Z_2^c}c \ . \tag{1.4.15}$$

We insert these expressions into the Lagrangian eq. (1.2.10), and then remove the dependence by defining the following set of *counterterms*:

$$\delta_2 = Z_2 - 1 \ , \qquad\qquad \delta_3 = Z_3 - 1 \ ,$$
$$\delta_2^c = Z_2^2 - 1 \ , \qquad\qquad \delta_m = Z_2 m_0 - m \ ,$$
$$\delta_1 = \frac{g_0}{g_s}Z_2(Z_3)^{1/2} - 1 \ , \qquad \delta_1^{3g} = \frac{g_0}{g_s}(Z_3)^{1/2} - 1 \ ,$$
$$\delta_1^{4g} = \frac{g_0^2}{g_s^2}(Z_3)^2 - 1 \ , \qquad \delta_1^c = \frac{g_0}{g_s}Z_2^c(Z_3)^{1/2} - 1 \ . \tag{1.4.16}$$

Each term absorbs the divergent but physically unobservable shifts in the parameters of the Lagrangian, which may then be split into two pieces:

$$\mathcal{L} = \mathcal{L}_{\text{ren}} + \mathcal{L}_{\text{c.t.}} \ . \tag{1.4.17}$$

The first term is simply of the form eq. (1.2.10), but where the fields, masses and couplings have been renormalised; the second term is given by:

$$\begin{aligned}
\mathcal{L}_{\text{c.t.}} &= -\frac{1}{4}\delta_3(\partial_\mu A_\nu^a - \partial_\nu A_\mu^a) + \bar{\psi}(i\delta_2\slashed{\partial} - \delta_m)\psi - \delta_2^c\bar{c}^a\partial^2 c^a \\
&= +g_s\delta_1 A_\mu^a\bar{\psi}\gamma^\mu\psi - g_s\delta_1^{3g}f^{abc}(\partial_\mu A_\nu^a)A^{b\mu}A^{c\nu} \\
&= \frac{1}{4}g_s^2\delta_1^{4g}(f^{eab}A_\mu^a A_\nu^b)(f^{edc}A^{c\mu}A^{d\nu}) - g_s\delta_1^c\bar{c}^a f^{abc}\partial^\mu A_\mu^b c^c \ . \tag{1.4.18}
\end{aligned}$$

We may now use the Feynman rules shown before using the renormalised values for m and g_s to compute any amputated tree-level diagram. To compute loop diagrams, we must also include contributions from the counterterms in eq. (1.4.18), for which the Feynman rules are listed in table 1.2. In this manner all UV divergences will safely cancel. Although we list eight counterterms in eq. (1.4.16), there are only 5 independent ones, and we can make the following three relations:

$$\delta_1 - \delta_2 = \delta_1^{3g} - \delta_3 = \frac{1}{2}(\delta_1^{4g} - \delta_3) = \delta_1^c - \delta_2^c \ . \tag{1.4.19}$$

Internal lines	
$i \longrightarrow \!\!\!\otimes\!\!\! \longrightarrow j$ $\quad p$	$= i(\not{p}\delta_2 - \delta_m)\delta_j^i$
$a,\mu \,\,\text{〰〰}\!\otimes\!\text{〰〰}\,\, b,\nu$ $\quad k$	$= -i\delta_3\delta^{ab}(k^2 g^{\mu\nu} - k^\mu k^\nu)$
$a \cdots\!\otimes\!\cdots b$ $\quad k$	$= i\delta_2^c\delta_{ab}k^2$

Vertices

$$= i\delta_1 g_s \gamma^\mu T_{ij}^a$$

$$= \delta_1^c g_s f^{abc} k^\mu$$

$$= g_s \delta_1^{3g} f^{abc} \left[\quad g^{\mu\nu}(k-p)^\rho \right.$$
$$+ g^{\nu\rho}(p-q)^\mu$$
$$\left. + g^{\rho\mu}(q-k)^\nu \right]$$

$$= -i g_s^2 \delta_1^{4g} \left[f^{abc} f^{cde}(g^{\mu\rho}g^{\nu\sigma} - g^{\mu\sigma}g^{\nu\rho}) \right.$$
$$+ f^{ace} f^{bde}(g^{\mu\nu}g^{\rho\sigma} - g^{\mu\sigma}g^{\nu\rho})$$
$$\left. + f^{ade} f^{bce}(g^{\mu\nu}g^{\rho\sigma} - g^{\mu\rho}g^{\nu\sigma}) \right]$$

Table 1.2: The momentum space Feynman rules for QCD counterterms [9].

The remaining five independent counterterms must be fixed to satisfy five renormalisation conditions.

Before we conclude this section, we now take a moment to consider the notion that the renormalised coupling strength and masses depend on the scale μ_R, a behaviour known as *running*. Calculations of physical observables should not depend on the choice of the renormalisation scale μ_R: a shift in the renormalisation scale can be compensated for by shifts in the field strengths, masses and couplings. This implies that the renormalised n-point Green's functions (containing n_q quark fields and n_A gluon fields respectively) must satisfy the following *Callan-Symanzik* equation [10]:

$$
\left[\mu_R \frac{\partial}{\partial \mu_R} + \beta \frac{\partial}{\partial g_s} + n_q \gamma_2 + n_A \gamma_3 + \sum_j m_j \gamma_{m_j} \frac{\partial}{\partial m_j} \right] G^{(n)}(x_1, \ldots, x_n) = 0 \ ,
$$

(1.4.20)

where β is known as the *beta function*; γ_i ($i = 2, 3$) is the *anomalous dimension* of the quark and gluon fields; γ_{m_j} is the *mass anomalous dimension* for quark field j with renormalised mass m_j. Each term has the following definition:

$$
\beta(g_s) \equiv \mu_R \frac{\partial g_s}{\partial \mu_R} \ , \qquad \gamma_i \equiv -\frac{\mu_R}{2 Z_i} \frac{\partial Z_i}{\partial \mu_R} \ , \qquad \gamma_{m_j} \equiv \frac{\mu_R}{m_j} \frac{\partial m_j}{\partial \mu_R} \ .
$$

(1.4.21)

The beta function gives the rate of change of the renormalised coupling as the renormalisation scale μ_R is increased. It may be calculated by applying the Callan-Symanzik equation to the three-point quark-gluon Green's function, and thereby related to counterterms. To lowest order we obtain [9]:

$$
\beta(g_s) = g_s \mu_R \frac{\partial}{\partial \mu_R} (-\delta_1 + \delta_2 + \frac{1}{2} \delta_3) \ .
$$

(1.4.22)

This is evaluated by choosing a renormalisation scheme to fix the counter terms, although there is no scheme dependence at the lowest order, and we obtain:

$$
\beta(g_s) = -\frac{g_s^3}{(4\pi)^2} \beta_0 \ ,
$$

(1.4.23)

where $\beta_0 = (11 C_A - 2 n_f)/3$. This has the solution [11]:

$$
\alpha_s(\mu_R^2) \equiv \frac{g_s^2(\mu_R^2)}{4\pi} = \frac{\alpha_s(\mu_0^2)}{1 + \alpha_s(\mu_0^2)\beta_0/(4\pi) \ln(\mu_R^2/\mu_0^2)} \ ,
$$

(1.4.24)

thereby defining the running of the strong coupling with respect to some reference scale μ_0 at which it may be measured. Typically this is taken to be the mass of the

Z boson, m_Z. The world average is currently found to be $\alpha_s(m_Z) = 0.1181 \pm 0.0011$ [31].

For small enough numbers of quarks n_f, the sign of the beta function is negative. This signifies that the coupling strength decreases as the scale is increased, that is, the coupling strength is weak at large scales and strong at low scales. This behaviour leads to the phenomena of *asymptotic freedom* at high energies, and *confinement* of partons into hadrons at low energies [25, 26].

1.5 Infrared Safety and Factorisation

In the previous section we discussed the procedure for the removal of large momentum UV divergences. However the loop integrals of eqs. (1.4.1) and (1.4.2) also suffer from another kind of divergence. For example, if we allow the virtual gluon exchanged in fig. 1.1b to go on-shell, that is, let $k^2 \to 0$, its propagator will diverge and so will the corresponding integral eq. (1.4.2). Since it is associated with low momentum modes, this is known as an *infrared* (IR) divergence.

These *virtual* corrections (that is, those which correspond to loop diagrams and contain a virtual particle) are just one class of higher order correction in which such IR divergences arise. Let us consider the process of electron-positron annihilation into hadrons. The timescale over which hadronisation occurs is much longer than that of the hard process, and thus it does not affect the probability for the annihilation to occur (an idea we revisit in the next section). At leading order we can therefore simply consider the annihilation process into a quark antiquark pair: $e^+e^- \to q\bar{q}$. At next-to-leading order (NLO), we would need to include the diagrams shown in fig. 1.2 where a gluon is radiated from one of the quark or antiquark lines. Such corrections are referred to as *real* since they correspond to the emission of on-shell final state partons. If we define energy fractions of the quark and antiquark to be $x_1 = 2E_q/\sqrt{s}$ and $x_2 = 2E_{\bar{q}}/\sqrt{s}$ respectively (for $\sqrt{s}$ the centre-of-mass energy), and neglect the masses of the quarks, then the contribution to the cross section from these real emissions is given by [11]:

$$\sigma^{q\bar{q}g} = \sigma_0 \int_0^1 dx_1 \int_0^1 dx_2 \, C_F \frac{\alpha_s}{2\pi} \frac{x_1^2 + x_2^2}{(1-x_1)(1-x_2)} \,, \qquad (1.5.1)$$
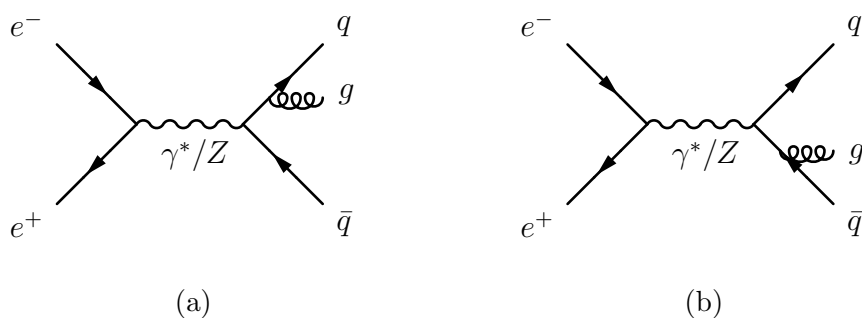
Figure 1.2: Examples of $O(\alpha_s)$ (NLO) real emission corrections to the process $e^+e^- \to q\bar{q}$.

where $\sigma_0 = 4\pi\alpha_{\text{EM}}^2/(3s) \cdot N_c \sum_f Q_f^2$ is the Born level cross section (where the sum is over quark flavours f with charge $e \cdot Q_f$, and α_{EM} is the electromagnetic coupling). The integrand will diverge when $x_i = 1$. Conservation of momentum implies that:

$$1 - x_1 = x_2 E_g (1 - \cos\theta_{\bar{q}g})/\sqrt{s} \,, \tag{1.5.2}$$

$$1 - x_2 = x_1 E_g (1 - \cos\theta_{qg})/\sqrt{s} \,, \tag{1.5.3}$$

where θ_{fg} ($f = q, \bar{q}$) is the angle between the gluon and quark or antiquark. Infrared divergences will thus occur for vanishing gluon energy ($E_g \to 0$), in which case the gluon is referred to as a *soft*, or when the gluon becomes *collinear* with either the quark or antiquark ($\theta_{fg} \to 0$) [5].

In order to understand why such divergences arise, we must recall that the S-matrix was defined as the transition amplitude between a set of asymptotic 'in' and 'out' states. While it might be possible for a massless quark to radiate any number of soft or collinear gluons, since any detector has a finite resolution we would not be able to experimentally distinguish between states with different numbers; in other words, these states are degenerate. It would be impossible to measure isolated partons that have gone on-shell; when the virtualities of the partons are low enough, hadronisation occurs. What we can measure is the energy

---

[5]It is worth noting collinear divergences are regularised by a non-zero quark mass since the denominator arises from the propagator term which for massive quarks is given by $s(1 - x_{1,2}) = (p_{\bar{q},q} + p_g)^2 + m^2 = 2E_g E_{\bar{q},q}(1 - \frac{\sqrt{E_{\bar{q},q}^2 - m^2}}{E_{\bar{q},q}} \cos\theta_{g\bar{q},gq})$. However there will still be a single logarithmic divergence for vanishing gluon momentum, where $x_1 = x_2$.

deposit from a cascade of hadrons, where any number of splittings could have occurred. The cross section for an *exclusive* process in which the number of final state partons is fixed will diverge. However if we compute the *inclusive* cross section for $e^+e^- \to$ hadrons, whereby we sum over all possible real and virtual diagrams to a given order in α_s the infrared divergences cancel, and we obtain a finite result. In practice this must be done by regularising the real and virtual contributions, either by giving the gluon a small mass, or more commonly, by performing the integrals in $d = 4 + 2\epsilon$ dimensions and isolating the divergences in the limit $\epsilon \to 0$, a procedure known as *dimensional regularisation.* It was shown, first by Bloch and Nordsieck for QED [32], and by Kinoshita [33], Lee and Nauenberg [34] for QCD, that the cancellation of infrared divergences holds to all orders in perturbation theory for any sufficiently inclusive quantity.

The seemingly innocuous statement 'sufficiently inclusive' has some important implications. The need sum over all degenerate configurations which give rise to the same asymptotic states applies not only to outgoing, but also incoming particles. In the previous example, there was conveniently no disparity between the asymptotic 'in' states and the incoming particles of the hard process. In hadron collider experiments however the hard scattering process involves incoming partons, and it is abundantly clear that these are quite different from the asymptotic incoming hadrons. To ensure that hadronic cross sections are sufficiently inclusive, we therefore need to sum over all incoming partons, which requires a knowledge of the structure of the colliding hadrons, which are normally protons (or antiprotons).

The proton may be understood in terms of structure functions, $F_{1,2}$, which parameterise the structure of the proton as seen by a photon of virtuality Q^2. The structure functions may be extracted through deep inelastic scattering (DIS) experiments from the cross section for charged lepton-proton scattering ($\ell(k)P(p) \to \ell(k')X$) [11]:

$$
\begin{aligned}
\frac{d^2\sigma}{dxdy} = &\frac{8\pi\alpha_{\mathrm{EM}}^2 ME}{Q^4} \left[\left(\frac{1 + (1-y)^2}{2} \right) 2xF_1(x, Q^2) \right. \\
&\left. + (1-y)(F_2(x, Q^2) - 2xF_1(x, Q^2)) - M/(2E)xyF_2(x, Q^2) \right] , \quad (1.5.4)
\end{aligned}
$$

where $q = k - k'$ and the standard DIS variables are given by:

$$Q^2 = -q^2 \ ,$$

$$M^2 = p^2 \ ,$$

$$\nu = p \cdot q = M(E' - E) \ ,$$

$$x = \frac{Q^2}{2\nu} = \frac{Q^2}{2M(E' - E)} \ ,$$

$$y = \frac{q \cdot p}{k \cdot p} = 1 - \frac{E'}{E} \ . \tag{1.5.5}$$

In the Bjorken limit $Q^2 \to \infty$ with x fixed, it is experimentally observed [24, 35–37] that the structure functions exhibit no dependence on the scale Q^2,

$$F_{1,2}(x, Q^2) \to F_{1,2}(x) \ , \tag{1.5.6}$$

an effect called *Bjorken scaling* [38]. It implies that for large Q^2, the proton appears as a loosely bound assemblage of point particles. Bjorken scaling arises because the timescales over which the struck quark interacts with the spectator quarks are much larger than the timescale of the hard interaction with the virtual photon. Using this feature and neglecting the proton mass M in eq. (1.5.4), and by comparing to the partonic cross section for $e^- q \to e^- q$ we find that the structure functions are related by

$$F_2(x) = 2x F_1(x) \ , \tag{1.5.7}$$

which is known as the *Callan-Gross* relation, and is a direct consequence of the fact that the partons seen by the photon are spin-$\frac{1}{2}$ particles. Furthermore, we find the structure functions may be written in terms of the probability distribution $f_i(x)$ to find a parton of type i with momentum fraction x:

$$F_2(x) = x \sum_i e_i^2 f_i(x) \ . \tag{1.5.8}$$

with e_i the electric charge of quark i.

Beyond leading order, Bjorken scaling is violated by logarithms of Q^2 arising from gluon interactions between struck and spectator quarks. Furthermore if we attempt to calculate the structure function from perturbative field theory, we discover it will contain a collinear divergence which cannot be cancelled due to the

fact a virtual photon cannot distinguish between a pair of collinear partons and a single parton of the same overall momentum. Although this sounds catastrophic, it is linked to unphysically taking the limit beyond a scale at which hadronisation would occur. Fortunately we can absorb the divergences into unmeasurable 'bare' distributions, $f_{i,0}(x)$, and introduce a *factorisation scale* μ_F which separates the long and short distance physics, such that we obtain the *parton distribution functions* (PDFs) $f_i(x, \mu_F^2)$. For example, at next-to-leading order the structure function $F_2(x, Q^2)$ would then be given by [11]:

$$F_2(x, Q^2) = x \sum_i e_i^2 \int_x^1 \frac{d\xi}{\xi} f_i(\xi, \mu_F^2) \left\{ \delta\left(1 - \frac{x}{\xi}\right) + \frac{\alpha_s}{2\pi} P\left(\frac{x}{\xi}\right) \ln\left(\frac{Q^2}{\mu_F^2}\right) \right\} . \tag{1.5.9}$$

Just as in renormalisation the finite part which is included in the definition of counter terms is determined by the renormalisation scheme, the finite part absorbed into the definition of the PDFs is determined by the *factorisation scheme*. The above expression has been derived in the DIS scheme; a more commonly used alternative is known as the $\overline{MS}$ scheme. The functions P which appear are the regulated Altarelli-Parisi splitting functions, which can be found in [11]; we shall meet the unregulated form of these functions in section 2.1.

The ability to factorise the long and short distance interactions in not just the structure functions but also in cross sections is a general principle known as the *factorisation theorem* and has been shown to hold to all orders in α_s by Collins, Soper and Sterman [39–41]. The implication of this procedure is that the PDFs $f_i(x, \mu_F^2)$ depend upon non-perturbative physics beyond the hadronisation scale and cannot be calculated from first principles - they must be derived empirically from data. They are however *universal*, meaning that the PDFs measured in DIS can also be employed in hadron-hadron collisions. The hadronic cross section (to leading twist[6]) for $AB \to X$ may therefore be given by the formula:

$$\sigma_{AB \to X} = \sum_{a,b} \int dx_a dx_b f_{a/A}(x_a, \mu_F^2) f_{b/B}(x_b, \mu_F^2) \hat{\sigma}_{ab \to X}(x_a p_A, x_b p_B, \mu_F^2, \mu_R^2) . \tag{1.5.10}$$

---

[6]Higher twist terms are those suppressed by powers of Q^2; for details see the discussion on the operator product expansion in [9].

The total cross section is often not the most useful quantity we could measure in a collider experiment. For performing precision tests of QCD, it is usually more informative to measure the differential cross section with respect to some observable T, evaluated as a function t that depends on the momenta of the n final state particles:

$$t_n(p_1, \cdots, p_n) = T \qquad \forall\, n\,. \tag{1.5.11}$$

The differential cross section is defined as:

$$\frac{d\sigma}{dT} = \sum_n \int \left\{ \frac{d\sigma^{(n)}(p_1, \cdots, p_n)}{d\Phi_n} \delta(t_n(p_1, \cdots, p_n) - T) \right\} d\Phi_n\,, \tag{1.5.12}$$

where $d\Phi_n$ is the n particle phase space integration measure, and $\sigma^{(n)}$ is the cross section for producing exactly n final state particles. Each individual term in eq. (1.5.12) depends upon the number of final state particles and can be expected to contain infrared divergences, but their sum should be free of divergences if the quantity t is *infrared safe*. For this to be true, the value of T that we measure should be unchanged if any of the momenta goes soft, or any pair of momenta become collinear. Formally, this may be expressed as the condition:

$$t_n(p_1, \cdots, p_i, p_j, \cdots, p_n) \xrightarrow{(p_i+p_j)^2 \to 0} t_{n-1}(p_1, \cdots, (p_i + p_j), \cdots, p_n)\,. \tag{1.5.13}$$

1.6 Observables for Collider Experiments

Theoretically we should now be able to calculate any inclusive differential cross section to any arbitrary fixed order in perturbation theory. Of course in reality, the multi-loop integrals required may be unavailable, and the organisation of the cancellation between virtual and real infrared singularities is not straightforward. Although general subtraction schemes (Catani-Seymour dipole [42], FKS [43], and antenna [44–46] subtraction) have been devised and even automated for NLO [47–50], there is currently no general solution for next-to-next-to-leading order (NNLO) calculations despite many recent developments in the field (for a recent overview, see [31] and references therein). However, we do not discuss these matters further here.

Supposing we now wish to understand the distribution of hadrons in the final state following some scattering process, we would need to construct an infrared safe observable which is sensitive to this distribution, but which is calculable from a finite number of parton momenta. This poses a challenge since (as we alluded to previously) the scale of the hard process is usually much higher than that of the hadronisation scale; thus before hadronisation can occur, the partons which participate in the hard interaction must evolve down to lower scales. A given parton is likely to undergo many soft and collinear splittings, resulting in a collimated stream of partons, each carrying a small fraction of the original parton momentum. (We discuss the equations which govern this evolution in the following chapter.) These partons subsequently hadronise and deposit a cone-like structure of energy in the detector, which we call a *jet*. These objects provide a meaningful discriminant between different event topologies since the number of jets may only be increased by hard, wide-angle splittings. We can make the correspondence both between partons and jets, and between jets and clusters of calorimeter cells in a detector, thus they also provide an invaluable link between theory and experiment. To quantify a jet in a consistent manner, however, requires a clustering algorithm.

For example, in the (inclusive) generalised k_T jet algorithm for hadron collisions [51], we define the following distance measure between particles (or calorimeter cells) i and j:

$$d_{ij} = \min(p_{T\,i}^{2p}, p_{T\,j}^{2p}) \frac{\Delta R_{ij}^2}{R^2} \ , \qquad (1.6.1)$$

where $p_{T\,i}$ is transverse momentum of particle i; $\Delta R_{ij}^2 = \sqrt{(\phi_i - \phi_j)^2 + (y_i - y_j)^2}$ is the angular distance between i and j, with azimuth ϕ_i and rapidity $y_i = \frac{1}{2}\ln\left(\frac{E_i + p_{z_i}}{E_i - p_{z_i}}\right)$ for beam axis defined along z; R is the jet radius parameter. The beam distance of particle i is defined as:

$$d_{iB} = p_{T\,i}^{2p} \ . \qquad (1.6.2)$$

The algorithm then proceeds as follows:

1. Calculate the measure d_{ij} for all possible pair of particles i and j. For every particle i calculate d_{iB}.

2. Find the minimum of all d_{ij} and d_{iB}. If the minimum is in the set of d_{ij},

merge particles i and j with some recombination scheme. (For example, summing their four-momenta is known as E-scheme recombination). If the minimum is in the set of d_{iB}, declare particle i a jet and remove it from the list of particles.

3. Return to step 1 and repeat until there are no particles remaining in the list.

In the above general algorithm, setting $p = 1$ corresponds to the (longitudinally invariant) k_T algorithm [52, 53], $p = 0$ to the Cambridge-Aachen algorithm [54, 55], and $p = -1$ to the anti-k_T algorithm [56]. Each of these provide infrared safe procedures to define jets. The differences stem from the order in which clustering occurs; in the k_T algorithm, the softest and most collinear particles are clustered first, effectively undoing the most recent splittings which might have occurred. The Cambridge-Aachen algorithm clusters the most collinear particles first. In the anti-k_T algorithm, the hardest particles are clustered first, and attract all neighbouring particles. Anti-k_T jets therefore usually appear more cone-like than those of other algorithms; for this reason it is a popular choice amongst experimentalists.

We can now define the cross section for n-jet production, σ_{nj}. Assuming that $\mathcal{O}_{nj}^e(\{p_i\})$ returns one if there are exactly n jets and zero otherwise, then:

$$\sigma_{nj} = \sum_m \int \left\{ \frac{d\sigma^{(m)}(p_1, \ldots, p_m)}{d\Phi_m} \mathcal{O}_{nj}^e(\{p_i\}) \right\} d\Phi_m . \qquad (1.6.3)$$

We can also define the inclusive n-jet cross section, where here inclusive means the cross section for n or more jets. Defining $\mathcal{O}_{nj} = \sum_k \mathcal{O}_{kj}^e(\{p_i\})$, we have:

$$\sigma_{\geq nj} = \sum_m \int \left\{ \frac{d\sigma^{(m)}(p_1, \ldots, p_m)}{d\Phi_m} \mathcal{O}_{nj}(\{p_i\}) \right\} d\Phi_m . \qquad (1.6.4)$$

The quantity in brackets may be difficult to compute analytically, and such integrals are normally performed numerically. We discuss such numerical methods further in chapter 3.

The formalism explored during this chapter has proved highly successful. It has been applied to numerous processes, and through comparisons to experimental data it has provided many precision tests of perturbative QCD. For example, in fig. 1.3 (reproduced from [57]) NNLO QCD predictions [59–61] of the cross section for
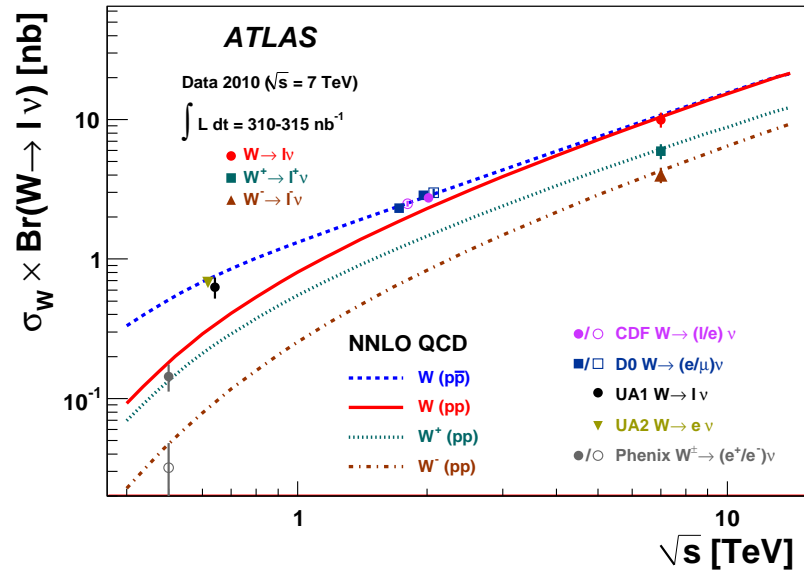
(a)
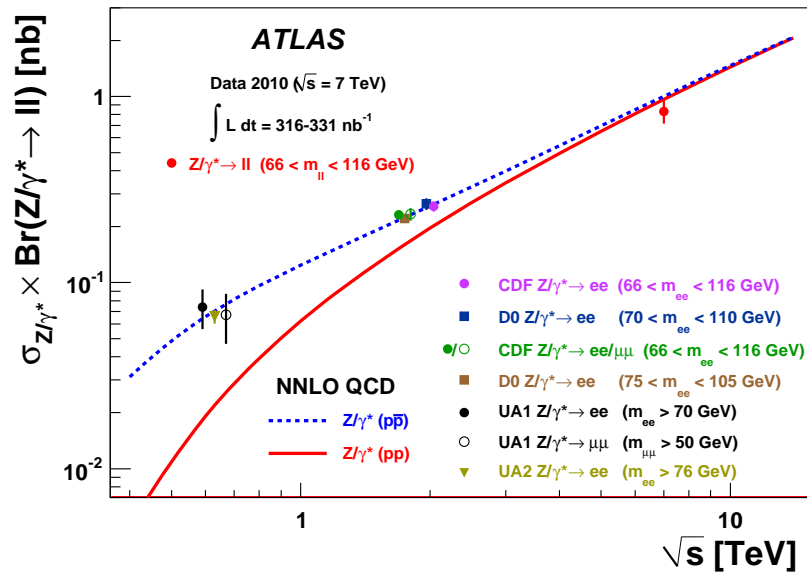
(b)

Figure 1.3: Cross section measurements for inclusive (a) W and (b) Z production over a range of centre-of-mass energies ($\sqrt{s}$) compared to NNLO QCD predictions, reproduced from [57].
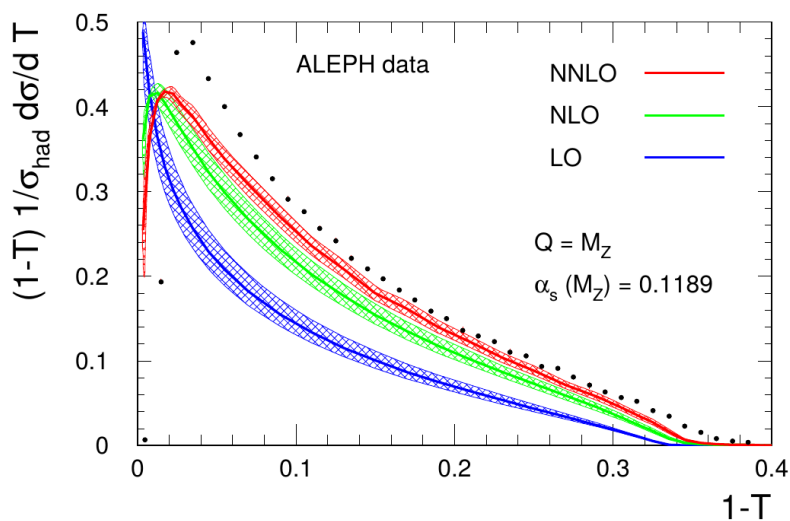
Figure 1.4: Comparison of fixed order calculations to data for the thrust distribution, reproduced from [58].

inclusive W and Z boson production are compared to data collected from multiple experiments, covering a range of centre-of-mass energies ($\sqrt{s}$). We see excellent agreement between the predictions and data.

However, there exist regions of phase space in which discrepancies between fixed order predictions and data arise. For example the *thrust* distribution for $e^+e^- \to$ hadrons, produced by the ALEPH experiment at LEP [62, 63] is shown in fig. 1.4. The thrust variable T has the following definition [64, 65]:

$$T = \max_{\vec{n}} \left(\frac{\sum_i |\vec{p_i} \cdot \vec{n}|}{\sum_i |\vec{p_i}|} \right) \ . \tag{1.6.5}$$

Thrust is an example of an event shape variable, meaning that it provides a way of classifying the overall topology of an event; the limit $T \to 1$ would correspond to two collimated back-to-back jets, while small values of T would correspond to events with a spherically homogeneous distribution of hadrons. Despite the fact that thrust is an infrared safe observable, we see that the fixed order predictions diverge as $T \to 1$. This cannot however, be a physical divergence, because the data remain under control.

In order to have $T = 1$ and hence completely back-to-back jets would require that the outgoing quark-antiquark pair from the hard process $e^+e^- \to q\bar{q}$ emit extremely little radiation (which would act to decorrelate the jets). However, since

in reality the probability to emit soft and collinear radiation is very high, the probability to emit no radiation is very low, and so there is a suppression in the number of events having $T = 1$. It perhaps then comes as a surprise that the fixed order predictions diverge. In order to understand why this happens, we must examine the perturbative expansion of the differential cross section, where the first few orders are given by [11, 66]:

$$\frac{1}{\sigma}\frac{d\sigma}{dT} = \delta(1-T) + \alpha_s(\mu_R^2)A_1(T) + [\alpha_s(\mu_R^2)]^2 A_2(T) + [\alpha_s(\mu_R^2)]^3 A_3(T) + \dots \quad (1.6.6)$$

where:

$$A_n(T) \underset{T\to 1}{\sim} \frac{\ln^{2n-1}(1-T)}{1-T} \; . \quad (1.6.7)$$

Every power of the coupling in eq. (1.6.6) is accompanied by a double logarithm $L^2 = \ln^2(1-T)$ which becomes large in the region $T \to 1$, invalidating the use of a fixed order expansion of the cross section. To obtain a finite result, it would be necessary to sum terms of the form $\alpha_s^n L^{2n-1}$ to all orders n in the coupling. The appearance of large logarithms in certain regions of phase space is not restricted to the above example. In the next chapter we shall discuss some common themes which cause large logarithms to arise, and methods for summing them to all orders.

In this chapter we have introduced the essential ingredients for making theoretical predictions with QCD for hadron collider experiments. In particular we discussed the necessity of calculating sufficiently inclusive, infrared safe quantities to ensure the cancellation of real and virtual infrared divergences. For hadron collisions this has the consequence that the asymptotic incoming states which are needed in the definition of cross sections differ from the partonic states which appear in calculations of the amplitude. The factorisation theorem however enables us to compute hadronic cross sections from partonic cross sections with the use of PDFs.

We encountered an important example of infrared safe final states when we introduced jets. Although these are not fundamental objects, the number of jets is intimately related the number of hard partonic branchings and therefore cross sections for jet production are suitable quantities to compute using perturbative methods. Furthermore, since jets have a topology which can be reconstructed within

a detector, they help bridge the gap between theory and experiment. Measurements of jets allow us not just to test the Standard Model but also to constrain many Beyond the Standard Model (BSM) extensions. The remainder of this thesis will be dedicated to the development of techniques which improve the accuracy of calculations of multi-jet observables.

Chapter 2

Going Beyond Fixed Order QCD

As we saw in the last chapter the feature of asymptotic freedom in QCD entails that in computations of inclusive quantities, it is normally sufficient to perform a fixed order perturbative expansion in the strong coupling strength. We expect that higher order corrections, being accompanied by more powers of the coupling, should be suppressed. However, as we shall learn in this chapter, there are regions of phase space in which perturbative corrections are enhanced by large logarithms that compensate for the smallness of α_s, rendering a fixed order expansion in this parameter invalid.

In this chapter we will discuss two important scenarios in which large logarithms arise, and methods which allow the computation of inclusive quantities to all orders. To elucidate our discussion on this topic, we shall first revisit the example of thrust presented at the end of the previous chapter and introduce some common terminology. Rather than working with the distribution itself we define the event shape fraction:

$$f(\tau) = \int_{1-\tau}^{1} dT \frac{1}{\sigma} \frac{d\sigma}{dT} \, , \tag{2.0.1}$$

where we have introduced the quantity $\tau = 1 - T$. A common way to collect the large logarithms which accompany factors of α_s at each order is to demonstrate that such terms exponentiate. Using a slightly different notation to the previous section, $L = \ln(1/\tau)$, it is possible to write [11]:

$$f(\tau) = C(\alpha_s) \exp\left[G(\alpha_s, L)\right] + D(\alpha_s, \tau) \, , \tag{2.0.2}$$

where

$$C(\alpha_s) = 1 + \sum_{n=1}^{\infty} C_n \left(\frac{\alpha_s}{2\pi}\right)^n , \qquad\qquad (2.0.3)$$

$$G(\alpha_s, L) = \sum_{n=1}^{\infty} \sum_{m=1}^{n+1} G_{n,m} \left(\frac{\alpha_s}{2\pi}\right)^n L^m$$

$$= \sum_{n=1}^{\infty} \left\{ G_{n,n+1} \left(\frac{\alpha_s}{2\pi}\right)^n L^{n+1} + G_{n,n} \left(\frac{\alpha_s}{2\pi}\right)^n L^n + G_{n,n-1} \left(\frac{\alpha_s}{2\pi}\right)^n L^{n-1} + \dots \right\}$$

$$\equiv L g_1(\alpha_s L) + g_2(\alpha_s L) + \alpha_s g_3(\alpha_s L) + \dots \qquad\qquad (2.0.4)$$

The function $D(\alpha_s, \tau)$ is a remainder which vanishes as $\tau \to 0$ ($T \to 1$). In the expansion of $G(\alpha_s, L)$ in eq. (2.0.4), terms of the form $\alpha_s^n L^{n+1}$ for which the power m is maximal are known as the *leading logarithms*, and are collected in the function $g_1(\alpha_s L)$. Similarly, $g_2(\alpha_s L)$ collects terms of the form $\alpha_s^n L^n$, which are the *next-to-leading logarithms*. The function g_3 and those terms omitted in the last line of eq. (2.0.4) sum the subdominant logarithms $\alpha_s^n L^m$ for which $0 < m < n$. By expressing $G(\alpha_s, L)$ in this manner we have performed a reorganisation of the perturbative expansion of f, which may be calculated to leading (if g_1 is derived) or next-to-leading (if g_2 is derived) logarithmic accuracy. Furthermore, it is worth noting that the maximal power of L in $G(\alpha_s, L)$ is at most one higher than that of α_s ($m = n + 1$), which enables an accurate description of $\ln f$ in the region $\alpha_s L \lesssim 1$, which is a much less restrictive condition than that required of a fixed order expansion, namely $\alpha_s L \ll 1$. By expanding the exponential in eq. (2.0.2) to fixed order accuracy we may recover the double logarithms ($m = 2n$) seen in eq. (1.6.7).

The exponentiation of logarithms is a common feature in the computation of inclusive quantities to all-orders. The argument of the exponential, $G(\alpha_s, L)$, is often derived as the solution to integral equations; in the case where these may be cast as renormalisation group equations, this method is known as *resummation*. The derivation of these equations usually requires the application of an approximation; this entails that the solution will naturally become inaccurate away from the limit in which the approximation was designed to apply. This predicament is typically solved by combining all order and fixed order treatments; as we shall shortly see,

how to do this in a consistent way has been the subject of much consideration in the literature (for a review see [67]).

There are numerous cases where large logarithms arise, but many are typified by two disparate scales, the ratio of which is large. In sections 2.1 and 2.3 we discuss two examples of regions of phase space, the soft-collinear limit and the high energy limit, in which large logarithms arise. The phenomenology of these limits may be understood in terms of evolution equations, namely the *DGLAP equation* and the *BFKL equation* respectively, whose solutions sum the leading logarithmic contributions to all orders. In the first case, the solution can be interpreted as a no-emission probability that has a natural numerical implementation known as a *parton shower*. The challenge of how to combine parton showers with fixed order calculations is reviewed in section 2.2, with a focus on methods that will later be relevant for chapter 5. The BFKL equation has two solutions, one of which gives us the leading logarithmic amplitude for colour-octet exchange in the high-energy limit. The extension of these ideas in section 2.4 leads to the *High Energy Jets* formalism which forms the basis of the work in chapters 4 and 5. Finally, in section 2.5 we discuss a method for combining these two all order schemes with each other.

2.1 The Soft-Collinear Limit

As highlighted at the end of section 1.6, the reason that an all order treatment is required for the thrust observable relates to the fact that a fixed order computation of the cross section does not take into account the vanishingly small probability to emit zero soft or collinear radiation. Ultimately divergences arise because a parton surrounded by a cloud of soft and collinear gluons is indistinguishable from a single parton. For an accurate description of any observable which probes the soft-collinear limit will also require an all order treatment. In this section we will therefore explore this limit further, and describe a numerical formulation of the resulting all order prescription.

In section 1.5 we remarked that although matrix elements for soft and collinear real emissions diverge, we claimed such divergences were unphysical, since the

$$
\begin{aligned}
P_{q \to qg}(z) &= C_F \frac{1+z^2}{1-z} \\
P_{q \to gq}(z) &= C_F \frac{1+(1-z)^2}{z} \\
P_{g \to gg}(z) &= C_A \frac{(1-z)^2 + z^2 + z^2(1-z)^2}{z(1-z)} \\
P_{g \to q\bar{q}}(z) &= T_R(z^2 + (1-z)^2)
\end{aligned}
$$

Table 2.1: The unregulated Altarelli-Parisi splitting functions taken from [11].

incoming and outgoing partons would hadronise at at sufficiently low virtualities. In order to further probe the soft-collinear limit, it is therefore reasonable to suppose that the partons which participate in the hard scattering have some finite virtuality q^2. We could then compute the correction to the cross section caused by the additional splitting of one parton $a \to bc$, characterised by the energy fraction $z = E_b/E_a = 1 - E_c/E_a$ and opening angle θ. (These variables are related by $q^2 = z(1-z)E_a^2\theta^2$.) It has been shown that in this limit matrix elements factorise and their *universal* behaviour is encapsulated by the Altarelli-Parisi splitting functions $P_{ba}(z)$ listed in table 2.1 [11]. The differential cross section for one additional emission in the soft-collinear limit is then given by:

$$
d\sigma_{n+1} = d\sigma_n \frac{dq^2}{q^2} dz \frac{\alpha_s}{2\pi} P_{ba}(z) \ . \tag{2.1.1}
$$

If we were to perform the integral over the virtuality q^2 between the scale of the hard scattering Q^2 and some finite resolution parameter Q_0^2 we would expose the large double logarithms of the ratio of these two disparate scales, $[\alpha_s L^2]^n$ with $L = \ln(Q^2/Q_0^2)$. Instead, we can exploit the factorisation of eq. (2.1.1), and use this to state the probability of parton i having virtuality in the interval q^2 to $q^2 + dq^2$ and branching:

$$
d\mathcal{P}_i = \frac{dq^2}{q^2} \int_{Q_0^2/q^2}^{1 - Q_0^2/q^2} dz \frac{\alpha_s}{2\pi} P_{ji}(z) \ . \tag{2.1.2}
$$

This can be used to obtain the probability that there are no branchings between the hard scale Q^2 and q^2, denoted $\Delta_i(Q^2, q^2)$, called a *Sudakov factor*. It is given by the differential equation [11]:

$$
\frac{d\Delta_i(Q^2, q^2)}{dq^2} = \Delta_i(Q^2, q^2) \frac{d\mathcal{P}_i}{dq^2} \ . \tag{2.1.3}
$$

47

2.1. The Soft-Collinear Limit

This is known as the *DGLAP evolution equation*, and has the solution:

$$\Delta_i(Q^2, q^2) = \exp\left\{ -\int_{q^2}^{Q^2} \frac{dk^2}{k^2} \int_{Q_0^2/k^2}^{1-Q_0^2/k^2} dz \frac{\alpha_s}{2\pi} P_{ji}(z) \right\} . \qquad (2.1.4)$$

In solving eq. (2.1.3) we have resummed the leading double logarithms in the soft-collinear limit to all orders in α_s. In an expansion of the exponential in eq. (2.1.4) each term may be interpreted as the probability for an exact number of resolvable real emissions. Invoking unitarity to construct the no emission probability as one minus the probability of any number of resolvable emissions, virtual corrections have therefore been implicitly included to all orders.

We briefly note that this is not the only context in which DGLAP evolution arises. The DGLAP equation also determines the running of the PDFs $f_i(x, \mu_F^2)$ which we met in section 1.5, and may be viewed as an analogue to the QCD β-function equation. However in this context, its form is slightly different, and contains the regulated form of the splitting functions P. This has the consequence that the leading logarithms are instead single logarithms. To distinguish the two cases, the resummation performed in eq. (2.1.4) is known as *Sudakov resummation* whilst the resummation performed in the context of PDF evolution is known as *DGLAP resummation*.

Sudakov factors may be applied numerically to evolve the hard process down from large virtualities to the resolution scale Q_0^2 (typically around 1 GeV) as follows:

1. Choose a random number $r \in [0, 1]$.

2. Solve $\Delta_i(Q^2, q^2) = r$ to obtain the scale of the branching q^2.

3. If $q^2 > Q_0^2$, generate an emission and return to step 1, and otherwise stop the evolution.

Such a procedure is known as a *parton shower*. The variable q^2 used to evolve down is scale is known as the *ordering variable*. Although in the above discussion it was introduced as the virtuality of the branching parton there are other valid choices, such as transverse momentum ordering, as implemented in PYTHIA [68,69], or angular ordering as implemented in HERWIG [70]. These different choices are

equivalent in the soft-collinear limit, but give rise to different additional finite terms. For example, angular ordered showers account for some degree of interference known as *colour coherence* [71].

The branchings considered so far correspond to timelike branchings of final state partons down to the hadronisation scale. However, it is relatively simple to modify eq. (2.1.4) to account for the spacelike branchings of the incoming partons and evolve backwards to lower momentum fractions x [11]:

$$\Delta_i(Q^2, q^2; x) = \exp\left\{-\int_{q^2}^{Q^2}\frac{dk^2}{k^2}\int_{Q_0^2/k^2}^{1-Q_0^2/k^2}dz\frac{\alpha_s}{2\pi}P_{ji}(z)\frac{x/z f_j(x/z, k^2)}{x f_i(x, k^2)}\right\} \ . \quad (2.1.5)$$

We have so far reviewed the traditional approach to parton showers in which one parton is considered to split into two. However many modern showers use the dipole approximation [72–74], in which there exists a colour-anticolour dipole between every pair colour-connected partons (one for each colour index), each of which can radiate independently. Emissions arise as two to three splittings, and therefore naturally provide a framework for momentum conservation (by the recoil of the spectator in the dipole) at each step of evolution. This procedure is known as a *dipole shower*, and has been implemented in ARIADNE [75], SHERPA [76], PYTHIA [68,77] and HERWIG 7 [78]. We now briefly outline the approach used in ARIADNE since it will be relevant for section 2.5.

The differential cross sections for gluon emission from a dipole between two colour-connected partons, $ab \to 123$, where the two original partons retain momentum fractions x_1 and x_3 are given by [73]:

$$gg \text{ dipole}: \quad \frac{1}{\sigma}\frac{d\sigma}{dx_1 dx_3} = \frac{3\alpha_s}{4\pi}\frac{x_1^3 + x_3^3}{(1-x_1)(1-x_3)} \quad \equiv D_{gg}(x_1, x_3) \ , \quad (2.1.6)$$

$$qg \text{ dipole}: \quad \frac{1}{\sigma}\frac{d\sigma}{dx_1 dx_3} = \frac{3\alpha_s}{4\pi}\frac{x_1^2 + x_3^3}{(1-x_1)(1-x_3)} \quad \equiv D_{qg}(x_1, x_3) \ , \quad (2.1.7)$$

$$q\bar{q} \text{ dipole}: \quad \frac{1}{\sigma}\frac{d\sigma}{dx_1 dx_3} = \frac{2\alpha_s}{3\pi}\frac{x_1^2 + x_3^2}{(1-x_1)(1-x_3)} \quad \equiv D_{q\bar{q}}(x_1, x_3) \ , \quad (2.1.8)$$

where D_{ab} are the dipole splitting functions. In the limit $x_3 \to 1$ and with the variable substitution $p_\perp^2 = s_{\text{dip}}(1-x_1)(1-x_3)$ (with s_{dip} the dipole invariant mass squared) we recover the standard Altarelli-Parisi splitting functions, for example:

$$D_{gg}(z, x_3 \to 1)dzdx_3 + D_{gg}(1-z, x_3 \to 1)dzdx_3 = \frac{dp_T^2}{p_T^2}dz\frac{\alpha_s}{2\pi}P_{gg}(z) \ . \quad (2.1.9)$$

In this case two dipoles contribute to the $g \to gg$ splitting. It is therefore natural to define new ordering and splitting variables in terms of Lorentz invariants as follows [74]:

$$p_\perp^2 = s_{\text{dip}}(1 - x_1)(1 - x_3) = \frac{\hat{s}_{12}\hat{s}_{23}}{s_{\text{dip}}} \tag{2.1.10}$$

$$y = \frac{1}{2} \ln \left(\frac{1 - x_1}{1 - x_3} \right) = \frac{1}{2} \ln \left(\frac{\hat{s}_{23}}{\hat{s}_{12}} \right) , \tag{2.1.11}$$

where $\hat{s}_{ij} = (p_i + p_j)^2$ is the square of the invariant mass of the pair of partons i, j. The cross section for emission from a gg dipole for example is then given by (assuming $x_1, x_3 \sim 1$) [72, 73]:

$$d\sigma \sim \alpha_s \frac{dp_\perp^2}{p_\perp^2} dy . \tag{2.1.12}$$

This leads to a gg dipole splitting function given by

$$D_{gg}(p_\perp^2, y) \sim \frac{\alpha_s}{p_\perp^2} , \tag{2.1.13}$$

and the corresponding Sudakov factor is given by:

$$\Delta_{gg}(p_{1\perp}^2, p_{2\perp}^2) = \exp \left(- \int_{p_{2\perp}^2}^{p_{1\perp}^2} dp_\perp^2 \int dy D_{gg}(p_\perp^2, y) \right) . \tag{2.1.14}$$

2.2 Methods for Matching and Merging

Away from the soft-collinear limit, the parton shower approach described in the previous section becomes inaccurate, and as a result describes hard wide-angle emissions poorly. On the other hand, fixed order calculations perform better at describing such hard emissions, but fail to capture the logarithms present in the soft-collinear limit to all orders. Is is clearly desirable to address such deficiencies by combining the parton shower with a fixed order calculation. (Note however, that the number of hard emissions that are accurately described is implicitly limited by accuracy of the fixed order calculation, an issue which we will return to later).

This is not, however, a completely straightforward task. Firstly, to simply perform a parton shower on events generated in some fixed order computation in general would result in double counting. The parton shower already includes the

leading logarithmic contribution at each order in α_s, which therefore overlaps with the (exact) contributions added at that order by the fixed order calculation. What is needed is an approach that corrects the first n orders of the parton shower, where n is the accuracy of the fixed order calculation. Secondly, parton showers calculate the probability of having an exact number of emissions above some resolution scale in the final state, whereas fixed order calculations are necessarily inclusive (as we discussed in section 1.5). Thus before a parton shower may be applied to some fixed order calculation, it is first necessary to render it exclusive.

There are two classes of method for combining parton showers and fixed order calculations: *matching* and *merging*. Matching methods typically correct the distribution of the first parton shower emission such that it is accurate to NLO, and fall into two main categories, namely *multiplicative* and *subtractive*. The POWHEG method [79] is an example of a multiplicative method. This corrects the splitting kernel of the parton shower using the singular part of the NLO real emission matrix elements. The overall normalisation of the shower is then corrected to the NLO cross section using a local K-factor[1]. This method has the advantage that all weights are positive definite; however it has the downside that the parton shower may not appropriately sample the full phase space for the first emission.

In the subtractive approach of MC@NLO [80, 81] the splitting kernels are not corrected; instead the real emission subtraction terms are taken to be identical to the Altarelli-Parisi splitting functions. The normalisation of the shower is corrected to the sum of the contributions to the cross section from the Born and regularised virtual matrix elements. The contribution to the cross section from integration of the subtracted real matrix elements over the full real emission phase space is then added to recover the NLO accurate cross section. This approach should reproduce the correct NLO cross section. However, if the splitting functions overestimate the full real emission matrix elements, this leads to negative weights that can harm the convergence of the numerical integration.

The alternative approach of merging recognises that the shape of distributions

---

[1] A (local) K-factor is simply the ratio of the NLO to LO (differential) cross section.

is primarily affected by corrections from real emissions, with virtual contributions typically only affecting the normalisation. Therefore, one could partially correct the distributions of not just the first but of many emissions by generating tree-level samples of differing multiplicities (limited only by the availability of the corresponding matrix elements) and combining them. In order to apply a parton shower, such samples must first be made exclusive. This is achieved firstly by partitioning the phase space by introducing a merging scale $t_{ms} = Q_{ms}^2$ that acts as a cut-off to the matrix elements. Secondly by clustering with some jet measure and at each step reconstructing the shower variables, a Sudakov factor used to weight each event is calculated. Each event in the sample may then be subsequently showered as normal. In chapter 5 an algorithm inspired by such methods shall be presented, and it is therefore pertinent to review them in greater detail now.

The first example of merging, coined the *CKKW* method, was pioneered in [82] for $e^+e^- \to jets$ and later extended to include hadronic initial states [83]. In this method partons in each sample are required to exceed some resolution criterion, $d_{ij} > d_{\text{res}}$, where d_{ij} may be the distance measure (1.6.1) in the k_T clustering algorithm and the resolution parameter is given by the ratio of the merging scale to the scale of the hard process, $d_{\text{res}} = t_{ms}/Q^2$. Partons in the sample may then be identified as jets. We assume that tree-level matrix elements are available for $n \leq N$ additional jets with respect to the Born configuration. The algorithm then proceeds as follows:

1. Select the jet multiplicity $n \leq N$ and parton identities i with probability according to the relative size of the tree-level cross sections $\sigma_{n,i}(d_{\text{res}})$, using a fixed renormalisation scale choice $\mu_R^2 = t_{ms}$.

2. Select the parton momenta according to the n-parton tree-level matrix elements squared $|\mathcal{M}_{n,i}^2|$, also evaluated with a fixed scale choice $\mu_R^2 = t_{ms}$.

3. Cluster sequentially using the k_T jet algorithm (that is, merge partons i, j with the smallest d_{ij}) until a Born-level process is reached, determining the sequence of resolution values $d_0 = 1 > d_1 > ... > d_n > d_{n+1} = d_{\text{res}}$, and

thereby obtain the corresponding set of scales $t_i = Q^2/d_i$ (with $t_0 = Q^2$).

4. Calculate the weight:

$$w = \frac{\alpha_s(t_1)\alpha_s(t_2)\ldots\alpha_s(t_n)}{\alpha_s(t_{ms})^n} \prod_{j=0}^{n} \frac{\Delta_i(t_j, t_{ms})}{\Delta_i(t_{j+1}, t_{ms})} \ .$$

If $w > r \times [\Delta_i(t_0, t_{ms})]^2$, with $r \in [0,1]$ a random number, accept the configuration; otherwise veto the event and return to 2.

5. Assign a colour structure; if this is not unique, select one according to the relative contribution to the matrix element squared.

6. Continue the parton shower[2] from the scale t_{ms}.

A modified approach to the above method was presented in [84] and is known as the *CKKW-L* method. The first difference involves the clustering for reconstructing the intermediate scales t_i; instead of applying a jet-finding algorithm, all possible clusterings are performed, leading to a set of intermediate states known as a *history*, with each state having a reconstructed scale. A sequence of states of decreasing multiplicity starting from the original event is known as a *path*. If a state can be clustered back to the minimal process requested, a path is said to be *complete*. If the sequence of scales associated with the corresponding states in a path increase with decreasing multiplicity, then a path is said to be *ordered*. Where possible, an ordered, complete path is selected; in addition the path is selected according to its relative weight (calculated using the splitting functions for the branching at each reconstructed scale).

The parton shower is then started from the scale of the most clustered state and an emission is generated; if the scale of the branching is above that of the next reconstructed scale in the path the event is rejected. Otherwise, the same procedure is repeated for each reconstructed state; this is known as a *trial shower*. If at each step no emission is generated between consecutive scales the event passes. The final stage is to generate an emission from the original event, and veto if it

---

[2]If the parton shower is not ordered in hardness it is necessary to perform a truncated, vetoed shower. For details see [82].

has a scale above the merging scale and the multiplicity is less than the maximum multiplicity available in the tree-level samples. This probabilistic interpretation is logarithmically equivalent to vetoing according to analytic Sudakov factors, but has the advantage of using the full phase space, rather than using the approximate limits derived using a jet algorithm. A disadvantage is that it is computationally more intensive.

The CKKW method has been implemented in the general-purpose event generators SHERPA [85] and HERWIG [86], whilst CKKW-L has been implemented in PYTHIA 8 [87]. The two methods we have outlined thus far are those most relevant to work done in chapter 5, however other variants of merging exist, for example the MLM method [88, 89] which approximates the Sudakov factors by rejecting events for which the showered jets do not overlap with the partonic jets, and UMEPS [90] which provides a modification to CKKW-L that recovers the unitarity of the parton shower. There have also been many developments on NLO merging which are beyond the scope of this thesis [91–93].

2.3 The High Energy Limit

In this section we consider a limit which in contrast to section 2.1 is related to the region of semi-hard, wide-angle emissions. To render our discussion on this topic more transparent it is pertinent to first introduce the Lorentz invariant Mandelstam variables, which in two-to-two scattering $a\,b \to 1\,2$ are given by:

$$s = (p_a + p_b)^2 \, , \tag{2.3.1}$$

$$t = (p_a - p_1)^2 \, , \tag{2.3.2}$$

$$u = (p_a - p_2)^2 \, . \tag{2.3.3}$$

These variables correspond the scales of particles exchanged in s, t and u channel processes, of which examples are shown in fig. 2.1. The variable s is simply the centre-of-mass-energy squared; in proton-proton collisions we typically distinguish the partonic centre-of-mass energy squared as $\hat{s}$; it relates to the total by $\hat{s} = x_a x_b s$. Although we have listed three, there are only two independent variables as they
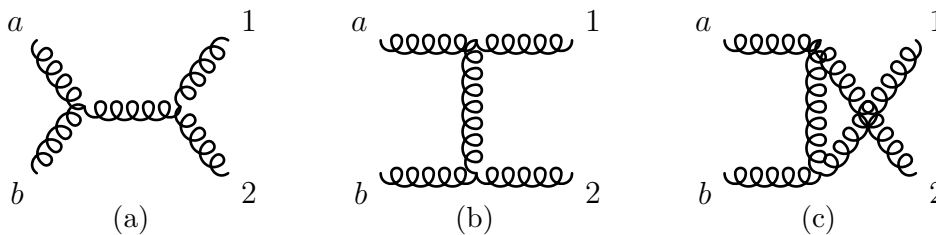
Figure 2.1: Feynman diagrams of two-to-two gluon scattering illustrating s (a), t (b) and u channel (c) processes.

are related by:

$$s + t + u = m_a^2 + m_b^2 + m_1^2 + m_2^2 \,. \qquad (2.3.4)$$

In 2 to n parton scattering $(ab \to 1 \ldots n)$ we can define the invariant mass squared between any pair of final state particles i, j as:

$$s_{ij} = (p_i + p_j)^2 \,. \qquad (2.3.5)$$

We can also define:

$$t_{ai} = (p_a - p_i)^2 \,, \qquad (2.3.6)$$

$$t_{bi} = (p_b - p_i)^2 \,. \qquad (2.3.7)$$

Again, not all of these invariants are independent; in 2 to n scattering processes there are only $3n - 4$ independent invariants.

The behaviour of the cross section for large invariant masses is an interesting observable to study in collider experiments for numerous reasons. Firstly, since exotic coloured particles could be expected to show up as resonances in the dijet invariant mass spectrum, this can provide a handle for BSM physics searches (see for example [94] and references therein, the recent analyses from CMS [95] and ATLAS [96], or for a review see [97]). Moreover, assuming that such exotic particles are heavy, they will likely decay into cascades of quarks and gluons, leading to the production of not just dijets, but multiple jets at large invariant masses.

Secondly, large cuts on the invariant mass of the dijet pair in Higgs plus dijet production may be used to suppress the gluon fusion channel with respect to the vector boson fusion (VBF) channel, thereby allowing for a cleaner extraction of the Higgs' couplings to vector bosons [98]. In addition, at large invariant dijet masses,

it may be possible to extract the CP structure of the Higgs' couplings from the azimuthal correlations of the dijets in the gluon fusion channel [99, 100]. Both of these tests are necessary tests for verifying whether the Higgs boson is consistent with Standard Model predictions. Finally, probing this region of phase space can also provide precision tests of QCD itself.

The aim of this section therefore is to understand the behaviour of multi-jet cross sections in the limit of large invariant mass. Historically, this field of study was known as *Regge theory* [101] (for a modern review, see [102]). To proceed, we must to quantify what is meant by 'large'. Starting with two-to-two parton scattering, since the cross section can only depend on $\hat{s}$ and $\hat{t}$ the relevant kinematics may be specified as:

$$\hat{s} \gg \hat{t} \, . \tag{2.3.8}$$

This is known as the *Regge limit*; sometimes this is referred to as the *semi-hard* region of phase space. To understand this limit further it is convenient to introduce light-cone co-ordinates:

$$p^{\pm} = E \pm p_z \, . \tag{2.3.9}$$

A general momentum may then be parameterised as [103]:

$$
\begin{aligned}
p &= (p^+, p^-; \vec{p}_\perp) \\
&= (m_\perp e^y, m_\perp e^{-y}; \vec{p}_\perp) \, ,
\end{aligned} \tag{2.3.10}
$$

where the transverse mass is given by

$$m_\perp = \sqrt{m^2 + p_\perp^2} \tag{2.3.11}$$

and the *rapidity* is defined as

$$y = \frac{1}{2} \ln \left(\frac{E + p_z}{E - p_z} \right) \, . \tag{2.3.12}$$

Note that in these co-ordinates, the scalar product of two four vectors is given by:

$$p \cdot q = \frac{1}{2}(p^+ q^- + p^- q^+) - \vec{p}_\perp \cdot \vec{q}_\perp \, . \tag{2.3.13}$$

For two to two scattering of massless partons $(ab \to 12)$, the momenta are given by:

$$p_a = (x_a\sqrt{s}, 0; \vec{0}) \ ,$$
$$p_b = (0, x_b\sqrt{s}; \vec{0}) \ ,$$
$$p_1 = (|\vec{k}_\perp|e^{y_1}, |\vec{k}_\perp|e^{-y_1}; \vec{k}_\perp) \ ,$$
$$p_2 = (|\vec{k}_\perp|e^{y_2}, |\vec{k}_\perp|e^{-y_2}; -\vec{k}_\perp) \ . \tag{2.3.14}$$

Noting that rapidity differences are invariant to boosts along the beam axis, we evaluate the Mandelstam variables in the zero momentum frame (for which $x_a = x_b$ and $y_1 = -y_2 = \frac{\Delta y}{2}$):

$$\hat{s} = 2|\vec{k}_\perp|^2(\cosh \Delta y + 1) \ , \tag{2.3.15}$$
$$\hat{t} = -\sqrt{\hat{s}}|\vec{k}_\perp|e^{-\Delta y/2} \ . \tag{2.3.16}$$

In order to satisfy eq. (2.3.8) we must have $\Delta y \to \infty$ for fixed $k_\perp = |\vec{k}_\perp|$, and:

$$\hat{s} \sim k_\perp^2 e^{\Delta y} \ ,$$
$$\hat{t} \sim -k_\perp^2 \ ,$$
$$\Delta y \sim \ln\left(\frac{\hat{s}}{|\hat{t}|}\right) \ . \tag{2.3.17}$$

Thus the limit eq. (2.3.8) may also be considered equivalent to the limit of large rapidity separation (for fixed transverse momenta). Generalising now to $2 \to n$ scattering, the appropriate limit may be specified as [103]:

$$y_1 \gg y_2 \gg \cdots \gg y_n; \qquad |\vec{k}_{i\perp}| \sim k_\perp \ \forall i \ . \tag{2.3.18}$$

This is known as the *Multi-Regge Kinematic* (MRK) limit. The Mandelstam variables are given by [103]:

$$\hat{s} \sim k_{1\perp}k_{n\perp}e^{y_1-y_n} \ ,$$
$$\hat{s}_{ij} \sim k_{i\perp}k_{j\perp}e^{|y_i-y_j|} \ ,$$
$$\hat{t}_{ai} \sim -k_{1\perp}k_{i\perp}e^{y_1-y_i} \ ,$$
$$\hat{t}_{bi} \sim -k_{n\perp}k_{i\perp}e^{y_i-y_n} \ . \tag{2.3.19}$$

2.3. The High Energy Limit

Defining:

$$q_1 = p_a - p_1, \qquad q_{i+1} = q_i - p_i, \qquad t_i = q_i^2, \qquad (2.3.20)$$

and using eq. (2.3.19) we find that $t_i \sim -k_{i\perp}^2$. Therefore:

$$\Delta y_{ij} \equiv |y_i - y_j| \sim \ln\left(\frac{\hat{s}_{ij}}{|\hat{t}_i|}\right) . \qquad (2.3.21)$$

Furthermore, we see that the MRK limit is equivalent to:

$$\hat{s} \gg \hat{s}_{ij} \gg \hat{t}_i . \qquad (2.3.22)$$

The limit is therefore alternatively known as the *high energy* limit, since the centre-of-mass energy is much larger than any other scale.

Now that we have stated the kinematics we may compute the cross section for dijet production, retaining only those terms relevant in the MRK limit. The tree-level matrix elements which contribute to dijet production may be readily calculated using the techniques of the previous section. Only those which may occur through t-channel gluon exchange are relevant in the large-y limit and are given by [11]:

$$|\mathcal{M}_{qq'\to qq'}|^2 = |\mathcal{M}_{q\bar{q}'\to q\bar{q}'}|^2 = 16\pi^2\alpha_s^2\left[\frac{4}{9}\frac{\hat{s}^2 + \hat{u}^2}{\hat{t}^2}\right] , \qquad (2.3.23)$$

$$|\mathcal{M}_{qq\to qq}|^2 = 16\pi^2\alpha_s^2\left[\frac{4}{9}\left(\frac{\hat{s}^2 + \hat{u}^2}{\hat{t}^2} + \frac{\hat{s}^2 + \hat{t}^2}{\hat{u}^2}\right) - \frac{8}{27}\frac{\hat{s}^2}{\hat{t}\hat{u}}\right] , \quad (2.3.24)$$

$$|\mathcal{M}_{q\bar{q}\to q\bar{q}}|^2 = 16\pi^2\alpha_s^2\left[\frac{4}{9}\left(\frac{\hat{s}^2 + \hat{u}^2}{\hat{t}^2} + \frac{\hat{t}^2 + \hat{u}^2}{\hat{s}^2}\right) - \frac{8}{27}\frac{\hat{u}^2}{\hat{t}\hat{s}}\right] , \quad (2.3.25)$$

$$|\mathcal{M}_{qg\to qg}|^2 = 16\pi^2\alpha_s^2\left[\frac{\hat{s}^2 + \hat{u}^2}{\hat{t}^2} - \frac{4}{9}\frac{\hat{s}^2 + \hat{u}^2}{\hat{s}\hat{u}}\right] , \qquad (2.3.26)$$

$$|\mathcal{M}_{gg\to gg}|^2 = 16\pi^2\alpha_s^2\left[\frac{9}{2}\left(3 - \frac{\hat{t}\hat{u}}{\hat{s}^2} - \frac{\hat{s}\hat{u}}{\hat{t}^2} - \frac{\hat{t}\hat{s}}{\hat{u}^2}\right)\right] . \qquad (2.3.27)$$

In the $\hat{s} \gg \hat{t}$ limit (and noting that $\hat{s} \to -\hat{u}$) these simplify to:

$$|\mathcal{M}_{gg\to gg}|^2 = 16\pi^2\alpha_s^2\frac{9}{2}\frac{\hat{s}^2}{\hat{t}^2} ,$$

$$|\mathcal{M}_{qg\to qg}|^2 = \left(\frac{C_F}{C_A}\right)|\mathcal{M}_{gg\to gg}|^2 ,$$

$$|\mathcal{M}_{qq'\to qq'}|^2 = |\mathcal{M}_{qq\to qq}|^2 = |\mathcal{M}_{q\bar{q}\to q\bar{q}}|^2 = \left(\frac{C_F}{C_A}\right)^2|\mathcal{M}_{gg\to gg}|^2 . \qquad (2.3.28)$$
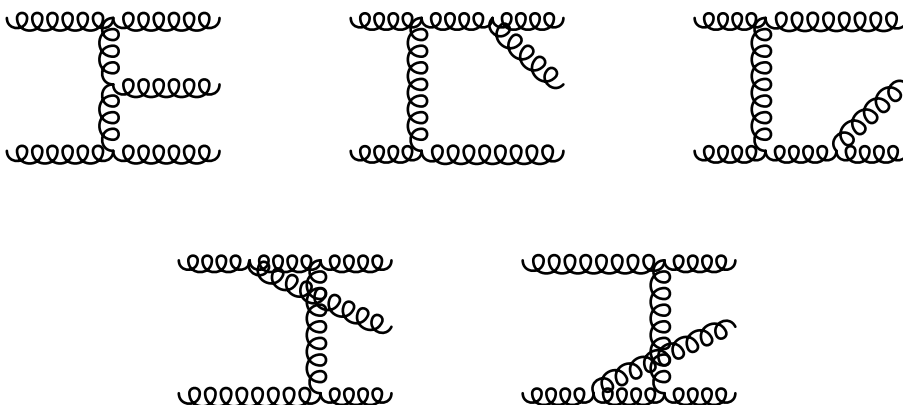
58

Figure 2.2: The tree-level diagrams which contribute in the MRK limit to $gg \to ggg$.

In the MRK limit all dominant partonic channels are related simply and it is therefore only necessary to consider a single channel, which we take here to be $gg \to gg$. This is a general feature which arises because (as we shall shortly see) the amplitude factorises, with the scattering of the incoming partons being captured by *impact factors* that differ only by colour factors.

To obtain the partonic cross section, $\hat{\sigma}_{gg \to gg}$, we must integrate over the phase space of the final state partons. The two particle phase space measure is given by [103]:

$$\mathcal{P}_2 = \int \frac{dy_1 d^2 \vec{k}_{1\perp}}{4\pi(2\pi)^2} \frac{dy_2 d^2 \vec{k}_{2\perp}}{4\pi(2\pi)^2} (2\pi)^4 \delta^4(p_a + p_b - p_1 - p_2)$$
$$\sim \int \frac{1}{2\hat{s}} \frac{d^2 \vec{k}_{1\perp}}{(2\pi)^2} \frac{d^2 \vec{k}_{2\perp}}{(2\pi)^2} (2\pi)^2 \delta^2(\vec{k}_{1\perp} + \vec{k}_{2\perp}) , \qquad (2.3.29)$$

where in the second line we have anticipated that the integrand will be independent of the rapidities, and we have thus performed the integrals over y_1, y_2 in the MRK limit. Therefore we obtain [103]:

$$\frac{d\sigma_{gg \to gg}}{dk_\perp^2} = \frac{|\mathcal{M}_{gg \to gg}|^2}{16\pi \hat{s}^2} = \frac{9}{2}\pi\alpha_s^2 \frac{1}{k_\perp^4} . \qquad (2.3.30)$$

We could then obtain the leading order dijet cross section by invoking eq. (1.5.10) (though we do not do so here as it is not necessary for our discussion).

Let us now consider the $\mathcal{O}(\alpha_s)$ corrections to the Born level cross section for $gg \to gg$. We simply state the matrix element for $gg \to ggg$ in the MRK limit (for

which the contributing diagrams are shown in fig. 2.2 and whose derivation may be found in [103]):

$$i\mathcal{M}^{\mu_a\mu_b\mu_1\mu_2\mu_3}_{abd_1d_2d_3} \sim 2i\hat{s}(ig_s f^{ad_1c_1}g^{\mu_a\mu_1})\frac{1}{\hat{t}_1}$$
$$\cdot (ig_s f^{c_1d_2c_2}C^{\mu_2}(q_1,q_2))\frac{1}{\hat{t}_2}$$
$$\cdot (ig_s f^{bd_3c_2}g^{\mu_b\mu_3}) ,\qquad (2.3.31)$$

where for simplicity the gluon polarisation vectors were omitted:

$$\mathcal{M}_{abd_1d_2d_3} = \mathcal{M}^{\mu_a\mu_b\mu_1\mu_2\mu_3}_{abd_1d_2d_3}\varepsilon_{\mu_a}\varepsilon_{\mu_b}\varepsilon_{\mu_1}\varepsilon_{\mu_2}\varepsilon_{\mu_3} .\qquad (2.3.32)$$

The non-local, gauge invariant *Lipatov vertex* is given by [104]:

$$C^{\mu}(q_1,q_2) = (q_1+q_2)^{\mu}_{\perp} - \left(\frac{\hat{t}_{a2}}{\hat{s}} + 2\frac{\hat{t}_2}{\hat{t}_{b2}}\right)p^{\mu}_b + \left(\frac{\hat{t}_{b2}}{\hat{s}} + 2\frac{\hat{t}_1}{\hat{t}_{a2}}\right)p^{\mu}_a .\qquad (2.3.33)$$

Gauge invariance allows us to use the polarisation sum 1.3.17, such that

$$C^{\mu}(q_1,q_2)C_{\mu}(q_1,q_2) = 4\frac{q^2_{1\perp}q^2_{2\perp}}{k^2_{1\perp}} .\qquad (2.3.34)$$

Summing and averaging over external gluon polarisations and colours, we therefore obtain:

$$|\mathcal{M}_{gg\to ggg}|^2 = \frac{16N^2_c g^6_s}{N^2_c-1}\frac{\hat{s}^2}{k^2_{2\perp}k^2_{1\perp}k^2_{3\perp}} .\qquad (2.3.35)$$

The three-parton phase space measure is given by [103]:

$$\mathcal{P}_3 \sim \int \frac{1}{2\hat{s}}\frac{d^2\vec{k}_{1\perp}}{(2\pi)^2}\frac{dy_2 d^2\vec{k}_{2\perp}}{4\pi(2\pi)^2}\frac{d^2\vec{k}_{3\perp}}{(2\pi)^2}(2\pi)^2\delta^2\left(\sum^3_{i=1}\vec{k}_{i\perp}\right) .\qquad (2.3.36)$$

As in eq. (2.3.29), integration over the extremal parton rapidities contributes one factor of invariant mass in the denominator, and the flux factor contributes another, and therefore the phase space integrand is independent of the internal rapidity y_2. Thus performing the integral over $y_2 \in [y_1, y_3]$, we obtain

$$\frac{d\hat{\sigma}_{gg\to ggg}}{dk^2_{1\perp}dk^2_{3\perp}d\phi} = \frac{N^3_c\alpha^3_s}{4\pi}\frac{\Delta y_{13}}{k^2_{1\perp}k^2_{3\perp}(k^2_{1\perp}+k^2_{3\perp}+2k_{1\perp}k_{3\perp}\cos\phi)}\qquad (2.3.37)$$

for the differential cross section [103]. Since $\Delta y_{13} = \ln(\hat{s}_{13}/k^2_{\perp})$, we see that the $\mathcal{O}(\alpha_s)$ correction to Born level cross section in eq. (2.3.30) arising from real gluon emission is logarithmically enhanced.

Figure 2.3: The 1-loop diagrams which contribute in the MRK limit to $gg \to gg$.

We now consider the virtual corrections for $gg \to gg$, for which the only diagrams that contribute are shown in fig. 2.3. The matrix element is given by [103]:

$$i\mathcal{M}_{abcd}^{\mu_a\mu_b\mu_c\mu_d} \sim -i8\pi\alpha_s g^{\mu_a\mu_b} g^{\mu_b\mu_c} f^{cde} f^{abe} \frac{\hat{s}}{\hat{t}} \ln\left(\frac{\hat{s}}{|\hat{t}|}\right) \hat{\alpha}(\hat{t}) \qquad (2.3.38)$$

where

$$\hat{\alpha}(\hat{t}) = \alpha_s N_c \hat{t} \int \frac{d^{D-2}\vec{k}_\perp}{(2\pi)^2} \frac{1}{|\vec{k}_\perp|^2 |(\vec{q}-\vec{k})_\perp|^2} \qquad (2.3.39)$$

is the *Regge trajectory*[3] [103], with D the number of dimensions. This integral has an infrared divergence that may be regulated either by introducing a cutoff or by using dimensional regularisation (the latter being the method used in the next section). In either case it transpires that $\hat{\alpha}(0) = 0$. Comparing eq. (2.3.38) to the matrix element for $gg \to gg$ given by [103]:

$$i\mathcal{M}_{abcd}^{\mu_a\mu_b\mu_c\mu_d} \sim -i8\pi\alpha_s g^{\mu_a\mu_b} g^{\mu_b\mu_c} f^{cde} f^{abe} \frac{\hat{s}}{\hat{t}} , \qquad (2.3.40)$$

we see that the $\mathcal{O}(\alpha_s)$ virtual correction to Born level cross section is also logarithmically enhanced. Note however in contrast to the Sudakov logarithms of section 2.1, these high energy logarithms are single logarithms, meaning that the leading logarithmic terms are of the form $[\alpha_s \ln(\hat{s}_{ij}/k_\perp^2)]^N$.

The appearance of large logarithms in eqs. (2.3.37) and (2.3.38) signals that a proper computation of the cross section in the (Multi-)Regge limit requires an all order treatment. We start by considering the elastic scattering of two partons with momentum transfer $\hat{t} = q^2$, and outline the steps for computing the all order corrections to this process (for a detailed treatment see [102, 103]). This will rely on three important postulates:

---

[3]In [102] the Regge trajectory is defined as $1 + \hat{\alpha}(\hat{t})$.
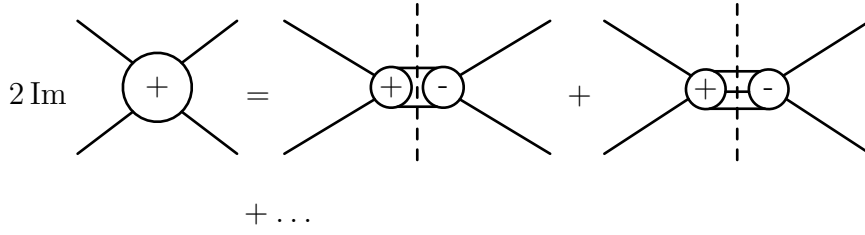
2.3. The High Energy Limit

Figure 2.4: A schematic representation of the Cutosky rules [102] for the case of the case of two particle scattering is shown. Each circle labelled with a plus (+) sign represents an amplitude for a set of incoming and outgoing legs. The minus (-) sign denotes that the hermitian conjugate of this amplitude should be taken. Each vertical dashed line denotes a 'cut', signifying the intermediate particle for each cut propagator must be made on-shell.

1. The S-matrix is Lorentz invariant.

2. The S-matrix is unitary.

3. The S-matrix is an analytic function of Lorentz invariants.

The first postulate means that we can can write the S-matrix, and hence the amplitude entirely in terms of the Mandelstam variables defined above. The second postulate gives us the Cutosky rules, which may be formally stated as [102]:

$$2 \operatorname{Im} \mathcal{A}_{ab} = (2\pi)^4 \delta^4 \left(\sum_a p_a - \sum_b p_b \right) \sum_c \mathcal{A}_{ac} \mathcal{A}_{cb}^\dagger . \qquad (2.3.41)$$

This equation tells us that we may calculate the imaginary part of the elastic amplitude by considering the amplitudes of the incoming and outgoing states into all possible intermediate states. For each intermediate state, the matrix element for the incoming particles is multiplied by the hermitian conjugate of the matrix element for the outgoing states. This is equivalent to evaluating a loop diagram where the propagator for the intermediate particle is 'cut', namely it is replaced by a delta function such that the particle is made on-shell. For two to two scattering, this may be summarised in fig. 2.4.

The postulate of analyticity has two important consequences. Firstly it allows us to relate the imaginary part of the amplitude, and hence eq. (2.3.41) to the

s-channel discontinuity:

$$\text{Im}\,\mathcal{A}(\hat{s},\hat{t}) = \frac{\mathcal{A}(\hat{s}+i\epsilon,\hat{t}) - \mathcal{A}(\hat{s}-i\epsilon,\hat{t})}{2i} = \frac{\text{Disc}\,\mathcal{A}(\hat{s},\hat{t})}{2i}\;. \tag{2.3.42}$$

Secondly, analyticity enables us to use dispersion relations and partial wave expansions to derive the full amplitude from the s-channel discontinuity:

$$\mathcal{A}_T(\hat{s},\hat{t}) = -\frac{1}{4\pi}\int_{\delta-i\infty}^{\delta+i\infty} dl\,\frac{(-1)^l + (-1)^T}{\sin \pi l}\left(\frac{\hat{s}}{|\hat{t}|}\right)^l \mathcal{F}_T(l,\hat{t}) \tag{2.3.43}$$

where the suffix T is used to denote that the scalar part of the amplitude is taken, and $(-1)^T = \pm 1$. $\mathcal{F}_T(l,\hat{t})$ is the Mellin transform of the discontinuity of the amplitude:

$$\mathcal{F}_T(l,\hat{t}) = \int_1^\infty d\left(\frac{\hat{s}}{|\hat{t}|}\right)\left(\frac{\hat{s}}{|\hat{t}|}\right)^{-l-1}\text{Disc}\,\mathcal{A}_T\left(\hat{s},\hat{t}\right)\;. \tag{2.3.44}$$

We can obtain the elastic amplitude for $gg \to gg$ by applying the Cutosky rules to all n parton intermediate states that are dominant in the MRK limit, namely the crossed and uncrossed ladder exchange diagram (as shown in fig. 2.5a), and cut the horizontal gluon propagators such that they are on-shell. This therefore requires the evaluation of the amplitude for Multi-Regge exchange, shown in fig. 2.5b, which corresponds to the exchange of $n-1$ t-channel gluons. We make ansatz that the gluon *reggeises*, namely that the i-th vertical gluon propagator, which previously in eq. (2.3.31) had the form $1/\hat{t}_i$, can be obtained by making the replacement:

$$\frac{1}{\hat{t}_i} \to \frac{1}{\hat{t}_i}\left(-\frac{\hat{s}_{i+1,i}}{\hat{t}_i}\right)^{\hat{\alpha}(\hat{t}_i)} = \frac{1}{\hat{t}_i}e^{\hat{\alpha}(\hat{t}_i)(y_{i+1}-y_i)}\;, \tag{2.3.45}$$

where $\hat{\alpha}(\hat{t}_i)$ is the Regge trajectory of eq. (2.3.39). This is known as the *Lipatov ansatz* [104], and is denoted in fig. 2.5b by replacing the conventional gluon propagator by a zig-zag line. The bold square vertices indicate that we should use the Lipatov vertex from eq. (2.3.33). The amplitude for Multi-Regge exchange is
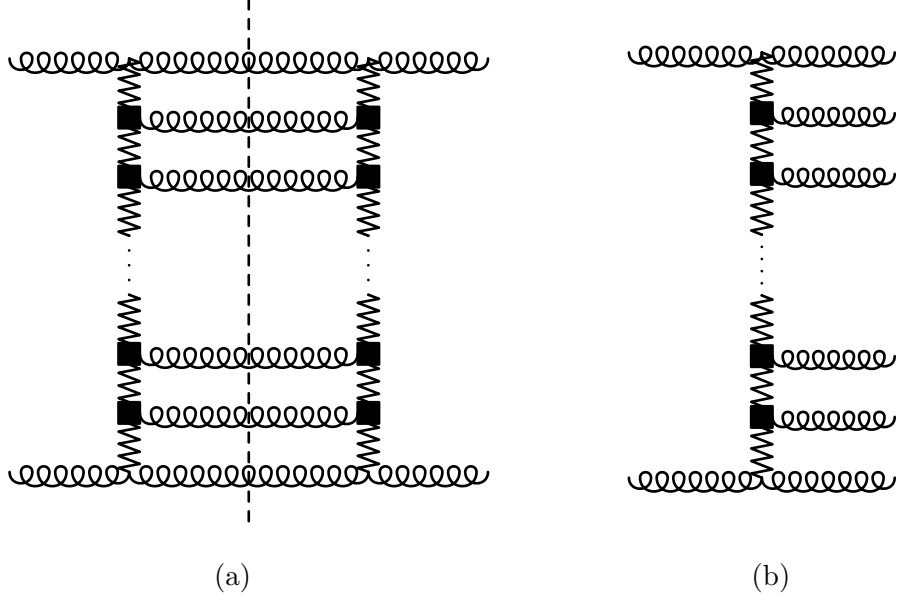
Figure 2.5: The (un-crossed) ladder diagram which contributes to the imaginary part of the elastic $gg \to gg$ scattering amplitude is shown in fig. 2.5a. The dashed line represents a cut, which indicates that the diagram may be evaluated using the Cutosky rules, and put the particles with cut propagators on-shell. The ladder diagram therefore may be evaluated in terms of the amplitude for Multi-Regge exchange, shown in fig. 2.5b. In both cases the dark squares represent Lipatov vertices, whilst the vertical zig-zag lines represent t-channel exchange of a reggeised gluon that may be evaluated using the Lipatov ansatz.

then given by [105, 106]:

$$
\begin{aligned}
i\mathcal{M}_{abd_1...d_n}^{\mu_a\mu_b\mu_1...\mu_n} \sim\ & 2i\hat{s}(ig_s f^{ad_1c_1}g^{\mu_a\mu_1})\frac{1}{\hat{t}_1}e^{\hat{\alpha}(\hat{t}_1)(y_1-y_2)} \\
& \cdot (ig_s f^{c_1d_2c_2}C^{\mu_2}(q_1,q_2))\frac{1}{\hat{t}_2}e^{\hat{\alpha}(\hat{t}_2)(y_2-y_3)} \\
& \cdot \ldots \\
& \cdot (ig_s f^{c_{n-2}d_{n-1}c_{n-1}}C^{\mu_{n-1}}(q_1,q_2))\frac{1}{\hat{t}_{n-1}}e^{\hat{\alpha}(\hat{t}_{n-1})(y_{n-1}-y_n)} \\
& \cdot (ig_s f^{bd_nc_{n-1}}g^{\mu_b\mu_n}) \ .
\end{aligned}
\tag{2.3.46}
$$

We can use eq. (2.3.46) to evaluate the discontinuity of the full amplitude.

By transforming to Mellin space[4], we find that the discontinuity of the (scalar part of the) elastic amplitude obeys a recursion relation, known as the *BFKL equation* [107–110]:

$$\mathcal{F}_T(l, \hat{t}) = -2i\hat{t}(4\pi\alpha_s)^2 C_T^2 \int \frac{d^2 q_{1\perp}}{(2\pi)^2} \frac{1}{q_{1\perp}^2 (q - q_1)_\perp^2} f_T(l, q_1, \hat{t}) \,, \qquad (2.3.47)$$

where C_T is a colour factor, and $f(l, q_1, \hat{t})$ obeys the integral equation:

$$[l - 1 - \hat{\alpha}(\hat{t}_i') - \hat{\alpha}(\hat{t}_i'')] f_T(l, q_1, \hat{t}) = 1 - 2\alpha_s C_T \int \frac{d^2 q_{2\perp}}{(2\pi)^2} \frac{\mathcal{K}(q_1, q_2)}{q_{2\perp}^2 (q - q_2)_\perp^2} f_T(l, q_2, \hat{t}) \tag{2.3.48}$$

with $\hat{t}_i' = q_{i\perp}^2$, $\hat{t}_i'' = (q - q_i)_{i\perp}^2$ and $\mathcal{K}(q_i, q_{i+1}) = -\frac{1}{2} C^\mu(q_i, q_{i+1}) C_\mu(q - q_i, q - q_{i+1})$.

The BFKL equation admits two possible solutions, one corresponding to colour-singlet exchange of a particle known as the *pomeron* ($C_T = N_c$), and another corresponding to colour-octet exchange ($C_T = N_c/2$). The latter is given by:

$$\mathcal{A}^{\text{octet}}(\hat{s}, \hat{t}) = 4\pi N_c \alpha_s \frac{\pi \hat{\alpha}(\hat{t})}{\sin(\pi \hat{\alpha}(\hat{t}))} \left(1 + e^{i\pi\hat{\alpha}(\hat{t})}\right) \left(\frac{\hat{s}}{-\hat{t}}\right)^{1+\hat{\alpha}(\hat{t})} . \qquad (2.3.49)$$

We note that since $\hat{\alpha}(0) = 0$, this implies that $\mathcal{A}^{\text{octet}}(\hat{s}, \hat{t} \to 0) \propto \hat{s}^J$, with $J = 1$ the spin of gluon. This is precisely the behaviour predicted by Regge theory, and we say that the gluon lies on the Regge trajectory $J(\hat{t}) = \hat{\alpha}(t) + 1$, which we can now interpret as the effective spin of the particle (or *reggeon*) exchanged in the t-channel, whose propagator should be given by eq. (2.3.45). The existence of the solution eq. (2.3.49) demonstrates the self-consistency of the original ansatz, which in fact has been found to hold to next-to-leading logarithmic accuracy[5] [113–116]. As a consequence, the amplitude for Multi-Regge exchange eq. (2.3.46) can be taken as a corollary [108]. Equations (2.3.45) and (2.3.46) are two very important results which shall be used in the next section.

Having verified the self-consistency of the Lipatov ansatz, one could obtain the total partonic cross section for the inclusive production of two gluons by performing the phase space integration over n final state gluons numerically, and explicitly

---

[4]In [103] the change of variables $z = -2\hat{s}/\hat{t}$ is made, and instead the Laplace transform is taken.

[5]At next-to-next-to-leading logarithmic accuracy however, two-loop contributions to the Regge trajectory have been found to violate high-energy factorisation [111, 112].

2.3. The High Energy Limit

summing over all n. This can be done provided the cancellation of real and virtual divergences has been performed to all orders; this will be the approach in the next section. Alternatively, the total partonic cross section may be extracted analytically using the optical theorem from the discontinuity of the elastic scattering amplitude for colour singlet exchange. This is the approach taken in [103]; the result to leading logarithmic accuracy is:

$$\frac{d\hat{\sigma}_{gg}}{dk_{1\perp}^2 dk_{2\perp}^2} = \left[\frac{C_A \alpha_s}{k_{1\perp}^2}\right] f(k_{1\perp}, k_{2\perp}, \Delta y_{12}) \left[\frac{C_A \alpha_s}{k_{2\perp}^2}\right] , \qquad (2.3.50)$$

where $f(k_{1\perp}, k_{2\perp}, y)$ is the inverse Laplace transform of the singlet solution to the BFKL equation:

$$f(k_{1\perp}, k_{2\perp}, y) = \int \frac{d\omega}{2\pi i} e^{\omega y} f(l, k_{1\perp}, k_{2\perp}) , \qquad (2.3.51)$$

and $\omega = l - 1$. Implicitly, ω accounts for the virtual corrections to all orders. It may be shown that for $\Delta y_{12} \to \infty$ this corresponds to an asymptotic behaviour of the cross section of $\hat{\sigma}_{gg} \sim \exp(A\Delta y_{12})$, with $A = 4\ln(2)\alpha_s C_A/\pi$.

We conclude this section by making some observations. According to Regge theory the amplitude for $2 \to n$ partonic scattering should be asymptotically proportional to $\hat{s}_{12}^{J(\hat{t}_1)} \hat{s}_{23}^{J(\hat{t}_2)} \ldots \hat{s}_{n-1,n}^{J(\hat{t}_{n-1})}$, with $J(\hat{t}_i)$ the spin of the i-th particle exchanged in the t-channel. This is consistent with the result for Multi-Regge exchange in eq. (2.3.46), namely:

$$\mathcal{A}_{ab \to 1g\ldots gn} \propto \hat{s}_{12}\hat{s}_{23}\ldots\hat{s}_{n-1,n} , \qquad (2.3.52)$$

which corresponds to the exchange of $n - 1$ spin-1 colour octets (or reggeised gluons). The partonic channels which give rise to the dominant contributions to the cross section for $2 \to n$ partonic scattering must therefore be those which at tree-level may proceed through gluon exchange in the t-channel. These are known as *FKL* configurations. Also note that the amplitude for the process where one or both initial state gluons are replaced with quarks is identical to eq. (2.3.46) up to an overall colour factor. We already saw this behaviour in eq. (2.3.28). This is a consequence of high energy factorisation, with extremal partons being captured by impact factors that differ only by colour factors. FKL configurations are therefore those in which the most forwards and backwards outgoing partons have the same

flavour as the incoming partons, and all additional $n-2$ final state partons are gluon emissions. This definition explicitly fixes the rapidity ordering of all final state partons.

The phase space integrand behaves as $|\mathcal{A}_{ab\to1g\ldots gn}|^2/\hat{s}^2$ since the integral over extremal rapidities contributes one factor of invariant mass and the flux factor contributes another. Noting that

$$
\begin{aligned}
\hat{s} \sim k_\perp^2 \exp(y_1 - y_n) &= k_\perp^2 \exp(y_1 - y_2 + y_2 - \cdots + y_{n-1} - y_n) \\
&= k_\perp^2 \prod_{i=1}^{n-1} \exp(y_i - y_{i+1}) \\
&= k_\perp^2 \prod_{i=1}^{n-1} \left(\frac{\hat{s}_{i,i+1}}{k_\perp^2} \right) ,
\end{aligned}
\tag{2.3.53}
$$

it should be clear that for FKL configurations $|\mathcal{A}_{ab\to1g\ldots gn}|^2/\hat{s}^2$ is independent of invariant mass and hence from internal rapidities. Therefore, by performing the phase integral over each of the rapidity-ordered final state partons, the Born level cross section for FKL configurations must behave as:

$$
\hat{\sigma}_{ab\to1g\ldots gn} \propto \sigma_{ab\to12} \prod_{i=2}^{n-1} \alpha_s \Delta y_{i-1,i+1} \sim \sigma_{ab\to12} \prod_{i=2}^{n-1} \alpha_s \ln \left(\frac{\hat{s}_{i-1,i+1}}{k_\perp^2} \right) ,
\tag{2.3.54}
$$

and hence we see that FKL configurations give rise to the leading logarithmic $[\alpha_s \ln(\hat{s}_{ij}/k_\perp^2)]^N$ contributions to the cross section.

Channels which proceed by fewer than $n-1$ t-channel gluon exchanges give rise to contributions to the amplitude that are systematically suppressed by powers of invariant mass. For example, if a quark were exchanged in the t-channel in place of a gluon, the amplitude would instead be proportional to $\hat{s}_{i,i+1}^{1/2}$, and hence the amplitude squared would be suppressed by $\hat{s}_{i,i+1}$ relative to an FKL channel. This suppression implies that $|\mathcal{A}_{ab\to1g\ldots gn}|^2/\hat{s}^2$ is not completely independent of the internal rapidities and results in one fewer logarithm at the level of the cross section. Such channels, known as *non-FKL* configurations, therefore only contribute at *subleading logarithm*, $\alpha_s^N \ln^M(\hat{s}_{ij}/k_\perp^2)$ with $M < N$. In chapter 4 we will see how such subleading logarithmic terms can arise from rapidity orderings which differ from the strict ordering of FKL configurations.

2.4 The High Energy Jets Formalism

In the previous section we considered the asymptotic behaviour of the amplitude and cross section for $2 \to n$ partonic scattering in the high energy limit. We now address the question of whether this limit is relevant for collider studies, and in particular whether an all order treatment is appropriate for multi-jet phenomenology at the LHC.

We review the approach of [117], in which the $\mathcal{O}(\alpha_s)$ contribution to the amplitude in the MRK limit for (1) $2 \to 2$, (2) $2 \to 3$ and (3) $2 \to 4$ partonic processes was compared to tree-level matrix elements. A phase space point with fixed transverse momenta $(k_{\perp i})$, and rapidities that depend on a parameter Δ was chosen for each case as follows:

1. $y_1 = -y_2 = \Delta$; $\phi_1 = 0$, $\phi_2 = \pi$,

2. $y_1 = -y_3 = \Delta$, $y_2 = 0$; $\phi_1 = 0$, $\phi_2 = -\phi_3 = 2\pi/3$,

3. $y_1 = -y_4 = \Delta$ $y_2 = -y_3 = \Delta/3$; $\phi_1 = 0$, $\phi_2 = -\phi_3 = \pi/2$, $\phi_4 = \pi$.

The parameter Δ, which represents half of the maximal rapidity separation, was then increased incrementally, and the matrix elements squared (normalised by the flux factor) was evaluated at each point. The results obtained in [117] are reproduced and shown in fig. 2.6.

In all cases, the MRK limit is independent of Δ and corresponds to a flat line; the tree level matrix elements approach this limit for large enough values of Δ. The point at which the limit is reached occurs between 6 and 16 units of rapidity separation between the most forward and backward partons. By comparison, the pseudorapidity[6] coverage of the calorimeters in the CMS and ATLAS detectors is $|\eta| \lesssim 5.0$ and $|\eta| \lesssim 4.9$ [118, 119] respectively. It is appears that for the majority of the phase space explored at these two detectors at the LHC, the strict MRK limit is not relevant.

---

[6] The pseudorapidity η is defined as $-\ln(\tan\frac{\theta}{2})$, and is equivalent to rapidity for massless particles.

(a)

(b)

(c)
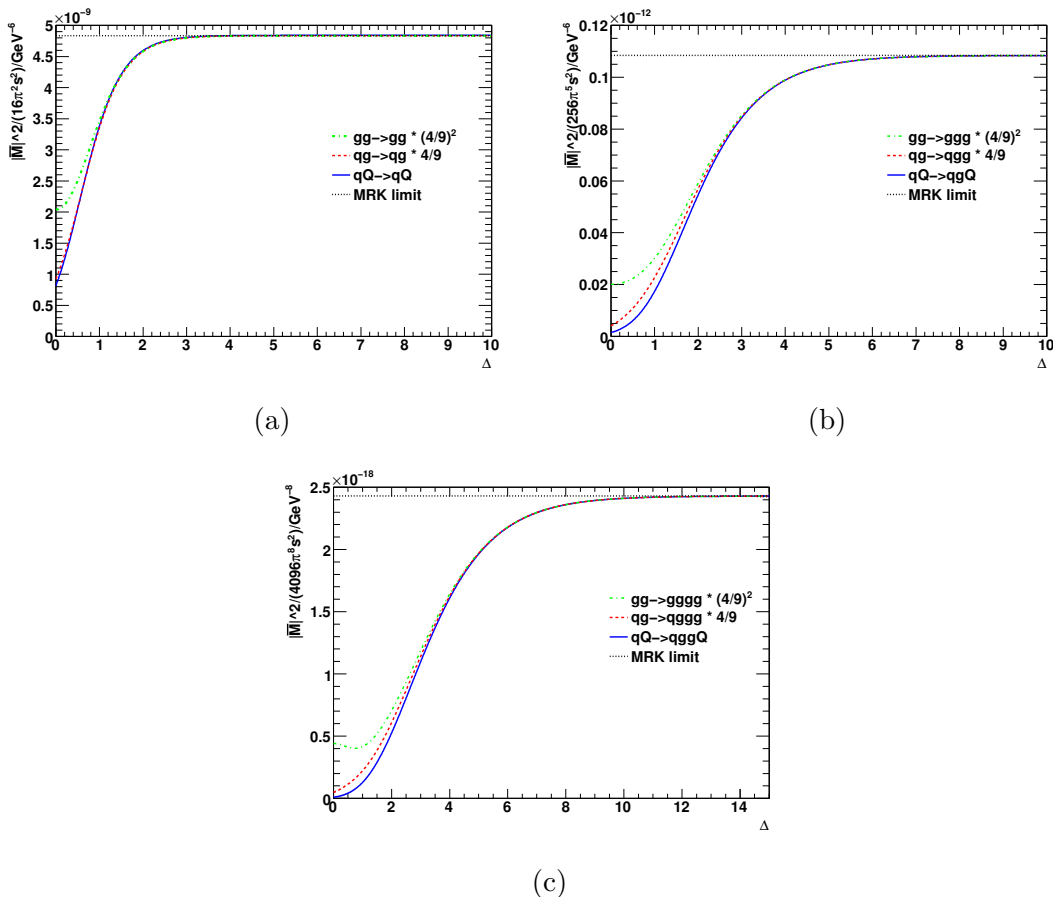
Figure 2.6: Plots are shown of leading order matrix elements squared $\overline{|\mathcal{M}|}^2/(2^{4(n-1)}\pi^{3n-4}\hat{s}^2) \cdot (C_F/C_A)^m$ for the $2 \to n$ partonic scattering processes, where m is the number of quarks in the initial/final state, evaluated for a phase space point parameterised in terms of Δ, half the rapidity separation between the rapidity separation between the most forward and backward partons. The configuration is chosen such that MRK kinematics are satisfied in the large Δ limit. The analytic MRK limit which is independent of Δ is shown as a flat line on the plots, which the matrix elements are seen to approach at large Δ. The plots are reproduced from [117].

If the strict MRK limit only becomes important at the edges of the phase space available at the LHC, this raises the question of whether such an all order treatment is necessary for LHC phenomenology. However, the only alternative formalism available for describing for hard jet production are schemes for combining a parton shower with a fixed order calculation. The logarithms handled by the parton shower are known not to describe hard jets (see for example [120–122]) thus the number of hard jets which may be accurately described is inherently limited by the accuracy of the fixed order calculation.

This is not necessarily a problem if one is only interested in studying sufficiently inclusive processes. However, it is a quite common practice to enhance the signal of a process with respect to the QCD background by placing a veto on jets appearing in a given rapidity interval; for example to suppress the gluon fusion channel with respect to the VBF channel in Higgs plus dijets production [98]. To understand the effect of such vetoes on the residual QCD backgrounds (which is necessary if they are to be safely applied in experiments), it is crucial to have an accurate description of more exclusive quantities such as the average number of hard jets in a rapidity interval, for which an all order approach should be necessary. This is the motivation for extending the BFKL model presented in the previous section, and leads to the **High Energy Jets** (HEJ) formalism [117, 123–127].

As we explore in the remainder of this section, the factorisation of the matrix element squared into impact factors, Lipatov vertices and t-channel poles in the MRK limit may be exposed away from the limit using spinor helicity formalism. The terms which violate factorisation necessarily vanish in the MRK limit and are neglected, however the remainder of the expression is less coarsely simplified. Although retaining more information, the factorised form of the matrix element is nevertheless sufficiently simple to permit a numerical Monte Carlo integration (for details, see section 3.1) in the entire phase space for obtaining the cross section. This is in contrast to the previous section, where regions of phase space in which the amplitude was subdominant were excluded. Such a procedure allows for the development of a formalism that is valid to all orders, and which despite reproducing the MRK limit is valid in a larger region of phase space and may therefore be used
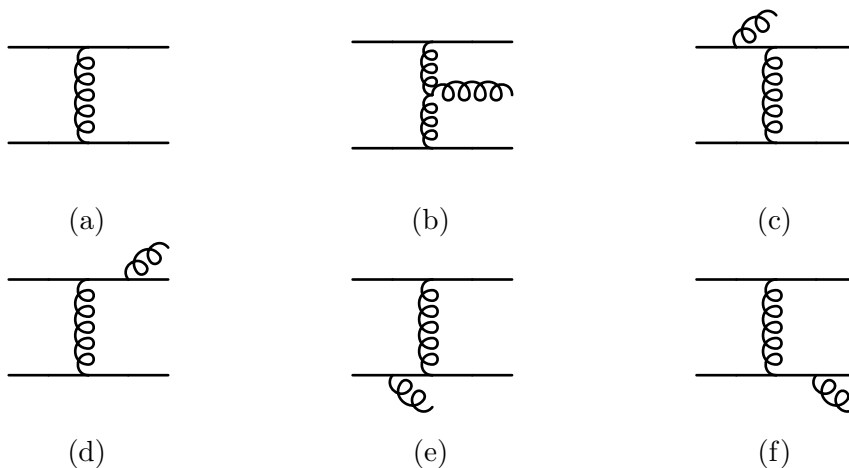
Figure 2.7: Diagrams used in the construction of the basic building blocks for the general factorised form of the $2 \to n$ matrix elements in the HEJ formalism: (a) is used for the derivation of the partonic currents, whilst (b-f) are used in the derivation of the modified Lipatov vertex.

for LHC phenomenology.

In the factorised form of the amplitude which will be derived, the dominance of the t-channel poles must be explicit, such that by application of the Lipatov ansatz from eq. (2.3.45) its form may be naturally extended to all orders, and moreover capture the defining property of Regge exchange. We start by considering the scattering of two partons $ab \to 12$ of helicities h_a, h_b, h_1, h_2 respectively, and later extend this to $2 \to n$ processes. Anticipating that the dominant partonic channels will be related by overall colour factors in the MRK limit, we first analyse the structure of the amplitude for the scattering of two non-identical quarks, $qQ \to qQ$. The only diagram which contributes to the process is shown in fig. 2.7a. Using the notation of section 1.3 we define the spinor string[7]:

$$S_{qQ \to qQ}^{h_a h_b \to h_1 h_2} = \langle 1^{h_1} | \mu | a^{h_a} \rangle g^{\mu\nu} \langle 2^{h_2} | \nu | b^{h_b} \rangle . \qquad (2.4.55)$$

The sum and average over final and initial helicities of the absolute square of this

---

[7]We also make use of the commonly used shorthand $\langle i^{\pm} | \mu | j^{\pm} \rangle = \langle p_i^{\pm} | \gamma^{\mu} | p_j^{\pm} \rangle$.

quantity is denoted as:

$$||S_{qQ \to qQ}||^2 = \sum_{h_a, h_b, h_1, h_2} |S_{qQ \to qQ}^{h_a h_b \to h_1 h_2}|^2 \ . \tag{2.4.56}$$

The exact matrix elements for $qQ \to qQ$, summed and averaged over helicities and colours may be written in the form [117]:

$$\overline{|\mathcal{M}_{qQ \to qQ}|}^2 = \frac{1}{4(N_c^2 - 1)} ||S_{qQ \to qQ}||^2$$
$$\cdot \left(g_s^2 C_F \frac{1}{\hat{t}_1} \right) \cdot \left(g_s^2 C_F \frac{1}{\hat{t}_2} \right) \ . \tag{2.4.57}$$

In this case $\hat{t}_1 = \hat{t}_2$, however this suggestive notation is used for later generalisation.

It was shown in [123] that for all non-vanishing helicity configurations in $qg \to qg$, the tree-level matrix elements squared factorise. In this case, the form of the matrix element squared may be obtained from eq. (2.4.57) by making the replacement:

$$C_F \to K_g \equiv \frac{1}{2} \left(C_A - \frac{1}{C_A} \right) \left(\frac{1 + z^2}{z} \right) + \frac{1}{C_A} \ . \tag{2.4.58}$$

In the MRK limit $z = \frac{p_n^-}{p_b^-} \to 1$, and this expression tends to C_A; we therefore recover the behaviour seen in eq. (2.3.28).

Equation (2.4.57) already gives us two of the building blocks required for the factorised amplitude: a contraction of currents describing the scattering of the incoming partons, and as before, a t-channel pole for each effective t-channel exchange. Crucially, the current factor $||S_{qQ \to qQ}||^2$ retains more of the full kinematics than the impact factors of the BFKL formalism presented in the previous section.

We now require the counterpart to the Lipatov vertex eq. (2.3.33). This may be derived by considering the process $qQ \to qgQ$, for which the diagrams are shown in figs. 2.7b to 2.7f. The diagram containing the three-gluon vertex is already in factorised form, and is given by:

$$\mathcal{A}_{3g} = \frac{-g_s^3 f^{abc} T_{i_1 i_a}^c T_{i_3 i_b}^b}{\hat{t}_1 \hat{t}_2} \langle 1|\mu|a\rangle \langle 3|\nu|b\rangle \varepsilon_\rho^*$$
$$\cdot \left((q_1 + q_2)^\rho g^{\mu\nu} + (p_2 - q_2)^\mu g^{\nu\rho} - (q_1 + p_2)^\nu g^{\mu\rho} \right) \ . \tag{2.4.59}$$

In the MRK limit this becomes:

$$\mathcal{A}_{3g} \sim g_s^3 f^{abc} T_{i_1 i_a}^c T_{i_3 i_b}^b \frac{S_{qQ \to qQ}}{\hat{t}_1 \hat{t}_2} \varepsilon_\rho^* \left(2p_a^\rho \frac{\hat{s}_{23}}{\hat{s}} - 2p_b^\rho \frac{\hat{s}_{12}}{\hat{s}} - (q_1 + q_2)^\rho \right) \ . \tag{2.4.60}$$

The other diagrams may be constructed from fig. 2.7a from gluon insertions on each external quark leg. Such gluons may be accounted for by treating them as soft and using the eikonal approximation to obtain:

$$
\mathcal{A}_q = \mathcal{A}_{qQ \to qQ} \times i(ig_s)\varepsilon_\rho^* \left((T^a T^b)_{i_1 i_a} T_{i_3 i_b}^b \frac{p_1^\rho}{p_1 \cdot p_2} - (T^b T^a)_{i_1 i_a} T_{i_3 i_b}^b \frac{p_a^\rho}{p_a \cdot p_2} \right.
$$
$$
\left. + T_{i_1 i_a}^c (T^a T^c)_{i_3 i_b} \frac{p_3^\rho}{p_3 \cdot p_2} - T_{i_1 i_a}^c (T^c T^a)_{i_3 i_b} \frac{p_b^\rho}{p_b \cdot p_2} \right) .
$$
$$(2.4.61)$$

In the MRK limit we have $p_a \sim p_1$ and $p_b \sim p_3$, so we make these replacements in order to combine the colour factors, and obtain:

$$
\mathcal{A}_q = \frac{S_{qQ \to qQ}}{q_1^2 q_2^2} \times (g_s^3) f^{abc} T_{i_1 i_a}^c T_{i_3 i_b}^b \varepsilon_\rho^* \left(q_1^2 \frac{p_1^\rho}{p_1 \cdot p_2} - q_2^2 \frac{p_3^\rho}{p_3 \cdot p_2} \right) .
$$
$$(2.4.62)$$

We can combine expressions eq. (2.4.61) and eq. (2.4.62), before reinstating the symmetry between p_a, p_1 and p_b, p_3, to obtain the factorised amplitude:

$$
\mathcal{A}_{qQ \to qgQ} = g_s^3 f^{abc} T_{i_1 i_a}^c T_{i_3 i_b}^b \frac{S_{qQ \to qQ}}{q_1^2 q_2^2} \varepsilon_\rho^* V^\rho (q_1, q_2)
$$
$$(2.4.63)$$

where

$$
V^\mu(q_i, q_{i+1}) = - (q_i + q_{i+1})^\mu
$$
$$
+ \frac{p_a^\mu}{2} \left(\frac{q_i^2}{p_{i+1} \cdot p_a} + \frac{p_{i+1} \cdot p_b}{p_a \cdot p_b} + \frac{p_{i+1} \cdot p_n}{p_a \cdot p_n} \right) + p_a \leftrightarrow p_1
$$
$$
- \frac{p_b^\mu}{2} \left(\frac{q_{i+1}^2}{p_{i+1} \cdot p_b} + \frac{p_{i+1} \cdot p_a}{p_b \cdot p_a} + \frac{p_{i+1} \cdot p_1}{p_b \cdot p_1} \right) - p_b \leftrightarrow p_n \qquad (2.4.64)
$$

is the modified Lipatov vertex and extension of eq. (2.3.33); we have written it in the most general form here, but in eq. (2.4.63) we have $n = 3$. It may be verified that eq. (2.4.64) is also gauge invariant. We thus propose the following general form of the factorised matrix element for the process $qQ \to qg \ldots gQ$ (with $n - 2$ final state gluons):

$$
\overline{|\mathcal{M}_{qQ \to qg \ldots gQ}|}^2 = \frac{1}{4(N_C^2 - 1)} \| S_{qQ \to qQ} \|^2
$$
$$
\cdot \left(g^2 \, C_F \frac{1}{\hat{t}_1} \right) \cdot \left(g^2 \, C_F \frac{1}{\hat{t}_{n-1}} \right)
$$
$$
\cdot \prod_{i=1}^{n-2} \left(\frac{-g^2 C_A}{\hat{t}_i \hat{t}_{i+1}} V^\mu(q_i, q_{i+1}) V_\mu(q_i, q_{i+1}) \right) .
$$
$$(2.4.65)$$

2.4. The High Energy Jets Formalism

To obtain the equivalent expression for qg or gg initial states, one need simply make the replacement eq. (2.4.58) for each initial state quark replaced by a gluon. We therefore now have the amplitude for all possible $2 \to n$ FKL configurations. This expression reproduces the MRK limit, and its form has an analogous structure, and yet retains a greater degree of the full kinematics.

The Lipatov ansatz (2.3.45) may now be applied to obtain an expression which reproduces the leading logarithmic terms to all orders in the coupling:

$$\overline{\left|\mathcal{M}^{\mathrm{HEJ}}_{f_1 f_2 \to f_1 g \cdots g f_2}\right|}^2 = \frac{1}{4(N_C^2 - 1)} \left\|S_{qQ \to qQ}\right\|^2$$
$$\cdot \left(g_s^2 \; K_{f_1} \frac{1}{\hat{t}_1}\right) \cdot \left(g_s^2 \; K_{f_n} \frac{1}{\hat{t}_{n-1}}\right)$$
$$\cdot \prod_{i=1}^{n-2} \left(\frac{-g^2 C_A}{\hat{t}_i \hat{t}_{i+1}} V^\mu(q_i, q_{i+1}) V_\mu(q_i, q_{i+1})\right)$$
$$\cdot \prod_{j=1}^{n-1} \exp\left[2\hat{\alpha}(q_i^2)\Delta y_{j-1, j+1}\right] \;, \quad (2.4.66)$$

where $K_q = C_F$ and K_g is given by eq. (2.4.58). This expression contains implicit infrared divergences corresponding to the i-th gluon becoming soft, which necessarily must cancel with the explicit divergences which appear in the Regge trajectory. However, in order to perform numerical integration, it is necessary to apply a regularisation procedure such that these divergences cancel explicitly. The divergence in the Regge trajectory may be regulated by evaluating the integral in eq. (2.3.39) in $D = 4 + 2\varepsilon$ dimensions [128]:

$$\hat{\alpha}(q_i^2) = -g_s^2 C_A \frac{\Gamma(1-\varepsilon)}{(4\pi)^{2+\varepsilon}} \frac{2}{\varepsilon} \left(\frac{q_i^2}{\mu^2}\right)^\varepsilon \;, \quad (2.4.67)$$

where μ is the mass scale acquired by the coupling.

In the limit that the transverse momentum of the ith internal gluon becomes soft, the matrix element eq. (2.4.65) has the following behaviour:

$$\overline{\left|\mathcal{M}_{ab \to 1 \ldots n}\right|}^2 \xrightarrow{|\vec{p}_{i\perp}|^2 \to 0} \left(\frac{4g_s^2 C_A}{|\vec{p}_{i\perp}|^2}\right) \overline{\left|\mathcal{M}_{ab \to 1 \ldots (n-1)}\right|}^2 \;. \quad (2.4.68)$$

Performing the phase space integral in the region $|\vec{p}_{i\perp}|^2 < \lambda^2$ (also in $D = 4 + 2\varepsilon$ dimensions) we obtain:

$$\int \frac{dy_i d^{2+2\varepsilon}\vec{p}_{i\perp}}{4\pi(2\pi)^{2+2\varepsilon}} \left(\frac{4g_s^2 C_A}{|\vec{p}_{i\perp}|^2}\right) \mu^{-2\varepsilon} = \frac{4g_s^2 C_A \Delta y_{i-1, i+1}}{(4\pi)^{2+\varepsilon}} \frac{1}{\Gamma(1+\varepsilon)} \frac{1}{\varepsilon} \left(\frac{\lambda^2}{\mu^2}\right)^\varepsilon \;. \quad (2.4.69)$$

Just as the matrix element for n partons has $n-2$ internal gluons, the matrix element for $n-1$ partons has $n-2$ propagators. Expanding the exponential for the ith propagator in $\overline{\left|\mathcal{M}_{ab\to 1\ldots(n-1)}\right|}^2$ at each order in α_s and ε leads to the necessary cancellation with the finite remainder

$$\omega^0(q_i^2, \lambda^2)\Delta y_{i-1,i+1} \tag{2.4.70}$$

where

$$\omega^0(q_i^2, \lambda^2) = -\frac{\alpha_s C_A}{\pi}\ln\left(\frac{q_i^2}{\lambda^2}\right) . \tag{2.4.71}$$

We can re-exponentiate this remainder (order by order in α_s), and obtain the following regularised matrix element[8]:

$$
\begin{aligned}
\overline{\left|\mathcal{M}^{\text{HEJ, reg}}_{f_1 f_2 \to f_1 g\cdots g f_2}\right|}^2 =& \frac{1}{4(N_C^2 - 1)}\left\|S_{qQ\to qQ}\right\|^2 \\
&\cdot\left(g_s^2\, K_{f_1}\frac{1}{\hat{t}_1}\right)\cdot\left(g_s^2\, K_{f_n}\frac{1}{\hat{t}_{n-1}}\right) \\
&\cdot\prod_{i=1}^{n-2}\left(\frac{-g^2 C_A}{\hat{t}_i \hat{t}_{i+1}}\left(V^\mu(q_i, q_{i+1})V_\mu(q_i, q_{i+1}) - \frac{4}{|\vec{p}_{i\perp}|^2}\theta(|\vec{p}_{i\perp}|^2 + \lambda^2)\right)\right) \\
&\cdot\prod_{j=1}^{n-1}\exp\left[\omega^0(q_j^2, \lambda^2)\Delta y_{j-1,j+1}\right] .
\end{aligned} \tag{2.4.72}
$$

The additional factor modifying the contraction of Lipatov vertices accounts for the fact that eq. (2.4.68) is not exact. The only remaining unregulated infrared divergences in eq. (2.4.72) correspond to one of the extremal partons in rapidity becoming soft or collinear with another emission. The former may be removed by simply requiring that the extremal parton must be a member of the extremal jet. The latter is removed by using an expression for the modified Lipatov vertex in which the final step of re-symmetrisation of p_a, p_1 and p_b, p_n has been undone.

By integrating the n-parton matrix elements over the phase space for n real emissions that gives rise to at least N jets (and summing over $n \geq N$) we could in principle now obtain the inclusive N-jet cross section to leading logarithmic

---

[8]There is a weak dependence of the cross section upon the regularisation parameter λ that was investigated in the appendix of [124]; the dijet and trijet cross sections were stable to 2 significant figures for λ in the range 0.2-2.0 GeV. The default value for λ is taken to be 0.5 GeV.

accuracy in the MRK limit. However, the expression eq. (2.4.68) will become inaccurate away from the limit. For this reason, prior to performing the phase space integral, the matrix elements are reweighted using leading order matrix elements (provided by MadGraph 4 [129]). This proceeds by first clustering into m jets to obtain the jet momenta $\{p_J\}$. The sum of unclustered momenta q is then redistributed between the jets according to their relative contribution to the scalar sum of transverse momentum, and such that their rapidities remain fixed. Finally the energies are adjusted to conserve momentum, and we obtain the following set of m massless momenta $\{p_{J'}\}$:

$$\vec{p}_{J'\perp} = \vec{p}_{J\perp} + \vec{q}_\perp \frac{|\vec{p}_{J\perp}|}{\sum_J |\vec{p}_{J\perp}|} \ ,$$

$$E_{J'} = |\vec{p}_{J'\perp}| \cosh y_J \ ,$$

$$p_{zJ'} = |\vec{p}_{J'\perp}| \sinh y_J \ . \tag{2.4.73}$$

The weight factor is then given by the ratio of leading order and HEJ matrix elements evaluated for the m shuffled momenta:

$$w_m = \frac{|\overline{\mathcal{M}_{\mathrm{LO}}}|^2 \left(\{p_{J'}\}\right)}{|\overline{\mathcal{M}_{\mathrm{HEJ}}}|^2 \left(\{p_{J'}\}\right)} \ . \tag{2.4.74}$$

The inclusive N-jet cross section at leading logarithmic accuracy in the MRK limit, matched to LO accuracy away from the limit is thus given by [124]:

$$\sigma_{Nj}^{\mathrm{FKL+matching}} = \sum_{f_1,f_2} \sum_{n=N}^\infty \prod_{i=1}^n \left(\int_{p_{i\perp}=\lambda}^{p_{i\perp}=\infty} \frac{\mathrm{d}^2\vec{p}_{i\perp}}{(2\pi)^3} \int \frac{\mathrm{d}y_i}{2} \right)$$

$$\cdot \frac{\left|\mathcal{M}_{f_1 f_2 \to f_1 g \cdots g f_2}^{\mathrm{HEJ, \ reg}}(\{p_i\})\right|^2}{\hat{s}^2} \sum_{m \geq N} \left[\mathcal{O}_{mj}^e(\{p_i\}) \ w_m\right] \mathcal{O}_{Nj}(\{p_i\})$$

$$\cdot x_a f_{A,f_1}(x_a, \mu_F) x_2 f_{B,f_2}(x_b, \mu_F) (2\pi)^4 \ \delta^2 \left(\sum_{i=1}^n \vec{p}_{i\perp}\right) \ , \tag{2.4.75}$$

where $\mathcal{O}_{mj}^e$ is an exclusive jet measure which is unity if there are exactly m jets, and zero otherwise; $\mathcal{O}_{Nj} = \sum_{m \geq N} \mathcal{O}_{mj}^e$ is the inclusive N-jet measure. This expression does not take into account the non-FKL partonic channels that we neglected to include in the all order treatment. To recover full LO accuracy away from the limit, these channels must be added in to obtain the inclusive N-jet cross section:

$$\sigma_{Nj}^{\mathrm{HEJ}} = \sigma_{Nj}^{\mathrm{FKL+matching}} + \sum_{m \geq N} \sigma_{mj}^{\mathrm{NFKL}} \tag{2.4.76}$$
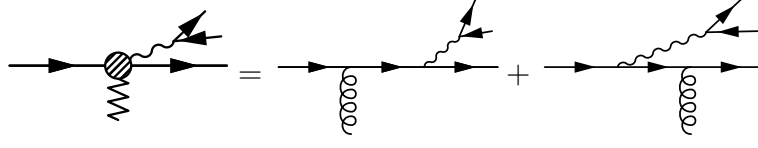
Figure 2.8: Schematic illustration of the effective current for W emission off a quark leg, reproduced from [125].

where $\sigma_{mj}^{\text{NFKL}}$ are the exclusive leading order cross sections for m jets corresponding to non-FKL partonic channels, for which the matrix elements are again provided by MadGraph. The maximum multiplicity of the number of jets matched is only limited by the availability of the tree-level matrix elements.

So far we have only described the HEJ formalism for pure QCD processes; however it is possible for modify this prescription to include other processes. For example, the emission of a $W^{\pm}$ boson may be included by viewing this as an electroweak correction to the current factor in eq. (2.4.56), and defining:

$$||S_{ud\to d\nu_\ell\bar{\ell}d}||^2 = \frac{g_W^4}{4}\left|\frac{1}{(p_\ell+p_{\bar{\ell}})^2-m_W^2+i\Gamma_W m_W}\right|^2\sum_{h_b,h_2}|S_{ud\to d\nu_\ell\bar{\ell}d}^{-h_b\to -h_2--}|^2\,, \quad (2.4.77)$$

where m_W is W boson mass, Γ_W is the decay width, g_W is the weak coupling strength, and we define:

$$S_{ud\to dd\nu_\ell\bar{\ell}}^{-h_b\to -h_2--} = J_W^\mu(p_a,p_\ell,p_{\bar{\ell}},p_1)\langle 2^{h_2}|\mu|b^{h_b}\rangle\,. \quad (2.4.78)$$

The effective current J_W^μ for $W^{\pm}$ emission off a quark leg, shown schematically in fig. 2.8, is given by [125]:

$$\begin{aligned}J_W^\mu(p_a,p_\ell,p_{\bar{\ell}},p_1) =&\langle 1^-|\left(\frac{\gamma^\nu(\not{p}_\ell+\not{p}_{\bar{\ell}}+\not{p}_1)\gamma^\mu}{(p_\ell+p_{\bar{\ell}}+p_1)^2}+\frac{\gamma^\mu(\not{p}_a-\not{p}_\ell-\not{p}_{\bar{\ell}})\gamma^\nu}{(p_a-(p_\ell+p_{\bar{\ell}}))^2}\right)|a^-\rangle\\&\cdot\langle\ell^-|\nu|\bar{\ell}^-\rangle\,.\end{aligned} \quad (2.4.79)$$

Here it should be understood that p_ℓ denotes the momentum of the lepton (e^-,ν) whilst $p_{\bar{\ell}}$ denotes the momentum of the antilepton $(\bar{\nu},e^+)$. Equation (2.4.77) may then be inserted into eq. (2.4.65) and one may proceed as before. This approach does not take into account the scenario where there is interference between W
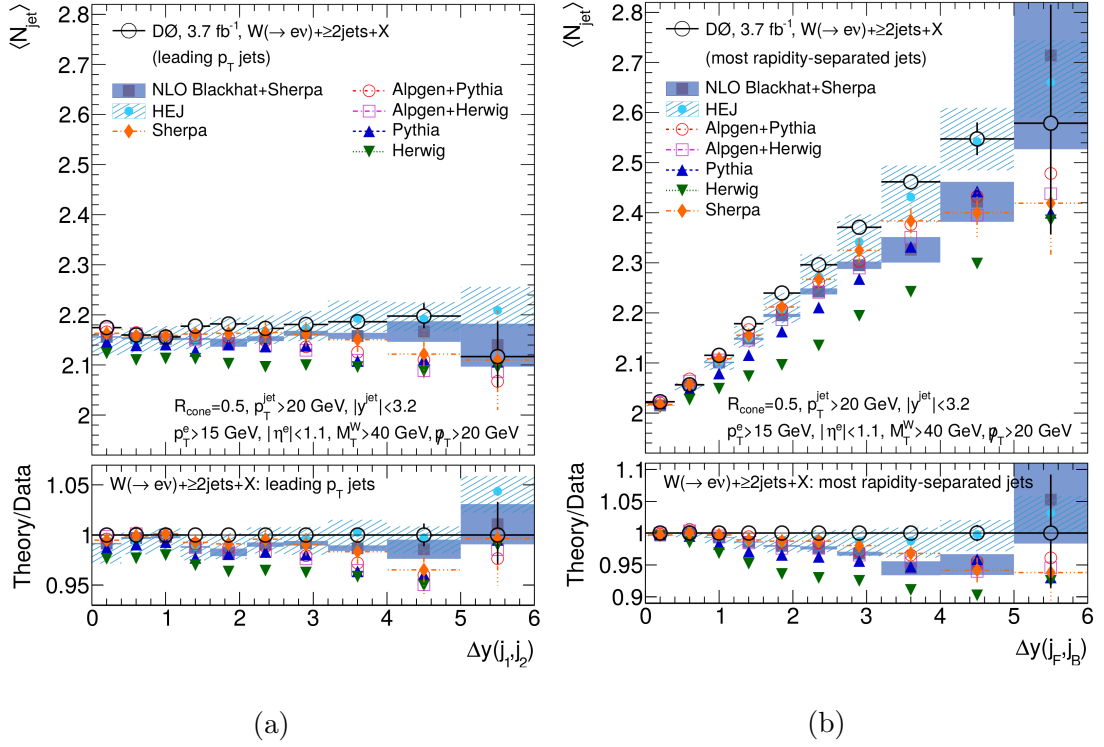
Figure 2.9: Plots reproduced from [130] showing the average number of jets in inclusive W plus dijet production from the Tevatron at $\sqrt{s} = 1.96$ TeV. This is shown as a function of the rapidity separation between (a) the two hardest jets, and (b) the most forwards and backwards jets. Predictions provided by HEJ give a good description of both distributions, whilst predictions for parton showers matched to LO and NLO notably underestimate the data.

emission from two identical quark legs, this effect however is found to be negligible in the high energy limit [125].

In figs. 2.9 and 2.10 we show a comparison of the HEJ formalism with data collected by the D0 [130] and ATLAS [131] collaborations respectively for inclusive W plus multi-jet production. The D0 analysis was performed at the Tevatron at $\sqrt{s} = 1.96$ TeV. In this analysis comparisons were made between the predictions from several parton showers matched to leading order (PYTHIA, HERWIG and SHERPA), one parton shower matched to NLO (BLACKHAT + SHERPA), and HEJ. In fig. 2.9 the average number of jets in inclusive dijet events is shown as a function of the rapidity separation between (a) the two hardest jets and (b) the most forward and backwards jet. In the first case, the average number of jets is independent
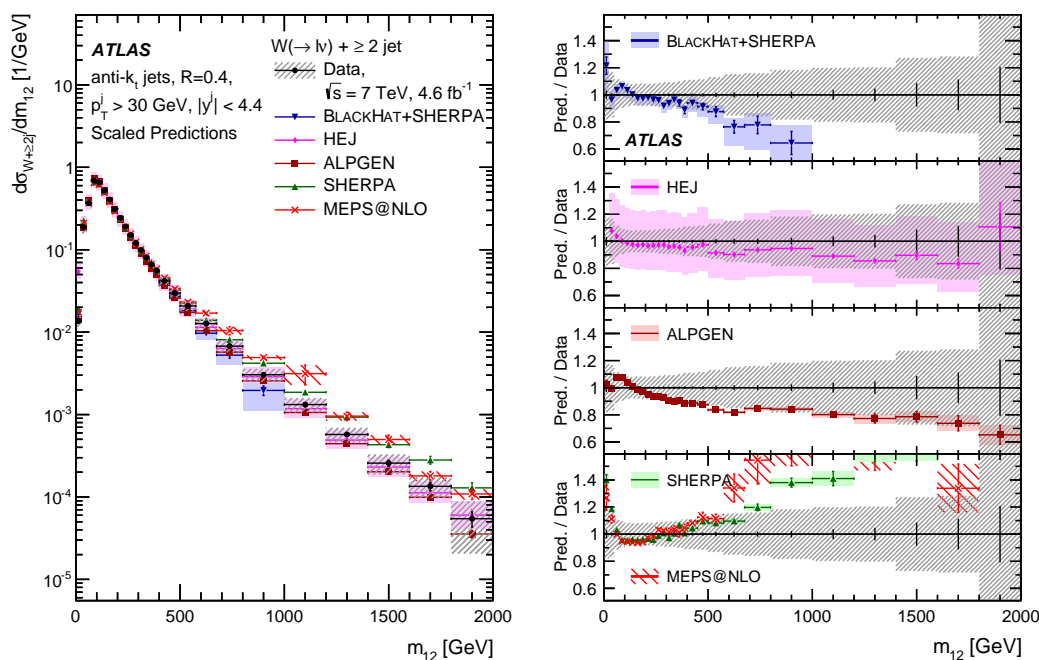
Figure 2.10: A plot of differential cross section with respect to the invariant mass between the two hardest jets in inclusive W plus dijet production from the LHC at $\sqrt{s} = 7$ TeV, reproduced from [131]. All predictions for parton shower matched and merged to fixed order show significant deviations from the data for large dijet invariant masses; only predictions from HEJ give a good description of the entire spectrum.

of the rapidity separation, whilst in the latter case there is linear growth as the rapidity separation increases; this is precisely the behaviour anticipated in the high energy limit. Notably the second distribution is only described well by HEJ, whilst other approaches (in which high numbers of jets may only be produced by the parton shower) underestimate the observed rate.

The ATLAS analysis was performed at the LHC at $\sqrt{s} = 7$ TeV. This analysis compared predictions for two LO merging methods (MLM in ALPGEN + HERWIG and CKKW in SHERPA), NLO merging (MEPS@NLO), NLO matching (BLACKHAT + SHERPA), and HEJ. In fig. 2.10 the differential cross section as a function of the invariant mass between the two hardest jets Δm_{12} in inclusive dijet events is shown. In the limit where Δm_{12} becomes large, the logarithms included to all orders in the HEJ formalism become important, and again HEJ gives the best description of

this observable, whereas other approaches that match or merge a parton shower to fixed order diverge from data in the limit of large invariant mass.

These experimental studies support the idea that an all order prescription at sufficiently high dijet invariant masses and large rapidity separations is required, and moreover that this region of phase space is accessible at the LHC (and even at the Tevatron). This further suggests that the formalism can indeed be relevant for analyses which utilise VBF cuts. Nevertheless, there are also numerous regions in phase space where the HEJ formalism does not provide an adequate description; in chapter 4 we shall extend the HEJ formalism, allowing it to be relevant for a broader range of experimental studies.

2.5 Adding a Parton Shower to HEJ

We have so far discussed two different regions of phase space, the soft-collinear limit and the high energy limit, where having an accurate description of QCD may only be achieved through an all order formalism. In both cases, this was achieved by only retaining the leading logarithmic terms; however away from the limit in which such logarithms dominate, these formalisms become increasingly less accurate. To some extent such inaccuracies can be corrected to fixed order accuracy through matching or merging methods; however these approaches are insufficient for variables that are sensitive to both types of logarithm (of which examples are presented later in the section; see also the review [132]). Furthermore, a parton shower is required to evolve the partonic final states produced by HEJ to a point at which a hadronisation model may be applied, and thereby obtain a more realistic picture of a given event. It is clearly worthwhile to combine the two schemes, and we therefore now review a method for matching HEJ to a parton shower that was presented in [133]. The dipole shower ARIADNE was chosen since although it does not itself describe BFKL-like dynamics, it is better than standard DGLAP-based parton showers at probing the region of small x and semi-hard emissions relevant in the high energy limit [134]. The method, however, is independent of the shower model selected.

The challenge of combining two all order prescriptions is quite different to those issues addressed in section 2.2; the singularities associated with a parton becoming soft are included already to all orders in HEJ, and thus it is necessary to prevent not just the double counting of a single term but infinitely many. An elegant solution exists however; what is required is the modification of the splitting kernels that are exponentiated in Sudakov factors, which may be achieved through subtraction terms.

In order to derive the appropriate subtraction term we first recall that the standard Altarelli-Parisi splitting functions may be related to the ratio of matrix elements squared in the soft-collinear limit:

$$\frac{|\mathcal{M}_{n+1}|^2}{|\mathcal{M}_n|^2} \frac{dp_\perp^2}{16\pi^2} dz \sim \frac{dp_\perp^2}{p_\perp^2} dz \frac{\alpha_s}{2\pi} P_{gg}(z) \ . \tag{2.5.80}$$

By comparing the form of the dipole splitting functions in the soft-collinear limit in eq. (2.1.9) with the right-hand side of eq. (2.5.80), it is possible to obtain the relation:

$$D(p_\perp^2, y) \sim \frac{z}{16\pi^2} \frac{|\mathcal{M}_{n+1}|^2}{|\mathcal{M}_n|^2} \ . \tag{2.5.81}$$

Therefore we can define a subtraction kernel in terms of a ratio of HEJ matrix elements:

$$D_{\text{HEJ}}(p_\perp^2, y) = \frac{z}{16\pi^2} \frac{|\mathcal{M}_{n+1}^{\text{HEJ}}|^2}{|\mathcal{M}_n^{\text{HEJ}}|^2} \ . \tag{2.5.82}$$

In the parton shower evolution we wish to calculate the modified Sudakov factor

$$\tilde{\Delta}(p_{1\perp}^2, p_{2\perp}^2) = \exp\left\{ -\int_{p_{2\perp}^2}^{p_{1\perp}^2} dp_\perp^2 \int dy \ D_{\text{subtracted}}(p_\perp^2, y) \right\} \tag{2.5.83}$$

where

$$D_{\text{subtracted}}(p_\perp^2, y) = D(p_\perp^2, y) - D_{\text{HEJ}}(p_\perp^2, y) \ . \tag{2.5.84}$$

This can be achieved using the Sudakov veto algorithm (see section 3.2) by generating emissions as usual but vetoing events with a probability:

$$\mathcal{P}_{\text{veto}} = \frac{D_{\text{HEJ}}(p_\perp^2, y)}{D(p_\perp^2, y)} = \frac{r_{\text{HEJ}}}{r_{\text{ARIADNE}}} \ , \tag{2.5.85}$$

and we define:

$$r_{\text{HEJ}} = \frac{|\mathcal{M}_{n+1}^{\text{HEJ}}|^2}{|\mathcal{M}_n^{\text{HEJ}}|^2} \qquad\qquad r_{\text{ARIADNE}} = \frac{16\pi^2}{z} D(p_\perp^2, y) \ . \tag{2.5.86}$$

2.5. Adding a Parton Shower to HEJ

In this way the double counting of soft emissions is avoided, but the kernel for collinear splittings is still properly accounted for to all orders.

The full algorithm for matching HEJ with ARIADNE proceeds as follows:

1. Generate a partonic state with HEJ with a cutoff on the transverse momentum of the partons.

2. Pass this event to ARIADNE in Les Houches format [135]. This requires choosing colour connections at random that give rise to non-crossing ladders of rapidity-ordered, colour-connected ladders (which dominate in the MRK limit [136, 137]).

3. Set up the internal dipole event record in ARIADNE and evolve the dipole cascade starting from the largest transverse momentum of any parton in the event.

4. For each potential emission, check if this emission could have been produced by HEJ, namely, it must be a gluon emission between the two jets extremal in rapidity. If the emission could not have been produced in HEJ:

   (a) Reject any gluon emission that is extremal in rapidity and is above the minimum scale of transverse momentum for extremal jets.

   (b) Otherwise, accept the emission.

   If the emission could have been produced in HEJ:

   (a) Calculate the ratio $r_{\text{HEJ}}/r_{\text{ARIADNE}}$.

   (b) Generate a random number $r \in [0, 1]$; if $r < r_{\text{HEJ}}/r_{\text{ARIADNE}}$ veto the emission, and otherwise accept it.

5. After the dipole cascade has evolved down to the hadronisation scale, pass the event to PYTHIA after which hadronisation and the decays of unstable particles is performed.

An ATLAS analysis which measured additional jet activity in dijet events in pp collisions at $\sqrt{s} = 7$ TeV at the LHC [138] was found to discriminate between

NLO matching to two parton showers (PYTHIA and HERWIG) using the POWHEG method, partonic HEJ, and HEJ matched to ARIDANE using the method described above. In this analysis, events were required to have at least two jets, the hardest having a transverse momentum $p_T > 60$ GeV and the second hardest having $p_T > 50$ GeV. The minimum jet transverse momentum for additional jets was set at either 20 or 30 GeV (corresponding to data collected in 2010 and 2011). Jets were defined using the anti-k_T algorithm with $R = 0.6$. In addition jets were required to have rapidity $|y_j| < 4.4$ or $|y_j| < 2.4$ for data collected in 2010 and 2011 respectively. We now review some of the more pertinent results from this study.

In fig. 2.11 we show the average number of jets in the rapidity interval defined between the two hardest jets, which in fig. 2.11a is shown as a function of increasing rapidity separation (Δy) between the tagging jets. The trend for an increasing number of jets as the separation increases that is expected from multi-Regge exchange is seen in the data; the plateau that is seen at large rapidities may arise from the combined effect of steeply falling PDFs and the increasing relative importance of colour singlet (pomeron) exchange. Both parton shower predictions with matching to NLO overestimate the number of jets for the largest rapidity separations. Partonic HEJ, while giving a better description of the data in this region, underestimates the data for lower rapidities. One might naïvely have expected HEJ to perform extremely well in such an observable. However, by requiring that the two tagging jets be harder than those counted in the interval, the event selection induces a hierarchy of jet transverse momenta, which cannot be accommodated for in the MRK limit. (This issue was investigated in [139].) It is found that the addition of a parton shower to HEJ leads to an improved description at lower rapidities, and furthermore qualitatively reproduces the shape of the spectrum much better than partonic HEJ.

Figure 2.11b instead shows the average number of jets in the rapidity interval as a function of the average transverse momentum of the tagging dijet system, $\bar{p}_T$, where the tagging jets were required to have a rapidity separation of greater than 1 unit ($\Delta y > 1$). As $\bar{p}_T$ increases, there is an enhanced probability for soft emissions; again at very large values of $\bar{p}_T$ the effect of PDF suppression becomes important.
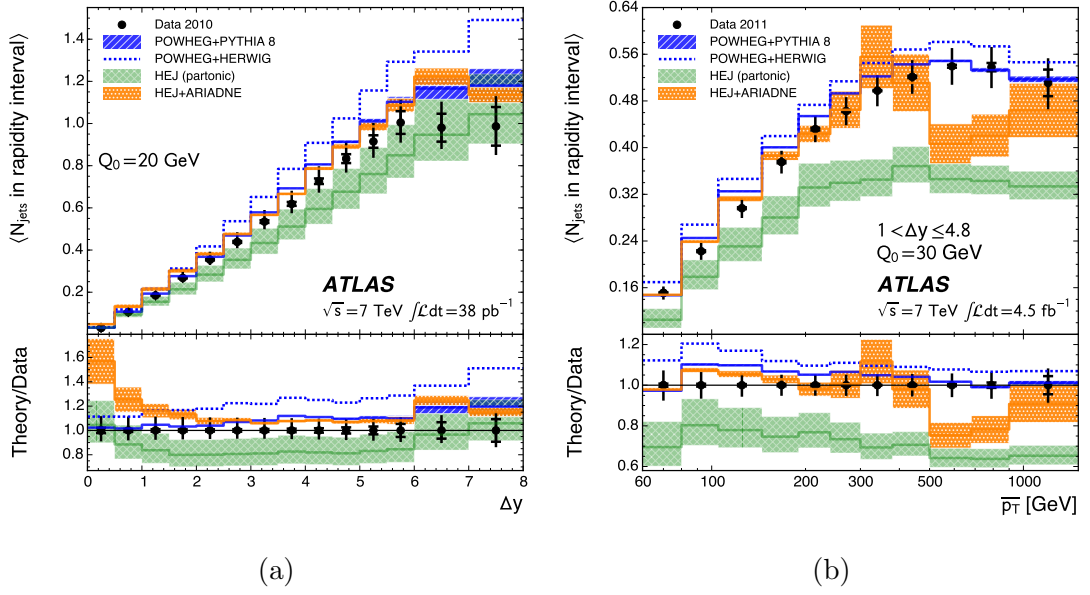
Figure 2.11: Plots reproduced from [138] showing the average number of jets in the rapidity interval between the two hardest jets, for dijet events at $\sqrt{s} = 7$ TeV at the LHC, as a function of (a) the rapidity difference Δy, and (b) the average transverse momentum of the dijet system $\bar{p}_T$.

It is unsurprising that parton shower plus fixed order predictions which account for soft emissions to all orders describe this observable well, whilst partonic HEJ underestimates the data. The improvement seen from adding a parton shower to HEJ is very apparent for this observable.

In figs. 2.12a and 2.12b the average azimuthal correlation of the dijet system $\langle \cos(\pi - \Delta\phi) \rangle$ is investigated. This observable is sensitive to the amount of additional radiation in the event; exclusive dijets must balance in azimuth, and the observable approaches one. Additional hard emissions shift the jets away from a back-to-back topology and the average correlation approaches zero.

The average correlation of the dijets as a function of Δy is shown in fig. 2.12a. The data behave qualitatively as expected; as the rapidity separation increases, the average number of hard emissions increases, which act to decorrelate the dijets. All theoretical predictions capture the shape of this observable, though partonic HEJ overestimates the correlation, while both shower predictions and HEJ+ARIADNE underestimate the correlation.

The average correlation as a function of $\bar{p}_T$ is shown in fig. 2.12b. As the transverse momentum of the dijet system increases, there is less phase space available for hard emissions; since soft emissions typically have little effect on the azimuthal distribution of the jets, the correlation is seen to increase for increasing $\bar{p}_T$. This effect is qualitatively captured by all theoretical distributions, however at small $\bar{p}_T$, the correlation is overestimated by HEJ, underestimated by the parton shower plus fixed order, while HEJ+ARIADNE gives a fairly good description of the entire distribution.

The second moment of azimuthal correlation $\langle \cos 2(\pi - \Delta\phi) \rangle = \langle \cos(2\Delta\phi) \rangle$ is expected to fall faster than the first moment for increasing hard radiation. Thus the ratio of the two, which is shown in figs. 2.12c and 2.12d is sensitive to the amount of radiation, but does not suffer from systematic errors in normalisation that might be present in the distributions in figs. 2.12a and 2.12b. This observable emphasises that both as function of Δy and $\bar{p}_T$ partonic HEJ typically overestimates the level of correlation and fixed order plus parton shower approaches underestimate the correlation; however, HEJ+ARIADNE gives a good description in both cases.

The results presented in this analysis demonstrate that certain variables which are sensitive to the amount, angular distribution and hardness of additional radiation in inclusive dijet production cannot be fully described either by either parton shower or HEJ approaches alone. Similar conclusions could also be drawn from an earlier analysis that made a comparable set of measurements [140]. This suggests that in such observables, both soft-collinear and high energy logarithms can become important, and that combining these schemes is well-motivated. However, in the method presented above, there is still room for improvement. It was observed in [133] that certain events produced by HEJ contained soft emissions that in the dipole cascade of ARIADNE would only have been produced at a late stage of evolution. This has the effect that the phase space available to the shower for such events is limited, which is not corrected for by the modified Sudakov factor. It was proposed that this limitation could be corrected by a modified merging algorithm that would reduce the impact of such events. The implementation of such an algorithm will be the subject of chapter 5.
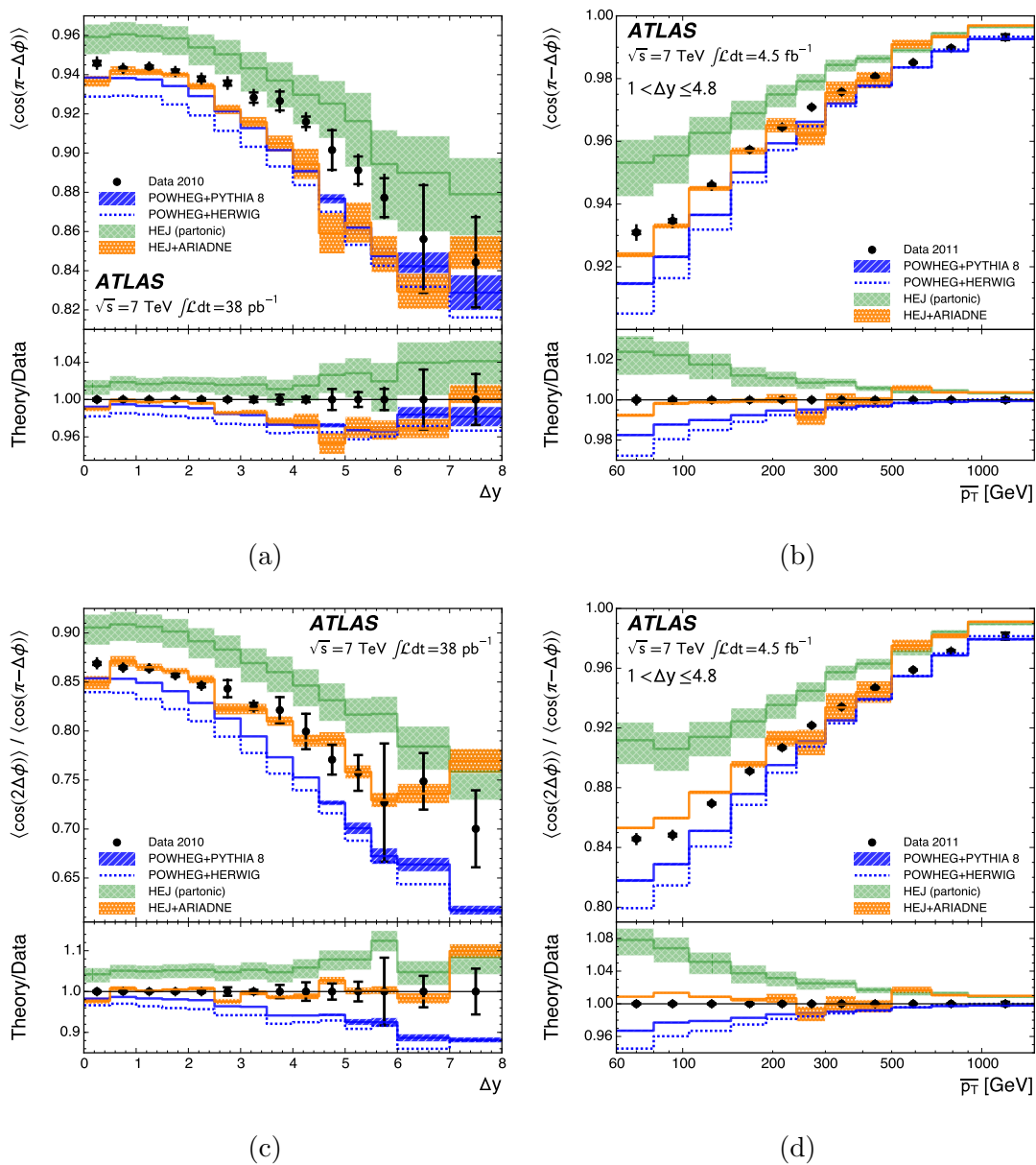
Figure 2.12: Plots reproduced from [138] showing moments of the azimuthal correlation of the dijet system for dijet events in *pp* collisions at $\sqrt{s} = 7$ TeV at the LHC. This is shown as a function of (a,c) the rapidity interval between the tagging jets, and (b,d) the average transverse momentum of the dijet system $\bar{p}_T$. In (a,b) the first moment $\langle\cos(\pi - \Delta\phi)\rangle$ is shown, whilst in (c,d) the ratio of the second to the first moment $\langle\cos(2\Delta\phi)\rangle/\langle\cos(\pi - \Delta\phi)\rangle$ is shown.

Chapter 3

Numerical Methods

In this chapter we briefly take a detour to discuss some of the practicalities involved in obtaining quantitative predictions from theory which may be compared with data from experiments. The quantities we typically wish to compute require performing integrals of distributions that are too cumbersome to perform analytically; it is therefore standard practice to rely on numerical tools to obtain a result. It is necessary that such tools produce stable results (they must converge to the correct values) and are efficient (otherwise it would be impossible to obtain results in finite amount of time). In the sections which follow we discuss some commonly used methods which satisfy these requirements.

3.1 The Monte Carlo Method

Let us assume we wish to compute some multi-dimensional integral; a common example might be the phase space integral for calculating the cross section; for m massless final state particles, there are $n = 3m - 4$ independent components of momentum, which we simply denote by the vector $\mathbf{x}$. The integrand, which would be the matrix element squared normalised by the flux factor, we simply denote as $f(\mathbf{x})$. We wish to compute the following integral over the volume V in an n-dimensional vector space:

$$I[f] = \int_V d^n x \ f(\mathbf{x}) \ . \tag{3.1.1}$$

For low numbers of dimensions there are many techniques to numerically evaluate an integral (for example, Simpson's rule or Gaussian integration [141]), however since there are usually many final state particles, the dimension n of the phase space is typically very large. One of the most efficient methods for many dimensions is known as the *Monte Carlo* method [142]. This involves randomly selecting N points $\mathbf{x}_i$ in the volume V, and estimating the integral as the average of f on those points:

$$I[f] \sim V \langle f \rangle \,, \tag{3.1.2}$$

where

$$\langle f \rangle = \frac{1}{N} \sum_{i=1}^{N} f(\mathbf{x}_i) \,. \tag{3.1.3}$$

The central limit theorem predicts that for large enough N this will be an unbiased estimate of the integral, for which an estimate of the error, or difference between the calculated and true value, is given by [142]:

$$E[f] = \sqrt{\frac{\mathrm{Var}(f)}{N-1}} \tag{3.1.4}$$

in which the *variance* of f is:

$$\mathrm{Var}(f) = \langle f^2 \rangle - \langle f \rangle^2 \,. \tag{3.1.5}$$

The error should therefore decrease as $1/\sqrt{N}$ as the number of points is increased. Fundamentally however, the error is proportional to the standard deviation of f ($\sigma(f) = \sqrt{\mathrm{Var}(f)}$). If the function f is strongly peaked in certain locations in V, then flatly selecting points

$$x_i^{(j)} = r_i (x_{\max}^{(j)} - x_{\min}^{(j)}) \tag{3.1.6}$$

with $r_1 \in [0, 1]$ a random number, will lead to a large variance and the result will be slow to converge.

Let us now suppose that we have a function $g(\mathbf{x})$ which captures the main features of $f(\mathbf{x})$ in V, then $h(\mathbf{x}) = f(\mathbf{x})/g(\mathbf{x})$ will be more slowly varying in V than the original function. We perform a change of variables $\mathbf{x} \to \mathbf{y} = \mathbf{G}(\mathbf{x})$, such that the Jacobian is given by:

$$\det\left(\frac{\partial \mathbf{y}}{\partial \mathbf{x}}\right) = g(\mathbf{x}) \,. \tag{3.1.7}$$

The integral is then given by:

$$I[h] = \int_V d^n x \ g(\mathbf{x}) h(\mathbf{x}) = \int_{V'} d^n y \ h(\mathbf{y}) \ . \tag{3.1.8}$$

Flatly selecting points in the new volume V',

$$y_i^{(j)} = r_i (y_{\max}^{(j)} - y_{\min}^{(j)}) \tag{3.1.9}$$

should now lead to a smaller variance, and faster convergence of the Monte Carlo estimate of I. However, transforming the integrand $f(\mathbf{x})$, which may be a very complicated function, to the function $h(\mathbf{y})$ in the new variables may not be straightforward. Moreover, due to the modular nature of many generators, the calculation of the matrix element may not be easily accessed. Furthermore, we are usually not just interested in the single numerical value of the integral, but rather the differential cross section as function of our variables $\mathbf{x}$. Thus while we wish to sample the phase space according to the transformed variable $\mathbf{y}$, we evaluate the integrand f in terms of $\mathbf{x}$ using the inverse of the Jacobian in eq. (3.1.7):

$$I[f] = \int_{V'} d^n y \ \det \left(\frac{\partial \mathbf{G}^{-1}(\mathbf{y})}{\partial \mathbf{y}} \right) f(\mathbf{G}^{-1}(\mathbf{y})) \ . \tag{3.1.10}$$

Evaluating I using the Monte Carlo method then yields:

$$I[f] \sim \frac{V'}{N} \sum_{i=1}^{N} w_i f(\mathbf{x}_i) \tag{3.1.11}$$

where:

$$\mathbf{x}_i = \mathbf{G}^{-1}(\mathbf{y}_i) \ , \tag{3.1.12}$$

$$w_i = \det \left(\frac{\partial \mathbf{G}^{-1}}{\partial \mathbf{y}} \right) \Bigg|_{\mathbf{y}_i} \ . \tag{3.1.13}$$

Thus we see the integral is simply calculated as a weighted average, where the weight is the Jacobian for the transformation and compensates for the fact that we select points flatly in the transformed volume V'. This procedure is known as *importance sampling* [142].

3.2 The Sudakov Veto Method

The Sudakov Veto method [67, 69] is a means of numerically generating a sequence of ordered values according to some probability distribution, for example the values

of the ordering variable corresponding to the emissions in a parton shower.

Let us suppose that we wish to generate $q_1 \in (0, Q)$ where the probability that $q_1 < q$ is given by $F(q)/F(Q)$ with $F(q)$ a monotonically increasing function with $F(0) = 0$. Recall that $\Delta(Q^2, q^2)$ from eq. (2.1.4) represents the probability that there are no emissions between the hard scale Q^2 and q^2. As $q^2 \to 0$, $\Delta(Q^2, q^2) \to 0$, that is, the probability of there being no emissions vanishes. Note also that $\Delta(Q^2, Q^2)$ is normalised to 1, meaning that there is a vanishingly small probability for an emission in a vanishingly small interval. Clearly $F(q) = \Delta(Q^2, q^2)$ satisfies the necessary requirements.

As discussed in section 2.1, in principle a value for q_1 can be selected by generating a random number $r \in [0, 1]$ and solving

$$F(q_1) = r F(Q) \tag{3.2.1}$$

for q_1. However, if $F(q)$ is too complicated for eq. (3.2.1) to be easily solvable, but we know $f(q) = dF/dq$, then if we can find another monotonic function $G(q) \geq 0$ with derivative $g(q) = dG/dq$ such that

$$\frac{f(q)}{F(q)} < \frac{g(q)}{G(q)} \tag{3.2.2}$$

is satisfied for $q < Q$ we can instead use the following veto method for generating the values of $\{q_i\}$.

1. Solve $G(q') = r_1 G(Q)$, with $r_1 \in [0, 1]$ a random number.

2. If $f(q)/F(q) > r_2 g(q)/G(q)$, with $r_2 \in [0, 1]$ another random number, set $q_1 = q'$ to be the generated value of the ordering variable.

3. Otherwise veto this choice for q_1, and set $Q = q'$ and return to step 1 and generate a new $q'' < q'$.

We now prove that this method generates the correct probability distribution for q_1, namely $\mathcal{P}(q_1 < q) = F(q)/F(Q)$, as stated above. We define

$$\mathcal{P}_n(q_1 < q; q_1 \in [0, Q]) \tag{3.2.3}$$

3.2. The Sudakov Veto Method

as the probability of finding $q_1 < q$ after n vetoes for $q_1 \in [0, Q]$, and in the following we will calculate:

$$\mathcal{P}(q_1 < q) = \sum_{n=0}^{\infty} \mathcal{P}_n(q_1 < q; q_1 \in [0, Q]) \, . \tag{3.2.4}$$

Since $G(q)$ is a monotonic function, for no vetoes we have:

$$\mathcal{P}_0(q_1 < q; q_1 \in [0, Q]) = \frac{G(q)}{G(Q)} \, . \tag{3.2.5}$$

The probability that having generated q' it is then vetoed is given by:

$$\mathcal{P}_{\text{veto}}(q') = 1 - \frac{f(q')/F(q')}{g(q')/G(q')} \, . \tag{3.2.6}$$

The probability that having first generated q', we have $q_1 < q$ after one veto is given by:

$$
\begin{aligned}
d\mathcal{P}_1(q_1 < q; q_1 \in [0, Q]) &= dq' \frac{g(q')}{G(Q)} \cdot \mathcal{P}_{\text{veto}}(q') \cdot \mathcal{P}_0(q_1 < q; q_1 \in [0, q']) \\
&= dq' \frac{g(q')}{G(Q)} \cdot \mathcal{P}_{\text{veto}}(q') \cdot \frac{G(q)}{G(q')} \, ,
\end{aligned}
\tag{3.2.7}
$$

where we have used the fact that the probability of finding q_1 in the interval $[q', q' + dq']$ is $g(q')dq'$. Thus integrating over q' we obtain:

$$
\begin{aligned}
\mathcal{P}_1(q_1 < q; q_1 \in [0, Q]) &= \int_q^Q dq' \frac{g(q')}{G(Q)} \mathcal{P}_{\text{veto}}(q') \frac{G(q)}{G(q')} \\
&= \frac{G(q)}{G(Q)} \int_q^Q dq' \left[\frac{g(q')}{G(q')} - \frac{f(q')}{F(q')} \right] \\
&= \frac{G(q)}{G(Q)} \left[\ln\left(\frac{G(Q)}{G(q)} \right) - \ln\left(\frac{f(Q)}{F(q)} \right) \right] \, .
\end{aligned}
\tag{3.2.8}
$$

Similarly, after two vetoes we have:

$$\mathcal{P}_2(q_1 < q; q_1 \in [0, Q]) = \frac{1}{2!} \frac{G(q)}{G(Q)} \left[\ln\left(\frac{G(Q)}{G(q)} \right) - \ln\left(\frac{f(Q)}{F(q)} \right) \right]^2 \, . \tag{3.2.9}$$

Generalising this to n vetoes, we have:

$$\mathcal{P}_n(q_1 < q; q_1 \in [0, Q]) = \frac{1}{n!} \frac{G(q)}{G(Q)} \left[\ln\left(\frac{G(Q)}{G(q)} \right) - \ln\left(\frac{f(Q)}{F(q)} \right) \right]^n \, . \tag{3.2.10}$$

Therefore

$$\mathcal{P}(q_1 < q) = \sum_{n=0}^{\infty} \mathcal{P}_n(q_1 < q; q_1 \in [0, Q])$$

$$= \sum_{n=0}^{\infty} \frac{1}{n!} \frac{G(q)}{G(Q)} \left[\ln \left(\frac{G(Q)}{G(q)} \right) - \ln \left(\frac{f(Q)}{F(q)} \right) \right]^n$$

$$= \frac{G(q)}{G(Q)} \exp \left[\ln \left(\frac{G(Q)}{G(q)} \right) - \ln \left(\frac{f(Q)}{F(q)} \right) \right]$$

$$= \frac{F(q)}{F(Q)} \tag{3.2.11}$$

as required. Although we have neglected the additional splitting variables associated with the emission, it can also be shown that a similar procedure will work for functions of two variables [143].

An example of the application of this method is in the generation of the parton shower with modified splitting kernel in the matching of HEJ with Ariadne described in section 2.5, or in the merging algorithm that we shall present in chapter 5. In both cases, we wish to generate some emissions according to a modified Sudakov factor $\tilde{\Delta}(Q^2, q^2)$, with a subtracted splitting kernel which we denote schematically by $P_{\text{subtracted}}(q^2)$. Then we would have (using the DGLAP equation 2.1.3):

$$\frac{f(q^2)}{F(q^2)} = \frac{1}{\tilde{\Delta}(Q^2, q^2)} \frac{d\tilde{\Delta}(Q^2, q^2)}{dq} = P_{\text{subtracted}}(q^2)$$

$$= P(q^2) - P_{\text{HEJ}}(q^2)$$

$$= P(q^2) \left(1 - \frac{P_{\text{HEJ}}(q^2)}{P(q^2)} \right) , \tag{3.2.12}$$

where $P(q^2)$ is assumed to be the standard Altarelli-Parisi splitting function. In this case, we would take $G(q^2)$ to be the normal Sudakov factor, assuming the generation of ordering variables in the normal shower is a solved problem. Then we have:

$$\frac{g(q^2)}{G(q^2)} = P(q^2) . \tag{3.2.13}$$

This choice should satisfy eq. (3.2.2) for a reasonable choice of $P_{\text{HEJ}}(q^2)$. The probability to veto an emission is then given by:

$$\mathcal{P}_{\text{veto}} = \frac{P_{\text{HEJ}}(q^2)}{P(q^2)} . \tag{3.2.14}$$

Chapter 4

Subleading Logarithms in HEJ for W plus jets

In section 2.4 we presented the HEJ formalism, a prescription for calculating multi-jet cross sections valid in the (MRK) limit of large invariant dijet masses compared to t-channel momenta:

$$\hat{s} \gg \hat{s}_{ij} \gg |\hat{t}_i| \sim |\vec{k}_{i\perp}|^2 \ . \tag{4.0.1}$$

This hierarchy of scales leads to the large logarithms that necessitate the all order treatment provided by HEJ; imposing the limit at the level of the amplitude allows an extraction of the leading logarithmic contributions. FKL configurations (having non-vanishing contributions in this limit) are included to all orders at leading logarithmic accuracy, whilst non-FKL configurations are included only at leading order via matching. This procedure has the consequence that in regions of phase space in which eq. (4.0.1) is no longer satisfied, FKL configurations may not provide the dominant contribution to cross section, and the accuracy of the prediction is limited to leading order. Leading order predictions are usually not sufficient to obtain an accurate description of data, so this behaviour leads to deviations between the predictions for HEJ and data.

This effect becomes visible in distributions of transverse momentum, for example the scalar sum of transverse momenta H_T in inclusive W plus dijets production as shown in fig. 4.1 (reproduced from [131]) . As the transverse momentum of the jets
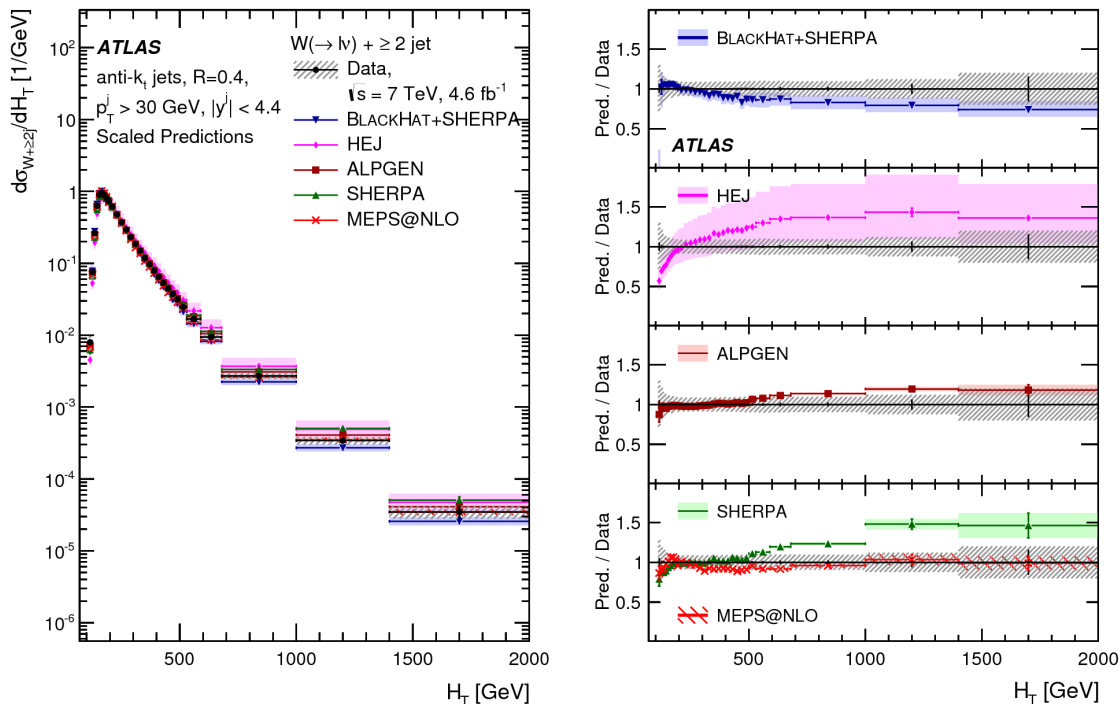
94

Figure 4.1: A plot of differential cross section with respect to the scalar sum of transverse momentum H_T in inclusive W plus dijet production from the LHC at $\sqrt{s} = 7$ TeV, reproduced from [131]. Large discrepancies for large H_T are seen between HEJ and data as the MRK limit is no longer satisfied in this region.

increases, it becomes increasingly difficult to satisfy the requirement that $\hat{s}_{ij} \gg |\hat{t}_i|$. The predictions are therefore increasingly dominated by non-FKL configurations in the large transverse momentum tail, and accordingly large deviations between HEJ and data are seen.

The purpose of this chapter is to discuss improvements which have been made to reduce the contributions to the cross section from fixed order and thereby improve the overall description of data. This has been achieved by including terms in the HEJ all order formalism that are associated with subleading logarithms in the MRK limit. Alternatively, this may be understood as extending the region of phase space in which the HEJ formalism is applicable. This work was performed in the W plus jets channel, which has been so precisely measured at the Tevatron and the LHC [130, 131, 144–147] that it may be used as a standard candle against which theoretical developments are tested.

4.1 Unordered Emissions in HEJ

In this section we now consider a type of emission which first contributes at next-to-leading logarithm (NLL) in the MRK limit. Let us consider the process $qQ \to qg \ldots gQ$. We recall from section 2.3 that for FKL configurations the $2 \to n$ amplitude squared is asymptotically proportional to the product of the invariant masses between each pair of rapidity-ordered partons:

$$|\mathcal{A}_{ab \to 1g \ldots gn}|^2 \propto \hat{s}_{12}^2 \hat{s}_{23}^2 \ldots \hat{s}_{n-1,n}^2 \, . \tag{4.1.1}$$

This behaviour corresponds to $n-1$ colour-octet exchanges in the t-channel between two quarks extremal in rapidity. Let us now consider the configuration in fig. 4.2. It has been shown [136,137] that in the MRK limit the only diagrams which contribute are those for which rapidity ordered partons have uncrossed colour connections. Therefore the vertical ordering of the final state particles in fig. 4.2 denotes their ordering in rapidity. It should be apparent that such a t-channel quark exchange occurs by allowing one final state gluon to be emitted more forwards than the most forwards outgoing quark. We refer to such a gluon as an *unordered* emission. By the arguments of section 2.3, the amplitude squared for such a configuration must be suppressed by $\hat{s}_{12}$ relative to eq. (4.1.1) and is no longer be independent of Δy_{12} and contributes to the cross section at NLL (corresponding to terms of the form $\alpha_s [\alpha_s \ln(\hat{s}_{ij}/k_\perp^2)]^N$ relative to Born level). Therefore, while imposing strict MRK kinematics results in capturing the leading logarithmic behaviour of the cross section, relaxing the kinematics to:

$$y_1 \sim y_2 \gg y_3 \gg \cdots \gg y_{n-1} \gg y_n; \qquad |\vec{k}_{i\perp}| \sim k_\perp \, \forall i \, . \tag{4.1.2}$$

allows the inclusion of certain NLL contributions. The same arguments apply for a gluon to be emitted more backward than the most backward outgoing quark, or:

$$y_1 \gg y_2 \gg \cdots \gg y_{n-2} \gg y_{n-1} \sim y_n; \qquad |\vec{k}_{i\perp}| \sim k_\perp \, \forall i \, . \tag{4.1.3}$$

We therefore also include such backward emissions in our definition of unordered emissions.

Due to the factorisation of the amplitude in the high energy limit, it is conceptually straightforward to extend the HEJ formalism to this class of correction.
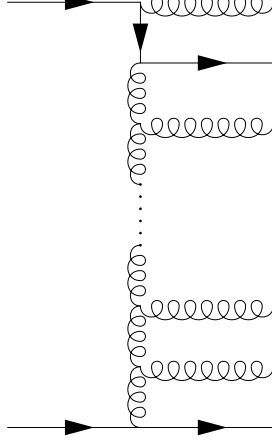
Figure 4.2: A tree-level diagram for the partonic process $qQ \to qg \ldots gQ$ in which there is a t-channel quark exchange. The vertical ordering of final state particles denotes their ordering in rapidity. Such a configuration, containing one 'unordered' gluon emission, would only contribute to the cross section at NLL.

Since the hierarchy of all $n-3$ remaining internal gluon emissions is preserved, this will still correspond to a product of Lipatov vertices. Only the external legs are modified, and hence only the current factors need be rederived. This may be done in a fashion similar to that presented in section 2.4 but where instead all diagrams contributing to $q(p_a)Q(p_b) \to q(p_1)g(p_g)Q(p_2)$ must be included, with the single requirement that $y_1, y_g \gg y_2$ for forwards unordered (or $y_1 \gg y_g, y_2$ for backwards unordered). It may be shown [127] that the amplitude in this case is given by:

$$\mathcal{A}_{\mathrm{uno}} = -g_s^3 \frac{\langle 2|\gamma_\mu|b\rangle}{\hat{t}_{b2}} j_{\mathrm{uno}}^\mu(p_a, p_1, p_g) \tag{4.1.4}$$

where the unordered current is given by

$$j_{\mathrm{uno}}^\mu(p_a, p_1, p_g) = \varepsilon_{g\nu} T_{2b}^d (iT_{1i}^c T_{ia}^d U_1^{\mu\nu} + iT_{1i}^d T_{ia}^c U_2^{\mu\nu} + f^{cde} T_{1a}^e L^{\mu\nu}) \, , \tag{4.1.5}$$

with

$$U_1^{\mu\nu} = \frac{1}{\hat{s}_{1g}} \left(\langle 1|\nu|g\rangle\langle g|\mu|a\rangle + 2p_1^\nu\langle 1|\mu|a\rangle \right) \, , \tag{4.1.6}$$

$$U_2^{\mu\nu} = \frac{1}{\hat{t}_{ag}} \left(2\langle 1|\mu|a\rangle p_a^\nu - \langle 1|\mu|g\rangle\langle g|\nu|a\rangle \right) \, , \tag{4.1.7}$$

4.1. Unordered Emissions in HEJ

$$L^{\mu\nu} = \frac{1}{\hat{t}_{a1}} \left(-2p_g^\mu \langle 1|\nu|a\rangle + 2g^{\mu\nu}\langle 1|\slashed{p}_g|a\rangle \right.$$
$$\left. + \langle 1|\mu|a\rangle \left[(q_1+q_2)^\nu + \frac{\hat{t}_{b2}}{2}\left(\frac{p_2^\nu}{p_g \cdot p_2} + \frac{p_b^\nu}{p_g \cdot p_b} \right) \right] \right) . \qquad (4.1.8)$$

The counterpart to eq. (2.4.56) may then be found by contracting the currents,

$$S_{qQ \to qgQ} = j_{\mathrm{uno}}^\mu \langle 2|\gamma_\mu|b\rangle , \qquad (4.1.9)$$

and computing the sum/average over final/initial state colours, helicities and polarisations. Inserting this into eq. (2.4.72) and performing the phase space integration as in eq. (2.4.75) (and summing over all numbers of final state particles) one obtains the NLL contribution to the cross section from unordered emissions.

In order to extend this framework to include the emission of a W boson there are two cases to consider. In the first case, the unordered emission and the W emission originate from opposite quark legs. In this case, we simply need to contract the unordered current j_{uno}^μ in eq. (4.1.9) with J_W^μ from eq. (2.4.79). In the second case, both the unordered and W emissions are associated with the same leg, which requires the derivation of a new effective current. This shall be performed in the following section. We note that while both cases represent NLL corrections, the latter is likely to have a greater impact. The reason for this is that the first configuration only arises for qQ initial states, whereas in the second case qg initial states are also allowed. This is significant because the gluon PDF usually exceeds the PDF for quarks at the energies of the LHC [31], and thus qg channels will contribute more to the cross section.

Before continuing with our discussion of unordered emissions in inclusive W plus dijet production, it is worth noting that these only constitute one class of NLL correction. Any configuration which arises from the replacement of one gluon t-channel exchange with a quark t-channel exchange will contribute at NLL. In particular this includes the insertion of a quark-antiquark pair in the final state. If this pair are the most forwards two partons or the most backwards two partons, then similarly to unordered emissions this will constitute a rederivation of the current factors. In section 4.1.6 we will demonstrate that such a current may be obtained through crossing symmetry from the current for unordered emissions. If

the quark-antiquark pair are emitted in between the most extremal partons in rapidity, this will constitute a correction to the Lipatov vertex. In this thesis such configurations will not be considered, although we expect them to give rise to a similar size of correction to the cross section. Nevertheless, it is justified to just consider unordered emissions here because they constitute a well-defined final state and therefore no interference between the different classes of NLL configurations is expected.

4.1.1 Derivation of the Current for W plus Unordered Emissions

In this section we demonstrate that the matrix element for $q(p_a)Q(p_b) \rightarrow q(p_1)g(p_g)W(p_W)Q(p_2)$ has a structure equivalent to eq. (4.1.4), and thereby extract the current corresponding to $q(p_a) \rightarrow q(p_1)g(p_g)W(p_W)$, where the W boson is emitted either from parton a or 1. This will be done by assuming the kinematics stated in eq. (4.1.3), which is equivalent to requiring $p_b \sim p_2 = p_-$. We further assume that the W boson is emitted in the same direction as the quark with which it is associated (in this case forwards) since the matrix element is suppressed away from this limit.

We start by considering the diagrams in figs. 4.3 and 4.4 in which the gluon is emitted from the same partonic leg as the W boson. The sum of diagrams in fig. 4.3, in which the gluon is emitted from the outgoing parton, is given by:

$$
\begin{aligned}
A_1 + A_2 + A_3 =& i(ig_s)^3 \left(\frac{ig_W}{\sqrt{2}} \right) \frac{\langle 2|\mu|b \rangle}{\hat{t}_{b2}} \varepsilon_{g\nu} \varepsilon_{W\rho} T_{2b}^d T_{1i}^g T_{ia}^d \\
& \cdot \left[\frac{\langle 1|\nu(\not{p}_1 + \not{p}_g)\mu(\not{p}_a - \not{p}_W)\rho P_L|a \rangle}{\hat{s}_{1g}\hat{t}_{aW}} \right. \\
& + \frac{\langle 1|\nu(\not{p}_1 + \not{p}_g)\rho P_L(\not{p}_1 + \not{p}_g + \not{p}_W)\mu|a \rangle}{\hat{s}_{1g}\hat{s}_{1gW}} \\
& + \left. \frac{\langle 1|\rho P_L(\not{p}_1 + \not{p}_W)\nu(\not{p}_1 + \not{p}_g + \not{p}_W)\mu|a \rangle}{\hat{s}_{1W}\hat{s}_{1gW}} \right] \qquad (4.1.10)
\end{aligned}
$$

$$
= (ig_s)^3 \left(\frac{ig_W}{\sqrt{2}} \right) \frac{\langle 2|\mu|b \rangle}{\hat{t}_{b2}} \varepsilon_{g\nu} \varepsilon_{W\rho} T_{2b}^d \left(iT_{1i}^g T_{ia}^d U_1^{\nu\mu\rho} \right) , \qquad (4.1.11)
$$

where P_L denotes the projection operator defined in eqs. (1.3.11) and (1.3.12), and

4.1. Unordered Emissions in HEJ

(a) A_1 (b) A_2 (c) A_3
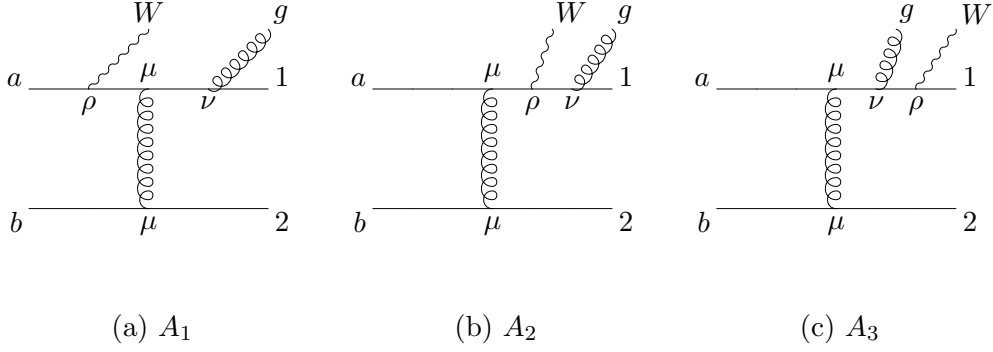
Figure 4.3: Feynman diagrams for the process $q(p_a)Q(p_b) \to q(p_1)g(p_g)W(p_W)Q(p_2)$ which contribute towards the $U_1^{\nu\mu\rho}$ tensor component of the W plus unordered current.

$\varepsilon_{W\rho}$ should be replaced by the lepton current from the decay of the W boson. We also use the notation $\hat{s}_{ijk} = (p_i + p_j + p_k)^2$ and $\hat{t}_{ijk} = (p_i - p_j - p_k)^2$.

The sum of diagrams in fig. 4.4, in which the gluon is emitted from the incoming parton, is given by:

$$
\begin{aligned}
B_1 + B_2 + B_3 =& i(ig_s)^3 \left(\frac{ig_W}{\sqrt{2}}\right) \frac{\langle 2|\mu|b\rangle}{\hat{t}_{b2}} \varepsilon_{g\nu}\varepsilon_{W\rho} T_{2b}^d T_{1i}^d T_{ia}^g \\
& \cdot \left[\frac{\langle 1|\mu(\slashed{p}_a - \slashed{p}_W - \slashed{p}_g)\nu(\slashed{p}_a - \slashed{p}_W)\rho P_L|a\rangle}{\hat{t}_{aWg}\hat{t}_{aW}} \right. \\
& + \frac{\langle 1|\mu(\slashed{p}_a - \slashed{p}_W - \slashed{p}_g)\rho P_L(\slashed{p}_a - \slashed{p}_g)\nu|a\rangle}{\hat{t}_{aWg}\hat{t}_{ag}} \\
& \left. + \frac{\langle 1|\rho P_L(\slashed{p}_1 + \slashed{p}_W)\mu(\slashed{p}_a - \slashed{p}_g)\nu|a\rangle}{\hat{s}_{1W}\hat{t}_{ag}} \right] \quad (4.1.12)
\end{aligned}
$$

$$
= (ig_s)^3 \left(\frac{ig_W}{\sqrt{2}}\right) \frac{\langle 2|\mu|b\rangle}{\hat{t}_{b2}} \varepsilon_{g\nu}\varepsilon_{W\rho} T_{2b}^d \left(iT_{1i}^d T_{ia}^g U_2^{\nu\mu\rho} \right) . \quad (4.1.13)
$$

In analogy with eqs. (4.1.6) and (4.1.7) we have defined:

$$
\begin{aligned}
U_1^{\nu\mu\rho} =& \frac{\langle 1|\nu(\slashed{p}_1 + \slashed{p}_g)\mu(\slashed{p}_a - \slashed{p}_W)\rho P_L|a\rangle}{\hat{s}_{1g}\hat{t}_{aW}} + \frac{\langle 1|\nu(\slashed{p}_1 + \slashed{p}_g)\rho P_L(\slashed{p}_1 + \slashed{p}_g + \slashed{p}_W)\mu|a\rangle}{\hat{s}_{1g}\hat{s}_{1gW}} \\
& + \frac{\langle 1|\rho P_L(\slashed{p}_1 + \slashed{p}_W)\nu(\slashed{p}_1 + \slashed{p}_g + \slashed{p}_W)\mu|a\rangle}{\hat{s}_{1W}\hat{s}_{1gW}} \quad (4.1.14)
\end{aligned}
$$

$$
\begin{aligned}
U_2^{\nu\mu\rho} =& \frac{\langle 1|\mu(\slashed{p}_a - \slashed{p}_W - \slashed{p}_g)\nu(\slashed{p}_a - \slashed{p}_W)\rho P_L|a\rangle}{\hat{t}_{aWg}\hat{t}_{aW}} + \frac{\langle 1|\mu(\slashed{p}_a - \slashed{p}_W - \slashed{p}_g)\rho P_L(\slashed{p}_a - \slashed{p}_g)\nu|a\rangle}{\hat{t}_{aWg}\hat{t}_{ag}} \\
& + \frac{\langle 1|\rho P_L(\slashed{p}_1 + \slashed{p}_W)\mu(\slashed{p}_a - \slashed{p}_g)\nu|a\rangle}{\hat{s}_{1W}\hat{t}_{ag}} . \quad (4.1.15)
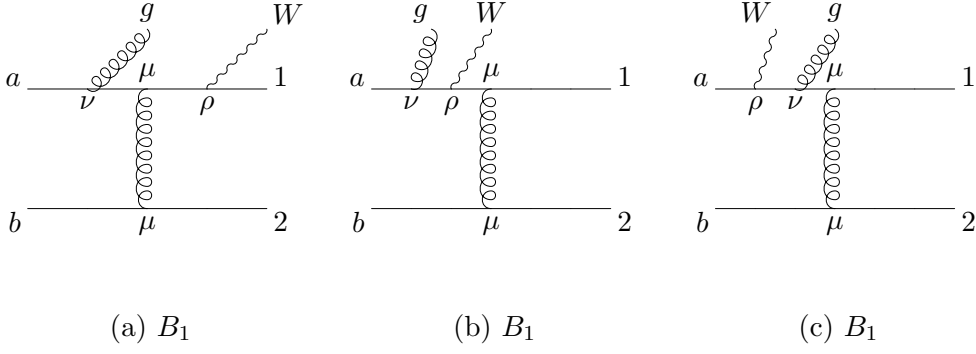\end{aligned}
$$

(a) B_1　　　　　　(b) B_1　　　　　　(c) B_1

Figure 4.4: Feynman diagrams for the process $q(p_a)Q(p_b) \to q(p_1)g(p_g)W(p_W)Q(p_2)$ which contribute towards the $U_2^{\nu\mu\rho}$ tensor component of the W plus unordered current.

These diagrams already have the structure we desire, therefore we make no approximation at this stage.

We now consider the diagrams shown in figs. 4.5a and 4.5b, in which the gluon is emitted off the t-channel gluon. The sum of the diagrams is given by:

$$
\begin{aligned}
C_1 + C_2 = & - i(ig_s)^2(g_s)\left(\frac{ig_W}{\sqrt{2}}\right)\left(f^{edg}T_{1a}^e T_{2b}^d\right)\frac{\langle 2|\mu|b\rangle}{\hat{t}_{b2}\hat{t}_{aW1}} \\
& \cdot \left[\frac{\langle 1|\sigma(\not{p}_a - \not{p}_W)\rho P_L|a\rangle}{\hat{t}_{aW}} + \frac{\langle 1|\rho P_L(\not{p}_1 + \not{p}_W)\sigma|a\rangle}{\hat{s}_{1W}}\right] \\
& \cdot \left(g^{\sigma\mu}(q_1 + q_2)^\nu + g^{\mu\nu}(-q_2 + p_g)^\sigma + g^{\nu\sigma}(-p_g - q_1)^\mu\right)\varepsilon_{g\nu}\varepsilon_{W\rho}\,, \quad (4.1.16)
\end{aligned}
$$

where q_1, q_2 are the t-channel momenta flowing into the 3-gluon vertex, given by:

$$
q_1 = p_a - p_1 - p_W\,,
$$
$$
q_2 = p_2 - p_b\,. \quad (4.1.17)
$$

Again, these diagrams are already factorised.

Finally we consider the remainder of the diagrams shown in fig. 4.5, in which the gluon and W are emitted from different partonic legs. We neglect terms of form
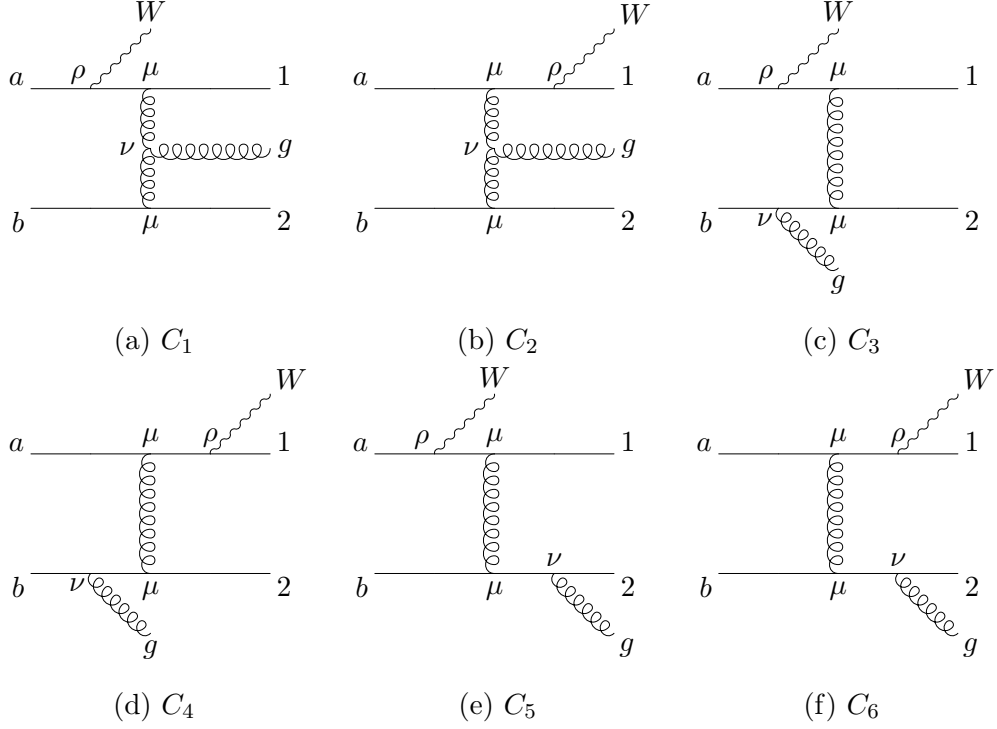
101

4.1. Unordered Emissions in HEJ

(a) C_1 (b) C_2 (c) C_3

(d) C_4 (e) C_5 (f) C_6

Figure 4.5: Feynman diagrams for the process $q(p_a)Q(p_b) \to q(p_1)g(p_g)W(p_W)Q(p_2)$ in which contribute towards the $L^{\nu\mu\rho}$ tensor component of the W plus unordered current.

$\langle 2|\mu \not{p}_g \nu|b\rangle$ which are suppressed in the MRK limit, and obtain:

$$C_3 = i(ig_s)^3 \left(\frac{ig_W}{\sqrt{2}}\right) T_{1a}^d T_{2i}^d T_{ib}^g \varepsilon_{g\,\nu} \varepsilon_{W\,\rho} \frac{\langle 1|\mu(\not{p}_a - \not{p}_W)\rho P_L|a\rangle\langle 2|\mu|b\rangle 2p_b^\nu}{\hat{t}_{aW}\hat{t}_{bg}\hat{t}_{b2g}} , \quad (4.1.18)$$

$$C_4 = i(ig_s)^3 \left(\frac{ig_W}{\sqrt{2}}\right) T_{1a}^d T_{2i}^d T_{ib}^g \varepsilon_{g\,\nu} \varepsilon_{W\,\rho} \frac{\langle 1|\rho P_L(\not{p}_1 + \not{p}_W)\mu|a\rangle\langle 2|\mu|b\rangle 2p_b^\nu}{\hat{s}_{1W}\hat{t}_{bg}\hat{t}_{b2g}} , \quad (4.1.19)$$

$$C_5 = i(ig_s)^3 \left(\frac{ig_W}{\sqrt{2}}\right) T_{1a}^d T_{2i}^g T_{ib}^d \varepsilon_{g\,\nu} \varepsilon_{W\,\rho} \frac{\langle 1|\mu(\not{p}_a - \not{p}_W)\rho P_L|a\rangle\langle 2|\mu|b\rangle 2p_2^\nu}{\hat{t}_{aW}\hat{s}_{2g}\hat{t}_{b2g}} , \quad (4.1.20)$$

$$C_6 = i(ig_s)^3 \left(\frac{ig_W}{\sqrt{2}}\right) T_{1a}^d T_{2i}^g T_{ib}^d \varepsilon_{g\,\nu} \varepsilon_{W\,\rho} \frac{\langle 1|\rho P_L(\not{p}_1 + \not{p}_W)\mu|a\rangle\langle 2|\mu|b\rangle 2p_2^\nu}{\hat{s}_{1W}\hat{s}_{2g}\hat{t}_{b2g}} . \quad (4.1.21)$$

We collect terms with the same colour factor to obtain:

$$\begin{aligned}
C_3 + C_4 + C_5 + C_6 =& i(ig_s)^3 \left(\frac{ig_W}{\sqrt{2}}\right) \varepsilon_{g\,\nu} \varepsilon_{W\,\rho} \frac{\langle 2|\mu|b\rangle}{\hat{t}_{b2g}} \left[T_{1a}^d T_{2i}^d T_{ib}^g \frac{2p_b^\nu}{\hat{t}_{bg}} + T_{1a}^d T_{2i}^g T_{ib}^d \frac{2p_2^\nu}{\hat{s}_{2g}} \right] \\
& \cdot \left[\frac{\langle 1|\mu(\not{p}_a - \not{p}_W)\rho P_L|a\rangle}{\hat{t}_{aW}} + \frac{\langle 1|\rho P_L(\not{p}_1 + \not{p}_W)\mu|a\rangle}{\hat{s}_{1W}} \right] .
\end{aligned}$$

$$(4.1.22)$$

Using $p_b \sim p_2 = p_-$, we can combine the colour factors (before reinstating their original symmetry):

$$
\begin{aligned}
C_3 + C_4 + C_5 + C_6 =& i(ig_s)^3 \left(\frac{ig_W}{\sqrt{2}}\right) \left(-if^{gde}T_{2b}^d T_{1a}^e\right) \varepsilon_{g\nu}\varepsilon_{W\rho} \\
& \cdot \frac{\langle 2|\mu|b\rangle}{\hat{t}_{b2g}} \frac{1}{2}\left(\frac{p_b^\nu}{p_b \cdot p_g} + \frac{p_2^\nu}{p_2 \cdot p_g}\right) \\
& \cdot \left[\frac{\langle 1|\mu(\not{p}_a - \not{p}_W)\rho P_L|a\rangle}{\hat{t}_{aW}} + \frac{\langle 1|\rho P_L(\not{p}_1 + \not{p}_W)\mu|a\rangle}{\hat{s}_{1W}}\right] .
\end{aligned}
\tag{4.1.23}
$$

The sum of diagrams in fig. 4.5 is therefore given by:

$$
\begin{aligned}
C =& (ig_s)^3 \left(\frac{ig_W}{\sqrt{2}}\right) \frac{\langle 2|\mu|b\rangle}{\hat{t}_{b2}} \varepsilon_{g\nu}\varepsilon_{W\rho}\left(T_{2b}^d f^{gde}T_{1a}^e\right) \\
& \left\{ \frac{\hat{t}_{b2}}{2\hat{t}_{b2g}}\left[\frac{\langle 1|\mu(\not{p}_a - \not{p}_W)\rho P_L|a\rangle}{\hat{t}_{aW}} + \frac{\langle 1|\rho P_L(\not{p}_1 + \not{p}_W)\mu|a\rangle}{\hat{s}_{1W}}\right] \cdot \left(\frac{p_b^\nu}{p_b \cdot p_g} + \frac{p_2^\nu}{p_2 \cdot p_g}\right) \right. \\
& + \frac{1}{\hat{t}_{aW1}}\left[\frac{\langle 1|\sigma(\not{p}_a - \not{p}_W)\rho P_L|a\rangle}{\hat{t}_{aW}} + \frac{\langle 1|\rho P_L(\not{p}_1 + \not{p}_W)\sigma|a\rangle}{\hat{s}_{1W}}\right] \\
& \left. \cdot \left(g^{\sigma\mu}(q_1 + q_2)^\nu + g^{\mu\nu}(-q_2 + p_g)^\sigma + g^{\nu\sigma}(-p_g - q_1)^\mu\right) \right\}
\end{aligned}
\tag{4.1.24}
$$

$$
= (ig_s)^3 \left(\frac{ig_W}{\sqrt{2}}\right) \frac{\langle 2|\mu|b\rangle}{\hat{t}_{b2}} \varepsilon_{g\nu}\varepsilon_{W\rho} T_{2b}^d \left(f^{gde}T_{1a}^e L^{\nu\mu\rho}\right) ,
\tag{4.1.25}
$$

where in analogy with eq. (4.1.8) we define:

$$
\begin{aligned}
L^{\nu\mu\rho} =& \frac{\hat{t}_{b2}}{2\hat{t}_{b2g}}\left[\frac{\langle 1|\mu(\not{p}_a - \not{p}_W)\rho P_L|a\rangle}{\hat{t}_{aW}} + \frac{\langle 1|\rho P_L(\not{p}_1 + \not{p}_W)\mu|a\rangle}{\hat{s}_{1W}}\right] \cdot \left(\frac{p_b^\nu}{p_b \cdot p_g} + \frac{p_2^\nu}{p_2 \cdot p_g}\right) \\
& + \frac{1}{\hat{t}_{aW1}}\left[\frac{\langle 1|\sigma(\not{p}_a - \not{p}_W)\rho P_L|a\rangle}{\hat{t}_{aW}} + \frac{\langle 1|\rho P_L(\not{p}_1 + \not{p}_W)\sigma|a\rangle}{\hat{s}_{1W}}\right] \\
& \cdot \left(g^{\sigma\mu}(q_1 + q_2)^\nu + g^{\mu\nu}(-q_2 + p_g)^\sigma + g^{\nu\sigma}(-p_g - q_1)^\mu\right) .
\end{aligned}
\tag{4.1.26}
$$

The full amplitude is given by sum of all diagrams $A + B + C$:

$$
\begin{aligned}
\mathcal{A}_{\mathrm{W,uno}} =& (ig_s)^3 \left(\frac{ig_W}{\sqrt{2}}\right) \frac{\langle 2|\mu|b\rangle}{\hat{t}_{b2}} \\
& \cdot \varepsilon_{g\nu}\varepsilon_{W\rho} T_{2b}^d \left(iT_{1i}^c T_{ia}^d U_1^{\nu\mu\rho} + iT_{1i}^d T_{ia}^c U_2^{\nu\mu\rho} + f^{cde}T_{1a}^e L^{\nu\mu\rho}\right) .
\end{aligned}
\tag{4.1.27}
$$

This is precisely the factorized form we are looking to obtain. From this we can extract the current for a W boson plus one unordered emission:

$$
j_{\mathrm{W,uno}}^{\mu,c} = \varepsilon_{g\nu}\varepsilon_{W\rho} T_{2b}^d \left(iT_{1i}^c T_{ia}^d U_1^{\nu\mu\rho} + iT_{1i}^d T_{ia}^c U_2^{\nu\mu\rho} + f^{cde}T_{1a}^e L^{\nu\mu\rho}\right) .
\tag{4.1.28}
$$

This expression has a very similar structure to eq. (4.1.5). This should not be surprising since the diagrams used in the derivation are only changed by the insertion of a W boson which does not affect the colour flow along the fermion lines.

4.1.2 Proof of Gauge Invariance

To test whether the matrix element obtained in the previous section is gauge invariant, it is necessary to show that the replacement of ε_{g_ν} by $p_{g\nu}$ in eq. (4.1.27) yields identically zero. Noting that

$$f^{cde}T^e_{1a} = -i(T^c_{1i}T^d_{ia} - iT^d_{1i}T^c_{ia}) \,, \tag{4.1.29}$$

it is sufficient to show

$$p_{g\nu}L^{\nu\mu\rho} = p_{g\nu}U^{\nu\mu\rho}_1 = -p_{g\nu}U^{\nu\mu\rho}_2 \tag{4.1.30}$$

to demonstrate gauge invariance. We start by considering $U^{\nu\mu\rho}_1$ and $U^{\nu\mu\rho}_2$ from eqs. (4.1.14) and (4.1.15). We will need to use the following properties of massless spinors [29]:

$$\slashed{p}|p\rangle = 0 \,, \qquad \langle p|\slashed{p} = 0 \,, \tag{4.1.31}$$

$$\langle p|\mu|p\rangle = 2p^\mu \,, \tag{4.1.32}$$

$$\langle p|\slashed{k}|p\rangle = 2p \cdot k \,, \tag{4.1.33}$$

$$\slashed{p} = |p^-\rangle\langle p^-| + |p^+\rangle\langle p^+| \,. \tag{4.1.34}$$

From the anti-commutation relations of the gamma matrices, $\{\gamma^\mu, \gamma^\nu\} = 2g^{\mu\nu}$ we also have that:

$$\slashed{p}\slashed{k} = -\slashed{k}\slashed{p} + 2p \cdot k \tag{4.1.35}$$

$$\slashed{p}\slashed{p} = p^2 \,. \tag{4.1.36}$$

We also note that:

$$\langle p|\gamma^{\mu_1}\gamma^{\mu_2}\gamma^{\mu_3}\gamma^{\mu_4}\gamma^{\mu_5}P_L|k\rangle = \langle p|\gamma^{\mu_1}\gamma^{\mu_2}\gamma^{\mu_3}P_L\gamma^{\mu_4}\gamma^{\mu_5}|k\rangle = \langle p|\gamma^{\mu_1}P_L\gamma^{\mu_2}\gamma^{\mu_3}\gamma^{\mu_4}\gamma^{\mu_5}|k\rangle$$

$$= \langle p^-|\gamma^{\mu_1}\gamma^{\mu_2}\gamma^{\mu_3}\gamma^{\mu_4}\gamma^{\mu_5}|k^-\rangle \,. \tag{4.1.37}$$

From hereon we drop P_L, but with the helicity of the spinors understood to be fixed. Contracting eq. (4.1.14) with p_g, and using eq. (4.1.36) with $p_g^2 = 0$, we obtain:

$$
p_{g\nu} U_1^{\nu\mu\rho} = \frac{1}{\hat{s}_{1g}\hat{t}_{aW}} \langle 1|\slashed{p}_g \slashed{p}_1 \mu (\slashed{p}_a - \slashed{p}_W)\rho|a\rangle + \frac{1}{\hat{s}_{1g}\hat{s}_{1gW}} \langle 1|\slashed{p}_g \slashed{p}_1 \rho (\slashed{p}_1 + \slashed{p}_g + \slashed{p}_W)\mu|a\rangle
$$
$$
+ \frac{1}{\hat{s}_{1W}\hat{s}_{1gW}} \langle 1|\rho(\slashed{p}_1 + \slashed{p}_W)\slashed{p}_g(\slashed{p}_1 + \slashed{p}_W)\mu|a\rangle \ . \tag{4.1.38}
$$

We then apply eqs. (4.1.33) and (4.1.34) to $\slashed{p}_1$ in the first two terms, whilst in the third term we use eq. (4.1.35) to evaluate $\slashed{p}_g(\slashed{p}_1 + \slashed{p}_W)$ and obtain:

$$
p_{g\nu} U_1^{\nu\mu\rho} = \frac{1}{\hat{t}_{aW}} \langle 1|\mu(\slashed{p}_a - \slashed{p}_W)\rho|a\rangle + \frac{1}{\hat{s}_{1gW}} \langle 1|\rho(\slashed{p}_1 + \slashed{p}_g + \slashed{p}_W)\mu|a\rangle
$$
$$
+ \frac{1}{\hat{s}_{1W}\hat{s}_{1gW}} \Big[2p_g \cdot (p_1 + p_W)\langle 1|\rho(\slashed{p}_1 + \slashed{p}_W)\mu|a\rangle
$$
$$
- (p_1 + p_W)^2 \langle 1|\rho(\slashed{p}_g)\mu|a\rangle \Big] \ . \tag{4.1.39}
$$

We again apply eq. (4.1.34) followed by eq. (4.1.32) to $\slashed{p}_a$ and $\slashed{p}_1$ in the first and second terms respectively, and rewrite the third by noting $\hat{s}_{1gW} = 2p_g \cdot (p_1 + p_W) + \hat{s}_{1W}$, so adding and subtracting $\langle 1|\rho(\slashed{p}_1 + \slashed{p}_W)\mu|a\rangle/\hat{s}_{1gW}$ we obtain:

$$
p_{g\nu} U_1^{\nu\mu\rho} = \frac{1}{\hat{t}_{aW}} \Big[2p_a^\rho\langle 1|\mu|a\rangle - \langle 1|\mu\slashed{p}_W\rho|a\rangle \Big]
$$
$$
+ \frac{1}{\hat{s}_{1gW}} \Big[2p_1^\rho\langle 1|\mu|a\rangle + \langle 1|\rho(\slashed{p}_g + \slashed{p}_W)\mu|a\rangle \Big]
$$
$$
+ \frac{1}{\hat{s}_{1W}} \langle 1|\rho(\slashed{p}_1 + \slashed{p}_W)\mu|a\rangle - \frac{1}{\hat{s}_{1gW}} \Big[2p_1^\rho\langle 1|\mu|a\rangle + \langle 1|\rho(\slashed{p}_g + \slashed{p}_W)\mu|a\rangle \Big]
$$
$$
= \frac{1}{\hat{t}_{aW}} \Big[2p_a^\rho\langle 1|\mu|a\rangle - \langle 1|\mu\slashed{p}_W\rho|a\rangle \Big]
$$
$$
+ \frac{1}{\hat{s}_{1W}} \Big[2p_1^\rho\langle 1|\mu|a\rangle + \langle 1|\rho\slashed{p}_W\mu|a\rangle \Big] \ . \tag{4.1.40}
$$

Finally for convenience we introduce the shorthand notation $j_{1a}^\mu = \langle 1|\mu|a\rangle$ and $J_{1Wa}^{\mu\rho} = \langle 1|\mu\slashed{p}_W\rho|a\rangle$, so the final result is:

$$
p_{g\nu} U_1^{\nu\mu\rho} = \frac{1}{\hat{t}_{aW}} [2p_a^\rho j_{1a}^\mu - J_{1Wa}^{\mu\rho}] + \frac{1}{\hat{s}_{1W}} [2p_1^\rho j_{1a}^\mu + J_{1Wa}^{\rho\mu}] \ . \tag{4.1.41}
$$

We now wish to calculate $p_{g\nu} U_2^{\nu\mu\rho}$, and contract p_g with eq. (4.1.15). Applying

eq. (4.1.36) we immediately obtain:

$$
\begin{aligned}
p_{g\nu}U_2^{\nu\mu\rho} =& \frac{1}{\hat{t}_{aWg}\hat{t}_{aW}}\langle 1|\mu(\slashed{p}_a - \slashed{p}_W)\slashed{p}_g(\slashed{p}_a - \slashed{p}_W)\rho|a\rangle \\
&+ \frac{1}{\hat{t}_{aWg}\hat{t}_{ag}}\langle 1|\mu(\slashed{p}_a - \slashed{p}_W - \slashed{p}_g)\rho\slashed{p}_a\slashed{p}_g|a\rangle \\
&+ \frac{1}{\hat{s}_{1W}\hat{t}_{ag}}\langle 1|\rho(\slashed{p}_1 + \slashed{p}_W)\mu\slashed{p}_a\slashed{p}_g|a\rangle \; .
\end{aligned}
\tag{4.1.42}
$$

We apply eq. (4.1.35) to $\slashed{p}_g(\slashed{p}_a - \slashed{p}_W)$ in the first term and $\slashed{p}_a\slashed{p}_g$ in the last two, then utilising eqs. (4.1.31) and (4.1.36) obtain:

$$
\begin{aligned}
p_{g\nu}U_2^{\nu\mu\rho} =& \frac{1}{\hat{t}_{aWg}\hat{t}_{aW}}\left[2p_g \cdot (p_a - p_W)\langle 1|\mu(\slashed{p}_a - \slashed{p}_W)\rho|a\rangle - (p_a - p_W)^2\langle 1|\mu\slashed{p}_g\rho|a\rangle\right] \\
&+ \frac{1}{\hat{t}_{aWg}\hat{t}_{ag}}\left[2p_a \cdot p_g\langle 1|\mu(\slashed{p}_a - \slashed{p}_W - \slashed{p}_g)\rho|a\rangle\right] \\
&+ \frac{1}{\hat{s}_{1W}\hat{t}_{ag}}\left[2p_a \cdot p_g\langle 1|\rho(\slashed{p}_1 + \slashed{p}_W)\mu|a\rangle\right] \; .
\end{aligned}
\tag{4.1.43}
$$

Again using eqs. (4.1.32) and (4.1.34) to evaluate $\slashed{p}_a$ and $\slashed{p}_1$ in all three terms we get:

$$
\begin{aligned}
p_{g\nu}U_2^{\nu\mu\rho} =& \frac{1}{\hat{t}_{aWg}\hat{t}_{aW}}\left[2p_g \cdot (p_a - p_W)(2p_a^\rho\langle 1|\mu|a\rangle - \langle 1|\mu\slashed{p}_W\rho|a\rangle)\right] - \frac{1}{\hat{t}_{aWg}}\langle 1|\mu\slashed{p}_g\rho|a\rangle \\
&- \frac{1}{\hat{t}_{aWg}}\left[2p_a^\rho\langle 1|\mu|a\rangle - \langle 1|\mu(\slashed{p}_W + \slashed{p}_g)\rho|a\rangle\right] \\
&- \frac{1}{\hat{s}_{1W}}\left[2p_1^\rho\langle 1|\mu|a\rangle + \langle 1|\rho\slashed{p}_W\mu|a\rangle\right] \; .
\end{aligned}
\tag{4.1.44}
$$

Noting that $\hat{t}_{aWg} = \hat{t}_{aW} - 2p_g \cdot (p_a - p_W)$ we now add and subtract the term $-(2p_a^\rho\langle 1|\mu|a\rangle - \langle 1|\mu\slashed{p}_W\rho|a\rangle)/\hat{t}_{aWg}$ to the first term and obtain:

$$
\begin{aligned}
p_{g\nu}U_2^{\nu\mu\rho} =& -\frac{1}{\hat{t}_{aW}}\left[2p_a^\rho\langle 1|\mu|a\rangle - \langle 1|\mu\slashed{p}_W\rho|a\rangle\right] \\
&+ \frac{1}{\hat{t}_{aWg}}\left[2p_a^\rho\langle 1|\mu|a\rangle - \langle 1|\mu\slashed{p}_W\rho|a\rangle - \langle 1|\mu\slashed{p}_g\rho|a\rangle\right] \\
&- \frac{1}{\hat{t}_{aWg}}\left[2p_a^\rho\langle 1|\mu|a\rangle - \langle 1|\mu(\slashed{p}_W + \slashed{p}_g)\rho|a\rangle\right] \\
&- \frac{1}{\hat{s}_{1W}}\left[2p_1^\rho\langle 1|\mu|a\rangle + \langle 1|\rho\slashed{p}_W\mu|a\rangle\right] \; .
\end{aligned}
\tag{4.1.45}
$$

So finally we have

$$
\begin{aligned}
p_{g\nu}U_2^{\nu\mu\rho} =& -\left\{\frac{1}{\hat{t}_{aW}}[2p_a^\rho j_{1a}^\mu - J_{1Wa}^{\mu\rho}] + \frac{1}{\hat{s}_{1W}}[2p_1^\rho j_{1a}^\mu + J_{1Wa}^{\rho\mu}]\right\} \\
=& -p_{g\nu}U_1^{\nu\mu\rho}
\end{aligned}
\tag{4.1.46}
$$

as required.

Having satisfied the first requirement that $p_{g\nu}U_2^{\nu\mu\rho} = -p_{g\nu}U_1^{\nu\mu\rho}$ we now need to show that $p_{g\nu}L^{\nu\mu\rho} = p_{g\nu}U_1^{\nu\mu\rho}$. The first step is to note $\hat{t}_{b2g} = \hat{t}_{b2} - 2p_g \cdot (p_b - p_2)$, so we rewrite eq. (4.1.26) as:

$$
\begin{aligned}
L^{\nu\mu\rho} =& \frac{1}{2}\left[\frac{\langle 1|\mu(\not{p}_a - \not{p}_W)\rho|a\rangle}{\hat{t}_{aW}} + \frac{\langle 1|\rho(\not{p}_1 + \not{p}_W)\mu|a\rangle}{\hat{s}_{1W}}\right] \cdot \left(\frac{p_b^\nu}{p_b \cdot p_g} + \frac{p_2^\nu}{p_2 \cdot p_g}\right) \\
&+ \frac{2p_g \cdot (p_b - p_2)}{2\hat{t}_{b2g}}\left[\frac{\langle 1|\mu(\not{p}_a - \not{p}_W)\rho|a\rangle}{\hat{t}_{aW}} + \frac{\langle 1|\rho(\not{p}_1 + \not{p}_W)\mu|a\rangle}{\hat{s}_{1W}}\right] \\
&\cdot \left(\frac{p_b^\nu}{p_b \cdot p_g} + \frac{p_2^\nu}{p_2 \cdot p_g}\right) \\
&+ \frac{1}{\hat{t}_{aW1}}\left[\frac{\langle 1|\sigma(\not{p}_a - \not{p}_W)\rho|a\rangle}{\hat{t}_{aW}} + \frac{\langle 1|\rho(\not{p}_1 + \not{p}_W)\sigma|a\rangle}{\hat{s}_{1W}}\right] \\
&\cdot (g^{\sigma\mu}(q_1 + q_2)^\nu + g^{\mu\nu}(-q_2 + p_g)^\sigma + g^{\nu\sigma}(-p_g - q_1)^\mu) \ . \quad (4.1.47)
\end{aligned}
$$

We now define:

$$
\begin{aligned}
L_a^{\nu\mu\rho} =& \frac{1}{2}\left[\frac{\langle 1|\mu(\not{p}_a - \not{p}_W)\rho|a\rangle}{\hat{t}_{aW}} + \frac{\langle 1|\rho(\not{p}_1 + \not{p}_W)\mu|a\rangle}{\hat{s}_{1W}}\right] \\
&\cdot \left(\frac{p_b^\nu}{p_b \cdot p_g} + \frac{p_2^\nu}{p_2 \cdot p_g}\right) \ , \quad (4.1.48) \\
L_b^{\nu\mu\rho} =& \frac{2p_g \cdot (p_b - p_2)}{2\hat{t}_{b2g}}\left[\frac{\langle 1|\mu(\not{p}_a - \not{p}_W)\rho|a\rangle}{\hat{t}_{aW}} + \frac{\langle 1|\rho(\not{p}_1 + \not{p}_W)\mu|a\rangle}{\hat{s}_{1W}}\right] \\
&\cdot \left(\frac{p_b^\nu}{p_b \cdot p_g} + \frac{p_2^\nu}{p_2 \cdot p_g}\right) \ , \quad (4.1.49) \\
L_c^{\nu\mu\rho} =& \frac{1}{\hat{t}_{aW1}}\left[\frac{\langle 1|\sigma(\not{p}_a - \not{p}_W)\rho|a\rangle}{\hat{t}_{aW}} + \frac{\langle 1|\rho(\not{p}_1 + \not{p}_W)\sigma|a\rangle}{\hat{s}_{1W}}\right] \\
&\cdot (g^{\mu\nu}(-q_2 + p_g)^\sigma + g^{\nu\sigma}(-p_g - q_1)^\mu) \ , \quad (4.1.50) \\
L_d^{\nu\mu\rho} =& \frac{1}{\hat{t}_{aW1}}\left[\frac{\langle 1|\mu(\not{p}_a - \not{p}_W)\rho|a\rangle}{\hat{t}_{aW}} + \frac{\langle 1|\rho(\not{p}_1 + \not{p}_W)\mu|a\rangle}{\hat{s}_{1W}}\right] \cdot (q_1 + q_2)^\nu \ , \quad (4.1.51)
\end{aligned}
$$

such that $L_a^{\nu\mu\rho} + L_b^{\nu\mu\rho} + L_c^{\nu\mu\rho} + L_d^{\nu\mu\rho} = L^{\nu\mu\rho}$. Contracting $L_a^{\nu\mu\rho}$ in eq. (4.1.48) with $p_{g\nu}$, and using eqs. (4.1.32) and (4.1.34), it is clear that:

$$
\begin{aligned}
p_{g\nu}L_a^{\nu\mu\rho} &= \frac{1}{\hat{t}_{aW}}\left[2p_a^\rho j_{1a}^\mu - J_{1Wa}^{\mu\rho}\right] + \frac{1}{\hat{s}_{1W}}\left[2p_1^\rho j_{1a}^\mu + J_{1Wa}^{\rho\mu}\right] \\
&= p_{g\nu}U_1^{\nu\mu\rho} \ . \quad (4.1.52)
\end{aligned}
$$

Therefore, in order to satisfy the condition $p_{g\nu}L^{\nu\mu\rho} = p_{g\nu}U_1^{\nu\mu\rho}$ what remains to be proved is:

$$
p_{g\nu}L_b^{\nu\mu\rho} + p_{g\nu}L_c^{\nu\mu\rho} + p_{g\nu}L_d^{\nu\mu\rho} = 0 \ . \quad (4.1.53)
$$

Contracting eq. (4.1.49) with $p_{g\nu}$ it is easy to see that:

$$p_{g\nu}L_b^{\nu\mu\rho} = \frac{2p_g \cdot (p_b - p_2)}{\hat{t}_{b2g}} \left\{ \frac{1}{\hat{t}_{aW}} [2p_a^\rho j_{1a}^\mu - J_{1Wa}^{\mu\rho}] + \frac{1}{\hat{s}_{1W}} [2p_1^\rho j_{1a}^\mu + J_{1Wa}^{\rho\mu}] \right\} .$$

(4.1.54)

We now note that by conservation of momentum $p_a - p_W - p_1 = -(p_b - p_2 - p_g)$ and so $\hat{t}_{aW1} = \hat{t}_{b2g}$. Furthermore, as $q_1 = p_a - p_W - p_1$ and $q_2 = p_2 - p_b$, then we have that $q_1 = q_2 + p_g$. Therefore when we contract $(q_1 + q_2)^\nu$ in eq. (4.1.51) by $p_{g\nu}$ we get a factor of $2q_2 \cdot p_g = -2 \cdot p_g(p_b - p_2)$, hence:

$$p_{g\nu}L_d^{\nu\mu\rho} = -\frac{2p_g \cdot (p_b - p_2)}{\hat{t}_{b2g}} \left\{ \frac{1}{\hat{t}_{aW}} [2p_a^\rho j_{1a}^\mu - J_{1Wa}^{\mu\rho}] + \frac{1}{\hat{s}_{1W}} [2p_1^\rho j_{1a}^\mu + J_{1Wa}^{\rho\mu}] \right\}$$

(4.1.55)

$$= -p_{g\nu}L_b^{\nu\mu\rho} .$$

(4.1.56)

Therefore the only thing remaining to be proved is that $p_{g\nu}L_c^{\nu\mu\rho} = 0$. Contracting eq. (4.1.50) with $p_{g\nu}$ we obtain:

$$p_{g\nu}L_c^{\nu\mu\rho} = \frac{1}{\hat{t}_{aW1}} \left[\frac{\langle 1|\sigma(\slashed{p}_a - \slashed{p}_W)\rho|a\rangle}{\hat{t}_{aW}} + \frac{\langle 1|\rho(\slashed{p}_1 + \slashed{p}_W)\sigma|a\rangle}{\hat{s}_{1W}} \right]$$
$$\cdot \left(p_g^\mu(-q_2 + p_g)^\sigma + p_g^\sigma(-p_g - q_1)^\mu \right) .$$

(4.1.57)

The term in round brackets reduces as follows:

$$p_g^\mu(-q_2 + p_g)^\sigma + p_g^\sigma(-p_g - q_1)^\mu = p_g^\mu p_g^\sigma - p_g^\mu p_g^\sigma - p_g^\mu q_2^\sigma - q_1^\mu p_g^\sigma$$
$$= -p_g^\mu q_2^\sigma - (q_2 + p_g)^\mu p_g^\sigma$$
$$= -p_g^\mu(q_2 + p_g)^\sigma - q_2^\mu p_g^\sigma$$
$$= -p_g^\mu q_1^\sigma - q_2^\mu p_g^\sigma .$$

(4.1.58)

At this point, it is necessary to recall that in the full expression for the matrix element in eq. (4.1.27) the μ index is contracted with the current $\langle 2|\mu|b\rangle$. Therefore we can drop the second term in the final line of eq. (4.1.58) because $\langle 2|\slashed{q}_2|b\rangle = \langle 2|\slashed{p}_2 - \slashed{p}_b|b\rangle = 0$ by eq. (4.1.31). Hence we have:

$$p_{g\nu}L_c^{\nu\mu\rho} = \frac{-p_g^\mu}{\hat{t}_{aW1}} \left[-\frac{\langle 1|(\slashed{p}_a - \slashed{p}_W)(\slashed{p}_a - \slashed{p}_W)\rho|a\rangle}{\hat{t}_{aW}} \right.$$
$$\left. + \frac{\langle 1|\rho(\slashed{p}_1 + \slashed{p}_W)(-\slashed{p}_1 - \slashed{p}_W)|a\rangle}{\hat{s}_{1W}} \right] ,$$

(4.1.59)

where we have written $q_1 = p_a - p_W - p_1$ and again used eq. (4.1.31). Finally using eq. (4.1.36), with $\hat{t}_{aW} = -(p_a - p_W)^2$ and $\hat{s}_{1W} = (p_1 + p_W)^2$ we obtain:

$$p_{g\nu} L_c^{\nu\mu\rho} = \frac{-p_g^\mu}{\hat{t}_{aW1}} \left[\langle 1|\rho|a\rangle - \langle 1|\rho|a\rangle \right]$$

$$= 0 \tag{4.1.60}$$

as required. We have thus proved that

$$p_{g\nu} L^{\nu\mu\rho} = p_{g\nu} U_1^{\nu\mu\rho} = -p_{g\nu} U_2^{\nu\mu\rho} \tag{4.1.61}$$

and therefore that the amplitude in eq. (4.1.27) is gauge invariant.

4.1.3 Changing Initial Flavour Configurations

Everything computed thus far has been for the case of two non-identical quarks. We must consider what happens if we replace one quark with an antiquark[1], or the quark which does not emit the W with a gluon. We recall that $P_L \nu(p) = \nu_+(p) = |p^-\rangle$, and:

$$\langle i^-|\mu|j^-\rangle = \langle j^+|\mu|i^+\rangle \,, \tag{4.1.62}$$

$$\langle i^-|\mu\slashed{p}\nu|j^-\rangle = \langle j^+|\nu\slashed{p}\mu|i^+\rangle \,, \tag{4.1.63}$$

$$\langle i^-|\mu\slashed{p}\nu\slashed{k}\rho|j^-\rangle = \langle j^+|\rho\slashed{k}\nu\slashed{p}\mu|i^+\rangle \,. \tag{4.1.64}$$

Therefore if we replace the quarks $b, 2$ with antiquarks we need simply make the replacement:

$$\langle 2^\pm|\mu|b^\pm\rangle \to \langle 2^\mp|\mu|b^\mp\rangle \,. \tag{4.1.65}$$

However, since we perform a sum over helicities, this replacement makes no difference to the total summed/averaged matrix element squared. If however, we replace the quark which emits the W with an antiquark, we find this is equivalent to making the replacements such as:

$$\langle 1^-|\mu\slashed{p}\nu\slashed{k}\rho|a^-\rangle = \langle 1|\mu\slashed{p}\nu\slashed{k}\rho P_L|a\rangle \to \langle a|\rho P_L\slashed{k}\nu\slashed{p}\mu|1\rangle = \langle 1^+|\mu\slashed{p}\nu\slashed{k}\rho|a^+\rangle \,. \tag{4.1.66}$$

---

[1]Also, recall from section 2.3 that interference between quark legs is negligible in the high energy limit.

In other words, we must change the helicity in these currents from $-$ to $+$. This has an impact in the evaluation, but the arguments for gauge invariance of the current presented in the previous section still hold as they were not dependent on the helicity of the spinors.

If alternatively we replace the second quark with a gluon, we need simply make the replacement given in eq. (2.4.58) at the level of the summed/averaged matrix element squared.

4.1.4   Obtaining the Amplitude Squared

With a view to ultimately constructing the cross section the quantity we need is the colour/ helicity/ polarisation summed and averaged amplitude squared. We introduce the convenient shorthand:

$$L = L^{\nu\mu\rho} j_{2b\mu} \varepsilon_{W\rho} \varepsilon_{g\nu} \quad U_1 = U_1^{\nu\mu\rho} j_{2b\mu} \varepsilon_{W\rho} \varepsilon_{g\nu} \quad U_2 = U_2^{\nu\mu\rho} j_{2b\mu} \varepsilon_{W\rho} \varepsilon_{g\nu} \quad (4.1.67)$$

with $j_{2b} = \langle 2|\mu|b \rangle$. Then using $f^{gde} T_{1a}^e = i(T_{1i}^g T_{ia}^d - T_{1i}^d T_{ia}^g)$ we have:

$$\mathcal{A}_{\text{W+uno}} = \frac{i(ig_s)^3 \left(\frac{ig_W}{\sqrt{2}} \right)^2}{\hat{t}_{b2}} \left(T_{2b}^d T_{1i}^g T_{ia}^d (U_1 - L) + T_{2b}^d T_{1i}^d T_{ia}^g (U_2 + L) \right) . \quad (4.1.68)$$

Noting $(T^a)^\dagger = T^a \Rightarrow (T^a)_{ij}{}^* = (T^a)_{ji}$

$$\sum_{\text{pol}} |\mathcal{A}_{\text{W+uno}}|^2 = \frac{|K|^2}{\hat{t}_{b2}^2} \Big\{ T_{2b}^d T_{1i}^g T_{ia}^d T_{b2}^{d'} T_{j1}^g T_{aj}^{d'} XX^* + T_{2b}^d T_{1i}^g T_{ia}^d T_{b2}^{d'} T_{j1}^{d'} T_{aj}^g XY^*$$

$$+ T_{2b}^d T_{1i}^d T_{ia}^g T_{b2}^{d'} T_{j1}^g T_{aj}^{d'} YX^* + T_{2b}^d T_{1i}^g T_{ia}^d T_{b2}^{d'} T_{j1}^{d'} T_{aj}^g YY^* \Big\} , \quad (4.1.69)$$

where $X = U_1 - L$ and $Y = U_2 + L$. We must now compute the colour sums:

$$\mathcal{C}_1 = \sum_{\{a,...,j\}=1}^{3} \sum_{\{d,d',g\}=1}^{8} (T_{2b}^d T_{ia}^d)(T_{1i}^g T_{j1}^g)(T_{b2}^{d'} T_{aj}^{d'}) ,$$

$$\mathcal{C}_2 = \sum_{\{a,...,j\}=1}^{3} \sum_{\{d,d',g\}=1}^{8} (T_{2b}^d T_{ia}^d)(T_{1i}^g T_{aj}^g)(T_{b2}^{d'} T_{j1}^{d'}) ,$$

$$\mathcal{C}_3 = \sum_{\{a,...,j\}=1}^{3} \sum_{\{d,d',g\}=1}^{8} (T_{2b}^d T_{1i}^d)(T_{ia}^g T_{j1}^g)(T_{b2}^{d'} T_{aj}^{d'}) ,$$

$$\mathcal{C}_4 = \sum_{\{a,...,j\}=1}^{3} \sum_{\{d,d',g\}=1}^{8} (T_{2b}^d T_{1i}^d)(T_{ia}^g T_{aj}^g)(T_{b2}^{d'} T_{j1}^{d'}) . \quad (4.1.70)$$

Using the Fierz identity,

$$T_{ij}^a T_{kl}^a = \frac{1}{2} \left(\delta_{il}\delta_{kj} - \frac{1}{N_C}\delta_{ij}\delta_{kl} \right) \tag{4.1.71}$$

we find $\mathcal{C}_1 = \mathcal{C}_4 = \frac{1}{2}C_A C_F^2$ and $\mathcal{C}_2 = \mathcal{C}_3 = -\frac{1}{4}C_F$, such that:

$$\overline{|\mathcal{A}_{\text{W+uno}}|^2} = \frac{1}{4C_A^2} \frac{(g_s^2)^3 \frac{g_W^4}{4}}{\hat{t}_{b2}^2} \sum_{\text{helicities}} \left\{ \frac{1}{2}C_A C_F^2 \left(XX^* + YY^* \right) - \frac{C_F}{4}\left(XY^* + YX^* \right) \right\}, \tag{4.1.72}$$

where the factor $\frac{1}{4C_A^2}$ comes from averaging over initial states.

To evaluate this expression we must now explicitly calculate the tensor contractions L, U_1 and U_2, using the definitions in eqs. (4.1.14), (4.1.15) and (4.1.26). Doing this by hand would be impractical; it is therefore done numerically. We note at this point that as the W boson decays, we must make the replacement

$$\varepsilon_{W\rho} \rightarrow -\frac{ig_{\rho\sigma}}{(p_\ell + p_{\bar{\ell}})^2 - m_W^2 + im_W\Gamma} \langle p_\ell^- |\sigma| p_{\bar{\ell}}^- \rangle \tag{4.1.73}$$

with $p_W = p_\ell + p_{\bar{\ell}}$. As the W propagator is common to all terms in eq. (4.1.74), we pull it outside the sum over helicities:

$$\overline{|\mathcal{A}_{\text{W+uno}}|^2} = \left(\frac{g_s^2}{\hat{t}_{a,1g\ell\bar{\ell}}} \right) \left(\frac{g_s^2}{\hat{t}_{b2}} \right) g_s^2 \frac{g_W^4}{4} \left| \frac{1}{(p_\ell + p_{\bar{\ell}})^2 - m_W^2 + im_W\Gamma} \right|^2$$
$$\cdot \sum_{\text{helicities}} \left\{ \frac{1}{8}\frac{C_F^2}{C_A}\left(XX^* + YY^* \right) - \frac{1}{16}\frac{C_F}{C_A^2}\left(XY^* + YX^* \right) \right\}. \tag{4.1.74}$$

We define

$$\|S_{qQ \rightarrow qg\ell\bar{\ell}Q}\|^2 = g_s^2 \frac{g_W^4}{4} \left| \frac{1}{(p_\ell + p_{\bar{\ell}})^2 - m_W^2 + im_W\Gamma} \right|^2 \sum_{\text{helicities}} |S_{qQ \rightarrow qg\ell\bar{\ell}Q}|^2 \tag{4.1.75}$$

where

$$|S_{qQ \rightarrow qg\ell\bar{\ell}Q}|^2 = \frac{1}{8}\frac{C_F^2}{C_A}\left(XX^* + YY^* \right) - \frac{1}{16}\frac{C_F}{C_A^2}\left(XY^* + YX^* \right) \tag{4.1.76}$$

such that

$$\overline{|\mathcal{A}_{\text{W+uno}}|^2} = \left(\frac{g_s^2}{\hat{t}_{a,1g\ell\bar{\ell}}} \right) \left(\frac{g_s^2}{\hat{t}_{b2}} \right) \|S_{qQ \rightarrow qg\ell\bar{\ell}Q}\|^2. \tag{4.1.77}$$

It is now straightforward to generalize this expression and obtain the amplitude squared for $2 \rightarrow n+1$:

$$\overline{|\mathcal{A}_{\text{W+uno}}|^2} = \left(\frac{g_s^2}{\hat{t}_{a,1g\ell\bar{\ell}}} \right) \left(\frac{g_s^2}{\hat{t}_{n-1}} \frac{K_{f_b}}{C_F} \right) \|S_{qf_b \rightarrow qg\ell\bar{\ell}f_n}\|^2$$
$$\cdot \prod_{i=1}^{n-2} \left\{ g_s^2 C_A \left(\frac{-1}{\hat{t}_i \hat{t}_{i+1}} V^\mu(q_i, q_{i+1}) V_\mu(q_i, q_{i+1}) \right) \right\} \tag{4.1.78}$$

where

$$K_g = \frac{1}{2}\left(C_A - \frac{1}{C_A}\right)\left(\frac{p_b^-}{p_2^-} + \frac{p_2^-}{p_b^-}\right) + \frac{1}{C_A} \tag{4.1.79}$$

$$K_q = C_F \ . \tag{4.1.80}$$

4.1.5 Validation of the Matrix Element

In order to validate the implementation of the amplitude squared from the previous section, in a manner similar to that of section 2.4 we evaluate $|\mathcal{M}|^2/(256\pi^2\hat{s}^2)$ in a slice of phase space. We compare between tree-level predictions (obtained using MadGraph 5 [148]), the standard HEJ matrix element, and the result from the previous section (which is denoted as 'HEJ uno' in the plots that follow). We choose the following phase space point parameterised in terms of a rapidity Δ:

$$
\begin{aligned}
k_1 &= (k_T\cosh(\Delta), k_T\cos(\phi_1), k_T\sin(\phi_1), k_T\sinh(\Delta)) \ , \\
k_2 &= (k_T, k_T, 0, 0) \ , \\
k_{\bar{\ell}} &= p_e = (k_{eT}\cosh(y_e), k_{eT}\cos(\phi_e), k_{eT}\sin(\phi_e), k_{eT}\sinh(y_e)) \ , \\
k_\ell &= p_{\nu_e} = (k_{\nu T}\cosh(y_\nu), k_{\nu T}\cos(\phi_\nu), k_{\nu T}\sin(\phi_\nu), k_{\nu T}\sinh(y_\nu)) \ , \\
k_3 &= (|\vec{k}_{3T}|\cosh(-\Delta), |\vec{k}_{3T}|\cos(\phi_3), |\vec{k}_{3T}|\sin(\phi_3), |\vec{k}_{3T}|\sinh(-\Delta)) \ , \\
p_a &= (x_a\sqrt{\hat{s}}/2, 0, 0, x_a\sqrt{\hat{s}}/2) \ , \\
p_b &= (x_b\sqrt{\hat{s}}/2, 0, 0, -x_b\sqrt{\hat{s}}/2) \ , \tag{4.1.81}
\end{aligned}
$$

where $k_T = k_{eT} = 40$ GeV, $k_{\nu T} = \frac{m_W^2}{2k_{eT}(\cosh(y_e - y_\nu) - \cos(\phi_e - \phi_\nu))}$, $y_e = y_\nu = \Delta$, $\phi_1 = 2\pi/3$, $\phi_e = \pi/2$, $\phi_\nu = -\pi/2$, and where $\vec{k}_{3T} = (|\vec{k}_{3T}|\cos(\phi_3), \vec{k}_{3T}\sin(\phi_3))$ is chosen to conserve transverse momentum. Longitudinal momentum conservation is ensured by:

$$
\begin{aligned}
x_a &= \sum_i \frac{k_{iT}}{\sqrt{\hat{s}}} e^{y_i} \ , \\
x_b &= \sum_i \frac{k_{iT}}{\sqrt{\hat{s}}} e^{-y_i} \ , \tag{4.1.82}
\end{aligned}
$$

in which the sum is over all outgoing particles. (The notation for the momentum of the outgoing partons k_i is deliberately chosen to be different from that of the

(a) $Q = q, X = q, q', q''$

(b) $Q = q, X = \bar{q}, \bar{q}', \bar{q}''$

(c) $Q = \bar{q}, X = q, q', q''$

(d) $Q = \bar{q}, X = \bar{q}, \bar{q}', \bar{q}''$

(e) $Q = q, X = g$
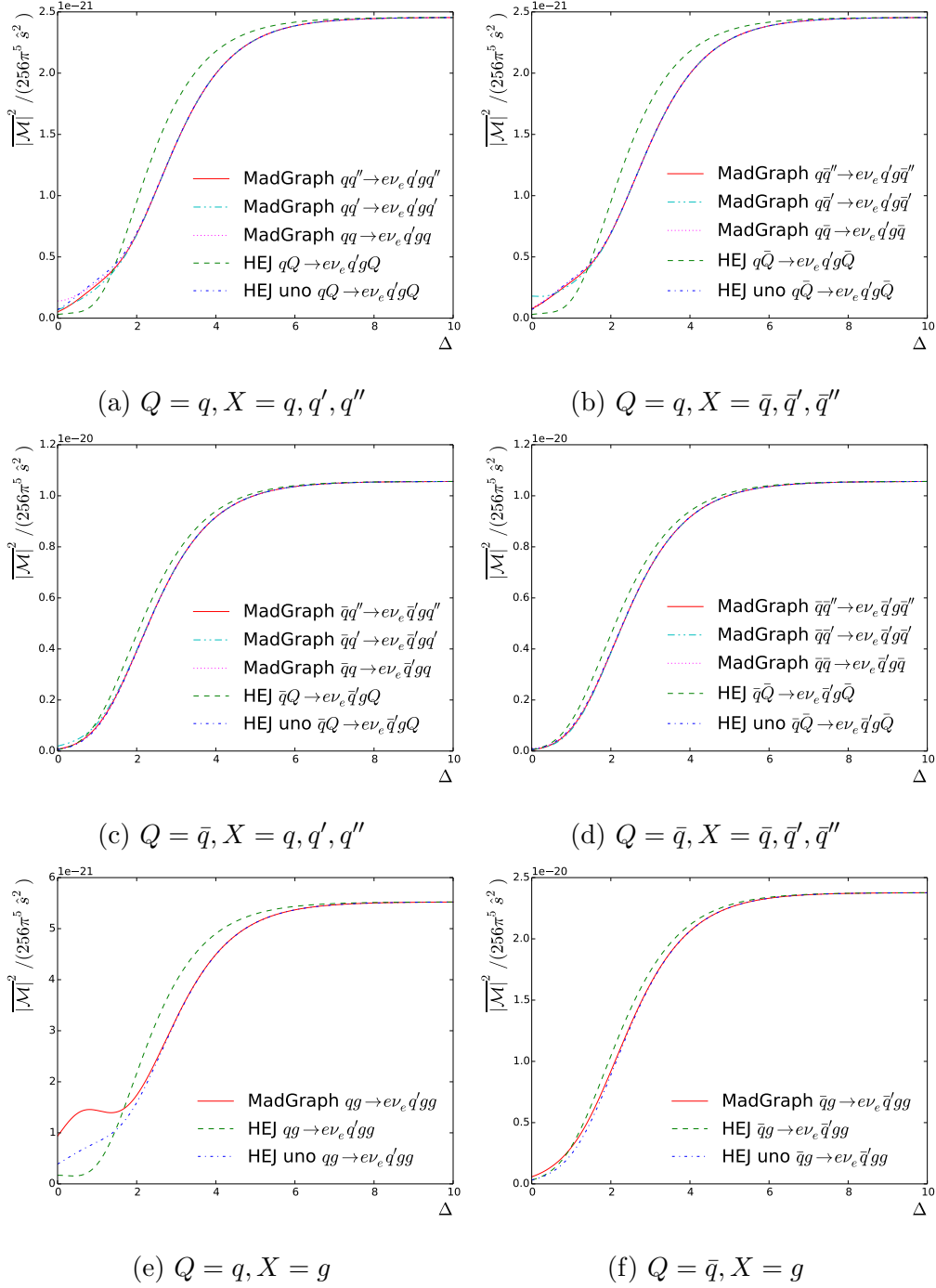
(f) $Q = \bar{q}, X = g$

Figure 4.6: A comparison of HEJ and tree-level matrix elements $|\mathcal{M}|^2/(256\pi^2\hat{s}^2)$ evaluated at the phase space point (4.1.81) for increasing Δ, for the process $QX \to e\nu Q'gX$, where $Q = q, \bar{q}$, $Q' = q', \bar{q}'$, and $X = q, q', q'', \bar{q}, \bar{q}', \bar{q}'', g$.

previous section to reinforce that here the suffix denotes the rapidity ordering, as opposed to the identity of parton in section 4.1.1.)

We initially consider the momentum assignment

$$Q(p_a)X(p_b) \rightarrow e(p_e)\nu(p_\nu)Q'(k_1)g(k_2)X(k_3) \,, \tag{4.1.83}$$

where here Q, Q' may denote a quark or an antiquark, and X may denote any partonic flavour. As the parameter Δ is increased in the range $0 \leq \Delta \leq 10$ such a configuration will increasingly satisfy Multi-Regge kinematics. Thus as Δ increases we anticipate that performance of the HEJ matrix element should improve, and qualitatively all three predictions should become independent of Δ. The is precisely what we see in fig. 4.6, where the results for six different initial state configurations are shown. Moreover, we observe that the new matrix element converges to the MadGraph result much more quickly than the previous HEJ formalism.

In the MRK limit there is a degeneracy of processes such as $uX \rightarrow e^+\nu_e dgX$ for $X = u, d, s, \bar{u}, \bar{d}, \bar{s}$; in HEJ these are all computed with the same matrix elements, whilst in MadGraph each case would need to be treated separately. For each unique HEJ configuration, we therefore test using multiple identities for X. The full list of processes tested and their respective momentum assignments is shown in table 4.1. The convergence between the unordered matrix element and MadGraph is good regardless of choice of the flavour of X.

We now change the momentum assignment to:

$$Q(p_a)X(p_b) \rightarrow e(p_e)\nu(p_\nu)g(k_1)Q'(k_2)X(k_3) \,. \tag{4.1.84}$$

Now when Δ is increased, this will correspond to a unordered configuration, which we expect to be suppressed by a factor of $\hat{s}_{1g}$ relative to a configuration that satisfies Multi-Regge kinematics. We can demonstate that the implementation of the amplitude exhibits this behaviour by now plotting $|\mathcal{M}|^2 \hat{s}_{1g}/(256\pi^2\hat{s}^2)$ as a function of Δ, for which the results are shown in fig. 4.7. Again the correct qualitative behaviour is observed, and the convergence of the predictions is excellent independent of the choice of flavour for X. A list of the processes tested is shown in table 4.1. The processes shown are for W^+ emission, however the matrix elements

for W^- emission can be obtained by assigning $p_\ell = p_e$ and $p_{\bar\ell} = p_\nu$, and were tested similarly.

The previous two tests were reproduced but with the rapidities reversed, namely $\Delta \to -\Delta$, in order to test the case in which the W-emitting quark is produced backwards. In particular, the matrix element for a backwards unordered emission was tested. As expected, these tests produced identical results. In addition, the assumption that the matrix element is suppressed when the W boson is produced in a different direction to the quark from which it is emitted was verified to be valid.

Figure	Process	MadGraph subprocesses
4.6a	$q(p_a)X(p_b) \to e(p_e)\nu(p_\nu)q(k_1)g(k_2)X(k_3)$	$X = q, X = q', X = q''$
4.6b	$q(p_a)\bar{X}(p_b) \to e(p_e)\nu(p_\nu)q(k_1)g(k_2)\bar{X}(k_3)$	$\bar{X} = \bar{q}, \bar{X} = \bar{q}', \bar{X} = \bar{q}''$
4.6c	$\bar{q}(p_a)X(p_b) \to e(p_e)\nu(p_\nu)\bar{q}(k_1)g(k_2)X(k_3)$	$X = q, X = q', X = q''$
4.6d	$\bar{q}(p_a)\bar{X}(p_b) \to e(p_e)\nu(p_\nu)\bar{q}(k_1)g(k_2)\bar{X}(k_3)$	$\bar{X} = \bar{q}, \bar{X} = \bar{q}', \bar{X} = \bar{q}''$
4.6e	$q(p_a)g(p_b) \to e(p_e)\nu(p_\nu)q(k_1)g(k_2)g(k_3)$	$X = g$
4.6f	$\bar{q}(p_a)g(p_b) \to e(p_e)\nu(p_\nu)\bar{q}(k_1)g(k_2)g(k_3)$	$X = g$
4.7a	$q(p_a)X(p_b) \to e(p_e)\nu(p_\nu)g(k_1)q(k_2)X(k_3)$	$X = q, X = q', X = q''$
4.7b	$q(p_a)\bar{X}(p_b) \to e(p_e)\nu(p_\nu)g(k_1)q(k_2)\bar{X}(k_3)$	$\bar{X} = \bar{q}, \bar{X} = \bar{q}', \bar{X} = \bar{q}''$
4.7c	$\bar{q}(p_a)X(p_b) \to e(p_e)\nu(p_\nu)g(k_1)\bar{q}(k_2)X(k_3)$	$X = q, X = q', X = q''$
4.7d	$\bar{q}(p_a)\bar{X}(p_b) \to e(p_e)\nu(p_\nu)g(k_1)\bar{q}(k_2)\bar{X}(k_3)$	$\bar{X} = \bar{q}, \bar{X} = \bar{q}', \bar{X} = \bar{q}''$
4.7e	$q(p_a)g(p_b) \to e(p_e)\nu(p_\nu)g(k_1)q(k_2)g(k_3)$	$X = g$
4.7f	$\bar{q}(p_a)g(p_b) \to e(p_e)\nu(p_\nu)g(k_1)\bar{q}(k_2)g(k_3)$	$X = g$

Table 4.1: A list of the processes and momentum assignments of the phase space point in eq. (4.1.81) used to test the unordered HEJ matrix elements. Where there are degenerate processes in the MRK limit, the different subprocesses tested with MadGraph are shown.

(a) $Q = q, X = q, q', q''$

(b) $Q = q, X = \bar{q}, \bar{q}', \bar{q}''$

(c) $Q = \bar{q}, X = q, q', q''$

(d) $Q = \bar{q}, X = \bar{q}, \bar{q}', \bar{q}''$
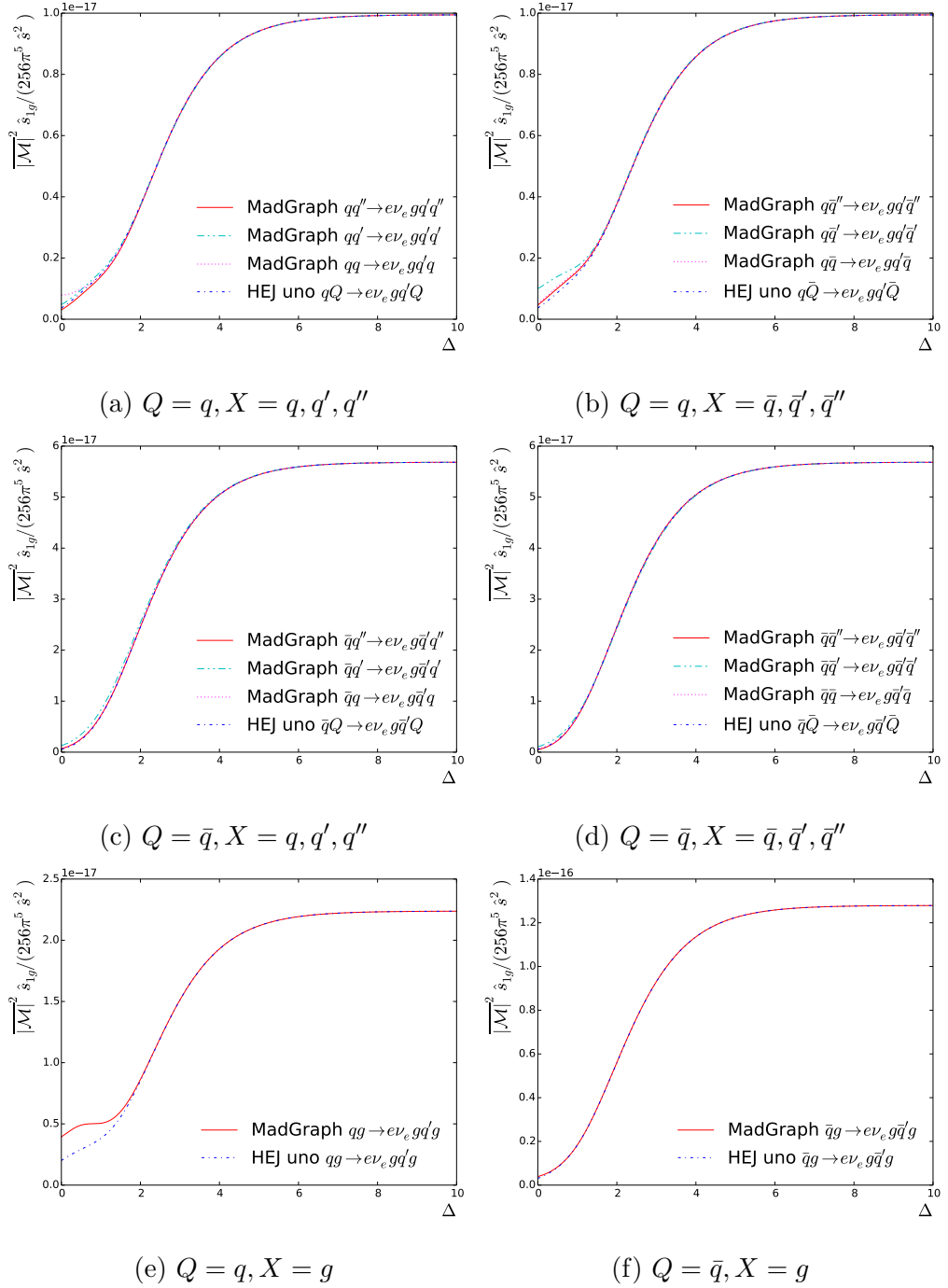
(e) $Q = q, X = g$

(f) $Q = \bar{q}, X = g$

Figure 4.7: A comparison of HEJ and tree-level matrix elements $|\mathcal{M}|^2 \hat{s}_{1g}/(256\pi^2 \hat{s}^2)$ evaluated at the phase space point (4.1.81) in an unordered configuration for increasing Δ, for the process $QX \to e\nu gQX$, where $Q = q, \bar{q}$ and $X = q, q', q'', \bar{q}, \bar{q}', \bar{q}'', g$.

4.1.6 Extension to Final State Quark-Antiquark Pairs

The only distinction between the incoming and outgoing asymptotic states which appear in the S-matrix is whether the spinors are associated with positive or negative frequency; this however is also how particles and antiparticles are distinguished. This has the consequence that it is possible to interchange an incoming particle of momentum p with an outgoing antiparticle of momentum $-p$ and the matrix elements as evaluated using Feynman rules will be unchanged. This is known as *crossing symmetry*, and may be formally stated as:

$$\mathcal{M}(\phi(p) + \cdots \rightarrow \dots) = \mathcal{M}(\cdots \rightarrow \cdots + \bar{\phi}(-p)) . \tag{4.1.85}$$

We may exploit this feature to obtain the amplitude for the process

$$g(p_a)Q(p_b) \rightarrow e(p_e)\nu_e(p_\nu)\bar{q}(k_1)q'(k_2)Q(k_3) \tag{4.1.86}$$

from the amplitude for

$$q(-k_1)Q(p_b) \rightarrow e(p_e)\nu_e(p_\nu)g(-p_a)q'(k_2)Q(k_3) . \tag{4.1.87}$$

The second process is identical to that which was used to derive the current for W plus unordered emissions. The only approximation that was used in this derivation was the constraint that $k_3 \sim p_b$, which has the important consequence that if we repeated the steps to derive the current for $g \rightarrow Wq\bar{q}$ by crossing each diagram in turn, we would obtain the same result as if we simply crossed the momenta in the factorised current for W plus unordered emissions, namely:

$$j^\mu(g(p_a) \rightarrow e(p_e)\nu_e(p_\nu)\bar{q}(k_1)q'(k_2)) = j^\mu(q(-k_1) \rightarrow e(p_e)\nu_e(p_\nu)g(-p_a)q'(k_2)) . \tag{4.1.88}$$

In other words we can obtain the current for $g \rightarrow Wq\bar{q}$ by evaluating the current for W plus unordered emissions with the normal arguments $k_a \leftrightarrow -k_1$ interchanged. This is a non-trivial statement: due to the minimality of the approximations made, the crossing symmetry normally present in the full amplitude may be extended to the factorised current. Similarly, we can obtain the current where the ordering of the quark and antiquark is reversed as follows:

$$j^\mu(g(p_a) \rightarrow e(p_e)\nu_e(p_\nu)q(k_1)\bar{q}'(k_2)) = j^\mu(\bar{q}(-k_1) \rightarrow e(p_e)\nu_e(p_\nu)g(-p_a)\bar{q}'(k_2)) . \tag{4.1.89}$$

Before we can utilise eqs. (4.1.88) and (4.1.89), we must first discuss how negative-energy spinors may be evaluated. This is a subtle problem, because spinors are only well-defined for positive energy. The spinor products may be analytically continued to negative energies as follows [149]:

$$\langle -p^- | q^+ \rangle = i \langle p^- | q^+ \rangle , \tag{4.1.90}$$

$$\langle q^+ | -p^- \rangle = i \langle q^+ | p^- \rangle , \tag{4.1.91}$$

where $p^0 > 0$. In order to see how currents and higher rank tensors transform, we note that each component of $\sigma^\mu | q^+ \rangle = \sigma^\mu_{ab} \lambda^+_b = \tilde{\lambda}^\mu_a$, is still a spinor (and likewise for the negative helicity Weyl spinors), thus each component of the tensor $\langle -p | \sigma^\mu \dots \sigma^\nu | q \rangle$ can be evaluated using $\langle p |$, with an overall factor of i. It transpires that each term in the current for W plus unordered emissions has the same spinor structure, and therefore receives the same number of factors of i; this is simply manifest as an overall phase of the amplitude that is irrelevant at the level of the amplitude squared. Thus the only place where the crossing has an impact is in products of four momenta, for which there is no issue with evaluation.

In order to test that our procedure for employing crossing symmetry to obtain the current for $g \to W q \bar{q}$ has been implemented correctly we compare the colour- and spin- summed/averaged matrix elements squared obtained using HEJ with those at tree-level (again provided by MadGraph) for the processes $gX \to W q \bar{q} X$, where X may be either a quark, antiquark or gluon. This requires, in addition to the interchange of momentum described above, that the colour-averaging of the intial state quark be corrected. The initial state quark is averaged over N_C colours, whilst the gluon must be averaged over $N_C^2 - 1$. Thus the matrix elements squared in addition receive the correction $N_C/(N_C^2 - 1) = 3/8$. The averaging from helicities does not have to be corrected as there are the same number of degrees of freedom in this case.

We again consider the phase space point given in eq. (4.1.81), and increase the rapidity Δ incrementally in the range $0 \leq \Delta \leq 10$. For large Δ we expect the amplitude squared for eq. (4.1.86) to be suppressed by the invariant mass between the quark-antiquark pair, $\hat{s}_{q\bar{q}}$ relative to FKL configurations in the MRK limit.

We therefore plot $|\mathcal{M}|^2 \hat{s}_{q\bar{q}}/(256\pi^2\hat{s}^2)$ as a function of Δ. The results are shown in fig. 4.8.

We note that there is again a degeneracy in the MRK limit of processes such as $gX \to Wu\bar{d}X$ for $X = u, d, s, \bar{u}, \bar{d}, \bar{s}$. For each unique HEJ configuration, we test using multiple identities for X; the list of processes tested with their respective momentum assignments is shown in table 4.2. Although we only present results for which the gluon is incoming along positive z we also tested the case in which the gluon is incoming along negative z. As in the previous section, the W boson is assumed to be produced in the same direction as the quark from which it was emitted. In all cases we find that the correct MRK limit is recovered, and moreover, the agreement with the leading order matrix elements is excellent over nearly the entire range of Δ.

Figure	Process	MadGraph subprocesses
4.8a	$g(p_a)X(p_b) \to e(p_e)\nu(p_\nu)\bar{q}(k_1)q'(k_2)X(k_3)$	$X = q, X = q', X = q''$
4.8b	$g(p_a)\bar{X}(p_b) \to e(p_e)\nu(p_\nu)\bar{q}(k_1)q'(k_2)\bar{X}(k_3)$	$\bar{X} = \bar{q}, \bar{X} = \bar{q}', \bar{X} = \bar{q}''$
4.8c	$g(p_a)X(p_b) \to e(p_e)\nu(p_\nu)q(k_1)\bar{q}'(k_2)X(k_3)$	$X = q, X = q', X = q''$
4.8d	$g(p_a)\bar{X}(p_b) \to e(p_e)\nu(p_\nu)q(k_1)\bar{q}'(k_2)\bar{X}(k_3)$	$\bar{X} = \bar{q}, \bar{X} = \bar{q}', \bar{X} = \bar{q}''$
4.8e	$g(p_a)g(p_b) \to e(p_e)\nu(p_\nu)\bar{q}(k_1)q'(k_2)g(k_3)$	$X = g$
4.8f	$g(p_a)g(p_b) \to e(p_e)\nu(p_\nu)q(k_1)\bar{q}'(k_2)g(k_3)$	$X = g$

Table 4.2: A list of the processes and momentum assignments of the phase space point in eq. (4.1.81) used to test the HEJ matrix elements that utilise the current for $g \to W^{\pm}\bar{q}q'$. Where there are degenerate processes in the MRK limit, the different subprocesses tested with MadGraph are shown.

4.2 Performing Phase Space Integration for Unordered Emissions

Finding the contribution to cross section from unordered emissions necessarily requires computing a phase space integral (using the methods described in sec-

(a) $X = q, q', q''$; $\bar{q}$ forwards

(b) $X = \bar{q}, \bar{q}', \bar{q}''$; $\bar{q}$ forwards

(c) $X = q, q', q''$; q forwards

(d) $X = \bar{q}, \bar{q}', \bar{q}''$; q forwards
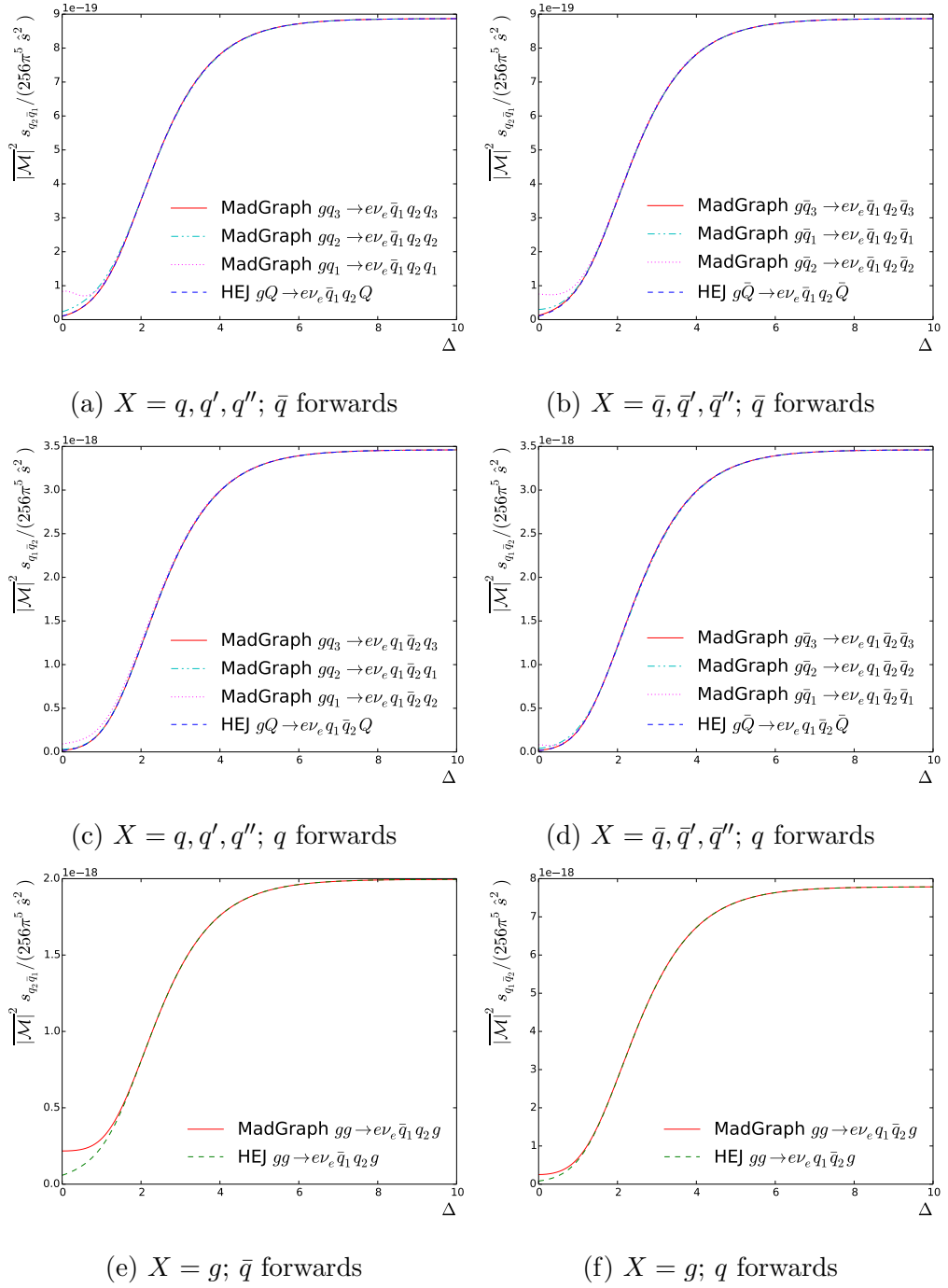
(e) $X = g$; $\bar{q}$ forwards

(f) $X = g$; q forwards

Figure 4.8: A comparison of HEJ and tree-level matrix elements $|\mathcal{M}|^2 \hat{s}_{q\bar{q}}/(256\pi^2 \hat{s}^2)$ evaluated at the phase space point (4.1.81) for increasing Δ, for the process $gX \to e\nu q\bar{q}'X$, where $X = q, q', q'', \bar{q}, \bar{q}', \bar{q}''g$.

tion 3.1). The numerical integration over the phase space for FKL emissions in HEJ is optimised to describe the asymptotic behaviour at large rapidity separations. However, as we demonstrated in the previous section, in this limit the matrix element for an unordered configuration is suppressed by $\hat{s}_{1g}$ (or $\hat{s}_{ng}$ in the case of an backwards unordered gluon) so the dominant contributions to the integral occur in the region in which $\hat{s}_{1g}$ is small. A sampling of phase space that is optimised for FKL configurations is therefore inappropriate for unordered configurations, meaning that a large number of sample points would be needed for the integral to converge. This is problematic because the implementation of the matrix element 4.1.78 is computationally intensive to evaluate. In this section we therefore discuss how the importance sampling was optimised for unordered configurations.

4.2.1 Importance Sampling for Unordered Emissions

Without loss of generality we will only discuss forwards unordered emissions; we will improve the importance sampling of the absolute angular distance of the unordered gluon to the nearest quark parameterised in rapidity (Δy) and azimuthal angle ($\Delta \phi$), so by symmetry of $z \to -z$ this has the same behaviour as a backwards unordered emission.

We start with the coarse assumption that the integrand behaves as $1/\hat{s}_{1g}$. To find the Jacobian g of our change of variables, we must first express this in terms of the integration variables, Δy_{1g} and $\Delta \phi_{1g}$:

$$\hat{s}_{1g} = 2k_{1\perp}k_{g\perp}(\cosh \Delta y_{1g} - \cos \Delta \phi_{1g}) . \tag{4.2.1}$$

Since we wish to capture the behaviour at small $\hat{s}_{1g}$, we expand using the small angle approximation:

$$\frac{\hat{s}_{1g}}{2k_{1\perp}k_{g\perp}} \sim (\Delta y_{1g})^2 + (\Delta \phi_{1g})^2 = (\Delta R_{1g})^2 . \tag{4.2.2}$$

We therefore propose the following change of variables:

$$\Delta y_{1g} = \Delta R_{1g} \sin \alpha , \tag{4.2.3}$$

$$\Delta \phi_{1g} = \Delta R_{1g} \cos \alpha . \tag{4.2.4}$$

121

4.2. Performing Phase Space Integration for Unordered Emissions

After this change of variables, the integrand will behave according to $1/\Delta R_{1g}$. We can now take this as the Jacobian and starting point for a second change of variables, and (using the notation of section 3.1) take

$$g(\Delta R) = \frac{1}{\Delta R} \ . \tag{4.2.5}$$

This gives us the transformation:

$$r = G(\Delta R) = \frac{\int_{\Delta R_{\min}}^{\Delta R} \mathrm{d}R' g(R')}{\int_{\Delta R_{\min}}^{\Delta R_{\max}} \mathrm{d}R'' g(R'')} = \frac{\ln(\Delta R/\Delta R_{\min})}{\ln(\Delta R_{\max}/\Delta R_{\min})} \ , \tag{4.2.6}$$

where $\Delta R_{\max} = \sqrt{\Delta y_{\max}^2 + \pi^2}$, and $\Delta R_{\min}$ is chosen to be the jet radius parameter to ensure the unordered emission is in a separate jet. The integral has been normalised such that r may be selected flatly in the range $[0, 1]$. The inverse transformation is given by:

$$\Delta R = G^{-1}(r) = \Delta R_{\min} e^{ar} \ , \tag{4.2.7}$$

where $a = \ln(\Delta R_{\max}/\Delta R_{\min})$. The weight for a phase space point i is then given by:

$$w(r_i) = \frac{\mathrm{d}G^{-1}(r_i)}{\mathrm{d}r} = aG^{-1}(r_i) \ . \tag{4.2.8}$$

We must now discuss the integral over α. Naïvely one might think this should be selected flatly in the range $[0, \pi]$. However, in cases where $\Delta R > \Delta y_{\max}$ or $\Delta R > \Delta \phi_{\max}$ this range could generate points outside the allowed phase space region. In order to minimise how many phase space points are rejected we instead select α according to:
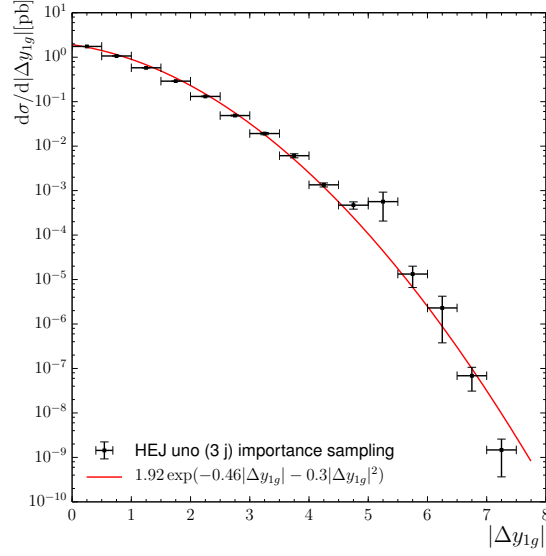
$$\alpha_j = \alpha_1 + 2(\alpha_2 - \alpha_1)r_j + (\pi - 2\alpha_2)\Theta(r_j - 0.5) \ , \qquad r_j \in [0, 1] \ , \tag{4.2.9}$$
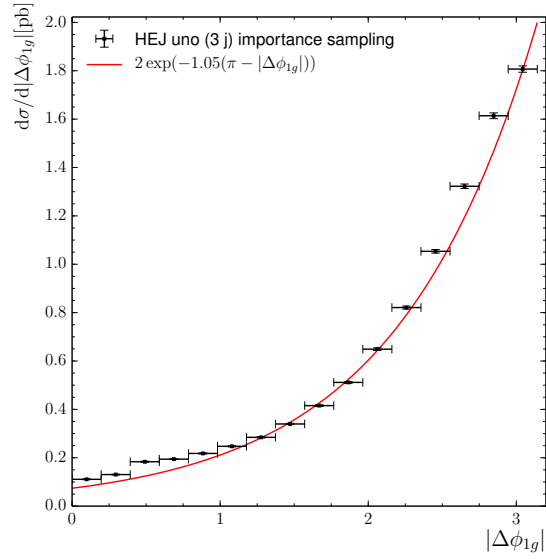
and define the phase space slices:

$$\alpha_1 = \begin{cases} \arccos(\frac{\pi}{\Delta R}) & \text{if } \Delta R > \pi \\ 0 & \text{otherwise,} \end{cases} \tag{4.2.10}$$

$$\alpha_2 = \begin{cases} \arcsin(\frac{\Delta y_{\max}}{\Delta R}) & \text{if } \Delta R > \Delta y_{\max} \\ \pi/2 & \text{otherwise.} \end{cases} \tag{4.2.11}$$

(a)

(b)

Figure 4.9: Distributions of the differential cross section as a function of the rapidity Δy_{1g} and azimuthal angle $\Delta\phi_{1g}$ of the unordered gluon relative to the central parton. The integral is evaluated using importance sampling assuming the integrand behaves similarly to $1/\hat{s}_{1g}$. These distributions may be used to fit the dependence of cross section upon Δy_{1g} and $\Delta\phi_{1g}$, that may be used to improve the importance sampling in a subsequent iteration.

4.2. Performing Phase Space Integration for Unordered Emissions

This prescription gives us the additional multiplicative weight $2(\alpha_2 - \alpha_1)$ in the Jacobian.

Since our original approximation was fairly coarse, the procedure for importance sampling may still not be optimal. However, we can iterate the procedure as follows. We calculate the contribution to the cross section (without FKL matching) from an unordered configuration of the partonic process $ab \to W(\to \ell\nu_\ell)g12$, evaluating the phase space integral for the unordered gluon using the importance sampling described above, assuming that this provides a reasonable estimate. We then produce plots of $\frac{d\sigma}{d\Delta y_{1g}}$ and $\frac{d\sigma}{d\Delta\phi_{1g}}$, and identify functions which approximate the $\Delta\phi_{1g}$ and Δy_{1g} dependence of the cross section. The identified functions can then be use to define a new g. The results are shown in fig. 4.9, and yield:

$$\frac{d\sigma}{d\Delta y_{1g}} \sim \exp\left(a\Delta y_{1g} + b(\Delta y_{1g})^2\right) , \tag{4.2.12}$$

$$\frac{d\sigma}{d\Delta\phi_{1g}} \sim \exp\left(k(\pi - \Delta\phi_{1g})\right) , \tag{4.2.13}$$

where $a = -0.46$, $b = -0.3$, and $k = -1.05$. For the rapidity interval this yields the transformation:

$$r = G(\Delta y) = \frac{B - e^{a\Delta y + b(\Delta y)^2}}{B - A} , \tag{4.2.14}$$

$$\Delta y = G^{-1}(r) = \frac{a}{2b}\left[-1 + \sqrt{1 + \frac{4b}{a^2}\ln(B - (B - A)r)}\right] , \tag{4.2.15}$$

$$w(r) = \frac{dG^{-1}(r)}{dr} = \frac{-\frac{1}{a}\frac{B-A}{B-(B-A)r}}{\left[-1 + \sqrt{1 + \frac{4b}{a^2}\ln(B - (B - A)r)}\right]} , \tag{4.2.16}$$

where $B = e^{ay_{min} + by_{min}^2} = 1$ and $A = e^{ay_{max} + by_{max}^2}$. For the azimuthal interval we obtain the transformation:

$$r = G(\phi) = \frac{\exp\left(k(\pi - \phi)\right) - K}{1 - K} , \tag{4.2.17}$$

$$\Delta\phi = G^{-1}(r) = \pi - \frac{1}{k}\ln((1 - K)r + K) , \tag{4.2.18}$$

$$w(r) = \frac{dG^{-1}(r)}{dr} = -\frac{1}{k}\frac{1 - K}{(1 - K)r + K} , \tag{4.2.19}$$

where $K = e^{k(\pi - \phi_{min})}$.

To ensure that the change of variables used in the two importance sampling procedures has been implemented correctly, we again evaluate the contribution

to the cross section from an unordered partonic configuration. By comparing the predictions of the different integration schemes for both the total and differential cross section we can ensure that the Jacobian weights have been correctly assigned. In particular, the first two methods (referred to as 'importance sampling' and 'improved sampling' respectively) are compared with the result of a flat sampling of Δy_{1g} and $\Delta \phi_{1g}$ in the allowed ranges.

The result for the total cross section having evaluated 10^8 phase space points is as follows:

$$\sigma_{\text{flat}} = 2.0667 \pm 0.0071 \text{ pb},$$

$$\sigma_{\text{importance}} = 2.0717 \pm 0.0075 \text{ pb},$$

$$\sigma_{\text{improved}} = 2.0804 \pm 0.0068 \text{ pb}.$$

The cross section for all three method agree within statistical error. This, in conjunction with the observation that the differential distribution for the transverse momentum for the W boson shown in fig. 4.10a agrees for all methods indicates that the Jacobian has been correctly evaluated in the two importance sampling schemes.

Although the statistical error increases with the first iteration of importance sampling, the distribution of the invariant mass between the unordered gluon and the W-emitting quark, m_{1g} shown in fig. 4.10b reveals that the flat sampling is far less stable than the first importance sampling method. This indicates that the estimate of the error for the flat sampling is an underestimate of the true error. The same effect to a lesser extent may also be seen in fig. 4.10c.

The statistical error does however decrease with the second iteration of importance sampling. The second method gives a 10% smaller error, which corresponds to requiring 20% fewer events to yield the same precision in the cross section. A slight improvement may also be seen in the distribution of the transverse momentum of the central parton shown in fig. 4.10c. A small improvement between the two methods of importance sampling is encouraging; a large difference between the two would indicate that our initial approximation was poor. That the description is nonetheless improved indicates that the second iteration was worthwhile.
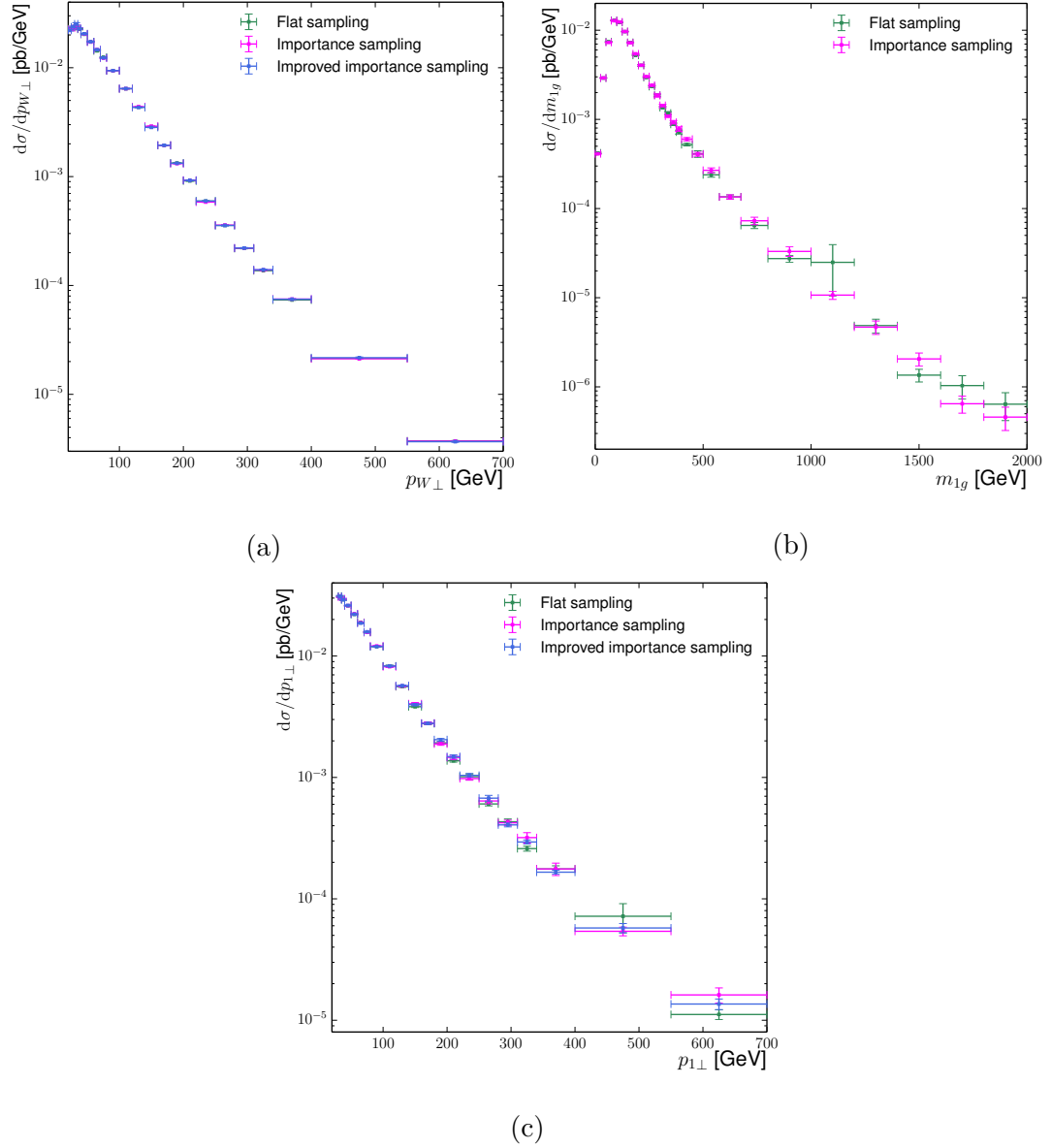
(a)

(b)

(c)

Figure 4.10: A comparison of differential distributions of the cross section between three different methods for generating the rapidity and azimuthal angle of the unordered emission.

4.2.2 Validation of Importance Sampling

Although we have validated the self-consistency of the phase space generation described in the previous section, it is still necessary to verify that the numerical result is correct. It is sufficient to ensure that the cross section for a given partonic process evaluated using the HEJ phase space generation agrees with the result at leading order, providing we replace the internal HEJ matrix elements with exact tree-level matrix elements. As in previous studies MadGraph 5 is used to generate the leading order predictions and also to provide the tree-level matrix elements.

The partonic channel chosen was $ug \to e^+\nu_e dgg$, where the incoming partons are ordered such that the up quark is incoming along the positive z axis. For this channel there are three unique rapidity orderings for the three final state partons. If the down quark is forwards, this is an FKL configuration; a central down quark corresponds to an unordered configuration; finally a backwards down quark is a non-FKL configuration. To extract the different channels from MadGraph, Les Houches event files were generated and analysed to process each channel separately. While it is only the integration of the unordered channel that we wish to validate, comparing all three configurations ensures that the classification of MadGraph events has been done properly.

Events contributing to the cross section were required to contain exactly three jets defined using the anti-k_T jet algorithm. In addition, the following cuts were used:

$$p_{Tj} > 30 \text{ GeV}, \qquad p_{T\ell} > 25 \text{ GeV}, \qquad p_{T\nu} > 25 \text{ GeV},$$

$$|y_j| < 4.5, \qquad |y_\ell| < 2.5, \qquad \Delta R_{jj} > 0.4, \qquad \Delta R_{\ell j} > 0.5,$$

$$75 \text{ GeV} \leq m_W \leq 85 \text{ GeV},$$

$$m_{jj} \leq 500 \text{ GeV}. \tag{4.2.20}$$

The last two cuts were chosen to improve the efficiency of the integration in MadGraph. The centre mass energy used was $\sqrt{s} = 7000$ GeV. A fixed scale choice was used, namely $\mu_F = \mu_R = m_Z = 91.188$ GeV; this was chosen to eliminate the coupling as a source of discrepancy. The PDF choice was MSTW2008nlo [150].

The total cross section for the three channels as given by MadGraph and HEJ

| Channel	MadGraph	HEJ
FKL	2.235 ± 0.001 pb	2.248 ± 0.001 pb
unordered	1.1098 ± 0.0009 pb	1.1093 ± 0.0001 pb
non-FKL	0.4965 ± 0.0006 pb	0.4957 ± 0.005 pb

Table 4.3: A comparison of the cross section in different channels for the process $ug \to e^+\nu_e dgg$ with the cuts shown in (4.2.20), used in the validation of the importance sampling.

respectively are shown in table 4.3. For the unordered and non-FKL channels we have agreement to 1‰ or better. There is a small discrepancy in the FKL channel, which we discuss later; however it only represents a difference of 0.5%, and thus we still have agreement at the percent level for this channel.
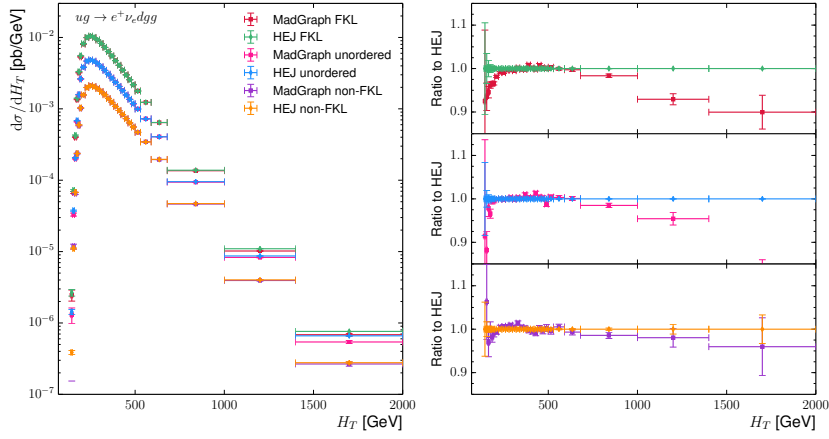
A breakdown of the differential cross section into FKL, unordered and non-FKL configurations as a function of various observables is shown in fig. 4.11. From the distributions of the azimuthal angle between the most forward and backward jets $\Delta\phi_{fb}$ shown in fig. 4.11a we observe that the break down into the three components appears to have been done correctly. From the distribution of the scalar sum of transverse momentum H_T shown in fig. 4.11b, although there is good agreement in the peak region, there are increasingly large deviations in all channels for large H_T. The size of the statistical error bars for the MadGraph predictions also increase in this region indicating that MadGraph undersamples the tail of this distribution. However, since this distribution is steeply falling, this does not have an impact on the total cross section.

In fig. 4.11c we show the invariant mass between the most forward and backwards jets, $m_{fb} = \sqrt{\hat{s}_{fb}}$. In this case, while the predictions for the unordered and non-FKL channels agree well, MadGraph systematically undershoots HEJ at large invariant masses in the FKL channel. The adaptive integration algorithm used in MadGraph assumes that the peaks are well localised [151]; if this is not the case then the integration is less efficient. The invariant mass distribution is less steeply falling for FKL than for other channels, therefore the peak region is not as well localised as in
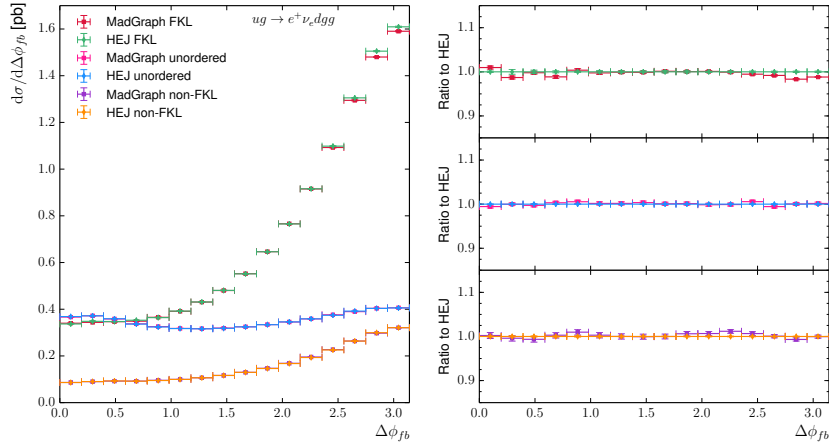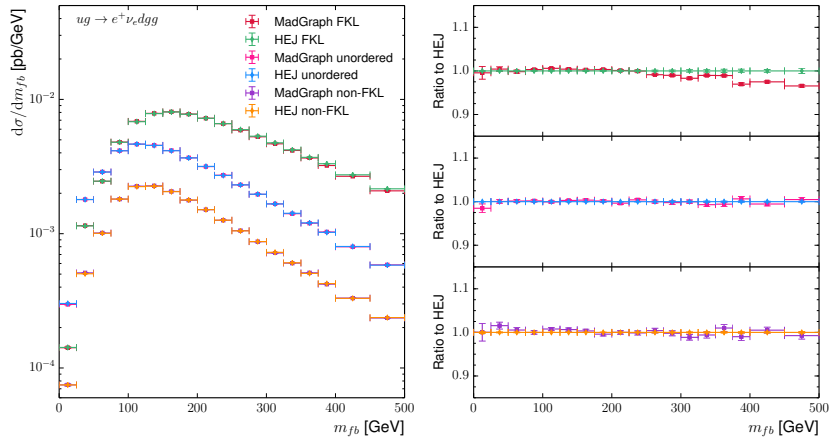
(a)

(b)

(c)

Figure 4.11: A comparison between HEJ and MadGraph of the differential cross section for the process $ug \to e^+\nu_e dgg$ for the three unique rapidity orderings of the final state partons.

the other channels. We therefore speculate that the invariant mass distribution is undersampled in the tail and that the statistical error bars give an underestimate of the true error in this region. We assume that this is the cause of the small discrepancy in the cross section observed above.

Finally, in fig. 4.12 we show differential distributions of the cross section in the unordered channel as a function of the variables for which the phase space generation was optimised, Δy_{uno} and $\Delta \phi_{\mathrm{uno}}$ (shown in figs. 4.12a and 4.12b respectively). The agreement appears to be good in both distributions.

The case where the ordering of the intial state partons is reversed, which permits the validation of a backwards unordered emission, was also investigated. The results should be identical by the symmetry of $z \rightarrow -z$, and this was found to be the case. This in conjunction with the observations made above fully validates the importance sampling of unordered emissions discussed in the previous section.
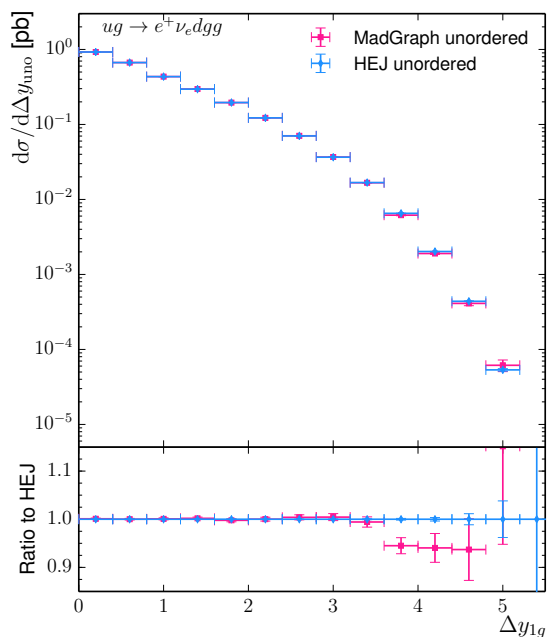
(a)
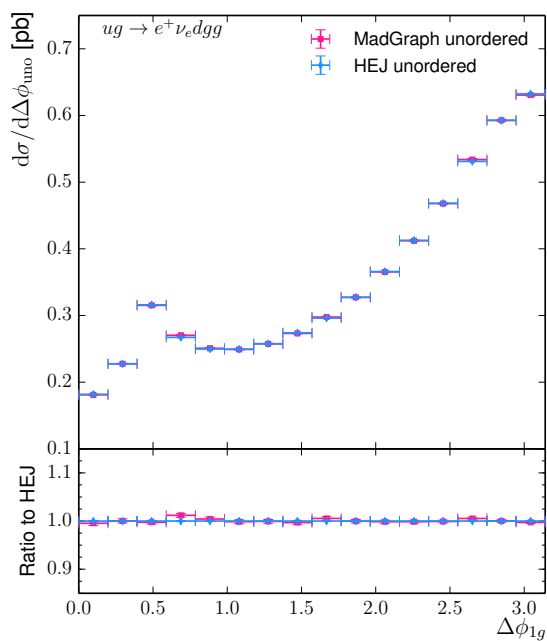
(b)

Figure 4.12: A comparison between HEJ and MadGraph of the differential cross section for the process $ug \to e^+\nu_e dgg$ for an unordered configuration of the final state partons. This is shown as a function of the variables Δy_{1g} and ϕy_{1g} used in the phase space generation of the unordered gluon.

4.3 Matching

As discussed in section 2.4, until now unordered configurations were included only through matching to leading order (see eq. (2.4.76)). This procedure entails first generating a rapidity-ordered phase space point, and assigning momenta to the final state partons by randomly selecting from the unique list of permutations of rapidity orderings not already included in HEJ. Having extended the HEJ formalism to include unordered configurations it is therefore necessary to remove these permutations from the matching. The number of possible permutations is flavour dependent, for example the process $us \to e^+ \nu_e dgs$ has 6 possible orderings, one of which is FKL and one which is unordered. The process $ug \to e^+ \nu_e dgg$ only has 3 orderings: one FKL, one unordered and one non-FKL. The task of removing unordered configurations from the matching must therefore be done case by case, and as such is extremely laborious. It is thus necessary to validate that this has been implemented correctly.

We shall demonstrate that the total cross section at leading order[2] for W plus exactly three or four jets is unchanged by the moving of unordered configurations from the non-FKL matching into the all order framework. In what follows, the cuts that were used are the same as those in the previous section; however to reduce the problems experienced with MadGraph undersampling in the region of large transverse momenta, the following additional cut was applied:

$$p_{Tj} < 300 \text{ GeV}. \tag{4.3.1}$$

We first ensure that the leading order predictions for HEJ are self-consistent. In fig. 4.13 we show the differential cross section for W plus exactly three jets for not just the total rate, but also for FKL and non-FKL components. Here 'non-FKL after' corresponds to the sum of the unordered component and the remaining channels included only via matching. The FKL component should in principle be unaffected by the changes, however it is worthwhile to verify this. That all

---

[2]Again, as in the validation of importance sampling, to obtain the leading order cross section internal HEJ matrix elements are replaced with those at leading order provided by MadGraph.

components agree indicate that all unordered configurations have been properly accounted for.

These conclusions may be strengthened by comparing directly with leading order predictions. In fig. 4.14 we compare the differential cross section for W plus exactly three jets between HEJ and MadGraph. In fig. 4.14b we see some discrepancies at large rapidities, but again these appear to be due to to undersampling in the large rapidity tail. Otherwise there is a good level of agreement, which is better than 1% at the level of the total cross section.

For validating the four jet matching, the leading order predictions were instead provided by ALPGEN [152] since this was found to have a more efficient phase space generation than MadGraph. In addition, to improve the convergence, the following set of very tight cuts were used:

$$30 \text{ GeV } < p_{Tj} < 100 \text{ GeV},$$
$$25 \text{ GeV } < p_{T\ell} < 100 \text{ GeV}, \qquad 25 \text{ GeV } < p_{T\nu} < 100 \text{ GeV},$$
$$|y_j| < 2.5 \qquad |y_\ell| < 1.0, \qquad \Delta R_{jj} > 0.4, \qquad \Delta R_{\ell j} > 0.5,$$
$$75 \text{ GeV } \leq m_W \leq 85 \text{ GeV},$$
$$m_{jj} \leq 300 \text{ GeV}. \tag{4.3.2}$$

A comparison of the differential cross section is shown is shown in fig. 4.15, and good agreement was found in the total rate for all distributions. Using ALPGEN has the disadvantage that unweighted event files are produced only with a severe reduction in efficiency, and thus a categorisation of events into the respective components of FKL, unordered and non-FKL was not possible.

In order to indirectly test that the breakdown into components is correct, one may check that the total cross section agrees for a variety of different cuts, as this affects the relative proportions of the different components in the total rate. In the six tests performed, the minimum jet transverse momentum p_{Tj} was varied, and in some cases an additional cut was placed on the rapidity separation of the hardest two jets: $|\Delta y_{12}| > 1.0$. The set of cuts which were used is summarised in table 4.4. All other cuts were reverted to those in eq. (4.2.20).

The results for the cross section are summarised in table 4.5. Overall there
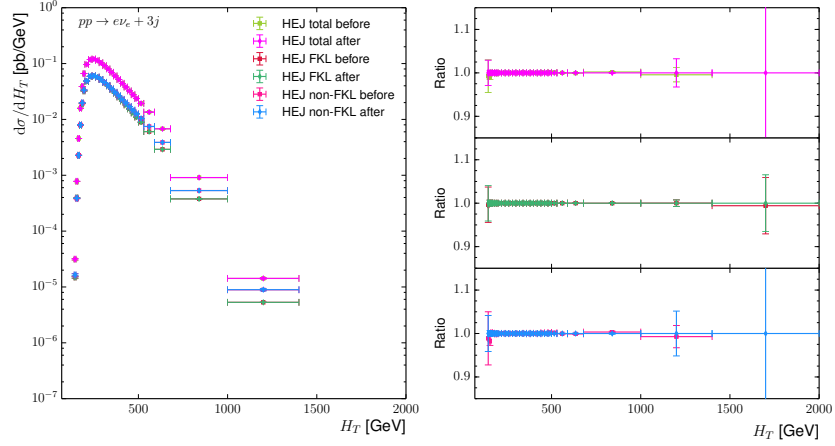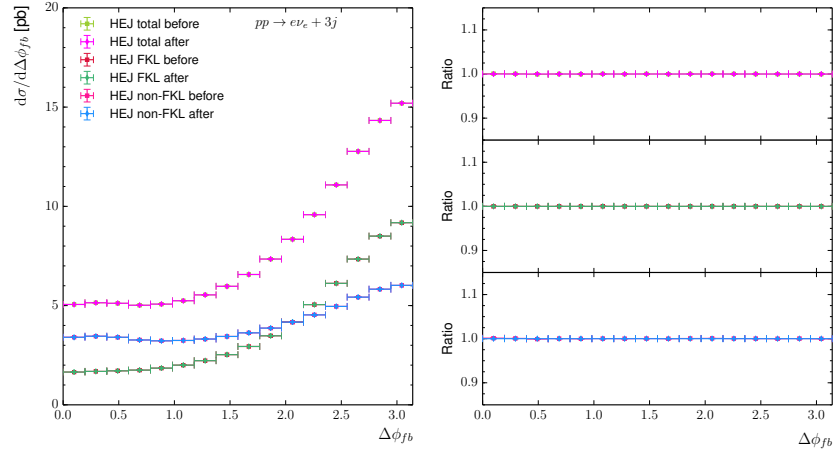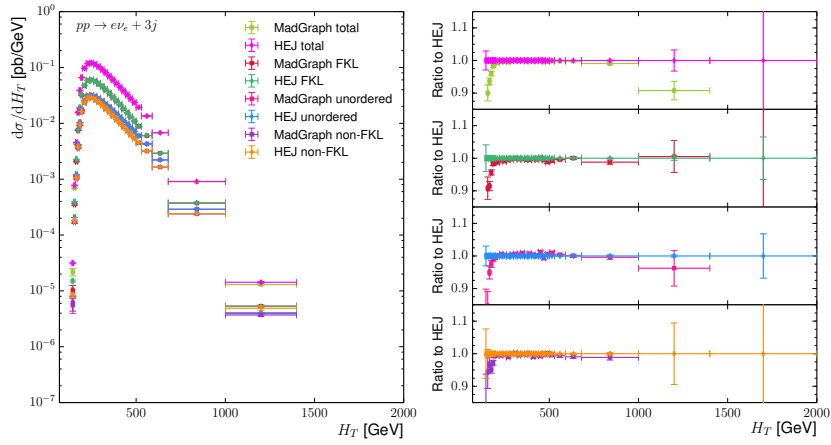
(a)
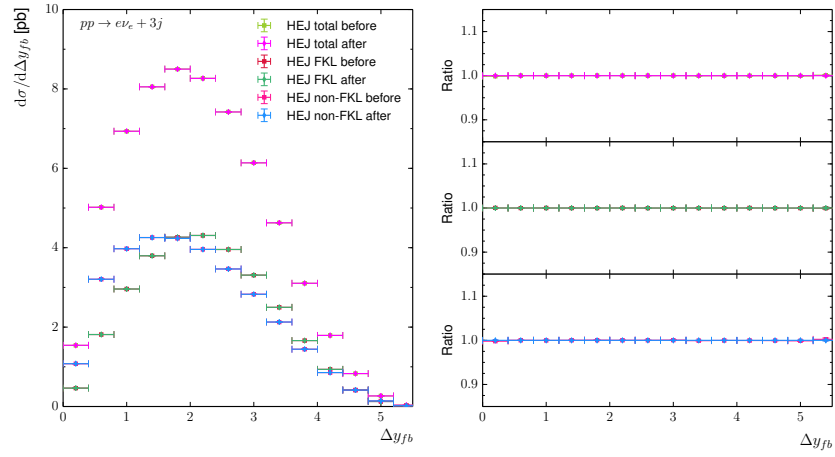
(b)

(c)

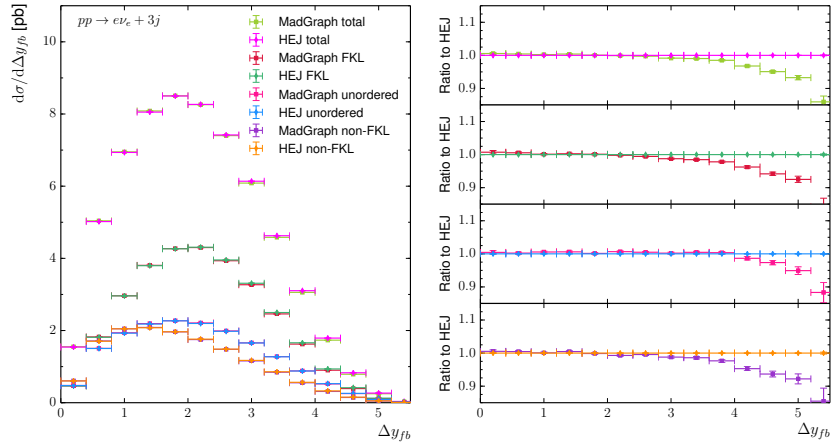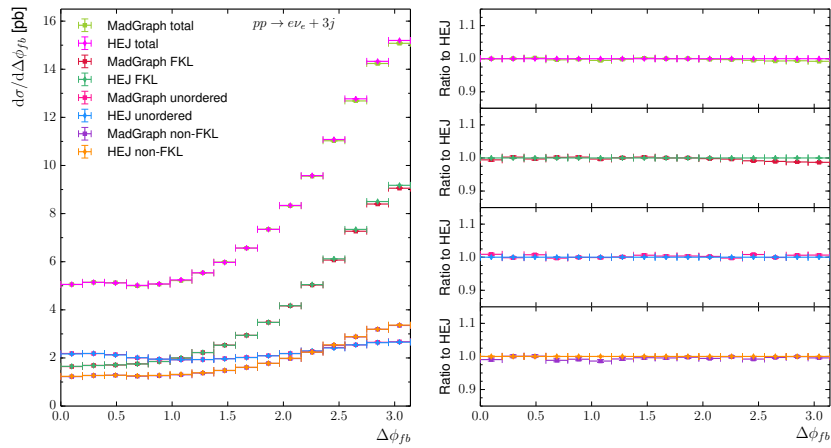Figure 4.13: Plots showing the differential cross section at leading order for the production of W plus exactly three jets. A comparison is made between HEJ before and after unordered configurations has been moved from non-FKL matching into the all order framework.

Figure 4.14: A comparison of the differential cross section between HEJ and MadGraph at leading order for the production of W plus exactly three jets.

is agreement for all cut sets; any small discrepancies are not deemed statistically significant. We can therefore conclude that the breakdown of the total four jet rate into FKL, unordered and non-FKL is correct, thereby completing the necessary validation of the matching.

Cut set	$p_{Tj\min}$ / GeV	$|\Delta y_{12}| > 1.0$?
1	30	No
2	60	No
3	100	No
4	30	Yes
5	60	Yes
6	100	Yes

Table 4.4: A summary of the cut sets used to test that the breakdown of the cross section into FKL, unordered and non-FKL components for W plus four jets.

Cut set	$\sigma_{\text{ALPGEN}}/\text{pb}$	$\sigma_{\text{HEJ,before}}/\text{pb}$	$\sigma_{\text{HEJ,after}}/\text{pb}$
1	$14.18 \pm (3.9 \times 10^{-1})$	$14.19 \pm (1.1 \times 10^{-2})$	$14.18 \pm (6.7 \times 10^{-3})$
2	$1.445 \pm (2.5 \times 10^{-3})$	$1.448 \pm (9.6 \times 10^{-4})$	$1.447 \pm (1.5 \times 10^{-3})$
3	$0.1845 \pm (2.6 \times 10^{-4})$	$0.1862 \pm (3.5 \times 10^{-4})$	$0.1859 \pm (2.0 \times 10^{-4})$
4	$8.884 \pm (1.5 \times 10^{-2})$	$8.94 \pm (9.6 \times 10^{-3})$	$8.93 \pm (5.9 \times 10^{-3})$
5	$0.851 \pm (1.4 \times 10^{-3})$	$0.857 \pm (1.2 \times 10^{-3})$	$0.857 \pm (8.2 \times 10^{-4})$
6	$0.1019 \pm (1.5 \times 10^{-4})$	$0.1024 \pm (2.6 \times 10^{-4})$	$0.1024 \pm (1.6 \times 10^{-4})$

Table 4.5: A summary of the leading order cross section for W plus exactly four jets as predicted by ALPGEN and HEJ before and after the inclusion of unordered configurations into the all order framework.
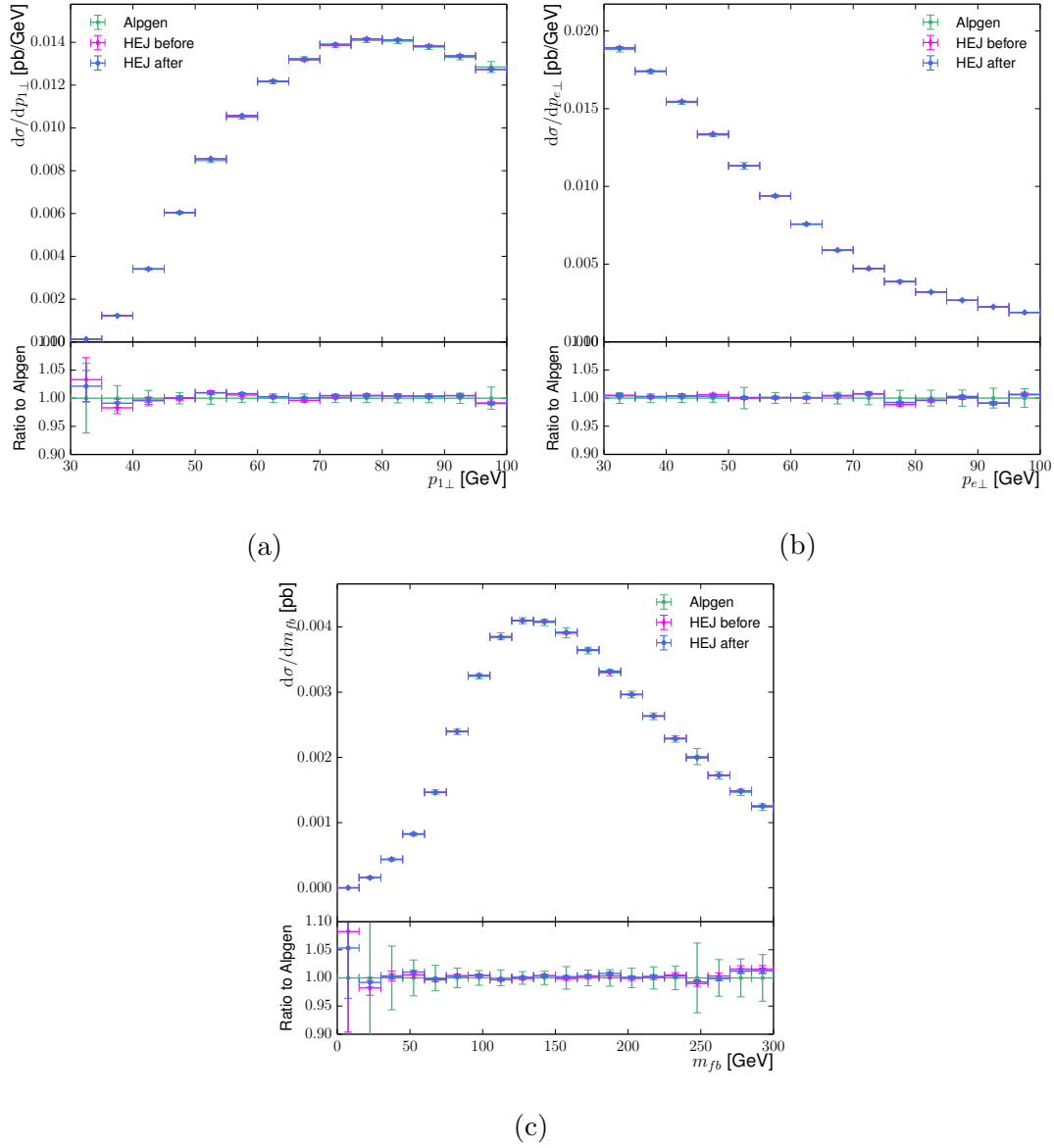
(a)

(b)

(c)

Figure 4.15: A comparison of the differential cross section between HEJ and ALPGEN at leading order for the production of W plus exactly four jets.

4.4 Results

In this section we present results for the extension of the HEJ formalism to unordered configurations in W plus jets. Our study is based on the 7 TeV ATLAS analysis originally presented in [131]. All distributions from this analysis were reproduced, and a comparison between the data and HEJ, with and without the inclusion of unordered configurations in the all order formalism, was made. The PDF set chosen was CT10nlo [153, 154], which was used to provide the original predictions in the aforementioned analysis. In addition two different choices for the central scale $\mu_R = \mu_F$ were investigated, namely the maximum jet transverse momentum, $p_{T\max}$, and $H_T/2$.

In order to quantitatively evaluate the level of improvement seen by including unordered configurations, the χ^2 statistic was calculated for each distribution. This is given by:

$$\chi^2 = \sum_i^{N_{\text{bins}}} \frac{(O_i - E_i)^2}{\sigma_i^2} \, , \tag{4.4.1}$$

where O_i is the measured value in bin i, E_i is the expected theoretical value, and σ_i is the experimental error on the measurement O_i. The results are summarised in table 4.6, and the sum of χ^2 over all the distributions is given in the final line. We observe that for both scale choices there is a reduction in the total χ^2 from the inclusion of unordered emissions, signifying a global improvement in the agreement with data. Furthermore, this simple calculation reveals that $H_T/2$ is the best overall scale choice. We now present a selection of plots for which $H_T/2$ was taken as the central scale choice.

As can be seen from table 4.6, in nearly all distributions that are related to the jet transverse momentum the HEJ predictions are brought closer to data by the inclusion of unordered emissions. In particular, we show the differential cross section with respect to H_T in fig. 4.16. The bands around the central line correspond to independently varying the scales μ_R and μ_F between twice and half of the central scale choice [3]. The shape of this distribution is notably improved;

---

[3]Only combinations of μ_R and μ_F are allowed for which the ratio does not exceed 2.

Distribution	$\mu = p_{T\max}$		$\mu = H_T/2$	
	Standard	Unordered	Standard	Unordered
N_j (inclusive)	12.46	5.691	0.6426	0.8459
$p_{T1}, N_j \geq 2$	219.4	131.6	124.3	72.19
$p_{T2}, N_j \geq 2$	426.9	250.2	218.7	114.8
$y_2, N_j \geq 2$	11.29	5.582	8.119	13.52
$H_T, N_j \geq 2$	232.9	135.9	77.59	45.61
$S_T, N_j \geq 2$	248.9	134.2	76.11	34.15
$m_{12}, N_j \geq 2$	7.785	4.084	17.72	37.11
$\Delta y_{12}, N_j \geq 2$	21.89	21.98	29.07	36.90
$\Delta \phi_{12}, N_j \geq 2$	21.94	17.44	8.967	13.75
$\Delta R_{12}, N_j \geq 2$	57.32	53.47	34.93	43.19
$p_{T1}, N_j \geq 3$	116.6	49.62	12.30	2.240
$p_{T3}, N_j \geq 3$	190.7	96.44	35.30	11.65
$y_3, N_j \geq 3$	113.4	59.58	11.33	4.219
$H_T, N_j \geq 3$	194.7	78.92	20.69	8.533
$S_T, N_j \geq 3$	225.6	94.08	22.80	3.802
$p_{T4}, N_j \geq 4$	20.55	12.20	1.722	3.515
$y_4, N_j \geq 4$	36.63	22.38	2.289	2.633
$H_T, N_j \geq 4$	75.10	40.19	2.249	8.337
$S_T, N_j \geq 4$	86.54	50.63	3.832	9.808
Sum	2320	1264	708.6	466.8

Table 4.6: Comparison of χ^2 statistic for a range of distributions for standard HEJ versus HEJ plus unordered for different scale choices.
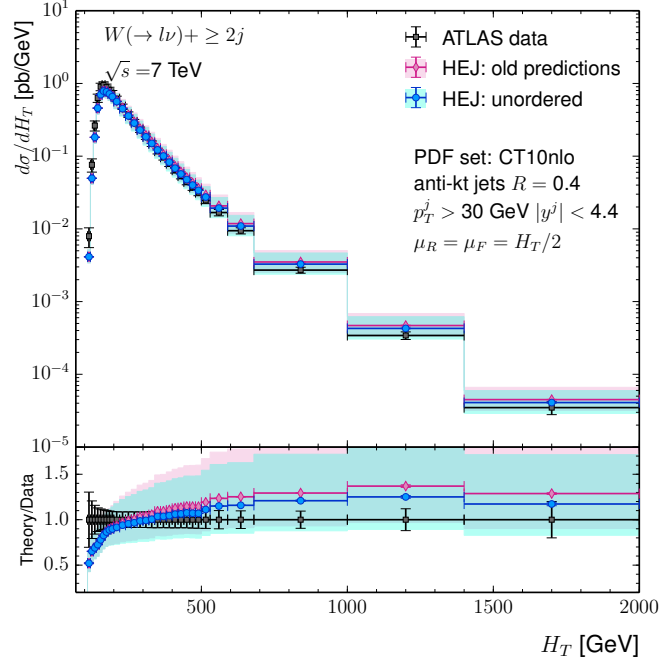
Figure 4.16: A comparison of HEJ, with and without unordered configurations included in the all order formalism, and ATLAS data for the differential cross section for W plus inclusive dijets as a function of H_T

the central line in HEJ is brought significantly closer to the data in nearly all bins. A similar effect was seen in the distributions of jet transverse momenta, and the scalar sum of jet transverse momenta S_T.

In fig. 4.17 we show the differential cross section as a function of the invariant mass between the two hardest jets, m_{12}. Previously this distribution agreed well with data for the standard leading logarithmic predictions of HEJ. We would therefore hope that this distribution is not significantly affected by the latest corrections. We see that although the shape is not strongly altered, the normalisation is reduced, such that the overall agreement in this distribution is slightly worse. To understand this, there are numerous points we should take into consideration. Firstly, the predictions for m_{12} are still mostly within one standard deviation of the data. The increase in χ^2 here is also smaller than the reduction in χ^2 for many of the other distributions. The variable m_{12} is defined between the two hardest jets (as opposed to rapidity ordered jets) so it is not the most optimal to be described by the HEJ formalism. We might anticipate a better description for the invariant mass between
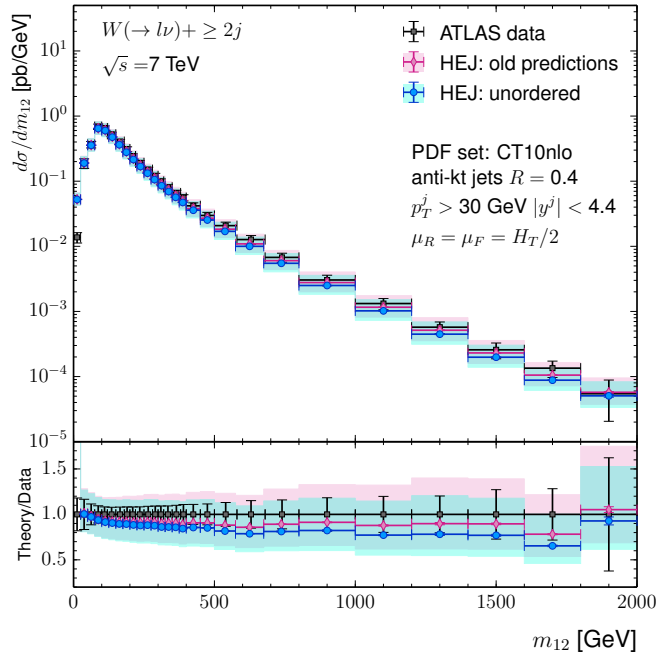
140

Figure 4.17: A comparison of HEJ, with and without unordered configurations included in the all order formalism, and ATLAS data for the differential cross section for W plus inclusive dijets as a function of m_{12}.

the most forward and backward jets m_{fb} (but this observable was not measured in the aforementioned analysis).

Furthermore, it is significant that the shape is not strongly affected. Typically we find that differences in scale choice only change the normalisation of distributions rather than their shape. While the scale choice $H_T/2$ leads to a slightly worse description, the choice $\mu = p_{T\,\mathrm{max}}$ actually gives a reduction in χ^2 when unordered emissions are included, and the value is also lower both with and without unordered emissions. It is apparent that there is some inherent arbitrariness in selecting a scale choice. The uncertainty associated with unphysical scale choices may be reduced by including higher orders, highlighting the necessity to match our description to beyond leading order. Finally the current predictions are not the final story; other NLL corrections have yet to be included in W plus jets.

The impact of including unordered configurations on the size of the scale uncertainty band was also investigated, and this was found to be very small. This is not surprising as the scale uncertainties in HEJ are not dominated by the relative

141

proportion of non-FKL, but by the reweighting with leading order matrix elements that is performed on the all order predictions.

It is illuminating to analyse not just the change in the total cross section, but also the differences in its decomposition into fixed order and all order components. The contributions of the all order and fixed order components to the differential cross section as a function of H_T before and after the inclusion of unordered emissions are shown in figs. 4.18a and 4.18b respectively. The bottom panel in each plot shows the relative contribution to the total of the fixed order component. When unordered emissions are included only at leading order, the fixed order component for large H_T saturates at around 60%. When the unordered emissions are included to all orders, the fixed order component is dramatically reduced to just above 30%. In fig. 4.18c we show the relative change in each component. Although the fixed order component is reduced by nearly 50%, the change in the total rate is more modest. This is important as it demonstrates that a large reduction in the fixed order component is nonetheless a perturbative correction within the HEJ formalism.

An equivalent set of plots to those in fig. 4.18 for the rapidity interval between the most forward and backward jets Δy_{fb} is shown in fig. 4.19. In the limit of large Δy_{fb}, the fixed order contribution should be sub-dominant, which is indeed the case. However with the inclusion of unordered configurations in fig. 4.19b the fixed order component falls more quickly. Figure 4.19c reveals that the decrease in the fixed order component is linearly proportional to $\Delta y_{fb} \sim \ln(\hat{s}/\hat{t})$ while the change in the total rate is consistent with zero for large rapidity separations, as we would expect for this type of subleading logarithmic contributions.
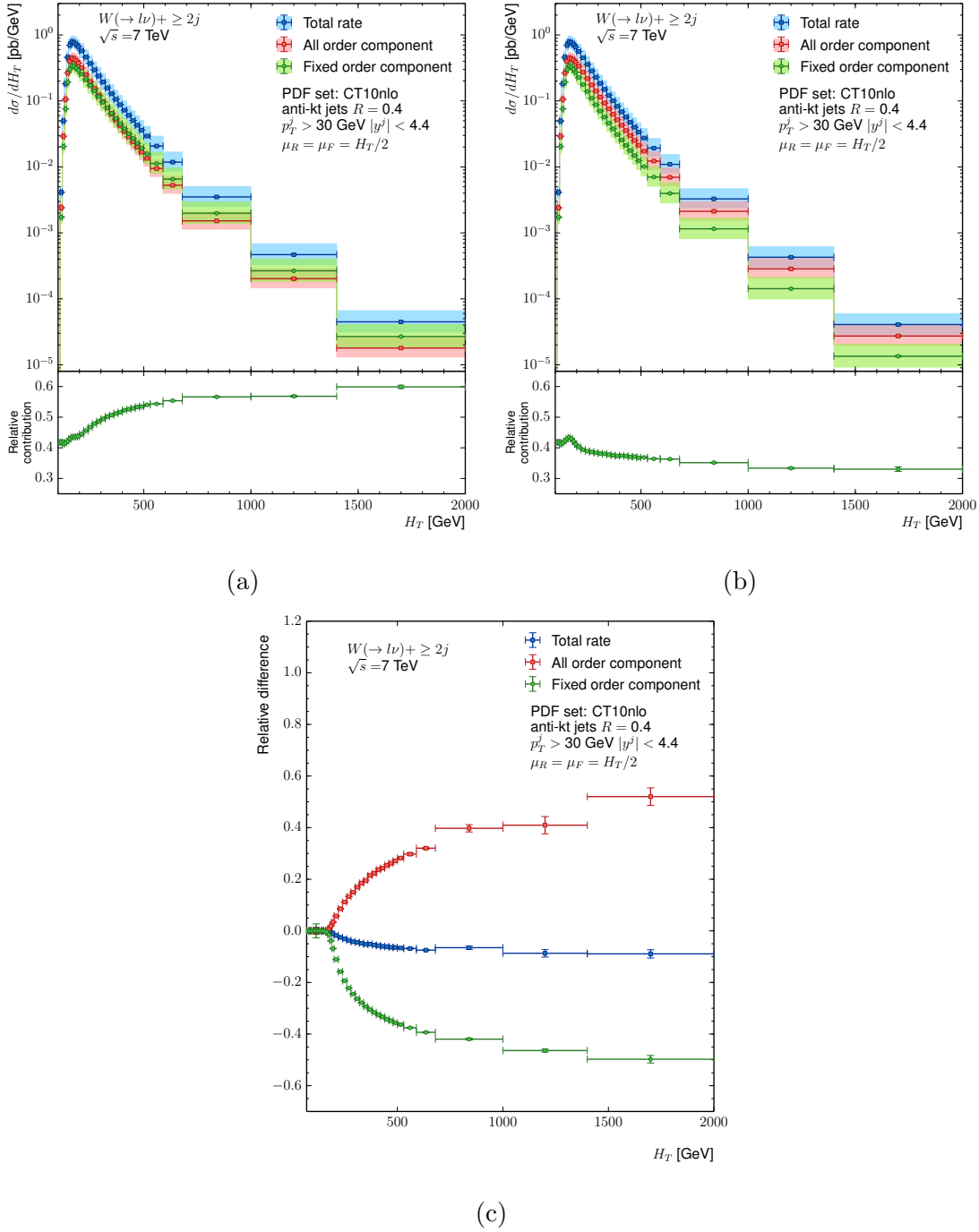
(a)

(b)

(c)

Figure 4.18: The breakdown into all order and fixed order components of the differential cross section for W plus inclusive dijet production as a function of H_T is shown for HEJ before (a) and after (b) the inclusion of unordered emissions in the all order formalism. In these plots the relative contribution to the total from fixed order is shown in the bottom panel. In c the relative difference of the fixed order and all order components, and the total differential cross section is shown also as a function of H_T.
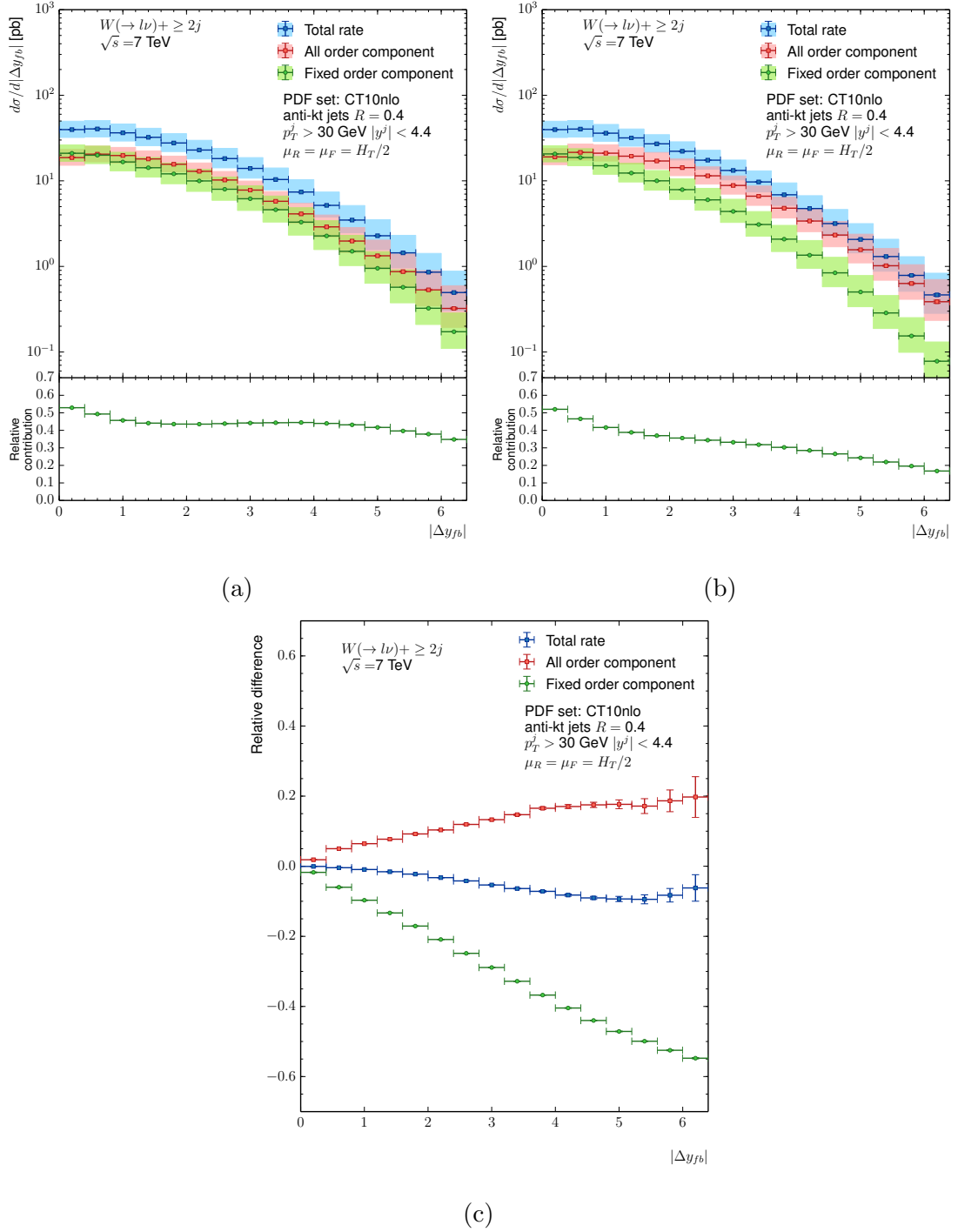
143

(a)

(b)

(c)

Figure 4.19: The breakdown into all order and fixed order components of the differential cross section for W plus inclusive dijet production as a function of Δy_{fb} is shown for HEJ before (a) and after (b) the inclusion of unordered emissions in the all order formalism. In these plots the relative contribution to the total from fixed order is shown in the bottom panel. In c the relative difference of the fixed order and all order components, and the total differential cross section is shown also as a function of Δy_{fb}.

4.5 Summary and Outlook

At the beginning of this chapter we highlighted the fact that although distributions such as the invariant mass are captured well by HEJ, distributions related to the transverse momentum of the jets such as H_T expose large deviations between the leading logarithmic predictions of HEJ and data. This problem may be ameliorated by extending the HEJ formalism to NLL accuracy. The first class of subleading logarithm, known as unordered emissions, has been implemented for W plus jets and has been extensively validated. The contribution to the cross section from configurations that are only included to leading order accuracy has been systematically reduced, which has lead to an overall improvement in the description of data, particularly in transverse momentum distributions as desired.

Although this work represents a significant development, we can anticipate further corrections of a similar order. The remaining NLL configurations involve the inclusion of quark-antiquark pairs in the final state, either as a correction to the Lipatov vertex or the current factors. These developments have been recently implemented for pure multi-jet production; it should be possible to integrate these corrections into W plus jets production without too much difficulty. The only additional correction for W plus jets relates to the effective current for $g \to e\nu q\bar{q}'$; however in section 4.1.6 it was demonstrated that this correction can be obtained from the current for W plus an unordered emission by crossing symmetry. The computation of the full NLL correction to W plus jets is therefore already accessible. The only additional task involves removing these configurations from the fixed order matching, which is in principle straightforward, albeit somewhat laborious.

This study has also underlined the importance of reducing the size of scale uncertainties, the dominant source of which is the reweighting with leading order matrix elements during FKL matching. Reweighting is essential as the approximations used to derive the HEJ matrix elements are only valid in the MRK limit; away from this limit the HEJ matrix elements are less accurate and must be corrected. The scale uncertainty may only be reduced by improving the accuracy to which matching is performed. However, this is not a trivial task as it is necessary to avoid double-counting. Work on this topic is currently in progress.

145

Notwithstanding the corrections which are currently outstanding, we view this work as a major step towards obtaining the full next-to-leading logarithmic correction in the high energy limit for W plus jets. With this addition, not only has the dependence upon fixed order matching been reduced, but the precision of the all order formalism has been improved, extending the region of phase space in which the HEJ formalism is accurate. This will facilitate a more rigorous testing of QCD at hadron collider experiments, and allow further examination of the relative importance of high energy logarithms in future analyses.

Chapter 5

Modified CKKW-L Merging for HEJ

In section 2.3 we argued that understanding the effect of vetoes on jet activity and azimuthal dijet correlations is important for Higgs phenomenology, and furthermore that an all order description of high energy logarithms might be necessary for such observables. However as reviewed in section 2.5, the analyses of [138, 140] revealed that neither HEJ nor a traditional parton shower approach could fully describe the data, whereas the combination of HEJ with the parton shower ARIADNE yielded a much better overall agreement with data. These studies therefore provide compelling evidence that such a combination is necessary to obtain an accurate description in the extreme regions of phase space probed through the application of jet vetoes.

Despite improving the predictions in many observables, HEJ+ARIADNE is not completely without deficiency. One particular observable which this approach cannot fully describe is jet shapes. Since jets in HEJ are largely unpopulated, any capacity to describe jet shapes should be entirely coming from the parton shower. Ideally HEJ+ARIADNE should capture these observables at least as well as ARIADNE alone, and any difference indicates that the matching procedure is incorrectly interfering with parton shower behaviour.

In fig. 5.1 we show a plot of the average jet profile $\rho(r)$ reproduced from [133]. This variable is defined as the fraction of the jet's transverse momentum $p_\perp$ that
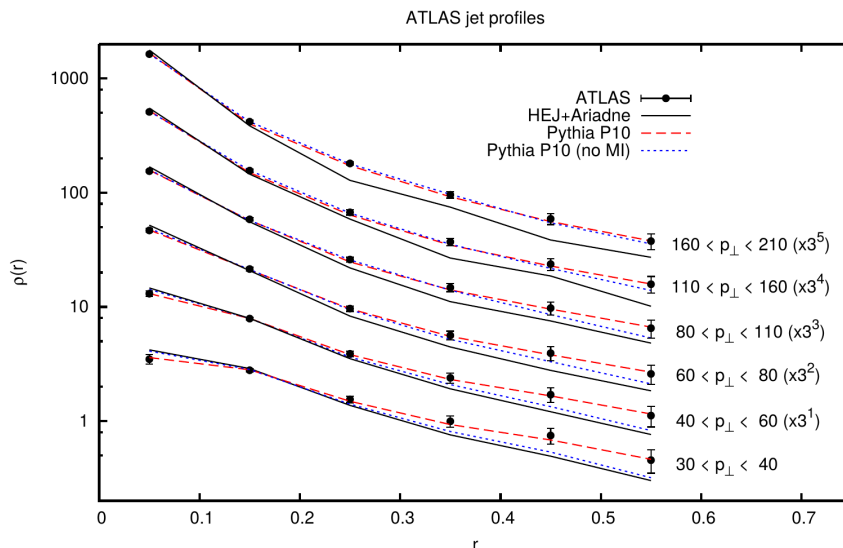
Figure 5.1: A comparison between HEJ+ARIADNE and PYTHIA (with and without multiple parton interactions) of jet profiles $\rho(r)$ in different slices of jet transverse momentum, reproduced from [133].

can be found at a radius r from the centre of jet, and is given by:

$$\rho(r) = \frac{1}{p_\perp(R)} \frac{dp_\perp(r)}{dr} \ , \tag{5.0.1}$$

where R is the jet radius used in the anti-k_T jet definition. The method of [133] for combining HEJ and ARIADNE includes hadronisation but not *multiple parton interactions* (MPI), namely the phenomenon where more than one pair of partons from the same pair of incoming protons are involved in separate hard scattering processes [155]. Therefore in fig. 5.1 the predictions for HEJ+ARIADNE are compared to PYTHIA 6 (using the Perugia 2010 tune [156]) both with and without MPI to understand the impact of this on the jet profile. For softer jets there is a larger disparity between the two PYTHIA predictions, indicating that MPI are important for obtaining the jet shape at low transverse momenta. That MPI affect the shape of softer jets is not surprising: it is rare to have more than one hard process so MPI are intrinsically soft [155]. Further, in an interleaved shower the phase space available for MPI is shared with initial state radiation (both modify the amount of energy available in the beam remnant [68]) and thus MPI modify the jet shape. The predictions of HEJ+ARIADNE are consistent with the PYTHIA prediction without MPI, so in this region we can interpret the difference with data

as arising from a lack of MPI. For harder jets however, the impact from MPI is smaller, but HEJ+ARIADNE is no longer consistent with PYTHIA.

The discrepancy in the profiles of high transverse momentum jets is linked to the shower ordering. The method for matching HEJ to a parton shower presented in section 2.5 correctly prevents double counting of soft emissions; however some HEJ events contain certain soft emissions that in a parton shower (due to ordering) would be included only at a late stage in evolution, typically after collinear emissions. In such events, the phase space for a full parton shower evolution is restricted.

One solution to this problem is to weight events by the probability the parton shower might have produced that event; improbable configurations which might interfere with normal shower ordering would be suppressed by small weights. Such a weight could be computed in a manner similar to the CKKW-L merging method of section 2.2, that is, by constructing a parton shower history, performing a trial shower, and vetoing events where trial emissions are above a given scale. The downside of this method is that certain hard configurations that are possible in the parton shower but not in HEJ can be missed. However, as we discuss in the next section, it is possible to adjust the method in such a way that these configurations can be inserted by the parton shower.

In this chapter we present the implementation, validation and results for such a procedure for combining HEJ with a parton shower for inclusive multi-jet production. We have chosen PYTHIA 8 for the parton shower; this has the advantage that it includes the interleaving of MPI, so these effects (which are important for jet shapes) may also be included with relative ease.

5.1   Overview of Method

In this section we explain the method for merging HEJ with a parton shower in greater detail; the algorithm will be detailed in full in section 5.1.3. As mentioned above, the primary feature which distinguishes this method from that discussed in section 2.5 is the construction of a parton shower history, and the performing of a trial shower which is equivalent to computing the relevant Sudakov factors. In this

respect the method is very similar to CKKW-L discussed in section 2.2. Indeed much of the technology used in the implementation of CKKW-L in PYTHIA can be recycled, an additional benefit to choosing PYTHIA for the implementation of our algorithm. However, as we are promoting CKKW-L from a tree-level merging method to an all order merging method, there are a number of important differences from CKKW-L that we now elucidate.

The first difference concerns the trial shower. Normally the procedure of generating trial emissions from each intermediate state, and vetoing events when the trial emission is above the reconstructed scale of the next state, is equivalent to weighting with events Sudakov factors (as discussed in section 2.2). For merging with HEJ, we wish to perform the equivalent of weighting with modified Sudakov factors with subtracted splitting kernels (just as in HEJ+ARIADNE the shower was evolved with subtracted Sudakov factors). To do this, we veto the trial emissions with a probability given by the ratio of HEJ and PYTHIA splitting functions (as discussed in sections 2.5 and 3.2; also see the discussion in section 5.1.2), with the trial shower continuing from the emission scale if the emission is vetoed. Additionally in CKKW-L the event is vetoed if the first parton shower emission is above the merging scale; this is equivalent to constructing the Sudakov factor $\Delta(t_n, t_{ms})$. Therefore, the above procedure for vetoing trial emissions must also be used when testing the first emission of the parton shower (for multiplicities below the maximum multiplicity).

In addition, so that the trial shower produces the correct Sudakov factor, the selected path in the parton shower history should be an *allowed* path, namely each intermediate state should correspond to a HEJ state (defined in section 5.1.1). In addition, as with regular CKKW-L, the path should preferentially also be ordered. If such a path does not exist, allowed paths are prioritised over ordered paths. If no allowed path exists, an ordered path is selected. The weight assigned to the path is given by the HEJ matrix element squared for the maximally clustered HEJ state in the path, multiplied by the product of PYTHIA splitting functions for each (allowed) clustering in the path. A path is then selected according to its relative weight. This information is summarised in fig. 5.2.

151

Finally, events are no longer vetoed when a trial emission that is not rejected is above the next reconstructed scale. Instead, when a trial emission is not vetoed, the resulting configuration replaces the hard event and is immediately passed to the shower for subsequent evolution. This allows the insertion of hard configurations which could not have been generated by HEJ. In the implementation of CKKW-L for PYTHIA, such a scenario would only have resulted from the generation of MPI, as these are the only configurations which could not have been generated in the hard process event samples.

5.1.1 Definition of HEJ States

For each trial emission it is necessary to identify whether the resulting event corresponds to a configuration which could have been produced by HEJ, namely a *HEJ state*. For the purposes of merging the following requirements must be met in order for the event to be considered a HEJ state:

1. The most forwards outgoing parton should have the same flavour as the parton incoming along the positive z axis.

2. The most backwards outgoing parton should have the same flavour as the parton incoming along the negative z axis.

3. All other outgoing partons must be gluons.

4. It must be possible to untangle the colour connections into two 'ladders' of rapidity-ordered partons.

5. The outgoing partons must cluster into at least two jets.

6. Each extremal (most forwards or backwards) parton must be a member of the corresponding extremal jet.

7. Each parton must have a transverse momentum above the merging scale t_{ms}.

The fourth requirement needs some further explanation. If we take a $2 \rightarrow n$ partonic state, it should always be possible to untangle the colour connections into
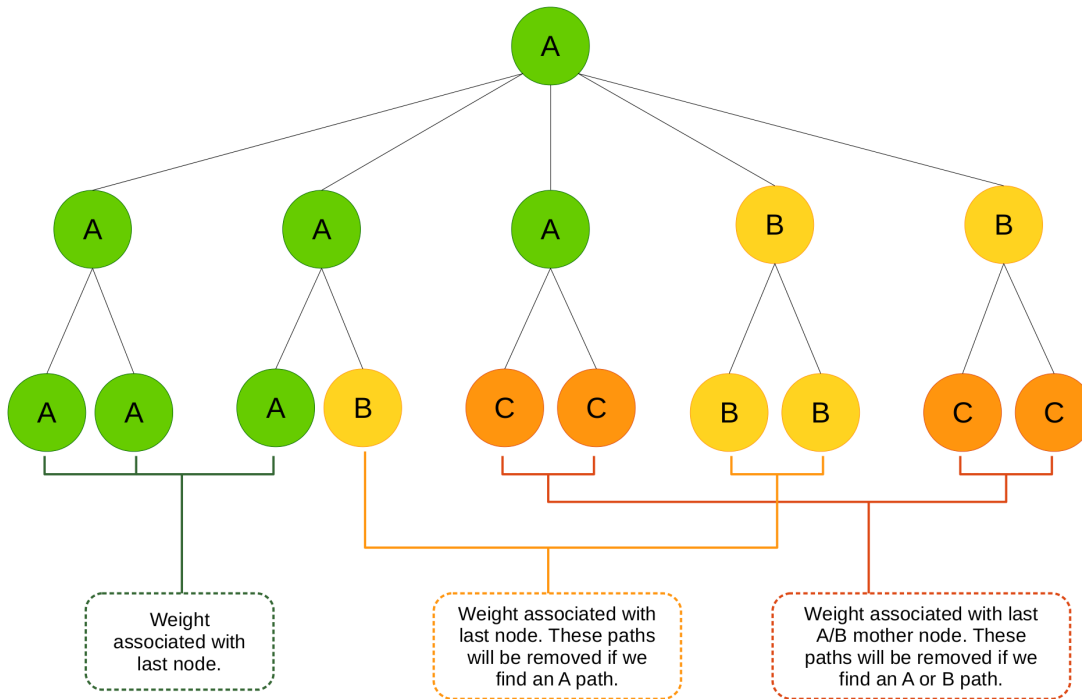
Figure 5.2: Schematic representation of how paths in the full history may be constructed. Circles denote intermediate states; states on the same horizontal level have the same multiplicity, with states in the bottom level having the lowest multiplicity. State which are connected with lines to one of higher multiplicity are the available child states obtained by clustering. States labelled 'A' are both allowed and ordered. States labelled 'B' are allowed, but not ordered. States labelled 'C' are not allowed, but may be ordered. Branches which terminate on 'A' are allowed, ordered, complete paths. Branches which terminate on 'B' are allowed complete paths. Branches which terminate on 'C' include, but are not limited to, ordered complete paths. Incomplete paths are not shown. In this example, there are three allowed, ordered, complete paths; only these would be retained, and the others would be discarded.
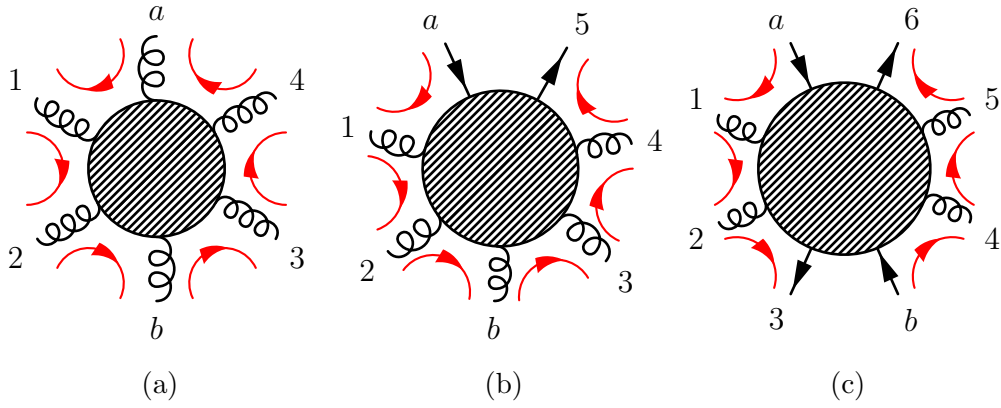
5.1. Overview of Method

Figure 5.3: Examples of some possible colour flows in (a) $gg \to gggg$, (b) $qg \to qgggg$ and (c) $qQ \to qggggQ$, each of which would give rise to colour chains of the same length. The labelling of legs corresponds to their rapidity ordering in the intial or final state.

a planar arrangement, for example as shown in fig. 5.3. It should be clear that inserting a quark into the initial and final state is equivalent to swapping a gluon for an outgoing $q\bar{q}$ pair.

If we start on the colour index of an incoming quark or gluon, or the anti-colour index of an outgoing antiquark, and follow the colour flow until we hit either an incoming gluon, or outgoing quark or incoming antiquark, we will obtain a set of colour connected partons, which we call a 'colour chain'. Since quarks (or antiquarks) only have one colour index, we should always obtain exactly two colour chains for HEJ states, provided we stop if we hit an incoming gluon. (For example, in fig. 5.3b the colour chains obtained would be $a12b$ and $b34a$.) It is then always possible to arrange the colour flow into two non-crossing 'ladders', with incoming legs vertical, and outgoing legs horizonal forming the rungs of the ladder; such as shown in fig. 5.4.

As in the matching of HEJ and ARIADNE, all events passed to PYTHIA in Les Houches format have colour connections that correspond to rapidity-ordered ladders since these are the configurations that dominate in the MRK limit. Since the colour connections are important for setting up the dipoles in the PYTHIA parton shower, having two non-crossing ladders of rapidity-ordered partons is stipulated as a requirement for a HEJ state.
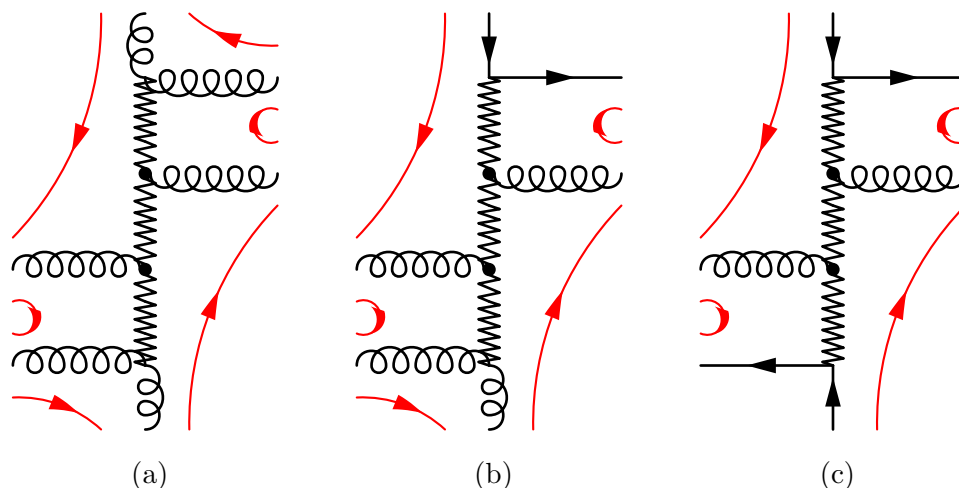
Figure 5.4: Examples of how colour connected partons may be arranged into 'ladders' for the initial states (a) gg, (b) qg and (c) qQ. Incoming legs are shown vertically, and outgoing legs are horizontal.

Before concluding this section, we note that although in principle there is no maximum multiplicity N for FKL events produced in HEJ, since various aspects of the algorithm are computationally intensive (such as the construction of the parton shower history) we set $N = 6$. The multiplicity in HEJ is first reduced by redistributing all soft momenta below a given scale - it is natural to take this to be the merging scale t_{ms}. This is done in such a way that the rapidities of the hard jet-like objects are fixed, using the same prescription applied in FKL matching in eq. (2.4.73).

If the events passed to PYTHIA still have a multiplicity greater than N, clustering is performed sequentially until the multiplicity is reduced to N. The clusterings performed are those considered to be most likely according to the parton shower (that is, that corresponding to maximal value of the splitting functions) provided this still gives rise to a HEJ states. Although the necessity to perform this 'pre-clustering' is potentially a limiting factor for the algorithm in its current formulation, we do not find it has a large impact upon the merging.

5.1.2 Evaluation of Subtracted Sudakov Factors

As in the matching for HEJ+ARIADNE we wish to use a modified Sudakov factor with subtracted kernel to generate trial emissions, which for the case of a timelike branching is given by:

$$\tilde{\Delta}(Q^2, q^2) = \exp\left\{ -\int_{q^2}^{Q^2} dk_T^2 \int_{Q_0^2/k_T^2}^{1-Q_0^2/k_T^2} dz \left(P_{\text{PYTHIA}}(k_T^2, z) - P_{\text{HEJ}}(k_T^2, z) \right) \right\}. \tag{5.1.1}$$

The PYTHIA splitting function is given by:

$$P_{\text{PYTHIA}}(k_T^2, z) = \frac{\alpha_s}{(2\pi)^2} \frac{1}{k_T^2} P_{ji}(z) , \tag{5.1.2}$$

where P_{ji} simply the standard Altarelli-Parisi splitting functions of table 2.1. There is an additional factor of $1/(2\pi)$ to average over azimuthal angle. The HEJ splitting function is given by:

$$P_{HEJ} = \frac{1}{2} \frac{1}{16\pi^2} \frac{|\mathcal{M}_{n+1}^{\text{HEJ}}|^2}{|\mathcal{M}_n^{\text{HEJ}}|^2} . \tag{5.1.3}$$

The factor of $\frac{1}{2}$ accounts for the fact that the matrix elements are summed over all possible colour connections, but for each parton shower emission we wish to calculate the splitting function for one of two possible choices (each of which contribute equally in the MRK limit). The modified Sudakov factor in eq. (5.1.1) may be evaluated by applying the Sudakov veto method from section 3.2 and vetoing trial emission with probability $\mathcal{P}_{\text{veto}} = P_{HEJ}/P_{\text{PYTHIA}}$.

To account for spacelike branchings which result in the momentum fractions of the initial state partons being modified, a ratio of PDFs must be included in the Sudakov factor, as in eq. (2.1.5). A spacelike branching $(i \to jk)$ at scale k^2 that results in the momentum fraction x_1 of parton j being reduced to $x_2 = z\, x_1$ can be accounted for by making the replacement:

$$P_{ji}(z) \to P_{ji}(z) \frac{x_1 f_j(x_1, k^2)}{x_2 f_i(x_2, k^2)} . \tag{5.1.4}$$

Similarly, to obtain the appropriate HEJ splitting function, we make the replacement:

$$P_{HEJ} \to \frac{1}{2} \frac{1}{16\pi^2} \frac{|\mathcal{M}_{n+1}^{\text{HEJ}}|^2}{|\mathcal{M}_n^{\text{HEJ}}|^2} \frac{x_1 f_j(x_1, \mu_F^2)}{x_2 f_i(x_2, \mu_F^2)} . \tag{5.1.5}$$

The PDFs and factorisation scale choice used in this expression should be those used in HEJ, and not necessarily constrained to be the same as those used in the parton shower.

5.1.3 The Merging Algorithm

The full algorithm for merging HEJ with PYTHIA proceeds as follows:

1. Generate samples of $n(< N)$-parton HEJ states. Introduce a merging scale, t_{ms}, based on the minimum transverse momentum of the partons.

2. For each n-parton state from HEJ ($2 < n \leq N$), reconstruct all possible PYTHIA shower histories where each clustering has the reconstructed scale t_i, and set $t_{n+1} = t_{ms}$. If $n = 2$ calculate the scale t_2 and continue to step 3, and otherwise continue as follows.

   (a) Throw away all histories that do not correspond to a sequence of HEJ states.

   (b) If there is at least one history that is correctly ordered in t_i, throw away every other history.

   (c) Give each history that is left a weight proportional to the HEJ matrix element squared for the lowest multiplicity (HEJ) state, times the product of PYTHIA splitting functions for the sequence of emissions that gives the original n-parton state. Pick a history at random according to its relative weight.

   (d) Starting from the most clustered state in the history, make a trial emission from each intermediate state in the selected history starting from t_i.

       i. If the emission scale is below the reconstructed scale of the next state in the history, t_{i+1} , continue to the next state in the history. If this is the original event we started with, continue to step 3.

       ii. If the emission scale is above the reconstructed scale of the next state in the history, but has produced a HEJ state, veto the emission

with probability $P_{\text{HEJ}}/P_{\text{PYTHIA}}$. If the emission is vetoed, generate a new trial emission starting from the current emission scale, and return to 2(d)i. If the emission is not vetoed replace the original event with this state and continue to step 3.

iii. If the emission scale is above the reconstructed scale and has not produced a HEJ state, we substitute the original event with this state and continue to step 3.

3. (a) If in the previous step we replaced the original event with one that could not have been produced by HEJ, continue the shower from the emission scale of the new state without restriction.

(b) If this is the original event and we have $n \leq N$ start the shower from the reconstructed scale t_n and check the first emission. If it gives a new HEJ state, discard the emission with probability $P_{\text{HEJ}}/P_{\text{PYTHIA}}$ and continue generating the first emission starting from the scale t_n. Once a first emission is accepted, the shower continues radiating freely.

(c) If $n = N$, let the shower radiate freely.

The method we are presenting should be viewed as a first attempt to combine HEJ with a parton shower using merging, and further refinements may be required. For completeness we mention two potential issues here.

One limitation of the proposed method is that only the hardest emissions (as ordered by PYTHIA) are correctly described by HEJ, which is not itself ordered in hardness. In principle it is possible to generate a HEJ state from a non-HEJ state above the merging scale in the parton shower, and such configurations will not have their splitting kernels subtracted. However, it is assumed that once an emission has been performed in the shower domain, this changes the phase space sufficiently that the HEJ matrix elements are no longer accurate.

In addition, it should be noted that the method we are presenting is currently only applicable to FKL configurations. To include non-FKL configurations, it would be necessary to extend the definition of what constitutes a HEJ state, and ensure that the appropriate tree-level matrix elements are used when calculating

the veto probability for non-FKL states. This is so that no problems arise from double counting. Primarily such changes would affect what states may be included in the parton shower history, and which states may be inserted by the parton shower.

5.2 Validation

5.2.1 Calculation of Splitting Functions

A crucial aspect of the merging algorithm is the vetoing of trial emissions that result in HEJ states with a probability given by the ratio of the HEJ to PYTHIA splitting functions. In this section we validate the evaluation of the respective splitting functions. This is done by generating samples of $2 \to 2$ events with HEJ, and calculating the splitting functions for the first trial emission in the parton shower (providing that this gives rise to a HEJ state)[1]. Where the trial emission resulted in initial state recoil and ratios of PDFs were used, these factors were removed for a direct comparison of the splitting functions themselves. For the same reason, due to potentially different scale choices for μ_R and conventions for the running of α_s in HEJ and PYTHIA, these factors were also removed in the comparison. In what follows, we present results for the hard process $qQ \to qQ$; equivalent tests were performed for gg and qg initial states and similar conclusions were drawn.

In fig. 5.5 we show the average splitting function $\langle P \rangle$ (defined for PYTHIA and HEJ in eqs. (5.1.2) and (5.1.3) respectively) as a function of the transverse momentum of the trial emission, with the additional requirement that the angular separation of the emission from the nearest parton ΔR exceeds the jet radius ($R = 0.6$), namely it is a wide-angle emission. We compare the average splitting function for HEJ and PYTHIA with the MRK limit of $C_A/(2\pi k_\perp^2)$. There are numerous observations that we can make. Firstly, HEJ is very close to the MRK

---

[1]Validation of the classification of states into HEJ and non-HEJ was performed separately on known samples of FKL and non-FKL events.
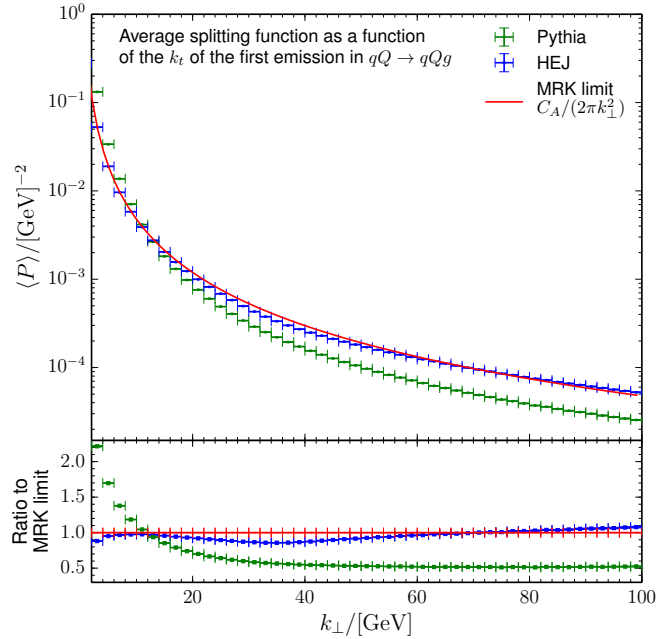
Figure 5.5: Average splitting function for $qQ \to qgQ$ as a function of the transverse momentum of the emission, where $\Delta R_{min} > 0.6$.

limit (with differences arising from contributions with finite rapidity separations). PYTHIA asymptotically behaves as $1/k_\perp^2$, with the constant of proportionality coming from integrating the Altarelli-Parisi splitting functions over the energy fraction z. Further, we see that the average HEJ splitting function is greater than that for PYTHIA for $k_\perp \gtrsim 10$ GeV, indicating that all but the softest wide-angle emissions will be accounted for by HEJ, and will be vetoed in the PYTHIA parton shower. This is in line with our intuition that HEJ should properly account for wide-angle emissions.

In fig. 5.6 we show the average splitting function as a function of the angular distance between the emission and the nearest parton, ΔR, for emissions having a transverse momentum greater than 10 GeV. The discontinuity in the average HEJ splitting function at the jet radius is due to the fact that a different (regulated) matrix element is used for emissions which are inside the jet cone. As before, qualitatively we see that for (semi-hard) wide-angle emissions the HEJ splitting function always exceeds that for PYTHIA, namely such emissions will always be vetoed in the parton shower. However, inside the jet cone, the splitting function
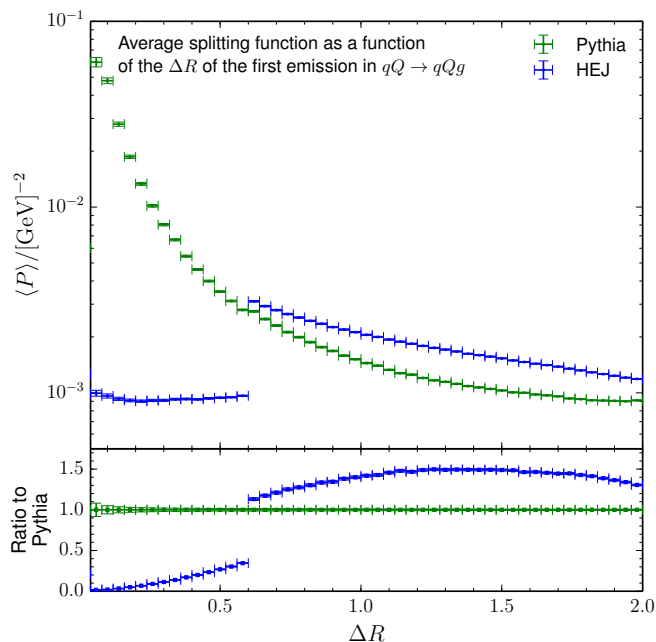
Figure 5.6: Average splitting function for $qQ \to qgQ$ as a function of the angular distance between the emission and the nearest parton ΔR, where $k_{T\min} > 10$ GeV.

for PYTHIA exceeds that for HEJ, thus there is a very low probability that such emissions will be vetoed. Again, this is in line with the expectation that collinear emissions should be handled by the parton shower.

5.2.2   Validation of Algorithm

In this section the validation of the merging procedure is discussed. Firstly, samples of 'fake HEJ' events containing two and three parton final states were produced using the following method.

1. Generate $2 \to 2$ hard QCD events with PYTHIA. Veto all events which do not correspond to HEJ states.

2. Start the parton shower as usual, but test the first emission.

   (a) If the resulting three parton state corresponds to a HEJ state and the scale of the shower is above the merging scale t_{ms}, accept the emission and stop the parton shower.

(b) Otherwise, veto the emission and generate a new first emission, starting from the scale of the previous trial emission. Stop the shower as soon as a three parton HEJ state is generated, or the scale falls below t_{ms}.

These 'fake HEJ' event samples are then merged using the algorithm detailed in section 5.1.3, but with a couple of modifications. Firstly, the maximum multiplicity N is now three. Secondly since the events were generated using PYTHIA, the ratio of splitting functions should always return unity; thus if a trial parton shower emission from a two parton hard event gives rise to a new HEJ state, this will always be vetoed.

The procedure for merging 'fake HEJ' events should give identical results to the case where we simply showered the subset of PYTHIA events that correspond to HEJ states directly. Therefore by comparing these two schemes we can ensure that the merging algorithm runs as anticipated and in particular that there is no double-counting of emissions. Events from each prescription were required to contain at least two jets, defined using the anti-k_T algorithm, each passing the following cuts:

$$p_{Tj} > 30 \text{ GeV}, \qquad \Delta R = 0.6, \qquad |\Delta y_j| < 4.4. \qquad (5.2.1)$$

The centre of mass energy used was $\sqrt{s} = 7$ TeV. The merging scale was taken as $t_{ms} = 20$ GeV. In addition two different prescriptions for selecting a path in the parton shower history were tested. Usually the path (which in this procedure only corresponds to single choice of clustering) is selected at random with a probability according to its relative weight, calculated using full shower splitting kernels including PDFs and potentially matrix element corrections. However, it is possible to override this behaviour and assign the weight according to the shower kernel divided by the transverse momentum scale of the clustering. The procedure for selecting a parton shower history should only correspond to a subleading logarithmic effect. Thus we do not expect to see significant differences between the two schemes.

In figs. 5.7a and 5.7b we show the differential cross section as a function of the transverse momentum of hardest and second hardest jets respectively. We compare the results of showering gg initial state HEJ events generated with PYTHIA that
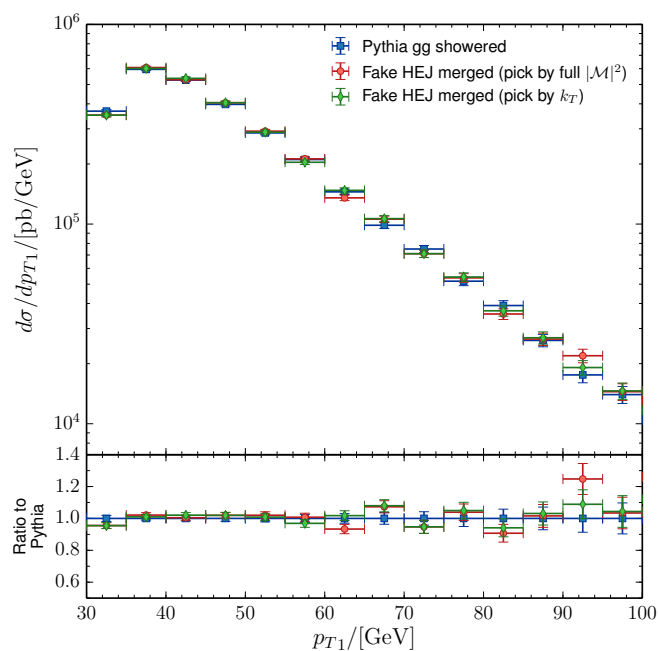
(a)
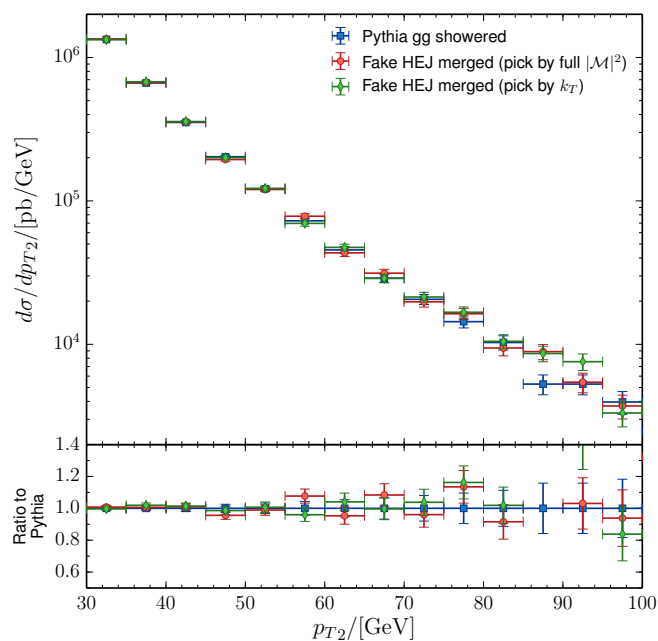
(b)

Figure 5.7: Plots showing the differential cross section as a function of the transverse momentum of hardest and second hardest jets, in which a comparison is made between a default showering of gg HEJ-like events in PYTHIA, and 'fake HEJ' events which have been merged using two different prescriptions for the construction of the parton shower history.

are showered directly, and samples of gg initial state 'fake HEJ' events merged using the method described above for the two different aforementioned procedures for selecting the parton shower history. There are no statistically significant differences between all three predictions in each distribution. The same tests were also performed for qg and qQ initial states.

The primary difference between the prescription for merging 'fake HEJ' events and the full algorithm is the evaluation of the ratio splitting functions, which has been validated independently. Since the extension to the full case is straightforward, this completes the necessary validation of our implementation.

5.3 Results

One of the goals for the implementation of this new method was to improve the description of jet shapes upon that predicted by HEJ+Ariadne. We therefore considered two observables from a study of inclusive jet production at the LHC with $\sqrt{s} = 7$ TeV performed by ATLAS [157]. The first is the jet profile $\rho(r)$ defined in eq. (5.0.1). The second is the integrated jet shape $\Psi(r)$ which gives the fraction of the jet transverse momentum that lies inside a cone of radius r:

$$\Psi(r) = \frac{p_\perp(r)}{p_\perp(R)} . \qquad (5.3.2)$$

Both observables are averaged over all jets in an event. We show results for Pythia 8 and HEJ+Pythia in fig. 5.8. Both predictions were fully showered with interleaved MPI and hadronised. In the shower and in the generation of HEJ events, the PDF set used was CT14nlo [154, 158]. All other parameters in Pythia were taken as their default values for the Monash 2013 tune [159]. The scale choice used in HEJ was $\mu = H_T/2$.

Not only is HEJ+Pythia completely consistent with the standalone predictions for Pythia, but both have excellent agreement with data across a range of transverse momentum slices. We emphasise that since jets in HEJ typically contain very few partons the ability to describe this observable is entirely coming from the parton shower and hadronisation. We found that in order to obtain agreement with data the inclusion of both MPI and hadronisation is necessary, indicating
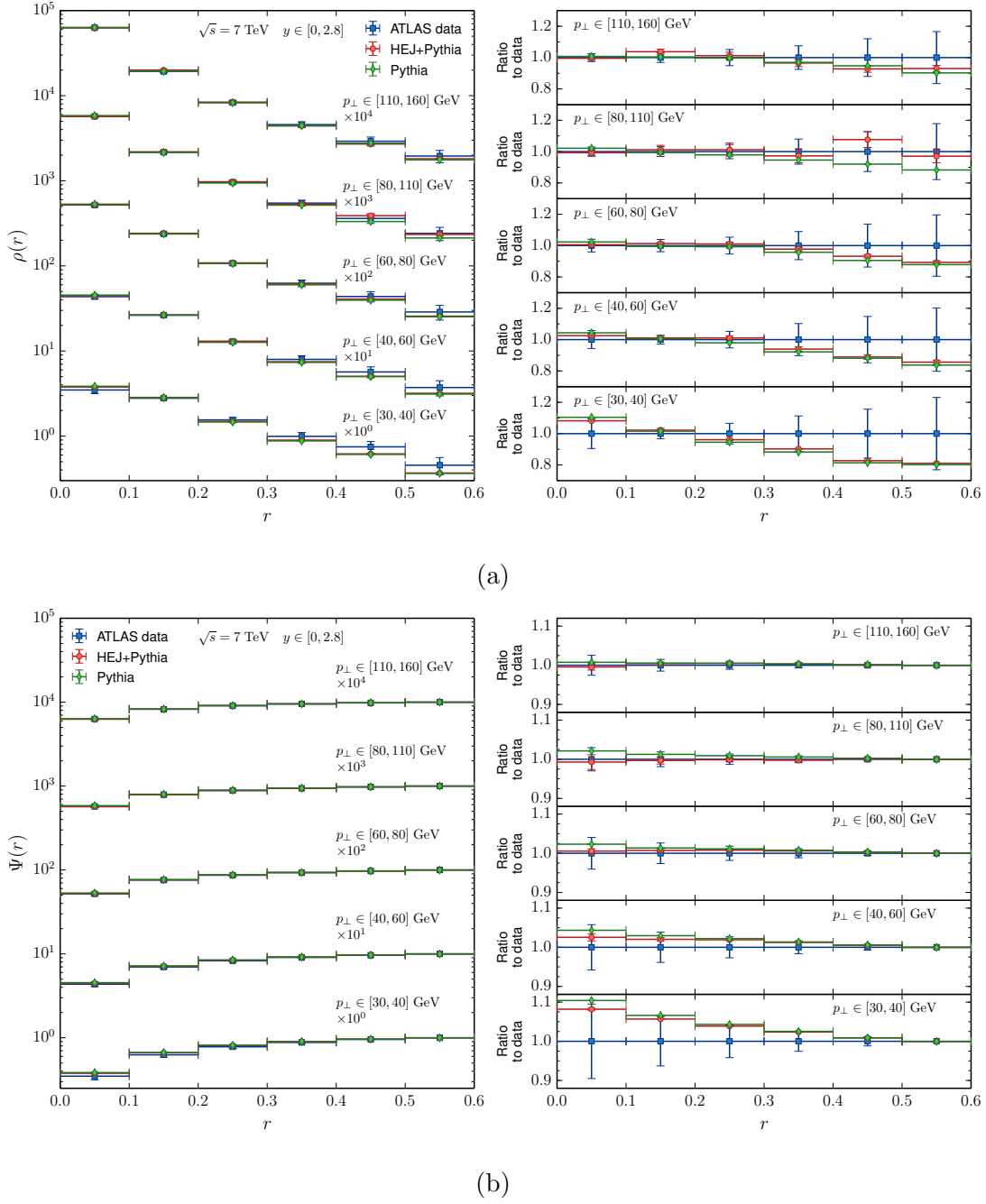
(a)

(b)

Figure 5.8: Plots showing a comparison PYTHIA and HEJ+PYTHIA to ATLAS data for the jet shape observables (a) $\rho(r)$ and (b) $\psi(r)$ for different slices of jet transverse momentum.

.

the importance of full particle level simulation for such observables. Unlike the approach of HEJ+Ariadne, these effects have been added to HEJ in such a way that shower evolution has not been artificially restricted.

In order to assess the performance of our merging algorithm we considered two analyses [138, 140] for inclusive dijet production at the LHC with $\sqrt{s} = 7$ TeV which measured the amount and impact of additional radiation, therefore implicitly probing higher order effects. In the results which follow, the PDF set, scale choices and tune were chosen as for the above study of jet shapes. We compare predictions for HEJ, Pythia, and HEJ+Pythia. The error bars on theoretical predictions correspond to statistical uncertainties; we have not included an estimate of scale uncertainties here. We defer a systematic investigation on the size of such uncertainties to future studies.

In the first analysis, which we discussed earlier in section 2.5, the hardest and second hardest jets were required to have $p_T > 60$ GeV and $p_T > 50$ GeV respectively; these were taken to be the tagging jets. Events containing no jets with transverse momentum above the veto scale Q_0 in the rapidity interval between the tagging jets were classified as *gap events*. The veto scale was taken to be $Q_0 = 20$ GeV and $Q_0 = 30$ GeV for data collected during 2010 and 2011 respectively. We define the contribution to cross section from such gap events as $\sigma_{jj}(Q_0)$. The *gap fraction* $f(Q_0)$ is then defined as:

$$f(Q_0) = \frac{\sigma_{jj}(Q_0)}{\sigma_{jj}} \, , \tag{5.3.3}$$

where σ_{jj} is the inclusive dijet cross section.

In fig. 5.9 we show (a) the average number of jets $\overline{N_j}$ in the rapidity interval between the tagging jets, and (b) the gap fraction as a function of the rapidity separation between the hardest two jets $|\Delta y|$. HEJ underestimates the number of jets across the spectrum of rapidities; as already mentioned in section 2.5 this is because the disparity between the minimum p_T cut for gap jets and for the hardest two jets induces a transverse momentum hierarchy that spoils the validity of the MRK limit even for large rapidities. HEJ performs slightly better for the more inclusive gap fraction observable, though it still has a tendency to overestimate the number of gap events. The are systematic shape differences between data and
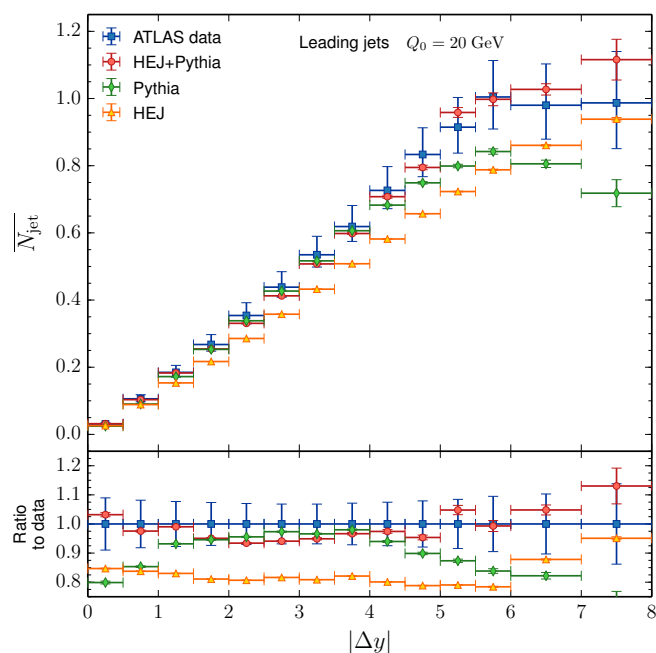
(a)
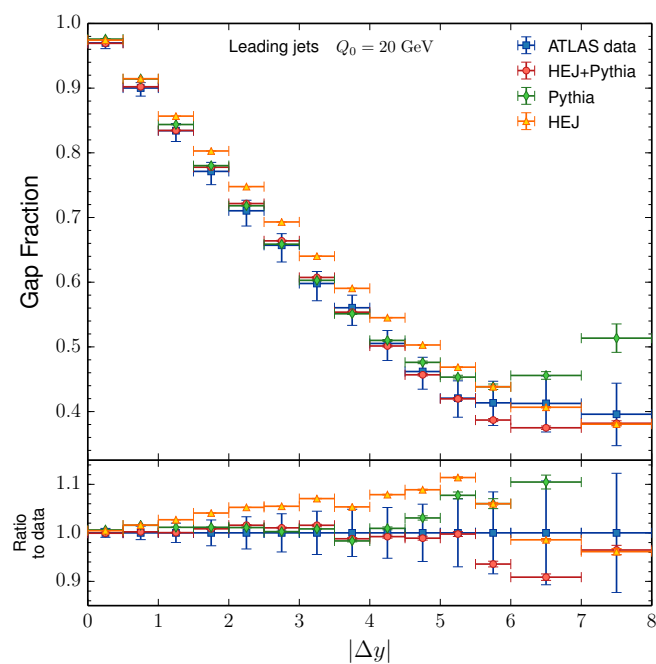
(b)

Figure 5.9: Plots showing a comparison of HEJ, PYTHIA and HEJ+PYTHIA to ATLAS data for (a) the average number of jets in the rapidity interval between the two hardest jets and (b) the gap fraction as a function of the size of the rapidity interval between the two hardest jets.

167

the predictions for PYTHIA, which appear to underestimate the number of jets at low and high rapidities. Similarly the fraction of events with no additional jets at large rapidities is overestimated by PYTHIA. Despite neither HEJ nor PYTHIA being able to fully describe these observables, the merging of HEJ+PYTHIA gives a close agreement with data across the entire range of rapidities. This is a positive indication that the merging algorithm is functioning properly, combining the necessary high energy and soft collinear logarithms in its description.

In fig. 5.10 we look at the ratio of the averages of the second to first moment of azimuthal decorrelation, $\langle\cos(2\Delta\phi)\rangle/\langle\cos(\pi-\Delta\phi)\rangle$, as a function of (a) $|\Delta y|$ and (b) the average transverse momentum of the tagging jets, $\overline{p_T}$. As previously discussed in section 2.5, this variable is a measure of the how correlated (or back-to-back) are the jets, with some cancellation of systematic uncertainties between the numerator and denominator. HEJ generally overestimates the correlation of the jets, particularly at low rapidities and small transverse momenta; this is due to missing radiation included by the parton shower. PYTHIA gives a good description of the azimuthal correlation for both observables, perhaps with the exception of large rapidities, where it is likely to underestimate the number of hard jets.

In the second analysis the tagging jets were required to have an average transverse momentum $\overline{p_T}$ of at least 50 GeV; additional jets were required to have a transverse momentum $p_T > 20$ GeV. Jets were defined using the anti-k_T algorithm with $R = 0.6$, and were required to have rapidity $|y_j| < 4.4$. In fig. 5.11 the tagging jets were again taken to be the two hardest jets; two observables are shown as a function of $\overline{p_T}$ in different slices of the tagging jets' rapidity separation. Figure 5.11a shows the average number of jets in the rapidity interval between the tagging jets, while fig. 5.11b shows the gap fraction. The predictions for HEJ systematically underestimate the number of jets at large transverse momenta, and systematically overestimate the gap fraction in the same region. PYTHIA performs well for the entire range of transverse momenta, and across the different rapidity slices. The disparity between HEJ and PYTHIA in this observable emphasises the need for a parton shower. The predictions for HEJ+PYTHIA are again consistent with both PYTHIA and data within statistical uncertainties, indicating that parton shower
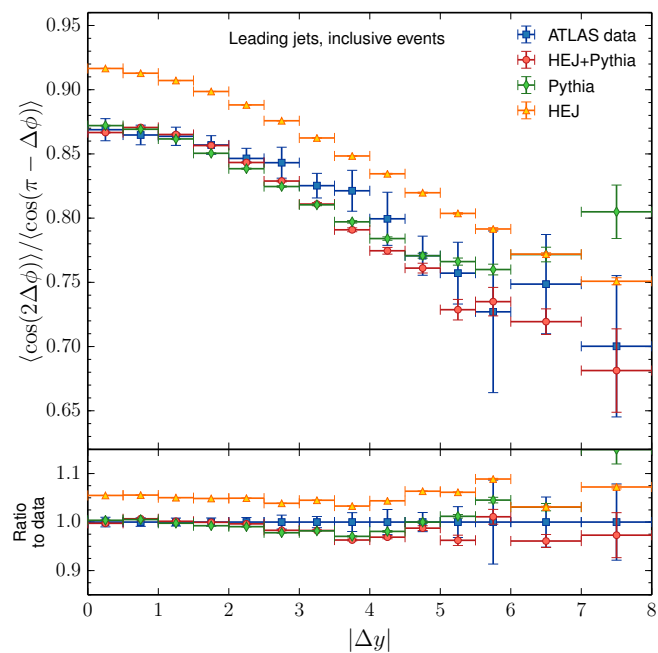
(a)
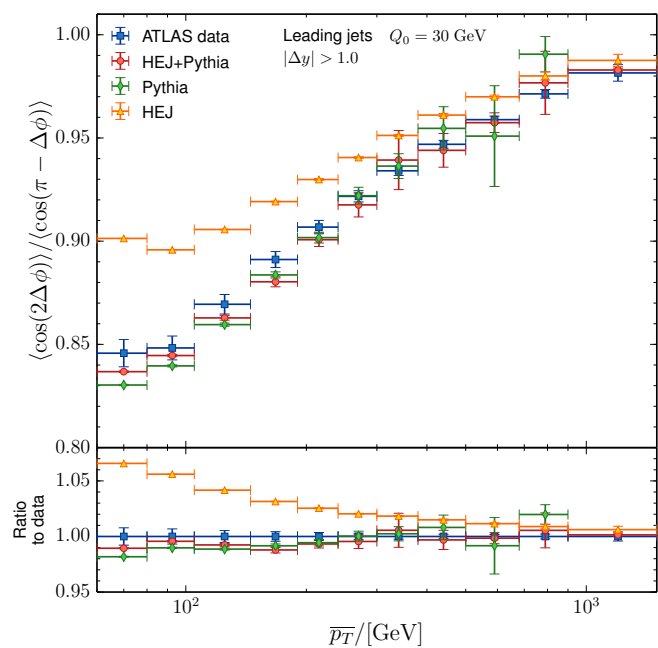
(b)

Figure 5.10: Plots showing a comparison of HEJ, PYTHIA and HEJ+PYTHIA to ATLAS data for the ratio of the average of the second and first moment of azimuthal decorrelation, $\langle\cos(2\Delta\phi)\rangle/\langle\cos(\pi - \Delta\phi)\rangle$, as a function of (a) $|\Delta y|$ and (b) $\overline{p_T}$.
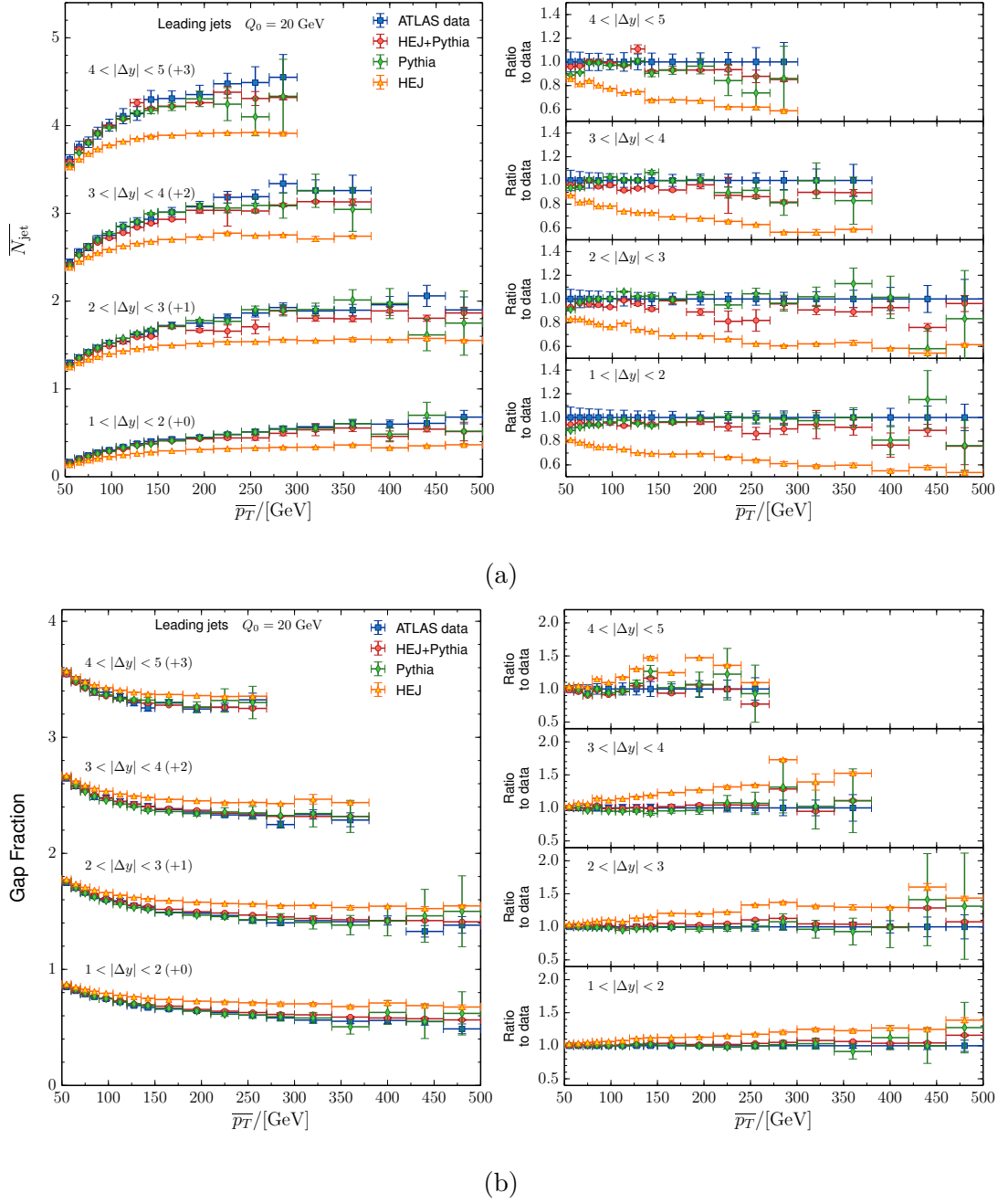
(a)

(b)

Figure 5.11: Plots showing a comparison HEJ, PYTHIA and HEJ+PYTHIA to ATLAS data for (a) the average number of jets in the rapidity interval between the two hardest jets and (b) the gap fraction as a function of the average transverse momentum of the two hardest jets, in slices of their rapidity separation.

effects have been successfully incorporated into HEJ.

Since neither of the previous two analyses adequately explore the phase space in which high energy logarithms become dominant, we performed a study of dijet production at $\sqrt{s} = 7$ TeV using the more inclusive cuts of [139]. Specifically, this required at least one jet with a transverse momentum $p_T > 45$ GeV and with all other jets having a transverse momentum $p_T > 35$ GeV. Jets were again defined using the anti-k_T algorithm, but with $R = 0.5$, and were required to have rapidity $|y_j| < 4.7$.

In fig. 5.12a we show the average number of jets as a function of the rapidity separation between the most forwards and backwards jets, Δy_{fb}. We can make numerous observations. Firstly, discrepancies between all three theoretical predictions are much more visible. For large rapidities, HEJ predicts an average number of jets that exceeds three, signifying that there is a non-trivial contribution from jet multiplicities of four or higher. This is precisely as one would expect from high energy logarithms becoming dominant. PYTHIA predicts far fewer jets at large rapidities, which is unsurprising since additional jets can only arise from the parton shower, which despite including higher order effects does not account for high energy logarithms. Until about 5 units of rapidity, there is fairly good agreement between HEJ and HEJ+PYTHIA. However, HEJ+PYTHIA predicts slightly fewer jets at large rapidities.

In fig. 5.12b we show the ratio of the inclusive three-jet cross section to the inclusive dijet cross section also as a function of Δy_{fb}. There is now good agreement between HEJ and HEJ+PYTHIA at large rapidities. This suggests the differences in fig. 5.12a correspond to multiplicities greater than three. The origin in the reduction of higher multiplicities in HEJ+PYTHIA is not yet completely understood. One possible explanation is that the parton shower induces a smearing such that fewer jets pass the necessary criterion. Alternatively it could be accounted for by the insertion of non-FKL configurations of lower multiplicity. This issue could be resolved by the extension of this method to merge non-FKL events. Refinements of the method may indeed be necessary, although without a comparison to data however, it is difficult to determine what is the correct prescription. We hope that
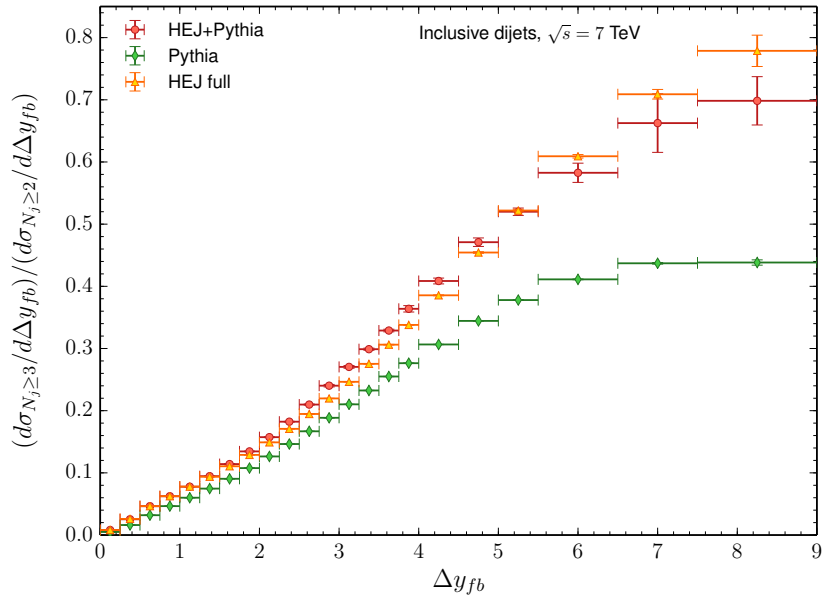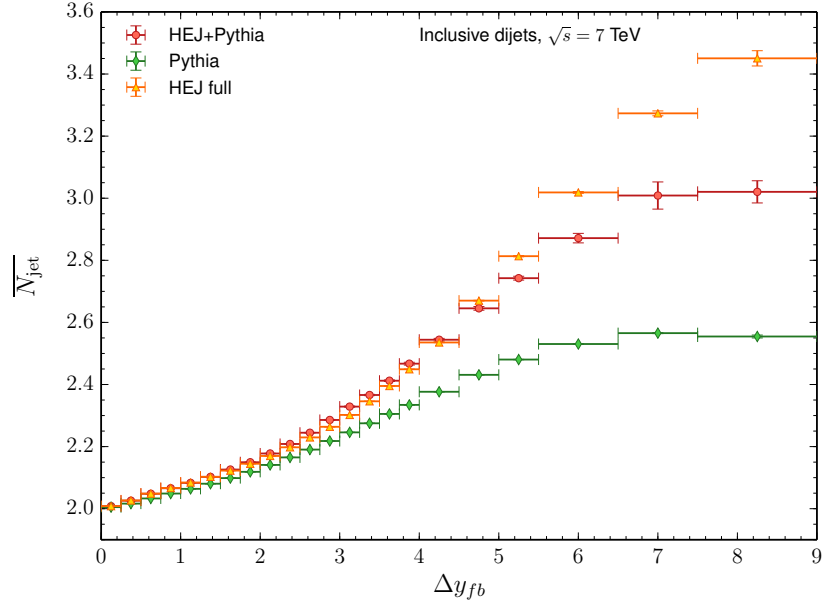
(a)

(b)

Figure 5.12: Plots showing a comparison HEJ, PYTHIA and HEJ+PYTHIA for (a) the average number of jets and (b) the ratio of the inclusive three jet cross section to the inclusive dijet cross section, both as a function of the rapidity separation of the most forwards and backwards jets.

an experimental study with similarly inclusive cuts will be conducted in future.

Notwithstanding the differences in the average number of jets between HEJ and HEJ+PYTHIA at large rapidities, this study indicates that additional hard jets are indeed being added to PYTHIA with this merging algorithm. The previous analyses explored indicated that this procedure also preserves the impact of the parton shower, MPI and hadronisation. We have therefore successfully combined effects corresponding to both high energy and soft collinear logarithms.

5.4   Summary and Outlook

In this chapter we have introduced a new CKKW-L-inspired merging algorithm for combining HEJ with a parton shower. For the first time HEJ events have been fully evolved down to particle level using a modern parton shower with effects such as MPI properly accounted for. This has resulted in the ability to correctly describe distributions of jet shapes. This method therefore ameliorates some of the limitations of the earlier method used to match HEJ with ARIADNE.

We assessed the performance of the algorithm by considering observables which measure the additional radiation in the rapidity interval between two tagging jets. In observables which require a parton shower, such as the average number of jets as a function of the average transverse momentum of the tagging jets, the description of HEJ+PYTHIA was consistent with standalone PYTHIA and data. The improvement upon HEJ in such distributions is notable. For the average number of jets as a function of the rapidity separation of the tagging jets, where a p_T hierarchy is induced by the disparity of cuts on jet transverse momentum, both high energy and soft-collinear logarithms become important. Though neither HEJ nor PYTHIA could fully describe the data, HEJ+PYTHIA was consistent with data. Furthermore, an investigation of related observables but with more inclusive cuts revealed the jet multiplicity for large rapidity intervals is increased relative to PYTHIA through merging. These results demonstrate that we have combined effects originating from both parton shower and from HEJ, and indicate that we have ensured there is no double counting of emissions. This work therefore provides

a proof of concept for this method. Nevertheless, it is still necessary to perform a systematic study on the impact of scale and PDF choices.

Notwithstanding what has been so far achieved, what has been presented constitutes a first attempt at merging HEJ with a parton shower. We envisage numerous refinements that can be made. There is a need to implement a prescription for incorporating non-FKL events into the merging procedure. In particular this is required to obtain the correct total cross section; it may also have an impact upon which states may be inserted by the parton shower, and potentially multiplicities in large rapidity intervals. Such a prescription would not require dramatic changes to the algorithm. Firstly, the definition of what constitutes a HEJ state would need to be extended; secondly, the appropriate tree-level matrix elements should be used when calculating the veto probability of trial emissions. In addition, as discussed in section 5.1.3, a limitation to the method is that only the hardest emissions are correctly described by HEJ. This is a problem because the parton shower may generate HEJ states from a non-HEJ states above the merging scale. To resolve this issue will require further study.

It is also important to implement this method for processes other than those which are purely QCD. Since one of the primary motivations was to assess the impact of jet vetoes that are relevant for Higgs plus dijets studies, this process is the next natural extension. Finally, although we chose to implement this method for PYTHIA, in principle it should be possible to implement for other parton showers. It would be interesting to compare the effect of merging HEJ with different choices of parton shower.

It is intriguing that PYTHIA performs as well or better than the predictions for PYTHIA+POWHEG provided for the original experimental studies. There are parameters in PYTHIA which are tuned to data that facilitate the modelling of non-perturbative effects; one would not expect this to have an impact on observables which measure the number of hard emissions. It would therefore be worthwhile to investigate what is the impact of tuning on the observables we have considered, and determine whether this is consistent with what is expected for soft QCD.

Although we have been able to draw many positive conclusions by comparing

174

with experimental data, in many cases the error bars on data are large, and the cuts that were chosen are not conducive to examining the effect of high energy logarithms. Both these points entail that it is difficult to discriminate between theoretical predictions that model different physics and should be expected to differ. We hope that as more data is collected, future analyses will examine a similar set of observables but with a more inclusive cut selection.

This work has reinforced the notion that the interplay between different types of logarithms is not necessarily straightforward, and that there are circumstances under which the combination of two all order summations is necessary. We hope that the merging algorithm we have developed may be used in future as a tool to inform analyses what selection of cuts and observables are sensitive to parton shower effects, high energy effects, or both.

Chapter 6

Conclusions

At its inception the LHC was often touted as a machine for discovering new physics, and yet so far there has been no conclusive evidence for physics beyond the Standard Model observed in any of its many searches. This has necessitated the exploration of increasingly extreme regions of phase space and the scrutiny of ever more rare Standard Model processes. These experimental activities are supported by the development of sophisticated theoretical tools for modelling the expected backgrounds in these searches.

As we have discussed earlier in this thesis, one area of particular interest is the production of a Higgs boson in association with dijets through vector boson fusion. This channel may be enhanced with respect to gluon fusion and thereby studied through the application of cuts requiring large invariant dijet masses, rapidity separations and jet vetoes. In addition, distributions of large invariant masses are of interest in their own right since undiscovered heavy coloured particles could appear here as resonances. In such scenarios, there is an opening of phase space and the probability for semi-hard wide-angle emissions is enhanced. Specifically, higher order corrections to the cross section are accompanied by the appearance of large logarithms that spoil the convergence of fixed order calculations. More traditional approaches that combine fixed order calculations with a parton shower were found to underestimate the number of hard jets in such regions. The HEJ formalism introduced in chapter 2 was developed to sum these high energy logarithms to all orders and thereby provide an accurate description of perturbative QCD in the

high energy limit.

The approach of HEJ improved upon the earlier BFKL formalism in numerous ways. By using spinor helicity formalism it exposes high energy factorisation with a minimal level of approximation, such that integration of the amplitude may be performed in the full phase space. Secondly by matching to fixed order calculations, the normalisation of the total cross section may be correctly obtained. These features entail that HEJ can provide accurate theoretical predictions for hadron colliders such as the LHC. It has proved successful at describing large invariant mass distributions and the average number of jets in the interval between the two most extremal jets in rapidity. However, in regions of large jet transverse momenta the fixed order component of the cross section begins to dominate and the accuracy of the predictions is reduced. To improve the reliability of predictions for observables which probe this region, it is necessary to extend the HEJ formalism to next-to-leading logarithmic accuracy.

In chapter 4 we introduced a certain type of next-to-leading logarithmic correction to the process-dependent current factor of the amplitude. In the high energy limit, scattering occurs through colour octet exchange in the t-channel. At leading logarithmic accuracy, in processes that involve initial state quarks the most extremal outgoing partons must also be quarks. However at next-to-leading logarithmic accuracy, a gluon emission more extremal than the outgoing quark leg is permitted; this is known as an unordered emission. Whilst quark-initiated processes can be suppressed by PDFs, in the W plus jets production where at least one quark (or antiquark) must participate in the hard scattering such corrections can become significant. This channel being experimentally well constrained provides a useful avenue in which new theoretical tools may be tested.

In section 4.1.1 we performed an analytic calculation of the unordered current with W emission, and verified that it was gauge invariant in section 4.1.2. The implementation of this current for use in numerical calculations of the amplitude was verified in section 4.1.5 by ensuring the correct high energy behaviour is reproduced. For the calculation of the cross section, an improved sampling of phase space was deemed to be necessary. A study of the phase space generation was

177

6. Conclusions

performed in section 4.2.1 and validated in section 4.2.2. Finally the channels which could now be accommodated into the all order formalism needed to be removed from the matching procedure. This and the resulting thorough validation which was performed was discussed in section 4.3.

Comparisons between the HEJ formalism and ATLAS data for an analysis of W plus inclusive dijet production were made in section 4.4. Across a range of jet transverse momentum distributions it was found that the inclusion of unordered emissions in the all order formalism both reduced the fixed order component at large transverse momenta, and improved the agreement with data. The normalisation of the distribution of the invariant mass between the two hardest jets was reduced, though the shape was found to be relatively unaffected. Although one might have anticipated there to be no change at all in this distribution, the high energy limit is most applicable when the jets used are the most forwards and backwards jets in rapidity. We analysed the distribution of the rapidity separation between the most forwards and backwards jets, and found that despite a linear reduction in the fixed order component, the change in the total rate for large rapidity separations was minimal, which is consistent with our expectations.

Corrections of a similar size are to be expected with the forthcoming inclusion of quark-antiquark pairs in the final state, either as a correction to the Lipatov vertex or to the currents factors. The former has already been implemented for pure jets, and simply needs integrating into the implementation for W plus jets. We have already demonstrated in section 4.1.6 that the correction to the effective W current may be obtained from the unordered current by crossing symmetry. Therefore, the only significant remaining task for obtaining the full NLL correction to W plus jets is the modification of the matching procedure. We expect that the full correction will become available in the near future.

The impact of extending the HEJ formalism to include subleading logarithmic effects is the ability to describe observables which are sensitive to large transverse momenta, entailing that predictions may be applicable in a greater number of scenarios. However, these corrections will not be sufficient in regions of phase space where there are large transverse momentum hierarchies and soft-collinear

logarithms become important. One example is the average number of jets in the rapidity interval between two tagging jets as a function of the tagging jets' average transverse momenta. Such observables require the inclusion of a parton shower for an accurate description to be obtained. The first attempt to combine HEJ with a parton shower, implemented for ARIADNE, was largely successful; however, there were two notable shortcomings with this approach. Firstly, the effect of multiple parton interactions was not included. Secondly, certain HEJ configurations limited the phase space for a full parton shower evolution. These effects were noticeable for example in distributions of jet shapes.

In order to address these issues, a merging algorithm inspired by CKKW-L was proposed. The implementation of this new approach was discussed in chapter 5. The implementation was validated in two ways. Firstly a comparison of the splitting functions for HEJ and PYTHIA, which are required to ensure the Sudakov factors are appropriately subtracted, was performed in section 5.2.1. The average splitting function for the first trial parton shower emission with respect to a $2 \to 2$ partonic configuration was shown as a function of both the transverse momentum of the trial emission, and the angular distance to the nearest parton. The splitting functions demonstrated the expected qualitative behaviour, and gave a visual representation of the expected outcome of the vetoing procedure. The second step of validation performed in section 5.2.2 involved the generation of two- and three-parton HEJ-like events using the parton shower, and ensuring that the effect of merging these events was indistinguishable from the process of simply showering two-parton HEJ-like events. This procedure ensures that there is a full coverage of phase space without any double counting of emissions.

In section 5.3 we demonstrated that our new merging algorithm indeed accommodates an improved description of jet shape observables, indicating that the parton shower evolution is no longer improperly restricted. We further examined a set of observables which measure the amount of additional radiation in the rapidity interval between a pair of jets. We find that in the average number of jets and gap fractions, both as a function of the size of rapidity interval and the dijets' average transverse momentum, there is a good agreement between HEJ+PYTHIA and data.

6. Conclusions

It appears that parton shower effects are being incorporated into HEJ, whilst high jet multiplicity events are added relative to PYTHIA. The work presented therefore delivers proof of concept for our merging procedure. As outlined in section 5.4, we envisage numerous extensions that can be made to the current implementation. Nevertheless, we hope that it proves informative for the design of future experimental analyses.

In this thesis, we have aimed to provide a more accurate modelling of QCD in extreme regions of phase space, allowing for increasingly rigorous testing of the Standard Model. Optimistically, we can hope this will facilitate the discovery of new physics. Alternatively, it will tighten the constraints on what BSM physics is allowed, whilst simultaneously improving our understanding of Standard Model phenomenology in the high energy limit.

Bibliography

[1] **ATLAS** Collaboration, G. Aad *et al.*, "Observation of a new particle in the search for the Standard Model Higgs boson with the ATLAS detector at the LHC," *Phys. Lett.* **B716** (2012) 1–29, `arXiv:1207.7214 [hep-ex]`.

[2] **CMS** Collaboration, S. Chatrchyan *et al.*, "Observation of a new boson at a mass of 125 GeV with the CMS experiment at the LHC," *Phys. Lett.* **B716** (2012) 30–61, `arXiv:1207.7235 [hep-ex]`.

[3] **ATLAS** Collaboration. `atlas.web.cern.ch/Atlas/GROUPS/PHYSICS/CombinedSummaryPlots/SM/`.

[4] **CMS** Collaboration. `twiki.cern.ch/twiki/bin/view/CMSPublic/PhysicsResultsCombined`.

[5] **Super-Kamiokande** Collaboration, Y. Fukuda *et al.*, "Evidence for oscillation of atmospheric neutrinos," *Phys. Rev. Lett.* **81** (1998) 1562–1567, `arXiv:hep-ex/9807003 [hep-ex]`.

[6] **SNO** Collaboration, Q. R. Ahmad *et al.*, "Measurement of the rate of $\nu_e + d \rightarrow p + p + e^-$ interactions produced by ^8B solar neutrinos at the Sudbury Neutrino Observatory," *Phys. Rev. Lett.* **87** (2001) 071301, `arXiv:nucl-ex/0106015 [nucl-ex]`.

[7] E. Ma, "Pathways to naturally small neutrino masses," *Phys. Rev. Lett.* **81** (1998) 1171–1174, `arXiv:hep-ph/9805219 [hep-ph]`.

[8] G. Bertone, D. Hooper, and J. Silk, "Particle dark matter: Evidence, candidates and constraints," *Phys. Rept.* **405** (2005) 279–390, `arXiv:hep-ph/0404175 [hep-ph]`.

[9] M. E. Peskin and D. V. Schroeder, *An Introduction to Quantum Field Theory*. Westview, 1995.

[10] M. D. Schwartz, *Quantum Field Theory and the Standard Model*. Cambridge University Press, 2014.

[11] R. K. Ellis, W. J. Stirling, and B. R. Webber, *QCD and Collider Physics*, vol. 8 of *Camb. Monogr. Part. Phys. Nucl. Phys. Cosmol.* Cambridge University Press, 1996.

[12] D. Griffiths, *Introduction to elementary particles*. Wiley, New York, NY, 2008.

[13] F. Halzen and A. Martin, *Quarks and Leptons: An Introductory Course in Modern Particle Physics*. Wiley, 1984.

[14] M. Gell-Mann and Y. Neemam, *The Eightfold Way: A Review, with a Collection of Reprints*. Frontiers in Physics. W.A. Benjamin, 1964.

[15] M. Gell-Mann, "A Schematic Model of Baryons and Mesons," *Phys. Lett.* **8** (1964) 214–215.

[16] G. Zweig, "An SU(3) model for strong interaction symmetry and its breaking. Version 1,".

[17] G. Zweig, "An SU(3) model for strong interaction symmetry and its breaking. Version 2," in *Developments in the Quark Theory of Hadrons, Volume 1.*, D. Lichtenberg and S. P. Rosen, eds., pp. 22–101. Hadronic Press, 1964.

[18] **E598** Collaboration, J. J. Aubert *et al.*, "Experimental Observation of a Heavy Particle J," *Phys. Rev. Lett.* **33** (1974) 1404–1406.

[19] **SLAC-SP-017** Collaboration, J. E. Augustin *et al.*, "Discovery of a Narrow Resonance in e^+e^- Annihilation," *Phys. Rev. Lett.* **33** (1974) 1406–1408. [Adv. Exp. Phys.5,141(1976)].

[20] S. W. Herb *et al.*, "Observation of a Dimuon Resonance at 9.5-GeV in 400-GeV Proton-Nucleus Collisions," *Phys. Rev. Lett.* **39** (1977) 252–255.

[21] **CDF** Collaboration, F. Abe *et al.*, "Observation of top quark production in $\bar{p}p$ collisions," *Phys. Rev. Lett.* **74** (1995) 2626–2631, `arXiv:hep-ex/9503002 [hep-ex]`.

[22] **D0** Collaboration, S. Abachi *et al.*, "Observation of the top quark," *Phys. Rev. Lett.* **74** (1995) 2632–2637, `arXiv:hep-ex/9503003 [hep-ex]`.

[23] O. W. Greenberg, "Spin and Unitary Spin Independence in a Paraquark Model of Baryons and Mesons," *Phys. Rev. Lett.* **13** (1964) 598–602.

[24] G. Miller *et al.*, "Inelastic electron-Proton Scattering at Large Momentum Transfers," *Phys. Rev.* **D5** (1972) 528.

[25] D. J. Gross and F. Wilczek, "Ultraviolet Behavior of Nonabelian Gauge Theories," *Phys. Rev. Lett.* **30** (1973) 1343–1346.

[26] H. D. Politzer, "Reliable Perturbative Results for Strong Interactions?," *Phys. Rev. Lett.* **30** (1973) 1346–1349.

[27] J. M. Pendlebury *et al.*, "Revised experimental upper limit on the electric dipole moment of the neutron," *Phys. Rev.* **D92** no. 9, (2015) 092003, `arXiv:1509.04411 [hep-ex]`.

[28] R. D. Peccei and H. R. Quinn, "Constraints Imposed by CP Conservation in the Presence of Instantons," *Phys. Rev.* **D16** (1977) 1791–1797.

[29] L. J. Dixon, "Calculating scattering amplitudes efficiently," in *QCD and beyond. Proceedings, Theoretical Advanced Study Institute in Elementary Particle Physics, TASI-95, Boulder, USA, June 4-30, 1995*, pp. 539–584. 1996. `arXiv:hep-ph/9601359 [hep-ph]`.

[30] H. Lehmann, K. Symanzik, and W. Zimmermann, "On the formulation of quantized field theories," *Nuovo Cim.* **1** (1955) 205–225.

[31] **Particle Data Group** Collaboration, C. Patrignani *et al.*, "Review of Particle Physics," *Chin. Phys.* **C40** no. 10, (2016) 100001.

[32] F. Bloch and A. Nordsieck, "Note on the Radiation Field of the electron," *Phys. Rev.* **52** (1937) 54–59.

[33] T. Kinoshita, "Mass singularities of Feynman amplitudes," *J. Math. Phys.* **3** (1962) 650–677.

[34] T. D. Lee and M. Nauenberg, "Degenerate Systems and Mass Singularities," *Phys. Rev.* **133** (1964) B1549–B1562. [,25(1964)].

[35] **BCDMS** Collaboration, A. C. Benvenuti *et al.*, "A High Statistics Measurement of the Proton Structure Functions $F_2(x, Q^2)$ and R from Deep Inelastic Muon Scattering at High Q^2," *Phys. Lett.* **B223** (1989) 485–489.

[36] **H1** Collaboration, T. Ahmed *et al.*, "A Measurement of the proton structure function $F_2(x, Q^2)$," *Nucl. Phys.* **B439** (1995) 471–502, `arXiv:hep-ex/9503001 [hep-ex]`.

[37] **ZEUS** Collaboration, M. Derrick *et al.*, "Measurement of the proton structure function F2 from the 1993 HERA data," *Z. Phys.* **C65** (1995) 379–398.

[38] J. D. Bjorken, "Asymptotic Sum Rules at Infinite Momentum," *Phys. Rev.* **179** (1969) 1547–1553.

[39] J. C. Collins, D. E. Soper, and G. F. Sterman, "Transverse Momentum Distribution in Drell-Yan Pair and W and Z Boson Production," *Nucl. Phys.* **B250** (1985) 199–224.

[40] J. C. Collins, D. E. Soper, and G. F. Sterman, "Factorization for Short Distance Hadron - Hadron Scattering," *Nucl. Phys.* **B261** (1985) 104–142.

[41] J. Collins, *Foundations of Perturbative QCD.* Cambridge Monographs on Particle Physics, Nuclear Physics and Cosmology. Cambridge University Press, 2011.

[42] S. Catani and M. H. Seymour, "A General algorithm for calculating jet cross-sections in NLO QCD," *Nucl. Phys.* **B485** (1997) 291–419, `arXiv:hep-ph/9605323 [hep-ph]`. [Erratum: Nucl. Phys.B510,503(1998)].

[43] S. Frixione, Z. Kunszt, and A. Signer, "Three jet cross-sections to next-to-leading order," *Nucl. Phys.* **B467** (1996) 399–442, `arXiv:hep-ph/9512328 [hep-ph]`.

[44] D. A. Kosower, "Antenna factorization of gauge theory amplitudes," *Phys. Rev.* **D57** (1998) 5410–5416, `arXiv:hep-ph/9710213 [hep-ph]`.

[45] J. M. Campbell, M. A. Cullen, and E. W. N. Glover, "Four jet event shapes in electron - positron annihilation," *Eur. Phys. J.* **C9** (1999) 245–265, `arXiv:hep-ph/9809429 [hep-ph]`.

[46] D. A. Kosower, "Antenna factorization in strongly ordered limits," *Phys. Rev.* **D71** (2005) 045016, `arXiv:hep-ph/0311272 [hep-ph]`.

[47] T. Gleisberg and F. Krauss, "Automating dipole subtraction for QCD NLO calculations," *Eur. Phys. J.* **C53** (2008) 501–523, `arXiv:0709.2881 [hep-ph]`.

[48] S. Platzer and S. Gieseke, "Dipole Showers and Automated NLO Matching in Herwig++," *Eur. Phys. J.* **C72** (2012) 2187, `arXiv:1109.6256 [hep-ph]`.

[49] G. Bevilacqua, M. Czakon, M. V. Garzelli, A. van Hameren, A. Kardos, C. G. Papadopoulos, R. Pittau, and M. Worek, "HELAC-NLO," *Comput. Phys. Commun.* **184** (2013) 986–997, `arXiv:1110.1499 [hep-ph]`.

[50] J. Alwall, R. Frederix, S. Frixione, V. Hirschi, F. Maltoni, O. Mattelaer, H. S. Shao, T. Stelzer, P. Torrielli, and M. Zaro, "The automated

computation of tree-level and next-to-leading order differential cross sections, and their matching to parton shower simulations," *JHEP* **07** (2014) 079, `arXiv:1405.0301 [hep-ph]`.

[51] M. Cacciari, G. P. Salam, and G. Soyez, "FastJet User Manual," *Eur. Phys. J.* **C72** (2012) 1896, `arXiv:1111.6097 [hep-ph]`.

[52] S. Catani, Y. L. Dokshitzer, M. H. Seymour, and B. R. Webber, "Longitudinally invariant K_t clustering algorithms for hadron hadron collisions," *Nucl. Phys.* **B406** (1993) 187–224.

[53] S. D. Ellis and D. E. Soper, "Successive combination jet algorithm for hadron collisions," *Phys. Rev.* **D48** (1993) 3160–3166, `arXiv:hep-ph/9305266 [hep-ph]`.

[54] Y. L. Dokshitzer, G. D. Leder, S. Moretti, and B. R. Webber, "Better jet clustering algorithms," *JHEP* **08** (1997) 001, `arXiv:hep-ph/9707323 [hep-ph]`.

[55] M. Wobisch and T. Wengler, "Hadronization corrections to jet cross-sections in deep inelastic scattering," in *Monte Carlo generators for HERA physics. Proceedings, Workshop, Hamburg, Germany, 1998-1999*, pp. 270–279. 1998. `arXiv:hep-ph/9907280 [hep-ph]`.

[56] M. Cacciari, G. P. Salam, and G. Soyez, "The Anti-k(t) jet clustering algorithm," *JHEP* **04** (2008) 063, `arXiv:0802.1189 [hep-ph]`.

[57] **ATLAS** Collaboration, G. Aad *et al.*, "Measurement of the $W \to \ell\nu$ and $Z/\gamma^* \to \ell\ell$ production cross sections in proton-proton collisions at $\sqrt{s} = 7$ TeV with the ATLAS detector," *JHEP* **12** (2010) 060, `arXiv:1010.2130 [hep-ex]`.

[58] A. Gehrmann-De Ridder, T. Gehrmann, E. W. N. Glover, and G. Heinrich, "NNLO corrections to event shapes in e+ e- annihilation," *JHEP* **12** (2007) 094, `arXiv:0711.4711 [hep-ph]`.

[59] R. Hamberg, W. L. van Neerven, and T. Matsuura, "A complete calculation of the order $\alpha - s^2$ correction to the Drell-Yan K factor," *Nucl. Phys.* **B359** (1991) 343–405. [Erratum: Nucl. Phys.B644,403(2002)].

[60] W. L. van Neerven and E. B. Zijlstra, "The $O(\alpha_s^2)$ corrected Drell-Yan K factor in the DIS and MS scheme," *Nucl. Phys.* **B382** (1992) 11–62. [Erratum: Nucl. Phys.B680,513(2004)].

[61] C. Anastasiou, L. J. Dixon, K. Melnikov, and F. Petriello, "High precision QCD at hadron colliders: Electroweak gauge boson rapidity distributions at NNLO," *Phys. Rev.* **D69** (2004) 094008, `arXiv:hep-ph/0312266 [hep-ph]`.

[62] **ALEPH** Collaboration, D. Buskulic *et al.*, "Studies of QCD in $e^+e^- \rightarrow$ hadrons at E_{cm} = 130 and 136 GeV," *Z. Phys.* **C73** (1997) 409–420.

[63] **ALEPH** Collaboration, A. Heister *et al.*, "Studies of QCD at e^+e^- centre-of-mass energies between 91 and 209 GeV," *Eur. Phys. J.* **C35** (2004) 457–486.

[64] S. Brandt, C. Peyrou, R. Sosnowski, and A. Wroblewski, "The Principal axis of jets. An Attempt to analyze high-energy collisions as two-body processes," *Phys. Lett.* **12** (1964) 57–61.

[65] E. Farhi, "A QCD Test for Jets," *Phys. Rev. Lett.* **39** (1977) 1587–1588.

[66] T. Becher and M. D. Schwartz, "A precise determination of α_s from LEP thrust data using effective field theory," *JHEP* **07** (2008) 034, `arXiv:0803.0342 [hep-ph]`.

[67] A. Buckley *et al.*, "General-purpose event generators for LHC physics," *Phys. Rept.* **504** (2011) 145–233, `arXiv:1101.2599 [hep-ph]`.

[68] T. Sjöstrand and P. Z. Skands, "Transverse-momentum-ordered showers and interleaved multiple interactions," *Eur. Phys. J.* **C39** (2005) 129–154, `arXiv:hep-ph/0408302 [hep-ph]`.

[69] T. Sjöstrand, S. Mrenna, and P. Z. Skands, "PYTHIA 6.4 Physics and Manual," *JHEP* **05** (2006) 026, `arXiv:hep-ph/0603175 [hep-ph]`.

[70] G. Corcella, I. G. Knowles, G. Marchesini, S. Moretti, K. Odagiri, P. Richardson, M. H. Seymour, and B. R. Webber, "HERWIG 6: An Event generator for hadron emission reactions with interfering gluons (including supersymmetric processes)," *JHEP* **01** (2001) 010, `arXiv:hep-ph/0011363 [hep-ph]`.

[71] G. Marchesini and B. R. Webber, "Simulation of QCD Jets Including Soft Gluon Interference," *Nucl. Phys.* **B238** (1984) 1–29.

[72] G. Gustafson, "Dual Description of a Confined Color Field," *Phys. Lett.* **B175** (1986) 453. [,193(1986)].

[73] G. Gustafson and U. Pettersson, "Dipole Formulation of QCD Cascades," *Nucl. Phys.* **B306** (1988) 746–758.

[74] B. Andersson, G. Gustafson, L. Lönnblad, and U. Pettersson, "Coherence Effects in Deep Inelastic Scattering," *Z. Phys.* **C43** (1989) 625.

[75] L. Lönnblad, "ARIADNE version 4: A Program for simulation of QCD cascades implementing the color dipole model," *Comput. Phys. Commun.* **71** (1992) 15–31.

[76] S. Schumann and F. Krauss, "A Parton shower algorithm based on Catani-Seymour dipole factorisation," *JHEP* **03** (2008) 038, `arXiv:0709.1027 [hep-ph]`.

[77] T. Sjöstrand, S. Mrenna, and P. Z. Skands, "A Brief Introduction to PYTHIA 8.1," *Comput. Phys. Commun.* **178** (2008) 852–867, `arXiv:0710.3820 [hep-ph]`.

[78] J. Bellm *et al.*, "Herwig 7.0/Herwig++ 3.0 release note," *Eur. Phys. J.* **C76** no. 4, (2016) 196, `arXiv:1512.01178 [hep-ph]`.

[79] P. Nason, "A New method for combining NLO QCD with shower Monte Carlo algorithms," *JHEP* **11** (2004) 040, `arXiv:hep-ph/0409146 [hep-ph]`.

[80] S. Frixione and B. R. Webber, "Matching NLO QCD computations and parton shower simulations," *JHEP* **06** (2002) 029, `arXiv:hep-ph/0204244 [hep-ph]`.

[81] S. Frixione and B. R. Webber, "The MC@NLO 3.3 Event Generator," `arXiv:hep-ph/0612272 [hep-ph]`.

[82] S. Catani, F. Krauss, R. Kuhn, and B. R. Webber, "QCD matrix elements + parton showers," *JHEP* **11** (2001) 063, `arXiv:hep-ph/0109231 [hep-ph]`.

[83] F. Krauss, "Matrix elements and parton showers in hadronic interactions," *JHEP* **08** (2002) 015, `arXiv:hep-ph/0205283 [hep-ph]`.

[84] L. Lönnblad, "Correcting the color dipole cascade model with fixed order matrix elements," *JHEP* **05** (2002) 046, `arXiv:hep-ph/0112284 [hep-ph]`.

[85] A. Schalicke and F. Krauss, "Implementing the ME+PS merging algorithm," *JHEP* **07** (2005) 018, `arXiv:hep-ph/0503281 [hep-ph]`.

[86] K. Hamilton, P. Richardson, and J. Tully, "A Modified CKKW matrix element merging approach to angular-ordered parton showers," *JHEP* **11** (2009) 038, `arXiv:0905.3072 [hep-ph]`.

[87] L. Lönnblad and S. Prestel, "Matching Tree-Level Matrix Elements with Interleaved Showers," *JHEP* **03** (2012) 019, `arXiv:1109.4829 [hep-ph]`.

[88] M. L. Mangano, M. Moretti, F. Piccinini, and M. Treccani, "Matching matrix elements and shower evolution for top-quark production in hadronic collisions," *JHEP* **01** (2007) 013, `arXiv:hep-ph/0611129 [hep-ph]`.

[89] S. Mrenna and P. Richardson, "Matching matrix elements and parton showers with HERWIG and PYTHIA," *JHEP* **05** (2004) 040, `arXiv:hep-ph/0312274 [hep-ph]`.

[90] L. Lönnblad and S. Prestel, "Unitarising Matrix Element + Parton Shower merging," *JHEP* **02** (2013) 094, `arXiv:1211.4827 [hep-ph]`.

[91] N. Lavesson and L. Lönnblad, "Extending CKKW-merging to One-Loop Matrix Elements," *JHEP* **12** (2008) 070, `arXiv:0811.2912 [hep-ph]`.

[92] K. Hamilton and P. Nason, "Improving NLO-parton shower matched simulations with higher order matrix elements," *JHEP* **06** (2010) 039, `arXiv:1004.1764 [hep-ph]`.

[93] L. Lönnblad and S. Prestel, "Merging Multi-leg NLO Matrix Elements with Parton Showers," *JHEP* **03** (2013) 166, `arXiv:1211.7278 [hep-ph]`.

[94] T. Han, I. Lewis, and Z. Liu, "Colored Resonant Signals at the LHC: Largest Rate and Simplest Topology," *JHEP* **12** (2010) 085, `arXiv:1010.4309 [hep-ph]`.

[95] **CMS** Collaboration, A. M. Sirunyan *et al.*, "Search for dijet resonances in proton-proton collisions at sqrt(s) = 13 TeV and constraints on dark matter and other models," *Phys. Lett. B* (2016) , `arXiv:1611.03568 [hep-ex]`.

[96] **ATLAS** Collaboration, M. Aaboud *et al.*, "Search for new phenomena in dijet events using 37 fb^{-1} of pp collision data collected at $\sqrt{s}$ =13 TeV with the ATLAS detector," `arXiv:1703.09127 [hep-ex]`.

[97] R. M. Harris and K. Kousouris, "Searches for Dijet Resonances at Hadron Colliders," *Int. J. Mod. Phys.* **A26** (2011) 5005–5055, `arXiv:1110.5302 [hep-ex]`.

[98] V. Del Duca, W. Kilgore, C. Oleari, C. Schmidt, and D. Zeppenfeld, "Gluon fusion contributions to H + 2 jet production," *Nucl. Phys.* **B616** (2001) 367–399, `arXiv:hep-ph/0108030 [hep-ph]`.

[99] G. Klamke and D. Zeppenfeld, "Higgs plus two jet production via gluon fusion as a signal at the CERN LHC," *JHEP* **04** (2007) 052, `arXiv:hep-ph/0703202 [HEP-PH]`.

[100] J. R. Andersen, K. Arnold, and D. Zeppenfeld, "Azimuthal Angle Correlations for Higgs Boson plus Multi-Jet Events," *JHEP* **06** (2010) 091, `arXiv:1001.3822 [hep-ph]`.

[101] P. D. B. Collins, *An Introduction to Regge Theory and High-Energy Physics.* Cambridge Monographs on Mathematical Physics. Cambridge Univ. Press, Cambridge, UK, 2009.

[102] J. R. Forshaw and D. A. Ross, "Quantum chromodynamics and the pomeron," *Cambridge Lect. Notes Phys.* **9** (1997) 1–248.

[103] V. Del Duca, "An introduction to the perturbative QCD pomeron and to jet physics at large rapidities," `arXiv:hep-ph/9503226 [hep-ph]`.

[104] L. N. Lipatov, "Reggeization of the Vector Meson and the Vacuum Singularity in Nonabelian Gauge Theories," *Sov. J. Nucl. Phys.* **23** (1976) 338–345. [Yad. Fiz.23,642(1976)].

[105] J. Bartels, "A Reggeon Calculus for the Production Amplitude. 1.," *Phys. Rev.* **D11** no. 10, (1975) 2977.

[106] L. N. Lipatov, "POMERON IN QUANTUM CHROMODYNAMICS," *Adv. Ser. Direct. High Energy Phys.* **5** (1989) 411–489.

[107] V. S. Fadin, E. A. Kuraev, and L. N. Lipatov, "On the Pomeranchuk Singularity in Asymptotically Free Theories," *Phys. Lett.* **B60** (1975) 50–52.

[108] E. A. Kuraev, L. N. Lipatov, and V. S. Fadin, "Multi - Reggeon Processes in the Yang-Mills Theory," *Sov. Phys. JETP* **44** (1976) 443–450. [Zh. Eksp. Teor. Fiz.71,840(1976)].

[109] E. A. Kuraev, L. N. Lipatov, and V. S. Fadin, "The Pomeranchuk Singularity in Nonabelian Gauge Theories," *Sov. Phys. JETP* **45** (1977) 199–204. [Zh. Eksp. Teor. Fiz.72,377(1977)].

[110] I. I. Balitsky and L. N. Lipatov, "The Pomeranchuk Singularity in Quantum Chromodynamics," *Sov. J. Nucl. Phys.* **28** (1978) 822–829. [Yad. Fiz.28,1597(1978)].

[111] V. Del Duca and E. W. N. Glover, "The High-energy limit of QCD at two loops," *JHEP* **10** (2001) 035, `arXiv:hep-ph/0109028 [hep-ph]`.

[112] V. Del Duca, G. Falcioni, L. Magnea, and L. Vernazza, "Analyzing high-energy factorization beyond next-to-leading logarithmic accuracy," *JHEP* **02** (2015) 029, `arXiv:1409.8330 [hep-ph]`.

[113] V. S. Fadin, M. G. Kozlov, and A. V. Reznichenko, "Radiative corrections to QCD amplitudes in quasimulti - Regge kinematics," *Phys. Atom. Nucl.* **67** (2004) 359–375, `arXiv:hep-ph/0302224 [hep-ph]`. [Yad. Fiz.67,377(2004)].

[114] V. S. Fadin, "The Gluon Reggeization in perturbative QCD at NLO," in *11th International Conference on Elastic and Diffractive Scattering: Towards High Energy Frontiers: The 20th Anniversary of the Blois Workshops, 17th Rencontre de Blois (EDS 05) Chateau de Blois, Blois, France, May 15-20, 2005.* 2005. `arXiv:hep-ph/0511121 [hep-ph]`.

[115] V. S. Fadin, R. Fiore, M. G. Kozlov, and A. V. Reznichenko, "Proof of the multi-Regge form of QCD amplitudes with gluon exchanges in the NLA," *Phys. Lett.* **B639** (2006) 74–81, `arXiv:hep-ph/0602006 [hep-ph]`.

[116] A. V. Bogdan and V. S. Fadin, "A Proof of the reggeized form of amplitudes with quark exchanges," *Nucl. Phys.* **B740** (2006) 36–57, `arXiv:hep-ph/0601117 [hep-ph]`.

[117] J. R. Andersen and J. M. Smillie, "Constructing All-Order Corrections to Multi-Jet Rates," *JHEP* **01** (2010) 039, `arXiv:0908.2786 [hep-ph]`.

[118] **CMS** Collaboration, G. L. Bayatian *et al.*, "CMS physics: Technical design report,".

[119] **ATLAS** Collaboration, G. Aad *et al.*, "The ATLAS Experiment at the CERN Large Hadron Collider," *JINST* **3** (2008) S08003.

[120] **D0** Collaboration, V. M. Abazov *et al.*, "Measurement of the ratios of the $Z/\gamma^*+ \geq n$ jet production cross sections to the total inclusive Z/γ^* cross section in p anti-p collisions at $\sqrt{s} = 1.96$ TeV," *Phys. Lett.* **B658** (2008) 112–119, arXiv:hep-ex/0608052 [hep-ex].

[121] **CDF** Collaboration, T. Aaltonen *et al.*, "Measurement of inclusive jet cross-sections in $Z/\gamma^* \to e^+e^- +$ jets production in $p\bar{p}$ collisions at $\sqrt{s} = 1.96$ TeV," *Phys. Rev. Lett.* **100** (2008) 102001, arXiv:0711.3717 [hep-ex].

[122] **D0** Collaboration, V. M. Abazov *et al.*, "Measurements of differential cross sections of Z/γ^*+jets+X events in proton anti-proton collisions at $\sqrt{s} = 1.96$ TeV," *Phys. Lett.* **B678** (2009) 45–54, arXiv:0903.1748 [hep-ex].

[123] J. R. Andersen and J. M. Smillie, "The Factorisation of the t-channel Pole in Quark-Gluon Scattering," *Phys. Rev.* **D81** (2010) 114021, arXiv:0910.5113 [hep-ph].

[124] J. R. Andersen and J. M. Smillie, "Multiple Jets at the LHC with High Energy Jets," *JHEP* **06** (2011) 010, arXiv:1101.5394 [hep-ph].

[125] J. R. Andersen, T. Hapola, and J. M. Smillie, "W Plus Multiple Jets at the LHC with High Energy Jets," *JHEP* **09** (2012) 047, arXiv:1206.6763 [hep-ph].

[126] J. R. Andersen, J. J. Medley, and J. M. Smillie, "Z/γ plus multiple hard jets in high energy collisions," *JHEP* **05** (2016) 136, arXiv:1603.05460 [hep-ph].

[127] J. R. Andersen, T. Hapola, A. Maier, and J. M. Smillie, "Higgs Boson Plus Dijets: Higher Order Corrections," arXiv:1706.01002 [hep-ph].

[128] V. S. Fadin, "BFKL news," in *High energy physics. Proceedings, LAFEX International School, Session C, Workshop on Diffractive Physics, LISHEP'98, Rio de Janeiro, Brazil, February 16-20, 1998*, pp. 742–776. 1998. arXiv:hep-ph/9807528 [hep-ph].

[129] J. Alwall, P. Demin, S. de Visscher, R. Frederix, M. Herquet, F. Maltoni, T. Plehn, D. L. Rainwater, and T. Stelzer, "MadGraph/MadEvent v4: The New Web Generation," *JHEP* **09** (2007) 028, `arXiv:0706.2334 [hep-ph]`.

[130] **D0** Collaboration, V. M. Abazov *et al.*, "Studies of W boson plus jets production in $p\bar{p}$ collisions at $\sqrt{s} = 1.96$ TeV," *Phys. Rev.* **D88** no. 9, (2013) 092001, `arXiv:1302.6508 [hep-ex]`.

[131] **ATLAS** Collaboration, G. Aad *et al.*, "Measurements of the W production cross sections in association with jets with the ATLAS detector," *Eur. Phys. J.* **C75** no. 2, (2015) 82, `arXiv:1409.8639 [hep-ex]`.

[132] M. Campanelli, "Forward jets and large rapidity gaps," *Int. J. Mod. Phys.* **A30** no. 31, (2015) 1546006, `arXiv:1508.04631 [hep-ph]`.

[133] J. R. Andersen, L. Lönnblad, and J. M. Smillie, "A Parton Shower for High Energy Jets," *JHEP* **07** (2011) 110, `arXiv:1104.1316 [hep-ph]`.

[134] L. Lönnblad, "Rapidity gaps and other final state properties in the color dipole model for deep inelastic scattering," *Z. Phys.* **C65** (1995) 285–292.

[135] E. Boos *et al.*, "Generic user process interface for event generators," in *Physics at TeV colliders. Proceedings, Euro Summer School, Les Houches, France, May 21-June 1, 2001*. 2001. `arXiv:hep-ph/0109068 [hep-ph]`.

[136] V. Del Duca, "Parke-Taylor amplitudes in the multi - Regge kinematics," *Phys. Rev.* **D48** (1993) 5133–5139, `arXiv:hep-ph/9304259 [hep-ph]`.

[137] V. Del Duca, "Equivalence of the Parke-Taylor and the Fadin-Kuraev-Lipatov amplitudes in the high-energy limit," *Phys. Rev.* **D52** (1995) 1527–1534, `arXiv:hep-ph/9503340 [hep-ph]`.

[138] **ATLAS** Collaboration, G. Aad *et al.*, "Measurements of jet vetoes and azimuthal decorrelations in dijet events produced in pp collisions at $\sqrt{s} = 7$ TeV using the ATLAS detector," *Eur. Phys. J.* **C74** no. 11, (2014) 3117, `arXiv:1407.5756 [hep-ex]`.

[139] S. Alioli, J. R. Andersen, C. Oleari, E. Re, and J. M. Smillie, "Probing higher-order corrections in dijet production at the LHC," *Phys. Rev.* **D85** (2012) 114034, `arXiv:1202.1475 [hep-ph]`.

[140] **ATLAS** Collaboration, G. Aad *et al.*, "Measurement of dijet production with a veto on additional central jet activity in pp collisions at $\sqrt{s} = 7$ TeV using the ATLAS detector," *JHEP* **09** (2011) 053, `arXiv:1107.1641 [hep-ex]`.

[141] K. F. Riley, S. J. Bence, and M. P. Hobson, *Mathematical methods for physics and engineering: a comprehensive guide.* Cambridge Univ. Press, Cambridge, 1997.

[142] F. James, "Monte Carlo Theory and Practice," *Rept. Prog. Phys.* **43** (1980) 1145.

[143] L. Lönnblad, "Fooling Around with the Sudakov Veto Algorithm," *Eur. Phys. J.* **C73** no. 3, (2013) 2350, `arXiv:1211.7204 [hep-ph]`.

[144] **CDF** Collaboration, T. Aaltonen *et al.*, "Measurement of the cross section for W^- boson production in association with jets in $p\bar{p}$ collisions at $\sqrt{s} = 1.96$ TeV," *Phys. Rev.* **D77** (2008) 011108, `arXiv:0711.4044 [hep-ex]`.

[145] **CMS** Collaboration, V. Khachatryan *et al.*, "Differential cross section measurements for the production of a W boson in association with jets in protonproton collisions at $\sqrt{s} = 7$ TeV," *Phys. Lett.* **B741** (2015) 12–37, `arXiv:1406.7533 [hep-ex]`.

[146] **CMS** Collaboration, V. Khachatryan *et al.*, "Measurements of differential cross sections for associated production of a W boson and jets in proton-proton collisions at $\sqrt{s} = 8$ TeV," *Phys. Rev. D* (2016) , `arXiv:1610.04222 [hep-ex]`. [Phys. Rev.D95,052002(2017)].

[147] **ATLAS** Collaboration, M. Aaboud *et al.*, "Measurements of electroweak Wjj production and constraints on anomalous gauge couplings with the ATLAS detector," `arXiv:1703.04362 [hep-ex]`.

[148] J. Alwall, M. Herquet, F. Maltoni, O. Mattelaer, and T. Stelzer, "MadGraph 5 : Going Beyond," *JHEP* **06** (2011) 128, arXiv:1106.0522 [hep-ph].

[149] J. F. Gunion and Z. Kunszt, "Improved Analytic Techniques for Tree Graph Calculations and the G g q anti-q Lepton anti-Lepton Subprocess," *Phys. Lett.* **B161** (1985) 333.

[150] A. D. Martin, W. J. Stirling, R. S. Thorne, and G. Watt, "Parton distributions for the LHC," *Eur. Phys. J.* **C63** (2009) 189–285, arXiv:0901.0002 [hep-ph].

[151] F. Maltoni and T. Stelzer, "MadEvent: Automatic event generation with MadGraph," *JHEP* **02** (2003) 027, arXiv:hep-ph/0208156 [hep-ph].

[152] M. L. Mangano, M. Moretti, F. Piccinini, R. Pittau, and A. D. Polosa, "ALPGEN, a generator for hard multiparton processes in hadronic collisions," *JHEP* **07** (2003) 001, arXiv:hep-ph/0206293 [hep-ph].

[153] H.-L. Lai, M. Guzzi, J. Huston, Z. Li, P. M. Nadolsky, J. Pumplin, and C. P. Yuan, "New parton distributions for collider physics," *Phys. Rev.* **D82** (2010) 074024, arXiv:1007.2241 [hep-ph].

[154] A. Buckley, J. Ferrando, S. Lloyd, K. Nordstrm, B. Page, M. Rfenacht, M. Schnherr, and G. Watt, "LHAPDF6: parton density access in the LHC precision era," *Eur. Phys. J.* **C75** (2015) 132, arXiv:1412.7420 [hep-ph].

[155] T. Sjostrand and M. van Zijl, "A Multiple Interaction Model for the Event Structure in Hadron Collisions," *Phys. Rev.* **D36** (1987) 2019.

[156] P. Z. Skands, "Tuning Monte Carlo Generators: The Perugia Tunes," *Phys. Rev.* **D82** (2010) 074018, arXiv:1005.3457 [hep-ph].

[157] **ATLAS** Collaboration, G. Aad *et al.*, "Study of Jet Shapes in Inclusive Jet Production in pp Collisions at $\sqrt{s} = 7$ TeV using the ATLAS Detector," *Phys. Rev.* **D83** (2011) 052003, arXiv:1101.0070 [hep-ex].

[158] S. Dulat, T.-J. Hou, J. Gao, M. Guzzi, J. Huston, P. Nadolsky, J. Pumplin, C. Schmidt, D. Stump, and C. P. Yuan, "New parton distribution functions from a global analysis of quantum chromodynamics," *Phys. Rev.* **D93** no. 3, (2016) 033006, arXiv:1506.07443 [hep-ph].

[159] P. Skands, S. Carrazza, and J. Rojo, "Tuning PYTHIA 8.1: the Monash 2013 Tune," *Eur. Phys. J.* **C74** no. 8, (2014) 3024, arXiv:1404.5630 [hep-ph].